



## 저작자표시-비영리-변경금지 2.0 대한민국

이용자는 아래의 조건을 따르는 경우에 한하여 자유롭게

- 이 저작물을 복제, 배포, 전송, 전시, 공연 및 방송할 수 있습니다.

다음과 같은 조건을 따라야 합니다:



저작자표시. 귀하는 원저작자를 표시하여야 합니다.



비영리. 귀하는 이 저작물을 영리 목적으로 이용할 수 없습니다.



변경금지. 귀하는 이 저작물을 개작, 변형 또는 가공할 수 없습니다.

- 귀하는, 이 저작물의 재이용이나 배포의 경우, 이 저작물에 적용된 이용허락조건을 명확하게 나타내어야 합니다.
- 저작권자로부터 별도의 허가를 받으면 이러한 조건들은 적용되지 않습니다.

저작권법에 따른 이용자의 권리는 위의 내용에 의하여 영향을 받지 않습니다.

이것은 [이용허락규약\(Legal Code\)](#)을 이해하기 쉽게 요약한 것입니다.

[Disclaimer](#)

공학박사 학위논문

Study on Radical Catalysis  
and Chemistry  
with Functionalized Metal Oxide  
Catalysts for Water Treatment

기능화된 금속산화물 수처리 촉매를 이용한  
라디칼 촉매반응과 화학에 관한 연구

2023 년 2 월

서울대학교 대학원  
재료공학부

최 윤 정

# Study on Radical Catalysis and Chemistry with Functionalized Metal Oxide Catalysts for Water Treatment

지도 교수 최 인 석

이 논문을 공학박사 학위논문으로 제출함

2023 년 2 월

서울대학교 대학원

재료공학부

최 윤 정

최 윤 정 의 공학박사 학위논문을 인준함

2022 년 12 월

위 원 장	남 기 태	(인)
부위원장	최 인 석	(인)
위 원	김 진 영	(인)
위 원	김 상 훈	(인)
위 원	김 종 식	(인)

# Abstract

This dissertation presents a method based on advanced oxidation processes for the efficient and stable treatment of sewage and wastewater, which is the key for controlling the pollution level of water systems in compliance with the recently strengthened water quality regulations and meet public expectations. Advanced oxidation processes are water treatment methods in which oxidizing and mineralizing organic matter are removed using a strong oxidizing agent such as the  $\cdot\text{OH}$  radical. Transition metal oxides have attracted considerable attention as materials that afford Lewis acidic metals to decompose hydrogen peroxide ( $\cdot\text{OH}$  radical precursor) and as alternatives to precious metals because of their reasonable price and their high stability. Organic matter is mineralized via  $\cdot\text{OH}$  addition or  $\cdot\text{H}$  abstraction in the presence of the  $\cdot\text{OH}$  radical. Although this radical exhibits the highest activity (highest reduction potential) among oxidizing agents for mineralization, but its use is limited because of its extremely short lifespan. In contrast, in the case of  $\text{SO}_4^{\cdot-}$  and  $\text{NO}_3^{\cdot}$ , have remarkably long lifetimes despite having slightly lower reduction potentials than that of  $\cdot\text{OH}$ ; moreover, they have can undergo electron transfer. Hence, if (1)  $\text{SO}_4^{\cdot-}$  and  $\text{NO}_3^{\cdot}$  can be respectively converted to  $\text{SO}_4^{2-}$  and  $\text{NO}_3^-$ , respectively, by receiving electrons from organic matter and subsequently reconverted to  $\text{SO}_4^{\cdot-}$  and  $\text{NO}_3^{\cdot}$ , respectively and (2) the oxidation–reduction phenomenon of the aforementioned radicals occurs stably, unlike that of  $\cdot\text{OH}$ , these radicals can be used numerous times to decompose organic matter. To this end, a methodology capable of easily generating radicals (such as  $\text{SO}_4^{\cdot-}$  and  $\text{NO}_3^{\cdot}$ ) only under limited or extreme



conditions must be developed. To achieve this, a methodology in which the  $\text{SO}_4^{2-}$  and  $\text{NO}_3^-$  functional groups are stably anchored on the surface of metal oxides and radicalized by losing one electron through a radical transfer mechanism is required.

This dissertation proposes a methodology to improve the mineralization efficiency of pollutants in sewage and wastewater using generated surface-immobilized radicals such as  $\text{SO}_4^{\bullet-}$  and  $\text{NO}_3^\bullet$  that are generated on various transition metal oxides. Metal oxides can be competitive platforms for accommodating Lewis acidic sites and the  $\text{SO}_4^{\bullet-}$  radical precursor ( $\text{SO}_4^{2-}$ ), both of which are suitable for activating the  $^\bullet\text{OH} \rightarrow \text{SO}_4^{\bullet-}$  pathway. We first utilized nickel oxide (NiO), which is a representative of monometallic oxide, and  $\text{Mn}_x\text{Fe}_{3-x}\text{O}_4$ —a model architecture—exhibiting system featuring bimetallic oxo-spinel surface modification with  $\text{SO}_4^{2-}$  functionalities—are activated by  $^\bullet\text{OH}$  species, thereby generating supported  $\text{SO}_4^{\bullet-}$  radicals via radical interconversion ( $^\bullet\text{OH} \leftrightarrow \text{SO}_4^{\bullet-}$ ). Additionally, manganese oxides ( $\alpha$ -/ $\beta$ -/ $\gamma$ - $\text{MnO}_2$ ) and zirconium oxide, which are applicable to reducible (heterolytic  $\text{H}_2\text{O}_2$  scission) and nonreducible metal oxides (homolytic  $\text{H}_2\text{O}_2$  scission) respectively, can be functionalized with  $\text{NO}_3^-$  species to verify the  $^\bullet\text{OH} \rightarrow \text{NO}_3^\bullet$  mechanism. This dissertation, hence, presents an altered methodology to mineralize the organic pollutants via radical transfer with higher efficiencies.

**Keywords :** Water treatment, Metal oxide, Lewis acidity, Radical catalysis, Functionalization

**Student Number :** 2018–30818

# Table of Contents

## Chapter 1. Introduction

1.1. Study Background.....	001
1.2. Advanced Oxidation Processes .....	003
1.2.1. Fenton reaction.....	003
1.2.2. Heterogeneous Fenton reaction.....	003
1.2.3. Photo-Fenton reaction .....	004
1.2.4. Sono-Fenton reaction .....	005
1.2.5. Electro-Fenton reaction .....	006
1.2.6. Sulfate-radical-based advanced oxidation processes .....	007
1.3. Thesis Objectives.....	008
1.4. Organization of the Thesis.....	009

## Chapter 2. Exploring catalytic traits of $\text{SO}_4^{2-}$ -functionalized NiO to prompt the radical interconversion of $\cdot\text{OH} \leftrightarrow \text{SO}_4^{\cdot-}$ exploited to decompose refractory pollutants

2.1. Introduction .....	012
2.2. Experimental Section.....	018
2.2.1. Catalysts .....	018
2.2.2. Characterizations.....	018
2.2.3. Reactions .....	021
2.2.4. Calculations.....	021
2.3. Results and Discussion.....	023
2.3.1. Catalysts .....	023
2.3.2. $\text{H}_2\text{O}_2$ scission cycle .....	032
2.3.3. Radical interconversion cycle .....	038
2.3.4. Sustainability .....	046
2.4. Conclusions .....	050

### Chapter 3. Tailoring Lewis acidic metals and $\text{SO}_4^{2-}$ functionalities on bimetallic Mn-Fe oxo-spinels to exploit supported $\text{SO}_4^{\bullet-}$ in aqueous pollutant fragmentation

3.1. Introduction .....	052
3.2. Experimental Section.....	059
3.2.1. Chemicals .....	059
3.2.2. Catalysts .....	060
3.2.3. Characterization techniques .....	061
3.2.4. Analytic techniques.....	063
3.2.5. Reactions .....	066
3.3. Results and Discussion.....	067
3.3.1. Generic properties for the catalysts .....	067
3.3.2. Properties germane to $\cdot\text{OH} \rightarrow \text{SO}_4^{\bullet-}$ for the catalysts.....	070
3.3.3. Kinetics of the $\cdot\text{OH} \rightarrow \text{SO}_4^{\bullet-}$ pathway .....	076
3.3.4. Feasibility of $\cdot\text{OH} \rightarrow \text{SO}_4^{\bullet-}$ .....	085
3.3.5. Practicability of $\cdot\text{OH} \rightarrow \text{SO}_4^{\bullet-}$ .....	095
3.4. Conclusions .....	100

### Chapter 4. Deciphering evolution pathway of supported $\text{NO}_3^{\bullet}$ enabled via radical transfer from $\cdot\text{OH}$ to surface $\text{NO}_3^-$ functionalized on $\text{MnO}_2$ for oxidative degradation of aqueous contaminants

4.1. Introduction .....	102
4.2. Experimental Section.....	109
4.2.1. Chemicals .....	109
4.2.2. Catalysts .....	110
4.2.3. Characterizations.....	111
4.2.4. Computations .....	114
4.2.5. Reactions .....	115
4.2.6. Analysis .....	116
4.3. Results and Discussion.....	119
4.3.1. Properties of $\alpha-\beta-\gamma-\text{MnO}_2$ .....	119
4.3.2. $\text{H}_2\text{O}_2$ scission kinetics on $\alpha-\beta-\gamma-\text{MnO}_2$ .....	125
4.3.3. Properties of $\alpha-\gamma-\text{MnO}_2\text{-N}$ .....	133
4.3.4. Viability of $\cdot\text{OH} \rightarrow \text{NO}_3^{\bullet}$ on $\alpha-\gamma-\text{MnO}_2\text{-N}$ .....	141
4.3.5. $\cdot\text{OH} \rightarrow \text{NO}_3^{\bullet}$ kinetics on $\alpha-\gamma-\text{MnO}_2\text{-N}$ .....	146
4.3.6. Merits of $\text{NO}_3^{\bullet}_{\text{SUP}}$ over $\cdot\text{OH}/\text{SO}_4^{\bullet-}_{\text{SUP}}$ .....	152
4.4. Conclusions .....	156

**Chapter 5. Deploying radical inter-transition from  $\cdot\text{OH}$  to supported  $\text{NO}_3^-$  on *mono*-dentate  $\text{NO}_3^-$ -modified  $\text{ZrO}_2$  to sustain fragmentation of aqueous contaminants**

5.1. Introduction .....	158
5.2. Methods .....	165
5.2.1. Catalysts .....	165
5.2.2. Characterizations.....	165
5.2.3. Computations .....	169
5.2.4. Reactions: textile wastewater degradation.....	172
5.3. Results and Discussion.....	173
5.3.1. Generic properties of $\text{ZrO}_2/\text{ZrO}_2\text{-N}$ .....	173
5.3.2. Acidic properties of $\text{ZrO}_2/\text{ZrO}_2\text{-N}$ .....	174
5.3.3. Properties of $\text{NO}_3^-$ functionalities .....	180
5.3.4. Proofs of $\cdot\text{OH} \rightarrow \text{NO}_3^-$ .....	183
5.3.5. Kinetics of homolytic $\text{H}_2\text{O}_2$ dissection and $\cdot\text{OH} \rightarrow \text{NO}_3^-$ cycles.....	189
5.3.6. Recyclability and practicability of $\text{ZrO}_2/\text{ZrO}_2\text{-N}$ .....	197
5.4. Conclusions .....	202

**Chapter 6. Summary and Future Work**

6.1. Summary .....	204
6.2. Future work and perspectives .....	208

<b>Bibilography.....</b>	<b>209</b>
--------------------------	------------

<b>Abstract in Korean.....</b>	<b>230</b>
--------------------------------	------------

## List of Figures

Figure 2-1. Proposed degradation mechanism for phenol .....	017
Figure 2-2. (A) HRTEM images and (B) SAED patterns of the pristine NiO, S400, and S600 catalysts. (C) Electric conductivities of the catalysts ( $\sigma$ ) and relative abundance of the surface $O_\alpha$ species present in the catalysts. (D) Quantities of CO-accessible sites present in one gram of the catalysts ( $N_{CO}$ ) and relative abundance of the surface $Ni^{\delta+}$ species present in the catalysts. (E) Molar ratios of the surface S to Ni species (S/Ni) and relative abundance of the surface $SO_4^{2-}$ species present in the catalysts .....	025
Figure 2-3. Background-subtracted, <i>in situ</i> DRIFT spectra of the catalysts upon their exposure to 1000 ppm $NH_3$ at (A) 50 ° C and (B) 200 ° C. ....	027
Figure 2-4. (A) XANES spectra of the catalysts at the S $L_{2,3}$ -edge. (B) Background-subtracted, <i>in situ</i> DRIFT spectra of pristine NiO upon exposure to 1000 ppm $SO_2$ and 3 vol. % $O_2$ at 300 ° C, 400 ° C, and 500 ° C. ....	031
Figure 2-5. (A) Initial reaction rates ( $-r_{H_2O_2, 0}$ ) of the catalysts obtained during the $H_2O_2$ scission runs used to simulate the phenol degradation runs at 1 V or 3 V. The $-r_{H_2O_2, 0}$ values of pristine NiO and S400 obtained during the $H_2O_2$ scission runs used to simulate the phenol degradation runs at (B) 1 V or (C) 3 V, while altering the particles size of the catalysts or stirring speed of the reaction mixtures. ....	035
Figure 2-6. Energetics on the catalyst surface of the (111) facet for the catalysts altered during the $H_2O_2$ scission cycle. Change in the charges for the $OH_1$ and $OH_2$ fragments during the $H_2O_2$ scission cycle.....	038
Figure 2-7. (A) The initial reaction rates ( $-r_{PHENOL, 0}$ ) of the catalysts obtained during the phenol degradation runs at 1 V or 3 V. The $-r_{PHENOL, 0}$ values of pristine NiO and S400 obtained during the phenol degradation runs at (B) 1 V or (C) 3 V, while altering the particles size of the catalysts or stirring speed	

of the reaction mixtures. (D) The EPR spectra of the reaction aliquots collected from the  $\text{H}_2\text{O}_2$  scission runs on pristine NiO and S400 in the presence of DMPO. (E) The  $-r_{\text{PHENOL}, 0}$  values of pristine NiO and S400 obtained during the phenol degradation runs at 3 V in the presence of the scavengers .....040

**Figure 2-8.** Schematic representation of the  $\cdot\text{OH}$  (green circle) and  $\text{H}^+$  (blue circle)-mediated radicalization of the  $\text{SO}_4^{2-}$  functionalities (orange circle) present on the surface of the (111) facet of the catalysts to form  $\text{SO}_4^{\cdot-}$ , while releasing  $\text{H}_2\text{O}$  (sky blue circle).....043

**Figure 2-9.** (A) Quantities of phenol consumed ( $N_{\text{PHENOL}}^*$ ) during the filtration runs in the absence (blank) and the presence of the catalysts. (B) The initial phenol consumption rates ( $-r_{\text{PHENOL}, 0}$ ) of S400 and S500-Fe obtained during the recycling experiments .....047

**Figure 3-1.** Schematic illustrations of the reactor set-up utilized (A), evolution mechanisms of  $\cdot\text{OH}$  (B) and  $\text{SO}_4^{\cdot-}$  (D) on  $\text{SO}_4^{2-}$ -functionalized surfaces (C) for  $\text{Fe}_3\text{O}_4$  (E),  $\text{Mn}_x\text{Fe}_{3-x}\text{O}_4$  (F), and  $\text{Mn}_3\text{O}_4$  (G).....055

**Figure 3-2.** HRTEM images ((A)–(E) for  $\text{Mn}_x$ ), SAED patterns ((F)–(J) for  $\text{Mn}_x$ ), and XRD patterns of the catalysts ((K) for  $\text{Mn}_x\text{Fe}_{3-x}\text{O}_4$ ; (L) for  $\text{Mn}_x$ ) .....069

**Figure 3-3.** Amounts of CO adsorbed per gram of the catalysts measured at  $40^\circ\text{C}$  ( $N_{\text{CO}}$ ). Isosteric heats of CO adsorption ( $-Q_{\text{ST}, \text{CO}}$ ) and  $\text{CO}_2$  adsorption ( $-Q_{\text{ST}, \text{CO}_2}$ ) for the catalysts measured at  $-25/-20/-15^\circ\text{C}$  and  $-20/0/20^\circ\text{C}$ . .....072

**Figure 3-4.** (A) Elemental ratios of S to metals present in the catalyst surfaces ( $\text{S}/(\text{Mn}+\text{Fe})$ ). (B) Raman spectra of the catalyst. (C) Background-subtracted *in situ* DRIFT spectra of the catalysts.....075

**Figure 3-5.** (A) Background-subtracted initial  $\text{H}_2\text{O}_2$  scission rates ( $-r_{\text{H}_2\text{O}_2, 0}$ ) of the catalysts obtained through the control runs to simulate the catalytic  $\text{H}_2\text{O}_2$  scission runs at 1–3 V. (B) Background-subtracted initial phenol degradation rates ( $-r_{\text{PHENOL}, 0}$ ) of the catalysts with the use of  $\text{Na}_2\text{SO}_4$  or  $\text{NaNO}_3$  as a supporting electrolyte at 1–3 V. (C) Energy barriers ( $E_{\text{BARRIER}}$ )

and pre-factors ( $k_{APP,0}$ ) of the catalysts obtained through phenol degradation runs at 3 V and 25–55 ° C.....079

**Figure 3–6.** Fittings of the reaction data to the pseudo–1<sup>st</sup>–order kinetics model (regression factors of  $\geq 0.94$ ) for the determination of the apparent reaction rate constants ( $k_{APP}$ ) for Mn<sub>1.5</sub> (A and B) and Mn<sub>0</sub> (C and D) and their background–subtracted initial phenol consumption rates ( $-r_{PHENOL,0}$ ) in the absence or the presence of a scavenger (1,4–benzoquinone/guaiacol for (E); catechol/hydroquinone for (F)) at 3 V.....087

**Figure 3–7.** EPR spectra of intact reaction aliquots (solid (catalyst) + liquid; black lines) or reaction aliquots subjected to the filtration (liquid; red lines) for the catalyst: (A) Mn<sub>2</sub>, (B) Mn<sub>1.5</sub>, (C) Mn<sub>1</sub>, and (D) Mn<sub>0</sub>.....090

**Figure 3–8.** Degradation profiles of phenol (phenol conversion ( $X_{PHENOL}$ ) versus time) in the absence (blank) or the presence of the catalysts at 3 V .....092

**Figure 3–9.** Fittings of the reaction data to the pseudo–1<sup>st</sup>–order kinetics model (regression factors of  $\geq 0.87$ ) for the determination of the apparent reaction rate constants ( $k_{APP}$ ) for Mn<sub>1.5</sub>Fe<sub>1.5</sub>O<sub>4</sub> (A), Fe<sub>3</sub>O<sub>4</sub> (B), Mn<sub>1.5</sub> (C), and Mn<sub>0</sub> (D) and their background–subtracted initial phenol consumption rates ( $-r_{PHENOL,0}$ ) in the absence or the presence of scavenger (TBA, 1,4–dioxane, IPA, or THF) at 3 V ((E) and (F)).....094

**Figure 3–10.** (A) Background–subtracted initial phenol degradation rates ( $-r'_{PHENOL,0}$ ) of the catalysts obtained through recycle runs at 3 V. (B) Background–subtracted initial degradation rates of phenol /aniline ( $-r_{PHENOL,0}/-r_{ANILINE,0}$ ) for the catalysts at 3 V. (C) Mineralization efficiencies (selectivities to CO<sub>A</sub> ( $\eta_C$ ; A=1 or 2) or NO<sub>A</sub>/N<sub>2</sub>O ( $\eta_N$ )) for the catalysts obtained after 8 hours of the reaction runs in the absence of an electric potential. ....097

**Figure 3–11.** HRTEM images of the used Mn<sub>1.5</sub> catalysts ((A) post the 1<sup>st</sup> run; (B) post the 2<sup>nd</sup> run; (C) post the 3<sup>rd</sup> run; (D) post the 4<sup>th</sup> run; and (E) post the 5<sup>th</sup> run) and their XRD patterns (F).....098

**Figure 4–1.** Schematic representation of (A)  $\text{H}_2\text{O}_2$  scission cycle on surface  $\text{Mn}^{n+}$  species ( $n=2$  or  $3$ ) and radical transfer from surface-unbound  $\cdot\text{OH}$  to  $\text{NO}_2^-$  or  $\text{NO}_3^-$  species supported on  $\alpha$ -/ $\beta$ -/ $\gamma$ - $\text{MnO}_2$  surfaces ( $\text{NO}_2^-_{\text{SUP}}$  or  $\text{NO}_3^-_{\text{SUP}}$ ), leading to the production of supported  $\text{NO}_2\cdot$  ( $\text{NO}_2\cdot_{\text{SUP}}$  in B) or  $\text{NO}_3\cdot$  ( $\text{NO}_3\cdot_{\text{SUP}}$  in C) utilized for degrading aqueous pollutants. Illustration of porous architectures for  $\alpha$ - $\text{MnO}_2$  (D),  $\beta$ - $\text{MnO}_2$  (E), and  $\gamma$ - $\text{MnO}_2$  (F), whose surfaces afford  $\text{NO}_2^-$  or  $\text{NO}_3^-$  species with various binding configurations. ....106

**Figure 4–2.** HRTEM images of  $\alpha$ - $\text{MnO}_2$  (A and D),  $\beta$ - $\text{MnO}_2$  (B and E), and  $\gamma$ - $\text{MnO}_2$  (C and F). (J) Atomic concentrations of  $\text{Mn}^{2+}/\text{Mn}^{3+}$  species present in or near the catalyst surfaces and the amounts of CO-accessible Mn species included per gram of the catalysts ( $N_{\text{CO}}$ ). (K) average oxidation states (AOS) of  $\text{Mn}^{2+}/\text{Mn}^{3+}/\text{Mn}^{4+}$  species present in or near the catalyst surfaces and the isosteric heats of  $\text{CO}_2$  adsorption ( $-Q_{\text{ST}, \text{CO}_2}$ ) for the catalysts at small  $\text{CO}_2$  coverages ( $\sim 5.1 \mu\text{mol g}_{\text{CAT}}^{-1}$  for  $\alpha$ - $\text{MnO}_2$  and  $\gamma$ - $\text{MnO}_2$ ;  $\sim 3.7 \mu\text{mol g}_{\text{CAT}}^{-1}$  for  $\beta$ - $\text{MnO}_2$ ) .....121

**Figure 4–3.** (A) Background-subtracted initial  $\text{H}_2\text{O}_2$  scission rates ( $-r_{\text{H}_2\text{O}_2, 0}$ ) and initial phenol decomposition rates ( $-r_{\text{PHENOL}, 0}$ ) of  $\alpha$ -,  $\beta$ -, or  $\gamma$ - $\text{MnO}_2$ , for which particle size or stirring speed was varied during phenol decomposition runs. (B) Change in  $-r_{\text{PHENOL}, 0}$  values for  $\alpha$ -,  $\beta$ -, or  $\gamma$ - $\text{MnO}_2$  in the absence or the presence of quencher (*tert*-butanol, 1,4-dioxane, or tetrahydrofuran) (C) Arrhenius plots ( $\ln(k_{\text{APP}})$  versus  $10^3/T$ ) for  $\alpha$ -,  $\beta$ -, or  $\gamma$ - $\text{MnO}_2$ , whose apparent reaction rate constants ( $k_{\text{APP}}$ ) were obtained from phenol decomposition runs at  $25\sim 55^\circ\text{C}$  .....127

**Figure 4–4.** (A) Formation mechanisms of DMPO-OH and DMPO-OOH adducts. EPR spectra of reaction aliquots (liquid) taken from reaction mixtures (solid (catalyst) + liquid) that underwent filtration using a  $0.45 \mu\text{m}$ -sized PES syringe (B–D). Reaction mixtures included DMPO as a spin trapper for  $\cdot\text{OH}/\cdot\text{OOH}/\text{O}_2\cdot^-$  and  $\alpha$ - $\text{MnO}_2$  (B),  $\beta$ - $\text{MnO}_2$  (C), or  $\gamma$ - $\text{MnO}_2$  (D) as a catalyst .....129

**Figure 4–5.** (A) Atomic concentrations of  $\text{Mn}^{2+}/\text{Mn}^{3+}$  species present in or near the surfaces of  $\alpha$ - $\text{MnO}_2$ -N and  $\gamma$ - $\text{MnO}_2$ -N and their  $N_{\text{CO}}$  values. (B) AOS values of  $\text{Mn}^{2+}/\text{Mn}^{3+}/\text{Mn}^{4+}$  species present in or near the surfaces of  $\alpha$ - $\text{MnO}_2$ -N and  $\gamma$ - $\text{MnO}_2$ -N and their  $-Q_{\text{ST}, \text{CO}_2}$  values with small  $\text{CO}_2$



coverages (C) Molar ratios of N to Mn (N/Mn) innate to  $\alpha$ -MnO<sub>2</sub>-N and  $\gamma$ -MnO<sub>2</sub>-N analyzed via XRF/EA (for bulk) and XP spectroscopy (XPS; for surface). (D) Relative abundance of labile O species (O<sub>a</sub>) inherent to  $\alpha$ -MnO<sub>2</sub>,  $\alpha$ -MnO<sub>2</sub>-N,  $\gamma$ -MnO<sub>2</sub>, and  $\gamma$ -MnO<sub>2</sub>-N analyzed via XPS and H<sub>2</sub>-TPR.....136

**Figure 4-6.** (A) Background-subtracted, *in situ* NO/O<sub>2</sub>-DRIFT spectra of  $\alpha$ -MnO<sub>2</sub> and  $\gamma$ -MnO<sub>2</sub> at 150 ° C. XP spectra of  $\alpha$ -MnO<sub>2</sub>-N (B) and  $\gamma$ -MnO<sub>2</sub>-N (D) in the N 1s domains. XANES spectra of  $\alpha$ -MnO<sub>2</sub>-N (C) and  $\gamma$ -MnO<sub>2</sub>-N (E) at the N K-edges, in which  $\pi^*$  (a and b) and  $\sigma^*$  resonances (a', b', and b'') of surface NO<sub>2</sub><sup>-</sup>/NO<sub>3</sub><sup>-</sup> species were observed at photon energies of  $\leq 407$  eV and  $> 407$  eV, respectively.....139

**Figure 4-7.** (A) Formation mechanisms of HDMPO-ONO<sub>Z</sub> adduct (Z= 1 or 2). EPR spectra of reaction aliquots taken from reaction mixtures (solid (catalyst) + liquid; B and C) or reaction solutions (liquid; D and E) .....141

**Figure 4-8.** Computed surface (110) facet of  $\alpha$ -MnO<sub>2</sub> with defective Mn species coordinated to NO<sub>3</sub><sup>-</sup> (A) or NO<sub>3</sub><sup>•</sup> (B) via *bi*-dentate configuration .....144

**Figure 4-9.** (A) Background-subtracted  $-r_{\text{H}_2\text{O}_2, 0}$  and  $-r_{\text{PHENOL}, 0}$  values of  $\alpha$ -MnO<sub>2</sub>-N and  $\gamma$ -MnO<sub>2</sub>-N, for which particle size or stirring speed was varied during phenol decomposition runs. Change in  $-r_{\text{PHENOL}, 0}$  values for the catalysts in the absence or the presence of quencher (guaiacol, catechol, hydroquinone, or 1,4-benzoquinone for B; *tert*-butanol, 1,4-dioxane, or tetrahydrofuran for D) (C) Arrhenius plots (ln ( $k_{\text{APP}}$ ) versus 10<sup>3</sup>/T) for  $\alpha$ -MnO<sub>2</sub>-N and  $\gamma$ -MnO<sub>2</sub>-N, whose apparent reaction rate constants ( $k_{\text{APP}}$ ) were obtained from phenol decomposition runs at 25~55 ° C.....145

**Figure 4-10.** (A) Mineralization efficiencies ( $\eta$ ) of the catalysts in decomposing phenol. (B) Background-subtracted initial degradation rates of textile wastewater for  $\alpha$ -MnO<sub>2</sub>-N, Fe<sub>2</sub>O<sub>3</sub>-S, and NiO-S in terms of carbon ( $-r_{\text{C}}$ ) or nitrogen component ( $-r_{\text{N}}$ ). (C) Background-subtracted initial phenol decomposition rates ( $-r'_{\text{PHENOL}, 0}$ ) for as-synthesized (1<sup>st</sup> cycle) or used  $\alpha$ -MnO<sub>2</sub>-N catalysts (2<sup>nd</sup>~5<sup>th</sup> cycles). (D) Background-subtracted initial degradation rates of textile wastewater ( $-r'_{\text{C}}$  and  $-r'_{\text{N}}$ ) for as-synthesized (1<sup>st</sup>

cycle) or used  $\alpha$ -MnO<sub>2</sub>-N catalysts (2<sup>nd</sup>~4<sup>th</sup> cycles). .....150

**Figure. 5-1.** (A) Illustration of ZrO<sub>2</sub> surface composed of Zr<sup>4+</sup>-O<sup>2-</sup>-Zr<sup>4+</sup>-O<sup>2-</sup>-Zr<sup>4+</sup> channels, where non-reducible, coordinatively-saturated Zr<sup>4+</sup> cations are inter-connected to O<sup>2-</sup> anions. (B) Proposed elementary steps of homolytic H<sub>2</sub>O<sub>2</sub> dissection on ZrO<sub>2</sub> surface mediated by LA<sub>II</sub> and BA: H<sub>2</sub>O<sub>2</sub> adsorption, H<sub>2</sub>O<sub>2</sub> distortion, H<sub>2</sub>O<sub>2</sub> scission, and ·OH desorption, wherein ·OH desorption stage dictates the efficiency of homolytic H<sub>2</sub>O<sub>2</sub> dissection as the rate-determining step. (C) Proposed elementary steps of radical transfer from ·OH to NO<sub>3</sub><sup>-</sup><sub>SUP</sub> to yield supported NO<sub>3</sub>· (NO<sub>3</sub>·<sub>SUP</sub>) on ZrO<sub>2</sub> surface, where surface-unbound oxygens of NO<sub>3</sub><sup>-</sup><sub>SUP</sub> (highlighted with orange circles) interact with ·OH for bearing radicals, whereas NO<sub>3</sub>·<sub>SUP</sub> is recovered to NO<sub>3</sub><sup>-</sup><sub>SUP</sub> via electron (e<sup>-</sup>) acceptance from a pollutant .....164

**Figure 5-2.** Background-subtracted, *in situ* NH<sub>3</sub>-DRIFT spectra of the catalysts at 50/150 ° C (ZrO<sub>2</sub> for (A); ZrO<sub>2</sub>-N for (B)). (C) Binding energies (E<sub>ADSORBATE</sub>) of the catalyst surfaces with H<sub>2</sub>O at 20-40 ° C, CO at 0-40 ° C, CO<sub>2</sub> at 0-40 ° C, and NH<sub>3</sub> at 50 ° C in tandem with surface areas of CO (or CO<sub>2</sub>)-accessible sites innate to the catalysts (S<sub>ADSORBATE</sub> in inset table)....175

**Figure 5-3.** (A) XP spectrum of ZrO<sub>2</sub>-N in the N 1s regime. (B) XANES spectrum of ZrO<sub>2</sub>-N at the N K-edge. (C) Background-subtracted, *in situ* NO/O<sub>2</sub>-DRIFT spectrum of ZrO<sub>2</sub> at 100 ° C .....181

**Figure 5-4.** (A) Proposed transformation routes of DMPO to DMPO-OH, DMPO-OOH, HDMPO-OH, and HDMPO-ONO<sub>Z</sub><sub>SUP</sub> (Z= 1 or 2). EPR spectra of reaction mixtures (ZrO<sub>2</sub> for (B); ZrO<sub>2</sub>-N for (C)) and reaction solution (ZrO<sub>2</sub>-N for (D)) collected through the filtration of reaction mixture with the use of a 0.45 μm-sized PES syringe .....184

**Figure 5-5.** Computations concerning the energies released/up-taken for the adsorption of gaseous NO<sub>3</sub><sup>-</sup> on the surface terminated at the (1 0 1) facet for tetragonal ZrO<sub>2</sub> to form supported NO<sub>3</sub><sup>-</sup> (NO<sub>3</sub><sup>-</sup><sub>SUP</sub>) with mono-dentate binding array and its radicalization to produce supported NO<sub>3</sub>· (NO<sub>3</sub>·<sub>SUP</sub>) under aqueous phase at 300 K. Bond lengths of O-O innate to NO<sub>3</sub><sup>-</sup>/NO<sub>3</sub><sup>-</sup><sub>SUP</sub>/NO<sub>3</sub>·<sub>SUP</sub>, Zr-Zr inherent to ZrO<sub>2</sub>, and O-Zr indigenous NO<sub>3</sub><sup>-</sup><sub>SUP</sub>/NO<sub>3</sub>·<sub>SUP</sub> on ZrO<sub>2</sub> were also computed for comparison. ....187

**Figure 5–6.** (A) Backgrounds–subtracted initial  $\text{H}_2\text{O}_2$  dissection rates per CO–accessible site basis ( $-\text{r}_{\text{H}_2\text{O}_2}$ ) for the catalysts with the variation of the amount of  $\text{H}_2\text{O}_2$  fed (0.07–0.12 mmol) at 0 V and 25 ° C. (B)  $-\text{r}_{\text{PHENOL}}$  values of the catalysts with the variation of a catalyst particle size and/or a stirring speed at 3 V and 25 ° C. (C)  $-\text{r}_{\text{PHENOL}}$  values of the catalysts in the absence or the presence of a scavenger (hydroquinone, catechol, tert–butanol, or guaiacol) at 3 V and 25 ° C. (D) Arrhenius plots (logarithmic apparent reaction rate constant ( $k_{\text{APP}}$ ) versus reciprocal of reaction temperature with regression factors ( $R^2$ ) of  $\geq 0.96$ ) for the catalysts to assess their energy barriers ( $E_{\text{BARRIER}}$  in inset table) and pre–factors directed by CO–accessible sites ( $k_{\text{APP},0}$  in inset table) at 3 V and 25–55 ° C.....192

**Figure 5–7.** (A)  $-\text{r}_{\text{PHENOL}}$  values of the catalysts exposed to recycle environments at 3 V and 25 ° C. (B) Fittings of background–subtracted phenol degradation data to pseudo–1st–order kinetic model. (C) Backgrounds–subtracted initial textile wastewater mineralization rates per mass basis ( $-\text{r}'_{\text{C}}/-\text{r}'_{\text{N}}$ ) for  $\text{ZrO}_2\text{–N}$  exposed to recycle environments in the presence of  $\text{H}_2\text{O}_2$  at 0 V and 25 ° C.....198

# Chapter 1

## Introduction

### 1.1. Study Background

Rapid industrial development has led to considerable research on environmental remediation. Climate change attributed to industrialization, population growth, and lifestyle has resulted in diverse ecosystem changes; therefore, environmentally friendly energy consumption and sustainable development have become emerging goals for society. Humans artificially produce thousands of compounds and release them, thereby contaminating the environment.

Environmental pollution is classified into air, soil, and water pollution based on the location where pollutants and toxic substances accumulate.[1] Water pollution includes the flow of sewage and wastewater into groundwater and seawater, which results in low water quality. Organic contaminants from sewage and wastewater generated from human and industrial activities are harmful to humans and animals; therefore, a water treatment process is required before discharge.[2]

Water treatment processes are divided into physical, biological, and chemical treatment processes.[3] Physical treatment processes are conducted to remove sediments through precipitation, filtration, and other methods. These processes have had the advantage of a simple driving principle but are limited by their low removal efficiency.[3] Biological treatment processes can be used for treating high concentrations of organic wastewater; however, they have the disadvantage of long operation times.[3] Finally, chemical treatment processes are applied to remove cohesive suspended solids or reactive dissolved substances.[4] Such processes comprise adsorption, oxidation, and ion exchange. Although they are limited by high sludge generation and involve a high maintenance cost,[4] these processes exhibit high wastewater removal

efficiencies and involve simple system. Moreover, chemical treatment processes used for the purification of contaminated liquids are faster and more diverse than current available physical and biological treatment processes.[4] They are also applicable to the treatment of organic compounds and have the advantage of relatively low facility costs. A simple system of various catalysts that can be used in chemical treatment processes has been actively developed. The advanced oxidation process uses a powerful oxidant and contributes to water quality improvement through a chemical reaction using  $\cdot\text{OH}$  or  $\text{SO}_4\cdot^-$  radicals. These chemical species called radicals contain electrons that exist alone; therefore, electrons and crystals in the material react with each other.

Various radicals used in the reaction have a high oxidation potential and allow the mineralization of various types of pollutants; however, their lifespan is short (half-life of  $10^{-3} \mu\text{s}$ ). Radical precursors and catalysts are used to generate radicals; thus, catalysts for use in the advanced oxidation processes have been widely investigated. Among them, metal oxide catalysts are considered advantageous because of their stability and price competitiveness and are, thus, actively being researched. Catalysts are not consumed during the reaction; however, they increase the reaction rate without inducing any chemical or overall Gibbs energy changes. Thus, they have been widely applied in energy- and environment-related fields.[5] Catalysts for use in the chemical treatment processes toward environmental remediation decompose hazardous substances released from all industries in the air, waste, and water sectors.[5] Thus, several reviews have discussed monometallic oxides or bimetallic oxides as Fenton reaction catalysts.[6]

## 1.2. Advanced Oxidation Processes

### 1.2.1. Fenton reaction

A representative example of the advanced oxidation processes is the Fenton reaction, which is divided into homogeneous and heterogeneous reactions based on the type of the iron source employed.[7] The homogeneous Fenton reaction refers to the nonselective decomposition of various organic contaminants using a reaction in which  $\text{Fe}^{2+}$  ions and hydrogen peroxide form a hydroxyl radical ( $\cdot\text{OH}$ ) with a high oxidation potential; the reaction rate constant ( $k$ ) is  $40 - 80 \text{ L mol}^{-1} \text{ s}^{-1}$ , as indicated by:[8–10]



Hydroxyl radicals have high reactivity and undergo nonselective reaction; therefore, they can be used to decompose various organic compounds under the influence of nature associated with the electron donation/withdrawal of chemicals.[11]

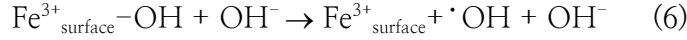
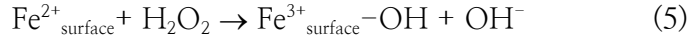
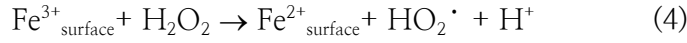
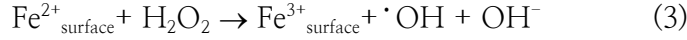


In the case of Equation 2,  $\text{Fe}^{3+}$  is reduced to  $\text{Fe}^{2+}$  to enable a chain reaction to realize the reaction in Equation 1, and the secondary rate constant ( $k$ ) value is  $0.001 - 0.01 \text{ L mol}^{-1} \text{ s}^{-1}$ ; this corresponds to the rate-determining step (RDS) that determines the overall reaction rate.[10, 12, 13]

### 1.2.2. Heterogeneous Fenton reaction

A Fenton reaction that uses a solid catalyst, namely, the heterogeneous Fenton reaction (pseudo-Fenton reaction); this reaction can overcome the aforementioned disadvantages of the homogeneous Fenton reaction.[14] Further, it can restrict the production of iron complex sludge, can be applied over a wider pH range (3–8), and promotes catalyst reclamation.[15] Although the heterogeneous Fenton reaction has the advantage of being an easy and simple system, it has a lower conversion rate than the homogeneous Fenton reaction because the pseudo-Fenton reaction occurs on a solid interface.[8] Further, the competitive adsorption of hydrogen peroxide and

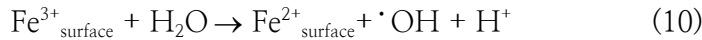
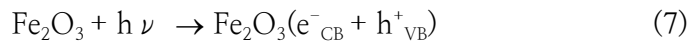
effluents can affect the rate of the pseudo-Fenton reaction.[16] The main reactions of the pseudo-Fenton reaction can be expressed as



where  $\text{Fe}_{\text{surface}}^{\text{X}+}$  represents the solid catalyst surface. Equation 4 correspond to the RDS ( $\text{Fe}_{\text{surface}}^{3+}$  reduction)[17]; however,  $\cdot\text{OH}$  radical desorption on the iron oxide surface becomes the RDS when an excess amount of hydrogen peroxide is present in the solution (Equation 6).[18]

### 1.2.3. Photo-Fenton reaction

Research has been conducted for improving the reaction efficiency by applying additional energy sources in the pseudo-Fenton reactions. These reactions can be largely subdivided into photo-Fenton, sono-Fenton, and electro-Fenton reactions based on the type of energy source employed. When a light source is applied to a pseudo-Fenton reaction system by using the photochemical method, the process is called the photo-Fenton reaction, wherein the general reaction formula is expressed as [19]

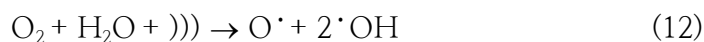


Holes from the valence band (VB) and electrons from the conduction band (CB) are formed when iron oxide is irradiated by photons ( $h\nu$ ), as indicated in Equation 7.[13] The reduction of  $\text{Fe}^{3+}$  is the RDS for the photo-Fenton reaction.[13, 20] However, unlike Equations 4–6 of the pseudo-Fenton reaction,  $\text{Fe}^{3+}$  can be reduced to  $\text{Fe}^{2+}$  via Equations 8 and 10. Therefore, the  $\text{Fe}^{3+}$  reduction rate for the RDS of the photo-Fenton reaction is increased efficiently.[21] The  $\cdot\text{OH}$  radical can be produced continuously without a

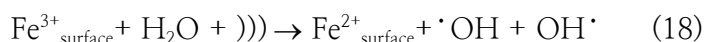
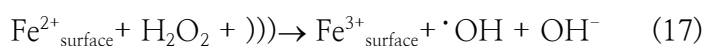
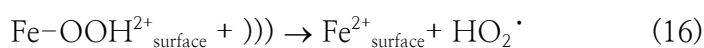
catalyst although hydrogen peroxide still remains (Equation 9). Meanwhile,  $\text{Fe}^{3+}$  and  $\text{H}_2\text{O}$  react to form the  $\cdot\text{OH}$  radical (Equation 10), and organic decomposition can be accelerated, in relation to that upon the pseudo-Fenton reaction, wherein only the catalyst and photo source continue to exist, and no hydrogen peroxide formed. Dye pollutants disturb photosynthesis by restricting light penetration. They decrease the quantity of dissolved oxygen by blocking the surface for oxygen interchange and by increasing the demand for biochemical oxygen.

#### 1.2.4. Sono-Fenton reaction

When ultrasonic waves are exposed to water, the reaction of water decomposition is called cavitation, wherein cavitation bubbles are generated and collapse. Sonolysis refers to a reaction in which  $\cdot\text{OH}$  and  $\text{H}\cdot$  radicals are respectively produced through the decomposition of water and oxygen using high-temperature and high-pressure energy as the cavitation bubbles collapse.



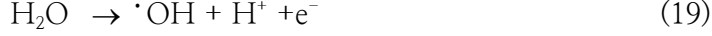
Equations 11 – 14 indicate that the bubbles form hydrogen peroxide via chain reactions and free radicals. Organic matter is decomposed by ultrasonic waves alone, resulting in a low decomposition performance. This has led to the emergence of the sono-Fenton reaction, which combines sonolysis and Fenton reactions have emerged.[22] The sono-Fenton reaction has the advantage of efficiently reducing  $\text{Fe}^{3+}$ , which is the RDS of the pseudo-Fenton reaction, upon the use of ultrasonic waves:





### 1.2.5. Electro–Fenton reaction

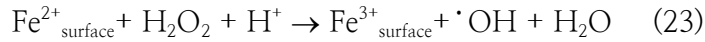
Finally, when a radical is generated using an electrochemical reaction, it is referred to as the electro–Fenton reaction. In this reaction,  $\cdot\text{OH}$ ,  $\text{O}_2$ , protons ( $\text{H}^+$ ), and electrons ( $\text{e}^-$ ) are generated by the oxidation reaction occurring at the anode.[9, 21]



In the electro–Fenton reaction,  $\text{O}_2$ ,  $\text{H}^+$ , and  $\text{e}^-$  are generated at the anode and migrate to the cathode to produce  $\text{H}_2\text{O}_2$  via cathodic reduction without additional  $\text{H}_2\text{O}_2$  injection.[9]



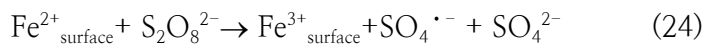
A reaction occurs on the catalyst surface, and the RDS of the electro–Fenton process is the  $\cdot\text{OH}$  radical desorption.[23–25]



The advantage of the electro–Fenton reaction is that it exhibits excellent performance toward the decomposition and mineralization of organic materials without additional chemicals. However, it has the disadvantages of reaction cost– and resource–ineffectiveness.[26]

### 1.2.6. Sulfate–radical–based Advanced Oxidation Processes (AOP–SR)

The abovementioned reactions are representatives of advanced oxidation processes based on hydroxyl radicals (AOP–HR). However, these reactions occur under limited pH conditions and the radicals have short lifespans.<sup>[27]</sup> These limitations can be overcome by sulfate–radical–based Advanced Oxidation Processes (AOP–SR) using  $\text{SO}_4^{\bullet-}$ , which has an oxidation potential similar to that of  $\cdot\text{OH}$  ( $\sim 2.5$  V for  $\text{SO}_4^{\bullet-}$ ;  $\sim 2.8$  V for  $\cdot\text{OH}$ ). Moreover,  $\text{SO}_4^{\bullet-}$  has a considerably longer lifetime ( $30 - 40 \mu\text{s}$  for  $\text{SO}_4^{\bullet-}$ ;  $\sim 10^{-3} \mu\text{s}$  for  $\cdot\text{OH}$ ) and is more flexible than  $\cdot\text{OH}$ .<sup>[26, 27]</sup> The precursors used include peroxomonosulfate (PMS,  $\text{HSO}_5^-$ ) or peroxydisulfate (PDS,  $\text{S}_2\text{O}_8^{2-}$ ) and metal oxides; the mechanisms for activating PMS and PDS for  $\text{SO}_4^{\bullet-}$  generation are explained below.<sup>[28]</sup> The RDS of the AOP–SR is  $\text{SO}_4^{\bullet-}$  desorption.<sup>[29]</sup>



However, AOP–SR has the disadvantage of generating sulfate ions based on Equation 24; thus, a chemical species is regulated to have a high concentration in an aqueous solution of  $500 \text{ mg L}^{-1}$  or less in aqueous solution.<sup>[26, 30]</sup> In addition, PMS, as a precursor of the  $\text{SO}_4^{\bullet-}$  radicals, is more expensive than other precursors used.

### 1.3. Thesis Objectives

The purpose of this thesis is to substitute the  $\cdot\text{OH}$  radical as the water treatment species. Both  $\text{SO}_4^{\cdot-}$  and  $\text{NO}_3^{\cdot}$  are regarded as a moderate initiator of pollutant radicalization ( $E_0$  of 2.4~2.7 V), with a longer half-life ( $10^{-3}$   $\mu\text{s}$  for  $\cdot\text{OH}$ ; 30~40  $\mu\text{s}$  for  $\text{SO}_4^{\cdot-}$ ; and 6  $\mu\text{s}$  for  $\text{NO}_3^{\cdot}$ ) and a greater tolerance to against aqueous backgrounds than the  $\cdot\text{OH}$  radical. Therefore, herein, we propose a unique, compelling methodology to readily produce  $\text{SO}_4^{\cdot-}$  or  $\text{NO}_3^{\cdot}$  species by locating their precursors ( $\text{SO}_4^{2-}$  or  $\text{NO}_3^-$ , respectively) vicinal to the surface  $\text{H}_2\text{O}_2$  activators ( $\cdot\text{OH}$  producers) and prompting radical transfer from the  $\cdot\text{OH}$  species to  $\text{SO}_4^{2-}$  or  $\text{NO}_3^-$  functionalities ( $\text{SO}_4^{2-}_{\text{SUP}}$  or  $\text{NO}_3^-_{\text{SUP}}$ ) for the generation of their supported  $\text{SO}_4^{\cdot-}$  or  $\text{NO}_3^{\cdot}$  analogues ( $\text{SO}_4^{\cdot-}_{\text{SUP}}$  or  $\text{NO}_3^{\cdot}_{\text{SUP}}$ ; denoted as  $\cdot\text{OH} \rightarrow \text{SO}_4^{\cdot-}_{\text{SUP}}$  or  $\text{NO}_3^{\cdot}_{\text{SUP}}$ , respectively) upon  $\text{H}_2\text{O}_2$  being fed to the catalyst surface. Notably, catalytic  $\text{H}_2\text{O}_2$  cleavage can be combined with exothermic  $\cdot\text{OH} \rightarrow \text{SO}_4^{\cdot-}_{\text{SUP}}$  or  $\text{NO}_3^{\cdot}_{\text{SUP}}$  and is referred to as overall  $\cdot\text{OH} \rightarrow \text{SO}_4^{\cdot-}_{\text{SUP}}$  or  $\text{NO}_3^{\cdot}_{\text{SUP}}$ . Metal oxide polymorphs served as platform because of their inclusion of  $\text{H}_2\text{O}_2$  activators ( $\text{M}^{\delta+}$ , M: metal,  $\delta \leq 2$ ) and as anchoring spots for  $\text{SO}_4^{2-}$  or  $\text{NO}_3^-$  species.

In summary, the objective of the thesis is to clarify and pioneer unique  $\cdot\text{OH} \rightarrow \text{SO}_4^{\cdot-}_{\text{SUP}}$  and  $\text{NO}_3^{\cdot}_{\text{SUP}}$  pathways. Moreover, it motivates the alteration of the platform used to accelerate  $\cdot\text{OH} \rightarrow \text{SO}_4^{\cdot-}$ , to afford more accurate results than those reported previously by employing metal oxides. It also supports that the surface reaction dynamics/energetics on  $\cdot\text{OH} \rightarrow \text{SO}_4^{\cdot-}_{\text{SUP}}$  or  $\text{NO}_3^{\cdot}_{\text{SUP}}$  are clarified via kinetic assessment and DFT calculation, both of which have never been implemented in the field of radical-mediated oxidation of recalcitrant contaminants

## 1.4. Organization of the Thesis

This thesis is organized in the following manner:

In Chapter 2, the sulfate radical ( $\text{SO}_4^{\bullet-}$ ) is deemed as a competitive oxidant of the hydroxyl radical ( $\cdot\text{OH}$ ). This is because of its (1) facile generation over a wide pH range, (2) longer lifetime of (30–40  $\mu\text{s}$  for  $\text{SO}_4^{\bullet-}$ ;  $10^{-3}$   $\mu\text{s}$  for  $\cdot\text{OH}$ ) and 3) comparable standard oxidation potential ( $\sim 2.6$  eV for  $\text{SO}_4^{\bullet-}$ ;  $\sim 2.8$  eV for  $\cdot\text{OH}$ ). Previous study has validated that compare to iron oxide, iron sulfide improves the  $\text{H}_2\text{O}_2$  scission rate and recalcitrant conversion. Furthermore,  $\text{SO}_4^{2-}$ -modified iron oxide outperforms its un-functionalized counterpart in terms of activity and recyclability to degrade pollutants. As a results, in this chapter the synthesis of nickel oxide and  $\text{SO}_4^{2-}$  functionalized nickel oxide to conclude the rate-determining step for  $\text{H}_2\text{O}_2$  fragment cycle and computed through DFT to demonstrate the advantages of using a surface metal $^{\delta+}$  ( $\delta \leq 2$ ).

In Chapter 3, this thesis discusses bimetallic oxo-spinel ( $(\text{M}_1)_x(\text{M}_2)_{3-x}\text{O}_4$ ;  $\text{M}_1$  and  $\text{M}_2$ : metal) as one of the fascinating metal oxide phases that afford the opening of Lewis acidic metals open to  $\text{H}_2\text{O}_2$  ( $\cdot\text{OH}$  precursor), thus enabling  $\text{H}_2\text{O}_2$  cleavage with dissimilar  $\cdot\text{OH}$  productivity upon changing the X values. In contrast, bimetallic oxo-spinel can also undergo surface modification with  $\text{SO}_4^{2-}$  functionalities, which in turn are activated by  $\cdot\text{OH}$  species for the generation of supported  $\text{SO}_4^{\bullet-}$  species via the radical interconversion of  $\cdot\text{OH} \leftrightarrow \text{SO}_4^{\bullet-}$ . While choosing  $(\text{Fe})_x(\text{Mn})_{3-x}\text{O}_4$  as a model architecture of the bimetallic oxo-spinel, in this part of the study we modified  $(\text{Fe})_x(\text{Mn})_{3-x}\text{O}_4$  compounds with  $\text{SO}_4^{2-}$  species. Subsequently, we regulated the properties of the resulting  $\text{SO}_4^{2-}$ -modified  $(\text{Fe})_x(\text{Mn})_{3-x}\text{O}_4$  architectures in terms of Lewis acidities and efficiencies on  $\cdot\text{OH} \leftrightarrow \text{SO}_4^{\bullet-}$  alongside the phenol degradation rates with the main use of supported  $\text{SO}_4^{\bullet-}$ , all of which are highlighted in herein. In this chapter, we also report the kinetic investigation on the  $\cdot\text{OH} \leftrightarrow \text{SO}_4^{\bullet-}$  dynamics on the  $(\text{Fe})_x(\text{Mn})_{3-x}\text{O}_4$  surfaces via a series of reaction runs under reaction-limited domains, in addition to contrasting kinetic

parameters such as energy barriers and pre-factors.

In Chapter 4, this thesis discusses that the nitrate radical ( $\text{NO}_3^\bullet$ ) has been verified to be particularly conducive to mineralize refractory contaminants present in wastewater owing to its long lifespan, high standard reduction potential, and significant tolerance toward being terminated by aqueous background scavengers. Nevertheless, the mineralization of aqueous pollutants enabled by  $\text{NO}_3^\bullet$  has not been extensively studied in comparison with that mediated by conventional  $^\bullet\text{OH}$  and/or the recently emerging  $\text{SO}_4^{\bullet-}$  radicals. This is mainly attributed to substantial demands on the evolution of  $\text{NO}_3^\bullet$  via radiolysis and/or photolysis, wherein a radio-active material, highly unstable  $\text{NO}_2^\bullet$ , or a highly energized electron is oftentimes deemed as a pre-requisite. To resolve this issue, in this chapter, coupled  $\text{NO}_3^-$  functionality and manganese oxide for use as a  $\text{NO}_3^\bullet$  precursor and a  $^\bullet\text{OH}$  producer is envisioned with  $\text{H}_2\text{O}_2$  fed to the resulting  $\text{NO}_3^-$ -functionalized manganese oxide surface. Specifically, hypothesis is that Lewis acidic surface manganese ( $\text{Mn}^{2+/3+}$ ) species can initially cleave  $\text{H}_2\text{O}_2$  to produce  $^\bullet\text{OH}$ , which in turn migrates to and interplays with  $\text{NO}_3^-$  functionality in proximity to  $\text{Mn}^{2+/3+}$  for the evolution of the supported  $\text{NO}_3^\bullet$  analogue via radical transfer from  $^\bullet\text{OH}$  to the  $\text{NO}_3^-$  functionality ( $^\bullet\text{OH} \rightarrow \text{NO}_3^\bullet$ ). The  $^\bullet\text{OH} \rightarrow \text{NO}_3^\bullet$  pathway is peculiar and unique, yet, is demonstrated to be highly tangible and readily recurrent under aqueous media. This can be corroborated by a series of control reaction runs and microscopy/spectroscopy experiments alongside with DFT calculations.

In Chapter 5, this thesis discusses the methodological alteration concerning how to catalyze  $^\bullet\text{OH}$  production from heterolytic  $\text{H}_2\text{O}_2$  dissection on a reducible metal oxide ( $\text{MnO}_2$ ) to the homolytic counterpart on a non-reducible metal oxide ( $\text{ZrO}_2$ ), whose mechanism/energetics/rate-determining step were clarified in Chapter 4. Therefore, this thesis reports on how  $\text{ZrO}_2$  modified with  $\text{NO}_3^-$  functionalities ( $\text{ZrO}_2\text{-N}$ ) was used to catalyze the overall  $^\bullet\text{OH} \rightarrow \text{NO}_3^\bullet_{\text{SUP}}$ , and how Lewis acidic  $\text{Zr}^{4+}$  (LA)/Brønsted acidic  $-\text{OH}$  (BA)

and  $\text{NO}_3^-$  species served to activate homolytic  $\text{H}_2\text{O}_2$  dissection and  $\cdot\text{OH} \rightarrow \text{NO}_3^-$  <sub>SUP</sub>, respectively. This thesis also discusses  $\text{ZrO}_2$  and  $\text{ZrO}_2\text{-N}$  surfaces that were BA-rich and LA-deficient, resulting from their inclination to adsorb  $\text{H}_2\text{O}$  via dissociation, as evidenced by  $\text{H}_2\text{O}$  isotherm experiments and *in situ*  $\text{NH}_3$ -DRIFT spectroscopy experiments. Consequently, the  $\text{ZrO}_2\text{-N}$  surface afforded  $\text{NO}_2^-/\text{NO}_3^-$  species, where the abundance of  $\text{NO}_3^-$  species was larger than that of its  $\text{NO}_2^-$  counterpart. In contrast, the binding configuration of the  $\text{NO}_3^-$  species was verified as being only *mono*-dentate only, as substantiated by *in situ*  $\text{NO}/\text{O}_2^-$  DRIFT/XP/XANES spectroscopy and DFT calculations.

## Chapter 2

# Exploring catalytic traits of $\text{SO}_4^{2-}$ –functionalized NiO to prompt the radical interconversion of $\cdot\text{OH} \leftrightarrow \text{SO}_4^{\cdot-}$ exploited to decompose refractory pollutants

The essence of Chapter 2 has been published in Chemical Engineering Journal. Reprinted with permission from [31].

### 2.1. Introduction

Sulfate ( $\text{SO}_4^{2-}$ ) is deemed as one of the most promising functional groups anchored on catalytic solids. This performance is mainly attributed to its electronic properties, which can modulate binding traits with reactive gases (*e.g.*,  $\text{CO}_2$ ,  $\text{CH}_4$ ,  $\text{C}_3\text{H}_8$ , and  $\text{NH}_3$ ) and synergize the solids, leading to the control of the activity and selectivity for various chemical reactions.[32] The unique electronic character offered by  $\text{SO}_4^{2-}$  functionalities is also deployable in the  $\text{SO}_4^{\cdot-}$ –enabled, oxidative degradation of aqueous pollutants.[9]  $\text{SO}_4^{\cdot-}$  is produced via the activation of  $\text{HSO}_5^-$  or  $\text{S}_2\text{O}_8^{2-}$  and is conducive toward the decomposition of contaminants.[9, 33] This is because  $\text{SO}_4^{\cdot-}$  can impart an prolonged lifetime over a wide pH range and a strong oxidation potential along with selective oxidation of pollutants, all of which are higher than those of  $\cdot\text{OH}$  ( $\sim 30 \mu\text{s}$  and 2.5–3.1 eV for  $\text{SO}_4^{\cdot-}$ ;  $\sim 10^{-3} \mu\text{s}$  and  $\sim 2.7$  eV for  $\cdot\text{OH}$ ).[9, 33, 34] Nonetheless, abundant  $\text{SO}_4^{\cdot-}$  species are formed in an aqueous environment when the pH conditions are appropriate for the activation of  $\text{HSO}_5^-$  or  $\text{S}_2\text{O}_8^{2-}$  by a Lewis acidic metal (detailed below).[35–37] In addition, it was reported that unsupported  $\text{SO}_4^{\cdot-}$  species can oftentimes oxidize Lewis acidic metals, leading to the formation of their oxidized analogues, which are far less active toward the activation of  $\text{HSO}_5^-$  or

$\text{S}_2\text{O}_8^{2-}$ . [35–38] Furthermore, the production of  $\text{SO}_4^{\bullet-}$  mediated by the activation of  $\text{HSO}_5^-$  or  $\text{S}_2\text{O}_8^{2-}$  can only be recurrent if these two ions are periodically fed to the Lewis acidic metals included in contaminated water. [39] Hence the development of a novel reaction system to sustain  $\text{SO}_4^{\bullet-}$  species is highly desirable. Meanwhile, it should be noted that the  $\text{H}_2\text{O}$ -assisted transformation of  $\text{SO}_4^{\bullet-}$  into  $\cdot\text{OH}$  is highly favorable with a rate constant of  $660 \text{ s}^{-1}$  at all pH values ( $\text{SO}_4^{\bullet-} + \text{H}_2\text{O} \rightarrow \text{SO}_4^{2-} + \cdot\text{OH} + \text{H}^+$ ;  $\text{SO}_4^{\bullet-} \rightarrow \cdot\text{OH}$ ). [40, 41] Interestingly, our previous study rectified the generic notion associated with  $\text{SO}_4^{\bullet-} \rightarrow \cdot\text{OH}$  so that it can be prompted in the reverse direction ( $\text{SO}_4^{2-} + \cdot\text{OH} + \text{H}^+ \rightarrow \text{SO}_4^{\bullet-} + \text{H}_2\text{O}$ ;  $\cdot\text{OH} \rightarrow \text{SO}_4^{\bullet-}$ ) when the  $\text{SO}_4^{2-}$  functionalities are supported by ubiquitous iron oxides ( $\text{Fe}_2\text{O}_3$  and/or  $\text{Fe}_3\text{O}_4$ ). [39] Moreover, the supported  $\text{SO}_4^{\bullet-}$  can outperform  $\cdot\text{OH}$  toward the degradation of a model refractory chemical (phenol) in terms of its activity and sustainability. [39] This was evidenced by the higher initial consumption rate of phenol observed on the supported  $\text{SO}_4^{\bullet-}$  relative to  $\cdot\text{OH}$ , whose trend was maintained throughout the phenol recycling experiments. [39] Hence, the desired function of the supported  $\text{SO}_4^{\bullet-}$  in oxidizing pollutants can be exploited by an appropriate choice of the metal oxide platform used to immobilize the  $\text{SO}_4^{2-}$  functionalities and the reaction configuration to favor  $\cdot\text{OH} \rightarrow \text{SO}_4^{\bullet-}$ , whose rationales are specified below.

We hypothesized that  $\cdot\text{OH} \rightarrow \text{SO}_4^{\bullet-}$  can proceed via two major catalytic cycles that involve the production of  $\cdot\text{OH}$  via  $\text{H}_2\text{O}_2$  scission and radical interconversion between  $\cdot\text{OH}$  and  $\text{SO}_4^{\bullet-}$ , respectively (Figure 2–1A and 2–B). To sustain the  $\cdot\text{OH} \rightarrow \text{SO}_4^{\bullet-}$  pathway, the reaction system must be fed with  $\text{H}_2\text{O}_2$ . This is because  $\text{H}_2\text{O}_2$  can be cleaved by O–modified Lewis acidic metals with the oxidation states of  $\leq 2$  ( $\text{M}^{\delta+}$  present on the metal oxide surface; activator of  $\text{H}_2\text{O}_2$ ). Specifically,  $\text{M}^{\delta+}$  can initially bind with the O atoms in  $\text{H}_2\text{O}_2$  via coordination ( $\text{M}^{\delta+}\text{-H}_2\text{O}_2$ ) and then cleave  $\text{H}_2\text{O}_2$  by donating an electron ( $e^-$ ) to  $\text{H}_2\text{O}_2$ . [42–47] This leads to the production of an oxidized analogue of the Lewis acidic metals ( $\text{M}^{(\delta+1)+}$ ),  $\cdot\text{OH}$  ion, and  $\text{SO}_4^{\bullet-}$



precursor ( $\cdot\text{OH}$ ), as shown in Figure 2-1A. [42–47] However, this requires the immediate reduction of metal ( $\text{M}^{(\delta+1)+}$ ), which is less active in the  $\text{H}_2\text{O}_2$  scission than  $\text{M}^{\delta+}$  with the additional need of a continuous supply of  $\text{H}_2\text{O}_2$ . [39, 42, 43] Such requisites make the  $\cdot\text{OH} \rightarrow \text{SO}_4^{\cdot-}$  route less compelling than the direct utilization of  $\cdot\text{OH}$  (driven by the  $\text{H}_2\text{O}_2$  scissor) toward the decomposition of pollutants. In this regard, we simply applied a small electric potential across two graphite electrodes ( $\leq 3\text{ V}$ ), both of which were soaked in contaminated water (Figure 2-1C). [24, 39, 48] At the anode,  $\cdot\text{OH}$  is produced as an adduct of  $\text{H}_2\text{O}$  oxidation and is prone to produce surface-labile O species ( $\text{O}_\alpha$ ) on the (graphite) anode. [9, 24, 39, 48–50]  $\text{O}_\alpha$  species were reported to be loosely coordinated to the (graphite) anode surface and thus, they are active in various redox-based chemical transformations. [51, 52] The  $\text{O}_\alpha$  species, therefore, can serve to degrade contaminants even in the absence of  $\text{M}^{\delta+}$  (anodic oxidation). [9, 24, 39, 48–50] In addition,  $\text{H}_2\text{O}$  can be also oxidized to form  $\text{H}^+$ ,  $\text{O}_2$ , and  $\text{e}^-$ . [24, 39, 48, 50] These species migrate into the cathode and experience  $\text{O}_2$  reduction to form a moderate quantity of  $\text{H}_2\text{O}_2$  on (or near) the cathode as long as an electric potential is applied (Figure 2-1C). [24, 39, 48, 50] Furthermore, a sufficient amount of  $\text{e}^-$  can migrate from the anode and serve to reduce the  $\text{M}^{(\delta+1)+}$  present in the surface of the metal oxide coated on the cathode. [24, 39, 48]

In this study, NiO was employed as a platform to disperse  $\text{SO}_4^{2-}$  functionalities as an alternative to  $\text{Fe}_2\text{O}_3$  owing to the following viewpoints stated below. The electric conductivity of NiO is  $10\text{--}10^2$  fold greater than that of  $\text{Fe}_2\text{O}_3$  ( $\leq 10^{-1}\text{ S m}^{-1}$ ). [53–55] Thus, NiO may outperform  $\text{Fe}_2\text{O}_3$  in delivering  $\text{e}^-$  to  $\text{H}^+/\text{O}_2$  and therefore can potentially produce a larger number of  $\text{H}_2\text{O}_2$  than  $\text{Fe}_2\text{O}_3$  (Figure 2-1C; (i)). Notably,  $\text{Ni}^{\delta+}$  was verified as the optimal species to accelerate the rate-determining step of  $\text{H}_2\text{O}_2$  cleavage ( $\cdot\text{OH}$  desorption) among the  $\text{M}^{\delta+}$  species located in the 4<sup>th</sup> period of the periodic table, as corroborated in our previous work on metal sulfides (chemical formula of MS; M= Mn, Fe, Co, Ni, and Cu). [24] Despite the fact

that the Ni atoms in NiO are confined in a hexa-coordinated, *octahedral*  $[\text{NiO}_6]^{10-}$  geometry that is inaccessible to  $\text{H}_2\text{O}_2$  ( $\text{Ni}_{\text{LATTICE}}$ ), [56] the catalytic defects on the NiO surfaces ( $\text{Ni}_{\text{DEFECT}}$ ) are highly likely to be formed during the synthesis of NiO, whose specific procedure is included in the Experimental section. Our previous study on metal sulfides then may then justify our hypothesis that the  $\text{Ni}_{\text{DEFECT}}$  species innate to NiO can act as  $\text{H}_2\text{O}_2$  activators (*i.e.*,  $\text{Ni}^{\delta+}$ ) and catalyze the  $\text{H}_2\text{O}_2$  scission more actively than their  $\text{Fe}^{\delta+}$  analogues inherent to  $\text{Fe}_2\text{O}_3$  (grey and blue circles in Figure. 2-1D; (ii)). [24] In addition, NiS was reported to exhibit substantial Ni leaching via its structural deformation during the  $\text{H}_2\text{O}_2$  scission in the presence of an electric potential. [24] However, NiO with a standard enthalpy change of formation ( $\Delta H_{\text{FORMATION}}$ ) of  $-240 \text{ kJ mol}^{-1}$  will require a higher electric energy for its dissociation than NiS ( $\Delta H_{\text{FORMATION}}$  of  $-80 \text{ kJ mol}^{-1}$ ). Therefore, NiO is expected to minimize the structural deformation or reduce the amount of Ni leaching during the reaction runs in relation to NiS (iii). In contrast, O atoms adjacent to  $\text{Ni}_{\text{DEFECT}}$  ( $\text{O}_\alpha$ ) can tentatively act as an O source used to produce  $\text{H}_2\text{O}_2$  on or near the cathode (red asterisk in Figure 2-1D; (iv)), which was also postulated based on our previous work on  $\text{SO}_4^{2-}$ -modified  $\text{Fe}_2\text{O}_3$ . [39] We also proposed another catalytic cycle, wherein  $\cdot\text{OH}$  can migrate to and interact with the  $\text{SO}_4^{2-}$  functionality to produce an  $\text{SO}_4^{\cdot-}-\text{OH}$  intermediate via  $\text{e}^-$  transfer from  $\text{SO}_4^{2-}$  to  $\cdot\text{OH}$  and an  $\text{SO}_4^{\cdot-}-\text{H}_2\text{O}$  intermediate after the reduction of  $\text{SO}_4^{\cdot-}-\text{OH}$  by  $\text{H}^+$  (Figure 2-1B).  $\text{SO}_4^{\cdot-}-\text{H}_2\text{O}$  then releases  $\text{H}_2\text{O}$  and is transformed into  $\text{SO}_4^{\cdot-}$ , which decomposes phenol to produce  $\text{CO}$ ,  $\text{CO}_2$ ,  $\text{H}_2\text{O}$ , *etc.* The resulting  $\text{SO}_4^-$  may accept two electrons to regenerate the  $\text{SO}_4^{2-}$  functionality. Importantly, we envisaged that the activity and recyclability of NiO during the decomposition of pollutants can be improved markedly upon the modification of NiO with  $\text{SO}_4^{2-}$  (NiO (S)), as shown in the yellow circles in Figure 2-1D. The S and O atoms inherent to the  $\text{SO}_4^{2-}$  functionality are more electronegative than Ni; thus, they may extract  $\text{e}^-$  from Ni (cyan arrows in Figure 2-1D). This is likely to promote the Lewis acidity

of  $\text{Ni}_{\text{DEFECT}}$  included in  $\text{NiO}$  (S) ( $\delta \uparrow$  in  $\text{Ni}^{\delta+}$ ), improve the interactions between  $\text{Ni}_{\text{DEFECT}}$  and  $\text{H}_2\text{O}_2$ , and thereby can accelerate the  $\text{H}_2\text{O}_2$  scission cycle more effectively than  $\text{SO}_4^{2-}$ -unmodified  $\text{NiO}$  (v). The potential  $\text{e}^-$  transfer from  $\text{NiO}$  to  $\text{SO}_4^{2-}$  may also decrease the bond length of  $\text{Ni-O}$  bond vicinal to the surface, potentially reinforce the strength of the surface  $\text{Ni-O}$  bonds in comparison with those of pristine  $\text{NiO}$ , and thus can tentatively help reduce the amount of  $\text{Ni}$  leaching during the reaction runs (vi). Importantly, our previous calculations on the energetics during the transition of the  $\text{SO}_4^{2-}$  functionality to its corresponding radical analogue could provide evidence that the  $\text{SO}_4^{2-} \rightarrow \text{SO}_4^{\bullet-}$  route is exothermic.[39] This result supports the plausibility of the supported  $\text{SO}_4^{\bullet-}$ ,[39] yet, it misses any insights into the elementary step vital to direct the overall rate of the  $\text{}^{\bullet}\text{OH} \rightarrow \text{SO}_4^{\bullet-}$  pathway. All these findings suggest the need to explore both the reaction energetics and strengths of the  $\text{Ni-O}$  bonds on the surface of  $\text{NiO}$  (S) using a theoretical approach.

This chapter highlights our efforts for examining our hypotheses in regard to the activity (i, ii, iv and v) and stability (iii and vi) of  $\text{NiO}$  (S) during the phenol decomposition process using experimental and computational techniques.  $\text{NiO}$  was synthesized and functionalized with  $\text{SO}_4^{2-}$  at 300–600 ° C to diversify the Lewis acidity of  $\text{Ni}^{\delta+}$  and the surface concentration of  $\text{O}_\alpha$  or  $\text{SO}_4^{2-}$ , *etc.* The activity and reusability of the catalysts were evaluated via kinetic assessment. The kinetic study was also used to determine the rate-determining step and explore the relative significance of  $\text{}^{\bullet}\text{OH}$  and  $\text{SO}_4^{\bullet-}$  during the decomposition of phenol. In addition, the pristine  $\text{NiO}$  and  $\text{Ni}$  (S) surfaces were also investigated using density functional theory (DFT) calculations, in which the octopolar (111) surface was selected because of its dominance with the lowest surface energy (Figure 2–1D).[57, 58] To simulate the  $\text{SO}_4^{2-}$ -modified  $\text{NiO}$  surface more effectively,  $\text{Ni}_{\text{LATTICE}}$  coordinated to three  $\text{O}$  atoms present in the sub-layer ( $\text{O}_{\text{SUB}}$ ) was removed from the surface, which promoted the formation of six  $\text{Ni}_{\text{DEFECT}}$  atoms accessible to  $\text{H}_2\text{O}_2$ . In

addition, the gas-phase  $\text{SO}_4^{2-}$  cluster settled on and was relaxed above the surface via a minimum energy pathway. This resulted in the coordination of  $\text{SO}_4^{2-}$  to the surface via a *tri*-dentate configuration, which was in exact agreement with our previous calculations on  $\text{SO}_4^{2-}$ -modified  $\text{Fe}_2\text{O}_3$ .<sup>[39]</sup> The resulting surface on the (111) plane served to calculate the charge separation between the Ni and O species adjacent to the surface together with their bond lengths. DFT calculations were also used to propose a series of elementary steps to account for the  $\cdot\text{OH} \rightarrow \text{SO}_4^{\cdot-}$  pathway in conjunction with its energetics.

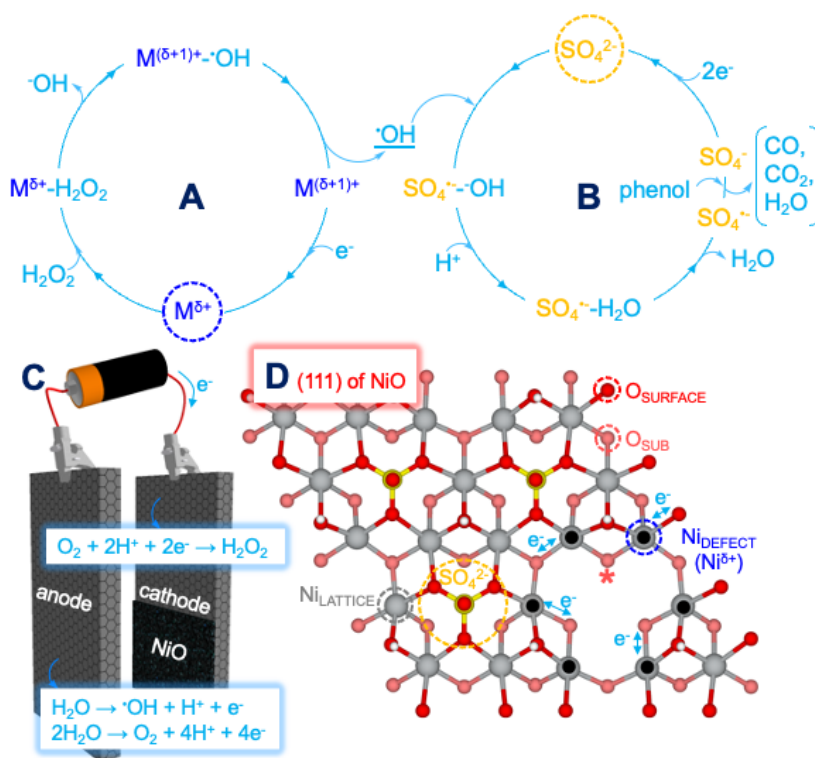


**Figure 2-1.** Proposed degradation mechanism for phenol: (A)  $\text{H}_2\text{O}_2$  is initially activated by  $\text{M}^{\delta+}$  to produce  $\cdot\text{OH}$ , whereas (B) the  $\text{SO}_4^{2-}$  functionality is radicalized by  $\cdot\text{OH}$  and is transformed into the  $\text{SO}_4^{\cdot-}$  analogue utilized in the degradation of phenol. (C) An illustration of electric potential-assisted  $\text{H}_2\text{O}_2$  production on (or near) the NiO surface coated on the cathode. (D) A schematic representation of the surface on the (111) facet inherent to NiO comparing the  $\text{SO}_4^{2-}$  functionalities (orange circle), lattice Ni atoms ( $\text{Ni}_{\text{LATTICE}}$ , grey circle), defective Ni atoms ( $\text{Ni}^{\delta+}$ , blue circle), O atoms located at the outer- or sub-layer ( $\text{O}_{\text{SURFACE}}$  or  $\text{O}_{\text{SUB}}$ , red or pink circle, respectively), surface-labile O atoms (\*), and electrons ( $\text{e}^-$ ).

## 2.2. Experimental Section

### 2.2.1. Catalysts

The NiO catalysts were synthesized according to a protocol that was slightly modified from those employed in our previous studies.[39, 59, 60] First, 20 mmol of oxalic acid ( $C_2H_2O_4 \cdot 2H_2O$ , Sigma–Aldrich,  $\geq 99.0\%$ ) and 20 mmol of  $NiSO_4 \cdot 7H_2O$  (Sigma–Aldrich,  $\geq 99.0\%$ ) were mixed in 100 mL de-ionized  $H_2O$ , stirred at  $50^\circ C$  for an hour, cooled to  $25^\circ C$ , and filtered using 500 mL of de-ionized  $H_2O$  and 500 mL of ethanol ( $C_2H_5OH$ , DAEJUNG, 94.5%).[39] The resulting sky-blue precipitate was collected and calcined at  $300^\circ C$  for an hour with the ramping rate of  $4^\circ C \text{ min}^{-1}$ ,[39] leading to the production of the pristine NiO catalyst. Pristine NiO was then modified with 500 ppm  $SO_2$  coupled with 3 vol.%  $O_2$  balanced by  $N_2$  at  $300\text{--}600^\circ C$  for an hour at the ramping rate of  $10^\circ C \text{ min}^{-1}$  and the total flow rate of  $500 \text{ mL min}^{-1}$ . [39, 59, 60] This resulted in the formation of the  $SO_4^{2-}$ -functionalized NiO catalysts.  $Fe_2O_3$  was synthesized using a procedure identical to that used for the synthesis of the pristine NiO catalyst with the exception of using  $FeSO_4 \cdot 7H_2O$  (Sigma–Aldrich,  $\geq 99.0\%$ ) as the precursor, whereas  $Fe_2O_3$  was functionalized with  $SO_4^{2-}$  using a method identical to that used for NiO at  $500^\circ C$  (S500–Fe).[39]

### 2.2.2. Characterizations

X-ray diffraction (XRD) patterns of the catalysts were collected using D8 Advance instrument (Bruker) with the use of monochromatic  $Cu K_\alpha$  radiation ( $\lambda = 1.54 \text{ \AA}$ ). The Scherrer equation (Eq. (1)) was employed to evaluate the crystallite size of the catalysts ( $d$ ). In Eq. (1),  $K$ ,  $\lambda$ ,  $\beta$ , and  $\theta$  denote the shape factor (0.89), monochromatic  $Cu K_\alpha$  radiation wavelength ( $\lambda = 1.54 \text{ \AA}$ ), line broadening at half the maximum intensity at (111), (200), or (220), and Bragg angle at the (111), (200), or (220) facets, respectively.[39, 61]

$$d = \frac{\kappa \times \lambda}{\beta \times \cos\theta} \quad (1)$$

N<sub>2</sub> physisorption experiments were conducted on an ASAP 2010 instrument (Micromeritics) at 77 K. X-ray fluorescence (XRF) experiments were performed on a ZSX Primus II instrument (Rigaku). High resolution transmission electron microscopy (HRTEM) images and selected area electron diffraction (SAED) patterns of the catalysts were gathered using a Titan 80–300<sup>TM</sup> instrument (FEI) at 300 keV. Scanning electron microscopy (SEM) images of the catalysts were collected using an Inspect F50 instrument (FEI) operated at 10 kV. X-ray photoelectron spectroscopy (XPS) experiments were carried out on a PHI 5000 VersaProbe spectrometer, in which adventitious carbon observed at a binding energy of 284.6 eV was utilized as a reference to correct the binding energies of the surface species for the catalysts. CO-pulsed chemisorption experiments were performed using an Autochem II instrument (Micromeritics). *In situ* diffuse reflectance Infrared Fourier transform (DRIFT) spectroscopy was conducted on an FT/IR/4200 spectrometer (Jasco). X-ray absorption near edge structure (XANES) experiments were conducted using the 10D (XAS KIST) beamline in Pohang Light Source (South Korea) operated in top-up mode at an energy of 3 GeV, storage current of 250 mA, and resolution of 0.2 eV. The XANES spectra of the catalysts were obtained under an ultra-high vacuum ( $\sim 10^{-9}$  torr) and 300 K. Inductively coupled plasma-atomic absorption spectrometry (ICP-AAS) experiments were carried out using an ICS 3000 spectrometer (Thermo Fisher Scientific). HI98191 instrument (HANNA) was used to monitor the electric conductivities of the reaction mixtures. Electron paramagnetic resonance (EPR) spectroscopy experiments were performed on EMX-plus spectrometer (Bruker) using 5,5-dimethyl-1-pyrroline *N*-oxide (DMPO, Sigma-Aldrich,  $\geq 98.0\%$ ) as a trapping agent for  $\cdot\text{OH}$  and  $\text{SO}_4^{\cdot-}$ . Reaction aliquots collected from the reaction mixtures containing DMPO after 2 minutes of reaction runs prior to analysis, whose conditions were a resonance frequency of 9.64 GHz, microwave power of 2.948 mW, modulation amplitude of 1.0 G, sweep width of 120 G, and sweep time of 48 seconds.

The 2,9-dimethyl-1,10-phenanthroline ( $C_{14}H_{12}N_2$ , Sigma-Aldrich,  $\geq 98.0\%$ ) method served to quantify the amount of hydrogen peroxide ( $H_2O_2$ ) formed during the reaction run.[62] Conversion of  $H_2O_2$  ( $X_{H_2O_2}$ ) was calculated using Eq. (2). In Eq. (2),  $C_{H_2O_2, 0}$  indicates the concentration of  $H_2O_2$  prior to the reaction run (0 stands for initial.), whereas  $C_{H_2O_2}$  indicates the concentration of  $H_2O_2$  at a specific reaction time. The initial  $H_2O_2$  scission rate of the catalyst ( $-r_{H_2O_2, 0}$ ) was calculated using Eq. (3).[24, 39, 48] In Eq. (3),  $k_{APP}$  indicates the apparent reaction rate constant obtained by the fitting of the reaction data to a pseudo-1<sup>st</sup>-order kinetic model, whereas  $N_{H_2O_2, 0}$  denotes the number of moles of  $H_2O_2$  prior to the reaction run (initial). [24, 39, 48]

$$X_{H_2O_2}(\%) = \frac{C_{H_2O_2,0} (mol_{H_2O_2} L^{-1}) - C_{H_2O_2} (mol_{H_2O_2} L^{-1})}{C_{H_2O_2,0} (mol_{H_2O_2} L^{-1})} \times 100 \quad (2)$$

$$-r_{H_2O_2,0} (mol_{H_2O_2} g_{CAT}^{-1} min^{-1}) = \frac{N_{H_2O_2,0} (mol_{H_2O_2}) \times k_{APP} (min^{-1})}{gram\ of\ catalyst\ used\ (g_{CAT})} \quad (3)$$

High performance liquid chromatography (HPLC. LC-20 A, Shimadzu) was utilized to quantify the amount of phenol ( $C_6H_5OH$ , DAEJUNG, 99%) formed during the reaction run using the reverse phase chromatography method, as reported previously.[24, 39, 48] Conversion of phenol ( $X_{PHENOL}$ ) was calculated using Eq. (4). In Eq. (4),  $C_{PHENOL, 0}$  indicates the phenol concentration prior to the reaction run (0 stands for initial.), whereas  $C_{PHENOL}$  indicate the phenol concentration at a specific reaction time. The initial phenol degradation rate of the catalyst ( $-r_{PHENOL, 0}$ ) was calculated using Eq. (5).[24, 39, 48] In Eq. (5),  $k_{APP}$  indicates the apparent reaction rate constant obtained by the fitting of the reaction data to a pseudo-1<sup>st</sup>-order kinetic model, whereas  $N_{PHENOL, 0}$  denotes the number of moles of phenol prior to the reaction run (initial).[24, 39, 48]

### 2.2.3. Reactions

All reactions were performed in accordance to the protocol used in our previous studies.[24, 39] First, 93 g of N-methyl-2-pyrrolidone ( $C_5H_9NO$ , Sigma-Aldrich,  $\geq 99.0\%$ ) was mixed with 7 g of poly (vinylidene fluoride)  $((CH_2CF_2)_n)$ , average  $M_w \sim 180,000$ , average  $M_n \sim 71,000$ , Sigma-Aldrich) to form the binder solution.[24, 39] The catalyst slurry was fabricated by mixing 0.2 g of the catalyst and 0.2 g of the binder solution, which was then coated onto the graphite cathode (Groupe Carbone Lorraine, grade 2124) with an area of 3 cm $\times$ 4 cm, and subsequently dried at 110 ° C for 18 hours.[24, 39] The catalyst-coated graphite cathode and bare graphite anode were then vertically positioned with a gap of 3 cm between them and soaked in the reaction solution.[24, 39] The composition of the aqueous reaction solutions are specified in the figure captions and include  $Na_2SO_4$  electrolyte (Sigma-Aldrich,  $\geq 99.0\%$ ),  $H_2O_2$  (Sigma-Aldrich, 29.0 – 32.0 wt.%,  $H_2O_2$  basis), phenol, and scavengers (*tert*-butanol ( $C_4H_9OH$ , DAEJUNG, 99.5%); 1,4-dioxane (DAEJUNG,  $> 99.0\%$ ); *iso*-propanol ( $C_3H_7OH$ , DAEJUNG, 99.5%); and tetrahydrofuran (DAEJUNG,  $> 99.0\%$ )). The reaction were carried out with or without an electric input (1 V and  $\sim 30$  mA; 3 V and  $\sim 15$  mA).[24, 39] Next, 1 mL of the reaction sample was collected from the reaction solution, quenched with 1  $\mu$ L of methanol ( $CH_3OH$ , Sigma-Aldrich, 99.8%), filtered through a 0.45  $\mu$ m-sized PES syringe filter (Whatman®), and analyzed to quantify the concentration of  $H_2O_2$  or phenol at a specific reaction time.[24, 39]

### 2.2.4. Calculations

Density-functional theory (DFT) calculations implemented in the Vienna ab-initio simulation package (version of 5.4.4) were used to analyze the surface properties of the  $SO_4^{2-}$ -modified NiO and the reactions taking place on its surface.[63–65] The Perdew–Burke–Ernzerhof (PBE) projector augmented-wave potentials and generalized gradient approximation were used to model



the core electrons and exchange–correlation functional, respectively.[66–68] In addition, Hubbard–U corrections were also applied to treat the strongly correlated *d* electrons in Ni. The effective Hubbard parameter and energy cut-off values were set to 6.45 and 550 eV, respectively, as recommended in the literature.[57] The Gaussian smearing method (smearing width = 0.05 eV) was chosen to describe the partial wave occupancies. All calculations for the bulk materials and surfaces were performed with consideration of the spin polarization. Bader charge analysis was performed to obtain the charge state of the NiO surface and the chemical species formed during the reactions.[69, 70] The structural optimization of the bulk NiO unit cell was performed using Monkhorst–Pack sampling for  $8 \times 8 \times 8$  k-point mesh.[71] As reported in the literature, an energetically stable NiO electronic structure was successfully obtained with the inclusion of antiferromagnetic order.[72] All related structural and electronic properties were in good agreement with those reported elsewhere.[57, 73–79] Based on the optimized unit cell structure of bulk NiO, a thermodynamically stable (111) octopolar–surface structure was constructed to analyze the charge state of the surface atoms and chemical species and to evaluate the reaction energetics. The  $(2 \times 2)$  and  $(4 \times 4)$  (111) NiO surfaces were composed of eight and six atomic layers with a 15 Å vacuum region on top of the surface layer and were optimized with  $4 \times 4 \times 1$  and  $2 \times 2 \times 1$  Monkhorst–Pack k-points meshes, respectively. The energy barrier for H<sub>2</sub>O<sub>2</sub> scission on the  $(4 \times 4)$  NiO (111) surface was obtained using the climbing image nudged elastic band method.[80] The H<sub>2</sub>O<sub>2</sub> and H<sub>2</sub>O molecules were optimized in the  $30 \text{ Å} \times 30 \text{ Å} \times 30 \text{ Å}$  vacuum region with a  $\Gamma$ -centered  $1 \times 1 \times 1$  k-points mesh.

## 2.3. Results and Discussion

### 2.3.1. Catalysts

NiO was synthesized according to the protocol described in the experimental section, in which oxalic acid served as a self-sacrificial porogen with the aim to highly disperse the  $\text{SO}_4^{2-}$  functionalities on the NiO surface.[39, 81]  $\text{NiSO}_4$  and oxalic acid initially fused to form Ni oxalate ( $\text{NiC}_2\text{O}_4$ ). This intermediate underwent a phase transition into NiO via calcination at  $300^\circ\text{C}$ , while generating mesopores.[39, 81] Pristine NiO was in turn modified upon treatment with  $\text{SO}_2/\text{O}_2$  at  $300\text{--}600^\circ\text{C}$  for an hour to vary the features of the catalyst surfaces bound to the  $\text{SO}_4^{2-}$  functionalities.[39, 59, 60] The resulting catalysts are denoted as SZZZ, where ZZZ indicates the temperature utilized to functionalize the NiO surface with  $\text{SO}_4^{2-}$ .

XRD analysis served to investigate the bulk structural features of the catalysts. The resultant XRD patterns showed the diffractions that could be assigned to those corresponding to *cubic* NiO with JCPDF No. of 03-065-2901. Scherrer equation was used to calculate the average crystallite sizes of the catalysts on the three major facets of (111), (200), and (220). Pristine NiO was comprised of  $\sim 5.4\text{ nm}$ -sized NiO poly-crystallites and its crystallite size increased to up to  $\sim 13.9\text{ nm}$  upon  $\text{SO}_4^{2-}$  functionalization at temperature  $\leq 600^\circ\text{C}$ . This was mainly attributed to the congregation of the NiO particulates during the  $\text{SO}_4^{2-}$  functionalization, which was more pronounced at higher temperatures. The aggregation of NiO particles could also affect the textural traits of the catalysts, as corroborated by the  $\text{N}_2$  physisorption experiments. The catalysts were mesoporous, which were as evidenced by their type IV  $\text{N}_2$  isotherms with hysteresis. Pristine NiO exhibited the highest porosity among all the catalysts studied, as corroborated by its Brunauer-Emmett-Teller (BET) surface area ( $S_{\text{BET}}$ ) of  $\sim 230\text{ m}^2\text{ g}_{\text{CAT}}^{-1}$  and Barrett-Joyner-Halenda pore volume ( $V_{\text{PORE}}$ ) of  $\sim 0.3\text{ cm}^3\text{ g}_{\text{CAT}}^{-1}$ . In contrast, the porosity was continuously reduced in the other catalysts, whose surfaces experienced  $\text{SO}_4^{2-}$  modification at higher temperatures ( $\text{S300} \rightarrow \text{S600}$ ;  $S_{\text{BET}}$  of  $\sim 180 \rightarrow \sim 50\text{ m}^2\text{ g}_{\text{CAT}}^{-1}$ ;  $V_{\text{PORE}}$  of  $\sim 0.2 \rightarrow$

$\sim 0.1 \text{ cm}^3 \text{ g}_{\text{CAT}}^{-1}$ ). Again, this trend was ascribed to the severe growth of NiO crystallites during the  $\text{SO}_4^{2-}$  functionalization at high temperature. The XRD and  $\text{N}_2$  physisorption results might suggest that  $300^\circ \text{C}$  circumvented the aggregation of porous NiO and therefore could be the optimal temperature for the  $\text{SO}_4^{2-}$  functionalization.

The bulk sulfur (S) content deposited per unit BET surface area of the catalysts ( $\text{N}_\text{S}/\text{S}_{\text{BET}}$ ) was of interest and was determined via XRF experiments. S400 and S500 had  $\text{N}_\text{S}/\text{S}_{\text{BET}}$  values of  $\geq 7.3 \mu \text{mol}_\text{S} \text{ m}^{-2}$ , which were far larger than those of the other catalysts ( $\leq 1.9 \mu \text{mol}_\text{S} \text{ m}^{-2}$ ). This interesting trend was also consistent with the molar ratio of the bulk S/Ni contents ( $\text{N}_\text{S}/\text{N}_{\text{Ni}}$ ) innate to S300–S600, wherein S400 and S500 revealed greater  $\text{N}_\text{S}/\text{N}_{\text{Ni}}$  values than those of the other catalysts ( $\geq 3.4 \mu \text{mol}_\text{S} \text{ mol}_{\text{Ni}}^{-1}$  for S400 and S500;  $\leq 2.6 \mu \text{mol}_\text{S} \text{ mol}_{\text{Ni}}^{-1}$  for S300 and S600). Bulk composition analysis on S300–S600 suggested that temperature of  $400^\circ \text{C}$  and  $500^\circ \text{C}$  could be desirable to produce a large number of  $\text{SO}_4^{2-}$  functionalities on the NiO surface.

Surface characterization was then employed to further verify the potential conclusions derived from the bulk characterization results. The morphological characteristics of the catalysts were explored using their HRTEM images, wherein the growth of NiO chunks was more conspicuous in the catalysts functionalized with  $\text{SO}_4^{2-}$  at higher temperatures (Figure 2–2A). This was in exact line with the trend of the catalyst properties obtained via XRD and  $\text{N}_2$  physisorption experiments, as discussed above. The SAED patterns of the catalysts were also used to observe their surface facets. The SAED patterns of pristine NiO, S300 (not shown), and S400 exhibited diffractions identical to those observed in their XRD patterns, all of which were identified as the planes corresponding to *cubic* NiO (Figure 2–2B). In contrast, the SAED patterns of S500 (not shown) and S600 showed additional facets that were assigned to *orthorhombic*  $\text{NiSO}_4$  (JCPDF No. of 01–076–0220). This suggested that the NiO surface could be seriously damaged upon modification with  $\text{SO}_4^{2-}$  at temperature  $\geq 500^\circ \text{C}$ , which might be detrimental to prompt

the  $\cdot\text{OH} \rightarrow \text{SO}_4^{\cdot-}$  pathway.

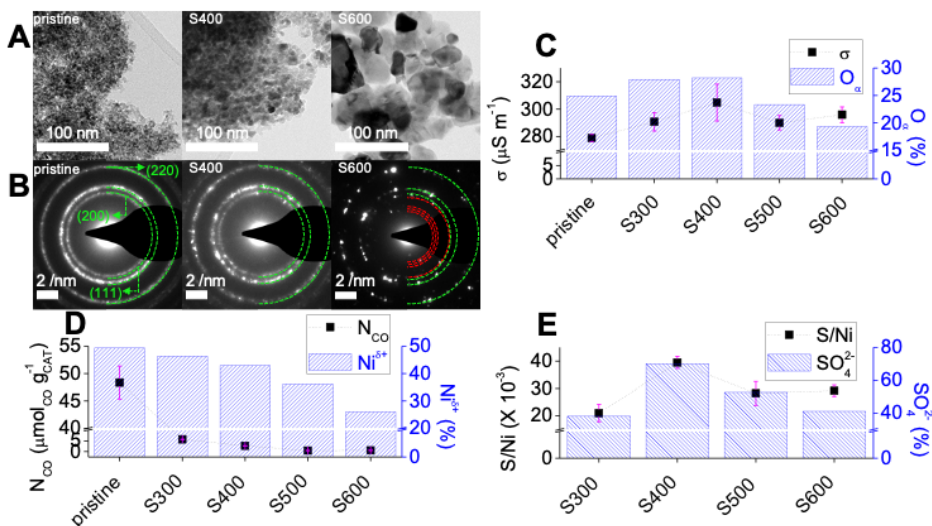


**Figure 2-2.** (A) HRTEM images and (B) SAED patterns of the pristine NiO, S400, and S600 catalysts. In (B), the green and red circles indicate the diffractions belonging to *cubic* NiO and *orthorhombic* NiSO<sub>4</sub>, respectively. (C) Electric conductivities of the catalysts ( $\sigma$ ) and relative abundance of the surface O<sub>α</sub> species present in the catalysts. (D) Quantities of CO-accessible sites present in one gram of the catalysts (N<sub>CO</sub>) and relative abundance of the surface Ni<sup>δ+</sup> species present in the catalysts. (E) Molar ratios of the surface S to Ni species (S/Ni) and relative abundance of the surface SO<sub>4</sub><sup>2-</sup> species present in the catalysts.

XPS was then utilized to explore the surface phases of the catalysts. The XPS spectra of the catalysts in the O 1s regime were featured by a broad peak. This could be deconvoluted into three sub-bands, which were assigned to the lattice O (O<sub>β</sub>), surface-labile O (O<sub>α</sub>), and O atom of chemisorbed H<sub>2</sub>O (O'<sub>α</sub>) with binding energies centered at ~529.2, ~530.8, and ~531.8 eV, respectively.[39, 59, 60] The relative abundance of the O<sub>α</sub> species was the greatest in the S400 surface (Figure 2-2C), which suggested that S400 might provide a surface most amicable to perform O<sub>α</sub>-mediated H<sub>2</sub>O<sub>2</sub> production on or near the cathode (Figure 2-1C).

The Lewis acidity of NiO is of great importance in directing catalytic  $\cdot\text{OH}$  production via H<sub>2</sub>O<sub>2</sub> scission. To determine how many Ni<sup>δ+</sup> species were present on the catalyst surface, the XPS spectra of the catalysts in the Ni 2p<sub>3/2</sub> regime were deconvoluted. This provided two sub-bands centered at

binding energies of  $\sim 853.8$  and  $\sim 855.6$  eV, which were assigned to the  $\text{Ni}^{\delta+}$  and  $\text{Ni}^{3+}$  species, respectively.[39, 82, 83] While the  $\text{Ni}^{\delta+}$  species were most abundant on the pristine NiO surface, the concentration of  $\text{Ni}^{\delta+}$  species decreased on the surfaces subjected to  $\text{SO}_4^{2-}$  modification at higher temperatures (Figure 2–2D). This trend was also in agreement with that obtained using CO–pulsed chemisorption experiments, in which the Lewis acidic sites accessible to CO were quantified at 40 ° C.[24, 39, 48, 59, 60] Indeed, the amount of CO–accessible sites present in one gram of the catalysts ( $N_{\text{CO}}$ ) decreased in the following order of pristine NiO  $\rightarrow$  S300  $\rightarrow$  S400  $\rightarrow$  S500  $\rightarrow$  S600. This was likely ascribed to the sintering of the NiO particles coupled with the oxidation of  $\text{Ni}_{\text{DEFECT}}$  to  $\text{Ni}_{\text{LATTICE}}$  during the  $\text{SO}_4^{2-}$  functionalization of the surfaces using  $\text{O}_2$  at elevated temperature.

To investigate the Lewis acidic strengths of the  $\text{Ni}^{\delta+}$  species present in the catalysts, their *in situ* DRIFT spectra were collected at 50 ° C and 200 ° C. The background spectra of the purged surfaces were initially collected under a  $\text{N}_2$  atmosphere at 50/200 ° C and served as the base to investigate the acidic traits of the surfaces accessible to  $\text{NH}_3$ . As shown in Figure 2–3A, the surfaces apparently interacted with  $\text{NH}_3$  via protonation or coordination at 50 ° C. This was corroborated by the Brönsted acidic (*B*) or Lewis acidic (*L*) bands, resulting from the vibrational features of the N–H bonds of  $\text{NH}_3$  molecules adsorbed on the surfaces.[84, 85] However, pristine NiO lost its ability to interplay with  $\text{NH}_3$  at an elevated temperature. This was supported by the *in situ* DRIFT spectrum of pristine NiO at 200 ° C, which lacked *B* and *L* bands (Figure 2–3B). Chemisorption and DRIFT experiments suggested that the pristine NiO catalyst possessed the greatest  $N_{\text{CO}}$  value among all the catalysts studied, yet it could hardly exploit the Lewis acidic  $\text{Ni}^{\delta+}$  species to interplay with  $\text{H}_2\text{O}_2$  because of their weak binding strength. Conversely, the  $\text{SO}_4^{2-}$ –modified surfaces retained their capabilities to bind with  $\text{NH}_3$  on the Lewis acidic  $\text{Ni}^{\delta+}$  species even at 200 ° C except for the surface modified by  $\text{SO}_4^{2-}$  at 600 ° C (Figure 2–3B). The SAED pattern of S600 could also be used to

justify our claim that the use of high thermal energy to functionalize the surface with  $\text{SO}_4^{2-}$  is not a desirable strategy. In spite of providing a moderate  $N_{\text{CO}}$  value, S400 showed the smallest decrease in the area under the  $L$  bands among the S300–S500 samples when the temperature of the  $\text{NH}_3$ –accessible surfaces was increased from 50 ° C to 200 ° C. These experimental results suggested that among all temperatures studied, 400 ° C could be the optimal temperature to create the Lewis acidic  $\text{Ni}^{\delta+}$  species desirable to interplay with  $\text{H}_2\text{O}_2$  among all temperatures studied.

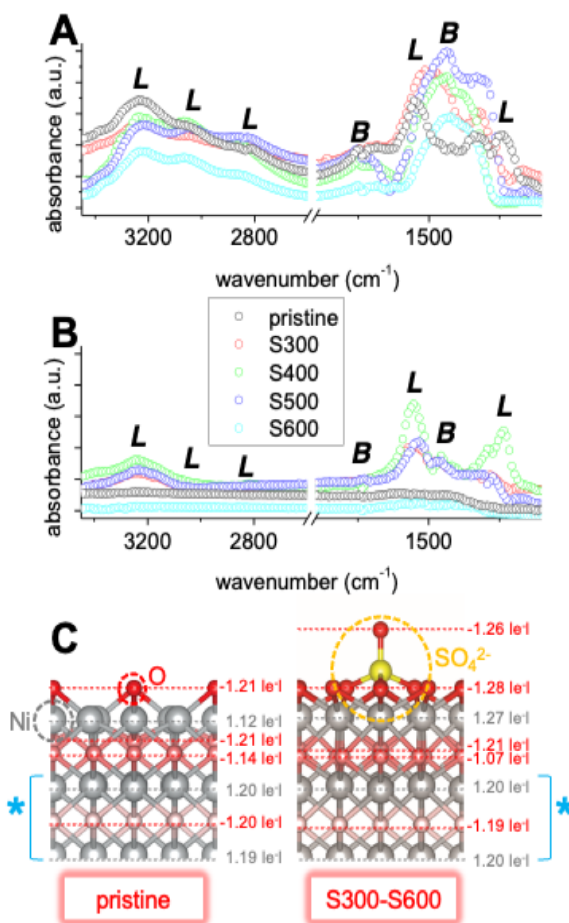


**Figure 2-3.** Background-subtracted, *in situ* DRIFT spectra of the catalysts upon their exposure to 1000 ppm  $\text{NH}_3$  at (A) 50 ° C and (B) 200 ° C.  $B$  and  $L$  indicate the Brønsted acid and Lewis acid sites bound to  $\text{NH}_3$ . (C) The Bader charge distributions of the Ni (grey circle) and O species (located at the outer-layer (red circle) or sub-layer (pink circle)) species bound to construct the (111) plane of pristine NiO and its  $\text{SO}_4^{2-}$ -modified analogue. In (C), the orange circle indicates the  $\text{SO}_4^{2-}$  functionality, whereas \* indicates the inner (bulk) layers indigenous to the (111) plane of the catalysts.

DFT calculations also served to explore the difference in the Ni charges and the lengths of the Ni–O bonds present in or near the catalyst surfaces. Again, the (111) plane of NiO was chosen to help clarify the reaction dynamics and sorption phenomena, because it is one of the main diffractions observed in the XRD patterns of the catalysts and had the lowest surface energy to help clarify the reaction dynamics as well as the sorption phenomena.[57, 58] Bader charge analysis was conducted and utilized to inspect the electronic features of the catalyst surfaces.[69, 70, 86] Charge separation among the Ni, O, or S atoms was evident and could be triggered by the difference in their electronegativities, as discussed in the introduction (Figure 2–3C). The pristine NiO and  $\text{SO}_4^{2-}$ -functionalized catalysts showed a Ni charge of  $\sim 1.20 \text{ le}^{-1}$  ( $\text{le}^{-1}$  denotes the elemental charge) in the bulk layers. In contrast, the pristine NiO surface showed a Ni charge of  $1.12 \text{ le}^{-1}$  ( $\text{e}^{-}$  denotes elemental charge), which was smaller than that of the  $\text{SO}_4^{2-}$ -functionalized surface ( $1.27 \text{ le}^{-1}$ ). In conjunction with the *in situ* DRIFT results, the computational results also validated the enhanced Lewis acidic strength of the surface  $\text{Ni}^{\delta+}$  species on S300–S500 in relation to that on pristine NiO.

In addition, the lengths of the Ni–O bonds located on or near the surface were also computed to verify our hypothesis that the binding strength of Ni–O can be promoted when the surface is modified with  $\text{SO}_4^{2-}$ . (The specifics are given in the introduction.) The pristine NiO and  $\text{SO}_4^{2-}$ -functionalized catalysts exhibited a Ni–O ( $D_{\text{Ni-O}}$ ) bond length of  $2.09 \text{ \AA}$  in the bulk layers. Interestingly, pristine NiO displayed reduced  $D_{\text{Ni-O}}$  values of  $2.00\text{--}2.06 \text{ \AA}$  on or near the surface, which were shorter than those on or near the surface functionalized with  $\text{SO}_4^{2-}$  ( $2.09\text{--}2.13 \text{ \AA}$ ). This could indicate that the amount of Ni species leached from the  $\text{SO}_4^{2-}$ -modified surface during the reaction might be similar to or greater than those released from the pristine NiO surface. Again, the  $\text{SO}_4^{2-}$ -functionalized surfaces might scarcely reduce the amount of Ni leaching during the reaction runs. Nonetheless, among all the catalysts studied, S400 provided  $\text{Ni}^{\delta+}$  species with the most desired Lewis

acidity together with the highest concentration of surface  $O_\alpha$  species among all the catalysts studied, thus potentially revealing outstanding  $H_2O_2$  scission performance.

The number of  $SO_4^{2-}$  functionalities on the catalyst surface is also paramount for the phenol degradation performance, in which the supported  $SO_4^{\cdot-}$  species are generated via the  $\cdot OH \rightarrow SO_4^{\cdot-}$  pathway and serve to the decomposer of phenol. The presence of supported  $SO_4^{\cdot-}$  precursors ( $SO_4^{2-}$ ) on the surface of the catalysts was of great plausibility, as evidenced by XANES experiments using  $Na_2SO_4$  and  $NiSO_4 \cdot 6H_2O$  as reference compounds.[87, 88] Notably, it was reported that  $SO_3^{2-}$  can be deposited on the catalyst surface as an adduct upon modification with  $SO_2/O_2$ . [89, 90] Hence, ideally,  $NiSO_3$  should also have been used as a reference compound to include the  $SO_3^{2-}$  functionality; however, this could not be achieved, owing to the absence of commercially available  $NiSO_3$ . This justified the utilization of  $Na_2SO_3$  as an alternative reference compound. In addition, the XANES spectra at the S  $K$ -edge were reported to exhibit dissimilar bands that could have resulted from the excitation of electrons innate to S with different local environments from the 1s to the antibonding molecular orbitals.[87] However, the beam source utilized for the XANES experiments could provide energy in the range of 50–1,300 eV. This was insufficient for obtaining the XANES spectra of the catalysts at the S  $K$ -edge,[91] thereby only allowing for the collection of their XANES spectra at the S  $L_{2,3}$ -edge. The XANES spectra of the reference compounds at the S  $L_{2,3}$ -edge exhibited a series of bands due to the excitation of the core-level electrons inherent to S from the 2p level to the unoccupied 3s  $\sigma^*$  or 3d level (Figure 2-4A).[87, 88, 92] The bands, however, could not be assigned because of the limited number of literature resources dealing with the elaboration of XANES spectra of inorganic sulfur-based compounds at the S  $L_{2,3}$ -edge. Nevertheless, the XANES spectra of the reference compounds showed distinct edge features, which could be caused by the different local geometries or charges of the S atoms confined in the *trigonal pyramidal* and



*tetrahedral* motifs of  $\text{SO}_3^{2-}$  and  $\text{SO}_4^{2-}$ , respectively.[87, 88] Importantly, the edge characters found in the XANES spectrum of  $\text{NiSO}_4 \cdot 6\text{H}_2\text{O}$  at the S  $L_{2,3}$ -edge were similar to those of S300–S600 (*e.g.*, the band shown with \* in Figure 2–4A), all of which were not alike to the band characteristics observed in the XANES spectrum of  $\text{Na}_2\text{SO}_3$ . Although the XANES spectra at the S  $L_{2,3}$ -edge were reported to be inadequate to quantify the relative compositions of  $\text{SO}_3^{2-}$  and  $\text{SO}_4^{2-}$  inherent to the compounds,[87, 93] they did provide evidence associated with the presence of  $\text{SO}_4^{2-}$  functionalities on the catalyst surfaces.

The molar ratio of the S to Ni contents (S/Ni) on the catalyst surface was also analyzed using XPS experiments. S400 provided the largest S/Ni value among all the catalysts modified with  $\text{SO}_4^{2-}$  species (Figure 2–2E), which was in close accordance with the trend observed for the bulk S/Ni values ( $N_{\text{S}}/N_{\text{Ni}}$ ) of S300–S600. The S400 surface also exhibited the highest concentration of surface  $\text{SO}_4^{2-}$  species among S300–S600. This was evidenced by their deconvoluted XPS spectra in the S 2p regime, where the surface  $\text{SO}_3^{2-}$  and  $\text{SO}_4^{2-}$  species were present at binding energies centered at  $\sim 167.7$  and  $\sim 168.8$  eV, respectively.[39, 94]

Furthermore, the *in situ* DRIFT spectra of pristine NiO were collected in the presence of  $\text{SO}_2$  and  $\text{O}_2$  at 300 ° C, 400 ° C, and 500 ° C to simulate the surfaces of S300–S500, on which the  $\text{SO}_3^{2-}$  and  $\text{SO}_4^{2-}$  functionalities were dispersed. It should be noted that the *in situ* DRIFT spectrum of pristine NiO at 600 ° C could not be obtained, owing to the limitation of the instrument, whose temperature could only be elevated up to 500 ° C.[39, 89, 90] Again, the background spectra of the purged surfaces were initially collected under a  $\text{N}_2$  atmosphere at 300 ° C and served as the basis to explore the configuration of the  $\text{SO}_3^{2-}/\text{SO}_4^{2-}$  functionalities bound to the catalyst surfaces at 300, 400, and 500 ° C.[39, 89, 90] Bands emerged in the wavenumber range of 950–1400  $\text{cm}^{-1}$  when the  $\text{SO}_2/\text{O}_2$  gas flow was turned on and stopped growing within 30 minutes of reaction run. The bands could be divided into two

domains, which were assigned as surface  $\text{SO}_3^{2-}/\text{SO}_4^{2-}$  species with *mono*-/*bi*-dentate and *tri*-dentate configurations located in the wavenumber range of  $950\text{--}1250\text{ cm}^{-1}$  and  $1280\text{--}1400\text{ cm}^{-1}$ , respectively (Figure 2-4B).[95–98] In contrast to S400 and S500, S300 barely presented any surface  $\text{SO}_3^{2-}/\text{SO}_4^{2-}$  species with a *tri*-dentate array (Figure 2-4B). This was in partial agreement with the smallest S/Ni value provided by S300 (Figure 2-2E). It also suggested that a temperature of  $300^\circ\text{C}$  might be insufficient to disperse the *tri*-dentate  $\text{SO}_4^{2-}$  species that were validated to be desirable for prompting the  $\cdot\text{OH} \rightarrow \text{SO}_4^{\cdot-}$  pathway, as discussed later. Indeed, the results highly suggested that S400 could reveal the highest efficiency in prompting the  $\text{H}_2\text{O}_2$  scission and radical interconversion cycles (Figure 2-1A and 2-1B).

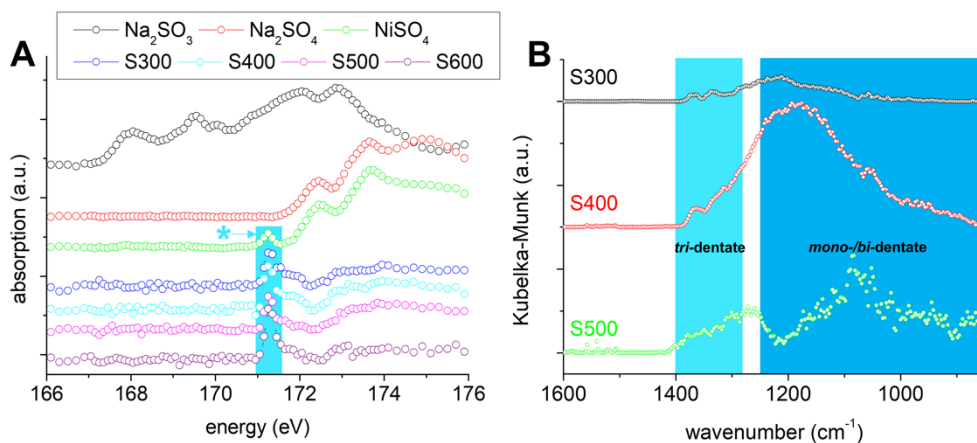


Figure 2-4. (A) XANES spectra of the catalysts at the S  $L_{2,3}$ -edge. \* denote the band observed in  $\text{NiSO}_4$  and S300–S600 only. (B) Background-subtracted, *in situ* DRIFT spectra of pristine NiO upon exposure to 1000 ppm  $\text{SO}_2$  and 3 vol. %  $\text{O}_2$  at  $300^\circ\text{C}$ ,  $400^\circ\text{C}$ , and  $500^\circ\text{C}$ . The domains shown with sky-shaded and blue-shaded rectangles indicate the surface  $\text{SO}_3^{2-}/\text{SO}_4^{2-}$  species with *tri*-dentate and *mono*-/*bi*-dentate configurations, respectively.

### 2.3.2. H<sub>2</sub>O<sub>2</sub> scission cycle

To compare the efficiencies of the catalyst surfaces during the degradation of phenol via  $\cdot\text{OH} \rightarrow \text{SO}_4^{\cdot-}$  with significant accuracy, it was necessary to first examine the cathodic H<sub>2</sub>O<sub>2</sub> productivities of the catalysts. We thus conducted H<sub>2</sub>O<sub>2</sub> production runs under conditions identical to those utilized during the phenol degradation runs to mimic their surface dynamics with the exception of the exclusion of phenol.[24, 39] In addition, the electric potential was adjusted to 1 or 3 V to vary the electric energy acting on the catalyst surface, whereas the use of 4 V was excluded because of the substantial liberation of the catalyst particles during the reaction runs (not shown).[24, 39, 48] The amounts of H<sub>2</sub>O<sub>2</sub> evolved at 3 V (N<sub>H<sub>2</sub>O<sub>2</sub></sub>) showed such a trend as to be saturated within an hour of the reaction runs and to substantially depend on the type of the catalysts with N<sub>H<sub>2</sub>O<sub>2</sub></sub> values of 0.34–0.60 mmol. Noteworthy, we previously found that the H<sub>2</sub>O<sub>2</sub> productivity ( $\text{O}_2 + 2\text{H}^+ + 2\text{e}^- \rightarrow \text{H}_2\text{O}_2$ ) can be directed by the two types of O sources, namely the O<sub>2</sub> dissolved in the reaction solution or fed by the anodic H<sub>2</sub>O oxidation ( $2\text{H}_2\text{O} \rightarrow \text{O}_2 + 4\text{H}^+ + 4\text{e}^-$ ), O<sub>α</sub>, and the e<sup>−</sup> innate to the catalyst surface[24, 39] The H<sub>2</sub>O<sub>2</sub> run in the absence of the catalyst (blank) was used to evaluate the contribution of the aqueous O<sub>2</sub> species and anodic H<sub>2</sub>O oxidation toward the generation of H<sub>2</sub>O<sub>2</sub>. [24, 39] The blank run rapidly saturated the N<sub>H<sub>2</sub>O<sub>2</sub></sub> value (~0.14 mmol) within 10 minutes and therefore left a N<sub>H<sub>2</sub>O<sub>2</sub></sub> of 0.2–0.45 mmol unidentified during the reaction runs in the presence of the catalysts. Based on our previous observation on SO<sub>4</sub><sup>2−</sup>-functionalized Fe<sub>2</sub>O<sub>3</sub>, the remaining N<sub>H<sub>2</sub>O<sub>2</sub></sub> was believed to partially originate from the O<sub>α</sub> species, whose quantities substantially relied on the temperature used to functionalize the surface with SO<sub>4</sub><sup>2−</sup>. [39] As shown in Figure 2–2C, among all the temperatures studied, a temperature of 400 ° C could aid in producing the largest concentration of O<sub>α</sub> species among all the temperatures studied. Meanwhile, e<sup>−</sup> was reported to react with H<sup>+</sup> and O<sub>2</sub> to form H<sub>2</sub>O<sub>2</sub> on or near the cathode.[24, 39] Hence, electric conductivities of the reaction mixtures were measured during the initial 2 hours of the reaction

runs to indirectly quantify the amount of  $e^-$  present in the reaction mixture in an indirect fashion.[24, 39] It was obvious that the reaction mixture on S400 exhibited a larger electric conductivity than that on the others ( $\sim 305 \mu S m^{-1}$  for S400;  $\leq \sim 295 \mu S m^{-1}$  for the others in Figure 2–2C). This proved that among the catalysts studied, S400 could provide the surface with the most desirable properties to improve the  $H_2O_2$  productivity among the catalysts studied.

The  $H_2O_2$  scission performance of the catalysts was then investigated at 3 V under identical environments to those used for the degradation of phenol with the exception that the reaction runs were performed in the absence of an electric potential and phenol (Figure 2–5A).[24, 39] The amount of  $H_2O_2$  used during the  $H_2O_2$  scission runs was determined based on the averaged  $N_{H_2O_2}$  values observed during the  $H_2O_2$  production runs at 3 V.[24, 39] In addition, the pH was set to seven prior to conducting the reaction runs to avoid any repercussions caused by the use of acidic and basic pH conditions, which potentially gave rise to severe Ni leaching and the instability of  $H_2O_2$  instability, respectively.[42, 43, 99] Notably, the  $H_2O_2$  scission runs provided the initial  $H_2O_2$  scission rates for the catalysts ( $-r_{H_2O_2, 0}$ ) after eliminating the background contribution (*i.e.*, the self-decomposition of  $H_2O_2$  in the absence of the catalysts).[24, 100] Here,  $-r_{H_2O_2, 0}$  is defined as the number of moles of  $H_2O_2$  consumed per gram of the catalyst per unit time.[24, 39, 48] (See how to obtain  $-r_{H_2O_2, 0}$  in the Experimental section.) In addition to showing the highest  $H_2O_2$  productivity, S400 also provided the highest  $\cdot OH$  productivity ( $-r_{H_2O_2, 0}$ ) among S300–S600. This could have resulted from the Lewis acidity of S400 being the most adequate to cleave  $H_2O_2$ , which was verified using a series of characterization experiments, as summarized below. Bader charge calculations provided evidence that S300–S600 could be bound to  $H_2O_2$  more strongly than pristine NiO because the Lewis acidic strengths of the  $Ni^{\delta+}$  species were promoted upon modification of the catalyst surface with  $SO_4^{2-}$  (Figure 2–3B). In the case of S300–S600, S400 contained the 2<sup>nd</sup> largest

amount of  $\text{Ni}^{\delta+}$  species accessible to  $\text{H}_2\text{O}_2$ , as corroborated by the CO-pulsed chemisorption and XPS experiments (Figure 2-2D). Nonetheless, the amount of  $\text{Ni}^{\delta+}$  species effectively bound to  $\text{H}_2\text{O}_2$  could be the largest when the  $\text{NiO}$  was functionalized with  $\text{SO}_4^{2-}$  at  $400^\circ\text{C}$ , as substantiated by the *in situ*  $\text{NH}_3$ -DRIFT experiments (Figure 2-3A). The characterization results again provided solid proof that S400 could provide the Lewis acidity (amount coupled with strength) most desirable to achieve the highest  $\cdot\text{OH}$  productivity via  $\text{H}_2\text{O}_2$  scission. In addition, the results observed using S400 were 2.5–3.5 fold greater than those obtained for  $\text{Fe}_2\text{O}_3$  functionalized with  $\text{SO}_4^{2-}$  at  $500^\circ\text{C}$  (the optimal catalyst denoted as S500-Fe[39]) in terms of the  $\text{H}_2\text{O}_2$  and  $\cdot\text{OH}$  productivities ( $N_{\text{H}_2\text{O}_2}$  of  $\sim 0.24\text{ mmol}$ ;  $-r_{\text{H}_2\text{O}_2, 0}$  of  $0.4\ \mu\text{mol}_{\text{H}_2\text{O}_2}\text{g}_{\text{CAT}}^{-1}\text{min}^{-1}$ ). This could allow us to assert that the  $\text{Ni}^{\delta+}$  species are indeed more effective than their  $\text{Fe}^{\delta+}$  counterparts in regard to the  $\text{H}_2\text{O}_2$  cleavage, which was in exact agreement with the results of our previous study on metal sulfides.[24]

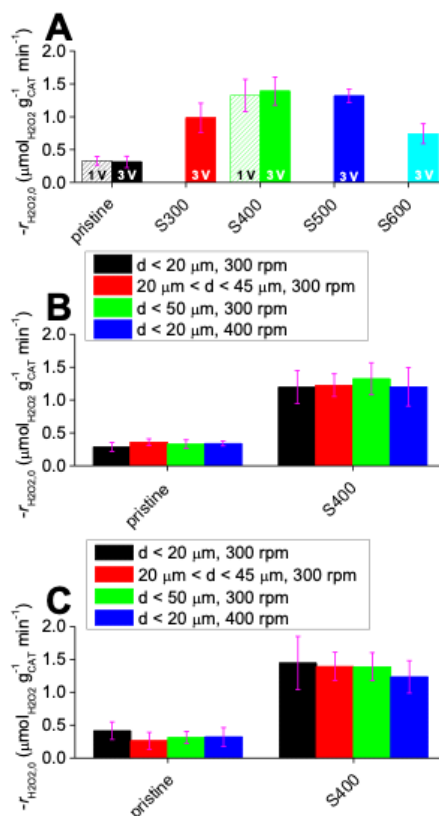


**Figure 2-5.** (A) Initial reaction rates ( $-r_{\text{H}_2\text{O}_2,0}$ ) of the catalysts obtained during the  $\text{H}_2\text{O}_2$  scission runs used to simulate the phenol degradation runs at 1 V or 3 V. The  $-r_{\text{H}_2\text{O}_2,0}$  values of pristine NiO and S400 obtained during the  $\text{H}_2\text{O}_2$  scission runs used to simulate the phenol degradation runs at (B) 1 V or (C) 3 V, while altering the particles size of the catalysts or stirring speed of the reaction mixtures. Reaction conditions: 0.2 g of catalyst (< 50  $\mu\text{m}$  for a); 0.2 mol of  $\text{Na}_2\text{SO}_4$ ; 100 mL of de-ionized  $\text{H}_2\text{O}$ ;  $\text{H}_2\text{O}_2$  with concentrations of 0.13 mmol (1 V) or 0.47 mmol (3 V) for pristine NiO, 0.55 mmol (3 V) for S300, 0.27 mmol (1 V) or 0.60 mmol (3 V) for S400, 0.43 mmol (3 V) for S500, and 0.33 mmol (3 V) for S600; 25 ° C; and 300 rpm (for A) or 400 rpm (for B and C)).

The  $\text{H}_2\text{O}_2$  scission performance of the catalysts at 1 V was also evaluated to determine the number of  $\text{H}_2\text{O}_2$  molecules that could be cleaved under different electric energies acting on the catalyst surface (*i.e.*, 1 V versus 3 V)[24] and to propose the rate-determining step dominating the  $\cdot\text{OH} \rightarrow \text{SO}_4^{\cdot-}$  pathway. Pristine NiO and S400 were selected for these reaction runs because they could decompose phenol primarily using  $\cdot\text{OH}$  (unsupported) and the supported  $\text{SO}_4^{\cdot-}$ , respectively, with the largest difference in the  $-r_{\text{H}_2\text{O}_2,0}$  values. The method to obtain the  $-r_{\text{H}_2\text{O}_2,0}$  values of these two catalysts and the controls

under the reaction conditions at 1 V was identical to that at 3 V. Notably, the rate-determining step can be clarified only when using the initial reaction rate measured under the reaction-limited regime.[39] The SEM images of the pristine NiO and S400 corroborated that their particle sizes were  $\leq 50 \mu\text{m}$  (not shown). This could justify the variation in the particle size of the catalysts from  $< 25 \mu\text{m}$  to  $20\text{--}45 \mu\text{m}$  to  $< 50 \mu\text{m}$  via sieving to ensure that the  $\text{H}_2\text{O}_2$  scission runs were carried out in the absence of internal diffusion limitation.[39] In addition, the stirring speed was also varied from 300 rpm to 400 rpm to affirm the lack of external diffusion limitation during the  $\text{H}_2\text{O}_2$  scission runs.[39] The  $-r_{\text{H}_2\text{O}_2, 0}$  values for pristine NiO and S400 had similar magnitudes throughout the control runs when varying the particle sizes or the stirring speeds at 1 and 3 V, as shown in Figure 2-5B and 2-5C, respectively, thereby validating that the  $\text{H}_2\text{O}_2$  scission runs were performed in the reaction-limited regime.[39] In addition, we concluded in our previous studies that a higher electric potential across the electrodes could provide a catalyst surface with a larger electric energy.[24, 47, 48] A larger electric energy acting on the catalyst surface then might likely result in a greater increase in the temperature of the catalyst surface, which in turn could prevent the  $\text{Ni}^{\delta+}$  species from binding with the O atoms in  $\text{H}_2\text{O}_2$  more significantly at a higher electric potential.[24, 47] Interestingly, in spite of increasing the electric energy exerted on the surface by altering the electric potential from 1 V to 3 V,[24, 47] the resulting  $-r_{\text{H}_2\text{O}_2, 0}$  values of the pristine NiO or S400 remained unchanged. (See Figure 2-5A). One can readily propose that if the rate-determining step were the adsorption of  $\text{H}_2\text{O}_2$  on the catalyst surface, a greater electric potential would hinder the interactions between the catalyst surface and  $\text{H}_2\text{O}_2$ , thus reducing the  $-r_{\text{H}_2\text{O}_2, 0}$  value of the catalyst.[24] Consequently, the  $\text{H}_2\text{O}_2$  scission runs could narrow down the tentative rate-determining step to  $\text{H}_2\text{O}_2$  cleavage or  $\cdot\text{OH}$  desorption.

To elucidate the  $\text{H}_2\text{O}_2$  scission mechanism occurring on the catalyst surface, the  $\text{H}_2\text{O}_2$  molecule was located adjacent to the surface  $\text{Ni}^{\delta+}$  moiety created

on the surface of the (111) plane of NiO (Figure 2-1D) and was monitored in terms of the transition of  $\text{H}_2\text{O}_2$  and its energetics (Figure 2-6). The two OH terminals of  $\text{H}_2\text{O}_2$  ( $\text{OH}_1$  and  $\text{OH}_2$ ) were initially bound with two  $\text{Ni}^{\delta+}$  species via complexation without any dissociation, in which both the energetics and charges of  $\text{OH}_1$  and  $\text{OH}_2$  were almost invariant. This was in agreement with our experimental results on the  $\text{H}_2\text{O}_2$  scission runs to demonstrate that  $\text{H}_2\text{O}_2$  adsorption was not the rate-determining step.  $\text{H}_2\text{O}_2$  then underwent cleavage to form  $\text{OH}_1$  and  $\text{OH}_2$  fragments, each of which was relaxed to bind with two  $\text{Ni}^{\delta+}$  species via bridging. Interestingly, the  $\text{H}_2\text{O}_2$  scission step was exothermic with an energetic change ( $\Delta E$ ) of  $-2.9$  eV relative to the  $\text{H}_2\text{O}_2$  adsorption stage, which suggested that the  $\text{H}_2\text{O}_2$  cleavage stage could not dominate the  $\text{H}_2\text{O}_2$  scission cycle. The  $\text{H}_2\text{O}_2$  scission stage also abated the charges of the two OH fragments by  $\sim 0.4$   $\text{e}^-$  in comparison with those at the  $\text{H}_2\text{O}_2$  adsorption stage.

In contrast, the formation of the radical derivative of the  $\text{OH}_1$  fragment (*i.e.*, the increase in the  $\text{OH}_1$  charge by  $\sim 0.3$   $\text{e}^-$ ) and its detachment from the two  $\text{Ni}^{\delta+}$  species required a  $\Delta E$  of  $\sim 3.0$  eV relative to the  $\text{H}_2\text{O}_2$  scission stage. Nonetheless, the energy of the  $\cdot\text{OH}$  desorption stage was  $\sim 0.2$  eV lower than that during the initial stage, which rendered the  $\text{H}_2\text{O}_2$  scission cycle energetically favorable. All of these results strongly suggested that  $\cdot\text{OH}$  desorption stage was the rate-determining step for the  $\text{H}_2\text{O}_2$  scission cycle. This also suggested that the overall rate-determining step could be the  $\cdot\text{OH}$  desorption stage unless the radical interconversion cycle included any endothermic stages.



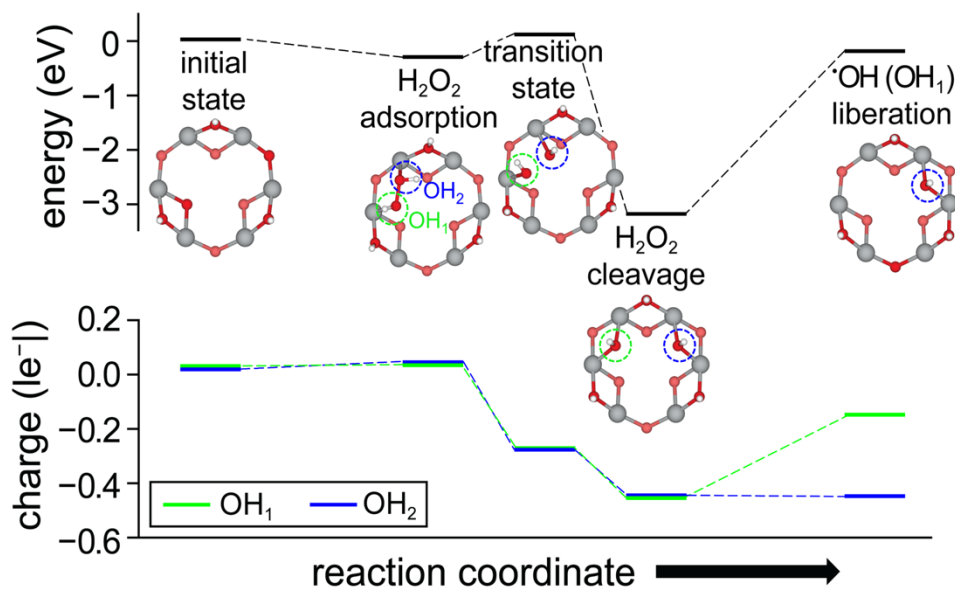


Figure 2-6. Energetics on the catalyst surface of the (111) facet for the catalysts altered during the H<sub>2</sub>O<sub>2</sub> scission cycle. Change in the charges for the OH<sub>1</sub> and OH<sub>2</sub> fragments during the H<sub>2</sub>O<sub>2</sub> scission cycle.

### 2.3.3. Radical interconversion cycle

The calculations on the catalytic H<sub>2</sub>O<sub>2</sub> scission cycle suggested the plausibility of  $\cdot\text{OH}$  desorption as the rate-determining step for the  $\cdot\text{OH} \rightarrow \text{SO}_4^{\cdot-}$  pathway. This, however, was only partially convincing until the other catalytic cycle to interconvert  $\cdot\text{OH}$  and  $\text{SO}_4^{\cdot-}$  was fully investigated. We performed the phenol degradation runs under comparable conditions to those employed to cleave H<sub>2</sub>O<sub>2</sub> except for applying an electric potential of 1 or 3 V and the use of phenol.[24, 39] The phenol degradation runs provided the initial phenol consumption rates primarily driven by the catalyst surfaces ( $-r_{\text{PHENOL}, 0}$ ) upon subtraction of the background contribution (*i.e.*, anodic oxidation).[24, 39, 50] Here,  $-r_{\text{PHENOL}, 0}$  denotes the number of moles of phenol consumed per gram of the catalyst per unit time, whereas a pseudo-1<sup>st</sup>-order kinetic model served to determine  $-r_{\text{PHENOL}, 0}$  by fitting the reaction data.[24, 39, 48] The  $-r_{\text{PHENOL}, 0}$  values of the catalysts obtained at 3 V served to contrast their ability to decompose phenol using  $\cdot\text{OH}$  or  $\text{SO}_4^{\cdot-}$ .

The pristine NiO catalyst provided a smaller  $-r_{\text{PHENOL}, 0}$  than those modified with  $\text{SO}_4^{2-}$  (Figure 2-7A). This indeed warranted the exploitation of

supported  $\text{SO}_4^{\bullet-}$  for the decomposition of phenol. ICP–AAS served to inspect the amount of Ni leached during the phenol degradation run. S300 and S400 leached 0.3–0.4 mol.% of Ni species, which was slightly larger than that observed for pristine NiO ( $\sim 0.2$  mol.% of Ni). This was in good agreement with the calculations of the Ni–O bond lengths in pristine NiO and the NiO catalyst functionalized with  $\text{SO}_4^{2-}$  and thus verified the minor contribution of the  $\text{SO}_4^{2-}$  functionalities to abating the Ni leaching. Nevertheless, the  $-r_{\text{PHENOL}, 0}$  was the highest when the pristine NiO was functionalized with  $\text{SO}_4^{2-}$  at  $400^\circ\text{C}$  (Figure 2–7A). In addition, the  $-r_{\text{PHENOL}, 0}$  value of S400 was even larger than that of S500–Fe ( $\sim 1.0 \mu\text{mol}_{\text{PHENOL}} \text{g}_{\text{CAT}}^{-1} \text{min}^{-1}$ ), which was obtained after the background correction and thus should be distinct from that reported in our study ( $\sim 1.5 \mu\text{mol}_{\text{PHENOL}} \text{g}_{\text{CAT}}^{-1} \text{min}^{-1}$ ).<sup>[39]</sup> This could demonstrate the benefits of NiO as a proper platform to accommodate  $\text{SO}_4^{\bullet-}$  formed via radical transfer from  $\cdot\text{OH}$ .

Notably, the greatest  $\text{H}_2\text{O}_2$  scission performance of S400 driven by its desired Lewis acidity might be responsible for the highest  $-r_{\text{PHENOL}, 0}$  value observed among all the catalysts studied. Meanwhile, the largest molar ratio of the surface S/Ni along with a significant concentration of surface  $\text{SO}_4^{2-}$  species might bring about the greatest  $-r_{\text{PHENOL}, 0}$  of S400 if the  $\cdot\text{OH} \rightarrow \text{SO}_4^{\bullet-}$  pathway were directed by an endothermic stage during the radical interconversion cycle. The two scenarios stated above could motivate the exploration of the feasibility of  $\cdot\text{OH} \leftrightarrow \text{SO}_4^{\bullet-}$  interconversion and its elementary steps suggested in Figure 2–1B.

To establish whether radical transfer from  $\cdot\text{OH}$  to  $\text{SO}_4^{\bullet-}$  was highly likely, we performed electron paramagnetic resonance (EPR) experiments using 5,5–dimethyl–1–pyrroline *N*-oxide (DMPO) as a trapping agent for  $\cdot\text{OH}$  and  $\text{SO}_4^{\bullet-}$ .<sup>[101–103]</sup> Pristine NiO and S400 catalysts were chosen for these experiments and the scavenging runs discussed below for the same reasons addressed in the previous section, in addition to them having the largest difference in the  $-r_{\text{PHENOL}, 0}$  values. We also benchmarked the  $\text{H}_2\text{O}_2$  scission

runs on the catalysts, wherein an excess amounts of  $\text{H}_2\text{O}_2$  served with no electric potentials exerted, whereas the catalysts were removed from the reaction aliquots prior to recording their EPR spectra.

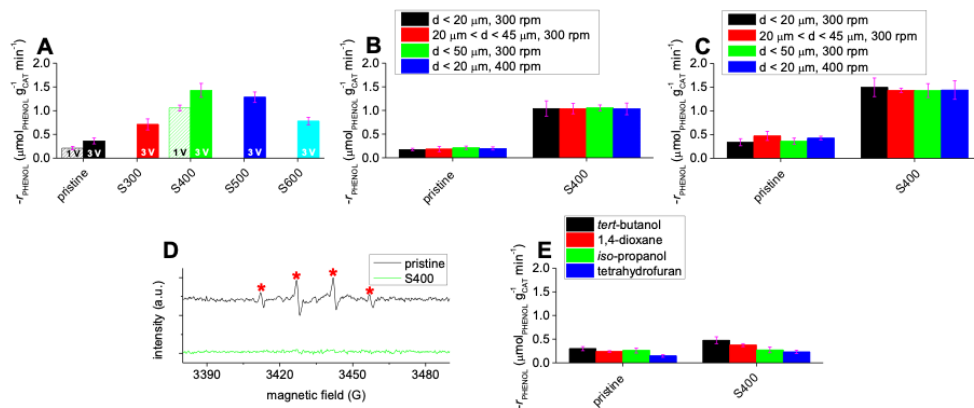


**Figure 2-7.** (A) The initial reaction rates ( $-r_{\text{PHENOL},0}$ ) of the catalysts obtained during the phenol degradation runs at 1 V or 3 V. The  $-r_{\text{PHENOL},0}$  values of pristine NiO and S400 obtained during the phenol degradation runs at (B) 1 V or (C) 3 V, while altering the particles size of the catalysts or stirring speed of the reaction mixtures. (D) The EPR spectra of the reaction aliquots collected from the  $\text{H}_2\text{O}_2$  scission runs on pristine NiO and S400 in the presence of DMPO. In (D), \* indicates the DMPO-OH adduct. (E) The  $-r_{\text{PHENOL},0}$  values of pristine NiO and S400 obtained during the phenol degradation runs at 3 V in the presence of the scavengers. Reaction conditions: 0.2 g of catalyst (< 50 μm for (A) and (E)); 0.2 mol of  $\text{Na}_2\text{SO}_4$ ; 100 mL of de-ionized  $\text{H}_2\text{O}$ ; 0.1 mmol of phenol; scavenger concentrations of 0.94 mmol for pristine NiO and 1.32 mmol for S400; 25 ° C; 300 rpm (for (A) and (E)). Analytical conditions for (D): 0.02 g of catalyst (< 50 μm); 0.02 mol of  $\text{Na}_2\text{SO}_4$ ; 10 mL of de-ionized  $\text{H}_2\text{O}$ ;  $\text{H}_2\text{O}_2$  concentrations of 0.47 mmol for pristine NiO and 0.60 mmol for S400; DMPO concentrations of 4.7 mmol for pristine NiO and 6.0 mmol for S400; 0 V; and 25 ° C.

Again, the pristine NiO only included  $\text{Ni}^{\delta+}$  species that activated  $\text{H}_2\text{O}_2$  for the liberation of  $\cdot\text{OH}$  to the reaction solution. Indeed, EPR spectrum of the aliquot taken from the pristine NiO run exhibited quartet peaks with an intensity ratio of 1:2:2:1 coupled with hyperfine splitting constants of  $\sim 15.0$  G (\* shown in Figure 2-7D). These peaks are characteristics of the  $\cdot\text{OH}$  adducted to DMPO (DMPO-OH), as reported elsewhere.[101–103] In addition, S400 also afforded  $\text{Ni}^{\delta+}$  species that could release  $\cdot\text{OH}$  into the reaction solution. Nonetheless, most of the  $\cdot\text{OH}$  species liberated were postulated to participate in the formation of the  $\text{SO}_4^{\cdot-}$  species bound to the

S400 surface. If this were the case, one should not observe the DMPO–OH as well as the DMPO adducted to  $\text{SO}_4^{\bullet-}$  (DMPO– $\text{SO}_4$ ) [101–103] in EPR spectrum of the aliquot taken from the S400 run. As anticipated, the EPR spectrum of this aliquot only exhibited the baseline signal, while lacking any peaks caused by the DMPO– $\text{SO}_4$  and DMPO–OH adducts (Figure 2–7D). Apparently, EPR spectroscopy could validate the likelihood of the interconversion of  $\cdot\text{OH}$  (unsupported)  $\leftrightarrow$   $\text{SO}_4^{\bullet-}$  (supported) on the S400 surface.

Addition proof associated with the interconversion of  $\cdot\text{OH} \leftrightarrow \text{SO}_4^{\bullet-}$  could be found in the phenol degradation runs using four scavengers with distinct rate constants to terminate  $\cdot\text{OH}$  ( $k_{\cdot\text{OH}}$ ) or  $\text{SO}_4^{\bullet-}$  ( $k_{\text{SO}_4^{\bullet-}}$ ). [39] The quantities of the scavengers used for the reaction runs were set based on two major hypotheses: 1) 1 mole of  $\text{H}_2\text{O}_2$  can be cleaved to produce 2 moles of  $\cdot\text{OH}$  and 2) 1 mole of bulk S content can be used to create 1 mole of  $\text{SO}_4^{2-}$  functionality. [24, 39] (Specifics can be found in Figure 2–7 caption.) The scavengers were reported to have larger  $k_{\cdot\text{OH}}$  values in the following order of *tert*–butanol  $\rightarrow$  *iso*–propanol  $\rightarrow$  1,4–dioxane  $\rightarrow$  tetrahydrofuran. [28, 104–106] The pristine NiO catalyst decomposed phenol with the primary use of unsupported  $\cdot\text{OH}$  and thus reduced its  $-r_{\text{PHENOL}, 0}$  value in the presence of a scavenger with a greater  $k_{\cdot\text{OH}}$  value (Figure 2–7E). A similar trend was observed in the S400 runs, where the use of a scavenger with a greater  $k_{\text{SO}_4^{\bullet-}}$  value led to a smaller  $-r_{\text{PHENOL}, 0}$  value (*i.e.*, a greater  $k_{\text{SO}_4^{\bullet-}}$  in the order of *tert*–butanol  $\rightarrow$  1,4–dioxane  $\rightarrow$  *iso*–propanol  $\rightarrow$  tetrahydrofuran). [28, 104–106] In particular, the  $k_{\cdot\text{OH}}$  values were  $10\text{--}10^3$  fold larger than the  $k_{\text{SO}_4^{\bullet-}}$  values for all the scavengers studied. This suggested that a noticeable reduction in the  $-r_{\text{PHENOL}, 0}$  value of the catalyst should be observed if  $\cdot\text{OH}$  were the main source that degraded phenol. [39] As anticipated, the  $-r_{\text{PHENOL}, 0}$  values of pristine NiO were consistently smaller than those of S400 throughout the reaction runs using the identical scavengers. This indicated that S400 could degrade phenol with the primary use of the supported  $\text{SO}_4^{\bullet-}$ .

In addition, the range of  $-r_{\text{PHENOL}, 0}$  values changed during the scavenger runs on S400 ( $0.25 \mu\text{mol}_{\text{PHENOL}} \text{g}_{\text{CAT}}^{-1} \text{min}^{-1}$ ) was  $\sim 1.5$  times that on pristine NiO ( $0.16 \mu\text{mol}_{\text{PHENOL}} \text{g}_{\text{CAT}}^{-1} \text{min}^{-1}$ ). This could be caused by the far larger difference in the magnitudes of  $k_{\text{SO}_4 \cdot^-}$  for the scavengers ( $10^5$ – $10^8 \text{mol L}^{-1} \text{sec}^{-1}$ ) when compared to the difference in their  $k_{\cdot\text{OH}}$  counterparts ( $10^8$ – $10^9 \text{mol L}^{-1} \text{sec}^{-1}$ ). [39] All of our results obtained from the scavenger experiments could validate that the supported  $\text{SO}_4 \cdot^-$  species were of substantial plausibility and indeed enabled the degradation of phenol.

The reaction  $\text{SO}_4^{2-} + \cdot\text{OH} + \text{H}^+ \rightarrow \text{SO}_4 \cdot^- + \text{H}_2\text{O}$  was also computed using the  $\text{SO}_4^{2-}$ -modified surface on the (111) facet of NiO to assert our argument associated with the supported  $\text{SO}_4 \cdot^-$ . The purpose of the calculations was to investigate the charge ( $e^-$ ) transfer among  $\cdot\text{OH}$ ,  $\text{SO}_4^{2-}$ , and Ni species in conjunction with the altered energetics (Figure 2–8). Initially,  $\text{H}^+$  approached the  $\text{SO}_4^{2-}$  functionality via hopping with the continuous formation of  $\text{H}_3\text{O}^+$  (blue circle), as shown in the yellow-shaded rectangle in Figure 2–8. The  $\cdot\text{OH}$  radical (green circle) also approached the  $\text{SO}_4^{2-}$  functionality (orange circle), whose three S–O bonds were coordinated to three Ni species adjacent to one another in a *tri*-dentate manner. This was in partial agreement with the *in situ* DRIFT spectra of the pristine NiO catalyst in the presence of  $\text{SO}_2/\text{O}_2$  at 300–500 ° C, all of which suggested the presence of  $\text{SO}_4^{2-}$  species bound to the surface in a *tri*-dentate array, as discussed above (Figure 2–4B). The  $\text{SO}_4^{2-}$  functionality was then coordinated to  $\cdot\text{OH}$  to produce an  $\text{SO}_4^{2-} \cdot\text{OH}$  intermediate (blue-shaded rectangle in Figure 2–8), which was presumably converted into  $\text{SO}_4 \cdot^- \cdot\text{OH}$  via  $e^-$  transfer from  $\text{SO}_4^{2-}$  to  $\cdot\text{OH}$ . (See Figure 2–1B.) The formation of the supported  $\text{SO}_4 \cdot^-$  was indeed highly likely, as supported by the increase in the charge of the  $\text{SO}_4^{2-}$  species by  $\sim 0.6 \text{le}^-$ . Interestingly, although  $\text{SO}_4 \cdot^- \cdot\text{OH}$  could be produced, the NiO platform could act as an  $e^-$  extractor to remove  $e^-$  away from  $\text{SO}_4 \cdot^- \cdot\text{OH}$ . This could be evidenced by the reduction in the charge of the three Ni species coordinated to  $\text{SO}_4^{2-}$  by  $\sim 0.1 \text{le}^-$ . In turn, this could be compensated by an increase in the

charge of  $^-\text{OH}$  innate to  $\text{SO}_4^{\cdot-}-^-\text{OH}$  by  $\sim 0.2 \text{ e}^-$ .

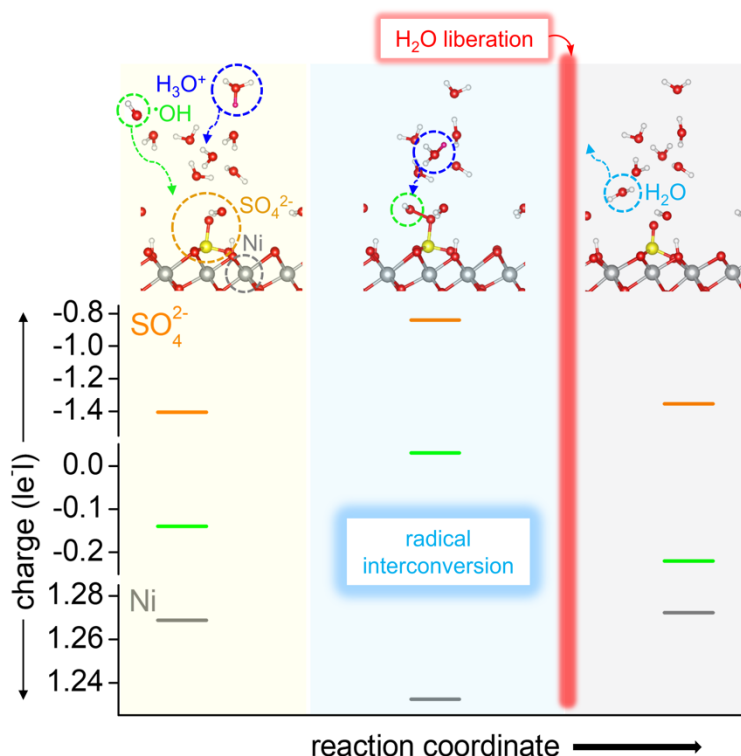


Figure 2-8. Schematic representation of the  $^-\text{OH}$  (green circle) and  $\text{H}^+$  (blue circle)-mediated radicalization of the  $\text{SO}_4^{2-}$  functionalities (orange circle) present on the surface of the (111) facet of the catalysts to form  $\text{SO}_4^{\cdot-}$ , while releasing  $\text{H}_2\text{O}$  (sky blue circle). The change in the charges for  $\text{SO}_4^{2-}$ ,  $^-\text{OH}$ , and surface Ni bound to  $\text{SO}_4^{2-}$  during the radical interconversion between  $^-\text{OH}$  and  $\text{SO}_4^{\cdot-}$ .

The Ni species could also function as an  $\text{e}^-$  reservoir to provide the  $\text{SO}_4^{\cdot-}-^-\text{OH}$  intermediate with  $\text{e}^-$ . This led to a decrease in the  $^-\text{OH}$  charge by  $\sim 0.2 \text{ e}^-$ , while degenerating the electronics of the Ni species near their initial state. (See grey-shaded regime in Figure 2-8.) The  $\text{SO}_4^{\cdot-}-^-\text{OH}$  intermediate then interacted with  $\text{H}^+$  ( $\text{H}_3\text{O}^+$ ) to form  $\text{H}_2\text{O}$  and could oxidize phenol at the moment that  $\text{H}_2\text{O}$  was liberated from the supported  $\text{SO}_4^{\cdot-}$  species, as shown with the red bar in Figure 2-8. The  $\text{SO}_4^{\cdot-}$  species that interplayed with phenol could also alter their electronics similarly to those of the initial  $\text{SO}_4^{2-}$  functionalities. Most importantly, all the elementary stages in the radical interconversion cycle were exothermic, which highly suggested that the  $^-\text{OH}$  desorption stage was the rate-determining step of the overall  $^-\text{OH} \rightarrow \text{SO}_4^{\cdot-}$ .

pathway.

Phenol degradation runs on pristine NiO and S400 at 1 V were carried out to gather additional experimental evidence associated with the rate-determining step. It should be noted that the phenol degradation runs using various particle sizes of the catalysts prepared via sieving or various stirring speeds of the reaction mixture revealed that the  $-r_{\text{PHENOL}, 0}$  values were unchanged (Figure 2-7B and 2-7C). This indicated that the  $-r_{\text{PHENOL}, 0}$  values were obtained in the reaction-limited regime, which was free from diffusion limitations[39] and thus could help justify our conclusion on the rate-determining step. As shown in Figure 2-7A, a higher  $-r_{\text{PHENOL}, 0}$  value was acquired at a larger electric potential during the phenol degradation runs on the pristine NiO and S400 catalysts. If the rate-determining step were the  $\text{H}_2\text{O}_2$  scission stage, the  $-r_{\text{PHENOL}, 0}$  values should be comparable even with an increase in the electric potential (*i.e.*, upon increasing the electric energy acting on the surface).[24] All the theoretical and experimental results strongly supported our claim that  $\cdot\text{OH}$  desorption from the  $\text{Ni}^{\delta+}$  species present in the  $\text{SO}_4^{2-}$ -functionalized surface can significantly direct the phenol decomposition performance ( $-r_{\text{PHENOL}, 0}$ ). Of note, although the phenol adsorption step was verified not to direct  $\cdot\text{OH} \rightarrow \text{SO}_4^{\cdot-}$  as the rate-determining stage, it could be deemed as a background. Hence, its contribution ( $X_{\text{PHENOL}}$ ) should be subtracted from the profile of  $X_{\text{PHENOL}}$  versus time for the catalyst via an identical manner to that utilized to correct the  $X_{\text{PHENOL}}$  profile of the catalyst with the use of another background (anodic oxidation), as stated above. Nonetheless, our kinetic data could not be corrected using the background caused by phenol adsorption because of the rarity of the electric environments, in which the catalyst surface only adsorbed phenol yet did not proceed with  $\cdot\text{OH} \rightarrow \text{SO}_4^{\cdot-}$ . Of additional note, one cannot completely exclude the tentative function of  $\cdot\text{OH}$  in degrading phenol, yet, could confidently claim that  $\cdot\text{OH}$  and  $\text{'SO}_4^{\cdot-}'$  do act as the minor and 'major' source used to decompose phenol, respectively. This could be partially evidenced by the exothermic nature of the radical transfer

from  $\cdot\text{OH}$  to  $\text{SO}_4^{\cdot-}$  clarified by DFT calculations (Figure 2–8), which could suggest that the formation of the supported  $\text{SO}_4^{\cdot-}$  might be as spontaneous as the degradation of phenol triggered by  $\cdot\text{OH}$ . Scavenging runs on the catalysts using various scavengers with dissimilar abilities to quench  $\cdot\text{OH}$  and  $\text{SO}_4^{\cdot-}$  could also corroborate the role of  $\text{SO}_4^{\cdot-}$  as the prime degrader of phenol, as detailed in the annotations in Figure 2–7E. The function of the supported  $\text{SO}_4^{\cdot-}$  as the main decomposer of phenol could be also substantiated using the EPR spectra of S400 (Figure 2–7D), wherein the peaks indexed to the DMPO–OH adduct should be observed, if the S400 catalyst primarily generated  $\cdot\text{OH}$  as the main source of phenol degradation. All the results could demonstrate our claim that S400 can degrade phenol with the main use of the supported  $\text{SO}_4^{\cdot-}$  species.



#### 2.3.4. Sustainability

NiO functionalized with  $\text{SO}_4^{2-}$  can sustain the  $\cdot\text{OH} \rightarrow \text{SO}_4^{\cdot-}$  pathway only when its surface degrades phenol with the primary use of the supported  $\text{SO}_4^{\cdot-}$ , while minimizing the leaching of the rate director ( $\text{Ni}^{\delta+}$ ) used to produce and desorb  $\cdot\text{OH}$ . Filtration runs on the catalysts were performed to ensure that the heterogeneous catalytic oxidation on the supported (unleached)  $\text{SO}_4^{\cdot-}$  species was the main reaction involved in the decomposition of phenol.[39] The filtration runs were conducted in a manner identical to the phenol degradation runs at 3 V with the exception of the inclusion of a filtration step performed after an hour of the reaction runs.[24, 39] (See grey-shaded rectangle in Figure 2-9A.) The reaction solutions were then collected and monitored in terms of the amount of phenol consumed at 3 V.[24, 39] This was because these solutions might contain  $\text{Ni}^{\delta+}$  and  $\text{SO}_4^{2-}$  species, both of which were leached from the catalyst surface yet were active in producing  $\cdot\text{OH}$  and  $\text{SO}_4^{\cdot-}$  utilized for the degradation of phenol, respectively.[24, 39] The phenol degradation run in the absence of a catalyst (blank) was dominated by anodic oxidation and therefore revealed the quantity of phenol consumed during 1-8 hours of reaction ( $N_{\text{PHENOL}}^*$ ) as  $\sim 15 \mu\text{mol}$ . The filtration run on pristine NiO showed a  $N_{\text{PHENOL}}^*$  value comparable to that of the blank run, which indicated that the unleached  $\text{Ni}^{\delta+}$  species acted as the main decomposer of phenol. The filtration runs on S300-S600 also provided  $N_{\text{PHENOL}}^*$  values that were of similar magnitudes that were similar to that of the blank run. These results provide sound evidence to substantiate that the  $\text{SO}_4^{\cdot-}$  species supported on NiO were the main decomposer of phenol.[24, 39]

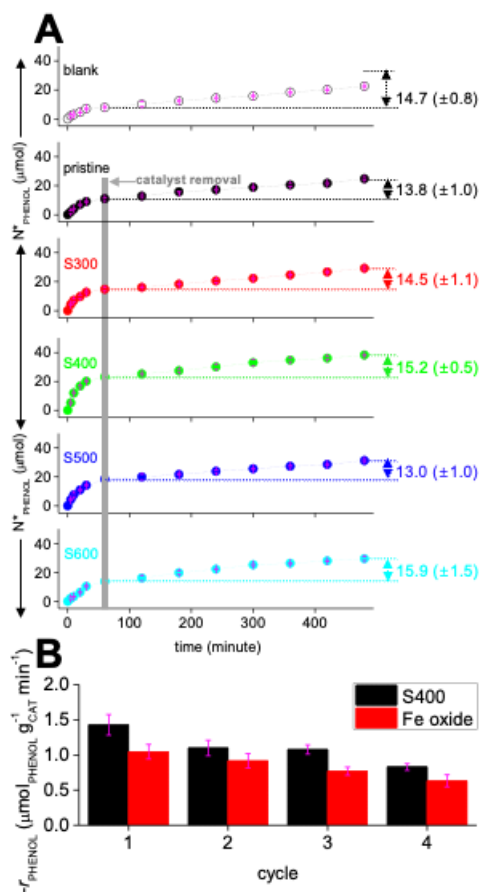


**Figure 2-9.** (A) Quantities of phenol consumed ( $N^*_{PHENOL}$ ) during the filtration runs in the absence (blank) and the presence of the catalysts. (B) The initial phenol consumption rates ( $-r_{PHENOL,0}$ ) of S400–Fe obtained during the recycling experiments. Reaction conditions: 0.2 g (or 0 g) of catalyst with the size of  $< 50 \mu\text{m}$  in size; 0.2 mol of  $\text{Na}_2\text{SO}_4$ ; 100 mL of de-ionized  $\text{H}_2\text{O}$ ; 0.1 mmol of phenol; 3 V;  $25^\circ\text{C}$ ; and 300 rpm.

In addition, the reusability of the catalysts in degrading phenol was also evaluated, while following a protocol identical to that used during the phenol degradation runs at 3 V.[24, 39] S400 was selected because of its highest phenol degradation performance, whereas S500–Fe was also utilized for comparison. The  $-r_{PHENOL,0}$  values also served to contrast the recyclability of these catalysts up to the 4<sup>th</sup> cycle, during which the catalyst coated on the cathode was washed with  $\text{H}_2\text{O}$  prior to the next cycle.[39] The bulk structure of S400 was retained up to the 4<sup>th</sup> cycle (not shown). This suggested that NiO was able to accommodate  $\cdot\text{OH}$  producers ( $\text{Ni}^{\delta+}$ ) and  $\text{SO}_4^{\cdot-}$  precursors

( $\text{SO}_4^{2-}$ ) for the recycling experiment, which was not the case with NiS, thereby revealing the drastic structural collapse to form Ni and S upon exposure to the identical reaction conditions.[24] Meanwhile, the XPS spectra in the O 1s, Ni 2p, and S 2p domains for the used S400 catalysts were collected after the 1<sup>st</sup>, 2<sup>nd</sup>, and 3<sup>rd</sup> recycle runs. These spectra were inspected to identify which catalyst between S400 and S500–Fe was more appropriate to bear the  $\text{H}_2\text{O}_2$  source ( $\text{O}_\alpha$ ),  $\cdot\text{OH}$  producers ( $\text{Fe}^{\delta+}/\text{Ni}^{\delta+}$ ), and  $\text{SO}_4^{2-}$ , all of which were invaluable to recur the  $\cdot\text{OH} \rightarrow \text{SO}_4^{\cdot-}$  pathway. S400 and S500–Fe showed a moderate decrease in the  $\text{O}_\alpha$ ,  $\text{Fe}^{\delta+}/\text{Ni}^{\delta+}$ , or  $\text{SO}_4^{2-}$  species after each of the recycle runs.[39] This was in close alignment with the trend observed for their  $-\tau_{\text{PHENOL}, 0}$  values, which were declined throughout the recycle runs (Figure 2–9B). Interestingly, the  $\text{O}_\alpha$  concentrations innate to S500–Fe were larger than those of S400 after each of the recycle runs (S400; 42.5%  $\rightarrow$  39.2% (after the 1<sup>st</sup>)  $\rightarrow$  37.8% (after the 2<sup>nd</sup>)  $\rightarrow$  27.1 % (after the 3<sup>rd</sup>) for S500–Fe in [39]). However, the amounts of  $\text{H}_2\text{O}_2$  ( $\text{N}_{\text{H}_2\text{O}_2}$ ) evolved in the presence of the catalysts ( $\geq \sim 0.3$  mmol) were larger than that of the phenol used for the reaction runs (0.1 mmol). In addition, the  $\text{N}_{\text{H}_2\text{O}_2}$  values observed for the catalysts stopped increasing within an hour of reaction runs at 3 V,[39] which was in contrast to the steady consumption of phenol in the presence of the catalysts up to 8 hours of reaction runs under a comparable environment. This indicated that the  $\text{H}_2\text{O}_2$  evolution stage could not dominate the  $\cdot\text{OH} \rightarrow \text{SO}_4^{\cdot-}$  pathway as the rate-determining step and validated the insignificance of the  $\text{O}_\alpha$  species in prompting the  $\cdot\text{OH} \rightarrow \text{SO}_4^{\cdot-}$  pathway for the decomposition of phenol. In contrast, the concentrations of  $\cdot\text{OH}$  producers ( $\text{Fe}^{\delta+}/\text{Ni}^{\delta+}$ ) and  $\text{SO}_4^{\cdot-}$  precursors ( $\text{SO}_4^{2-}$ ) vital to the  $\cdot\text{OH} \rightarrow \text{SO}_4^{\cdot-}$  pathway were consistently higher throughout each of the recycle runs on S400 in comparison with those on S500–Fe ( $\text{Fe}^{\delta+}$  of 32.6%  $\rightarrow$  27. % (after the 1<sup>st</sup>)  $\rightarrow$  25.1% (after the 2<sup>nd</sup>)  $\rightarrow$  20.4% (after the 3<sup>rd</sup>);  $\text{SO}_4^{2-}$  of 64.2%  $\rightarrow$  63.2% (after the 1<sup>st</sup>)  $\rightarrow$  43.6% (after the 2<sup>nd</sup>)  $\rightarrow$  44.0% (after the 3<sup>rd</sup>) for S500–Fe in [39]). Therefore, although S400 leached a comparable amount of  $\text{Ni}^{\delta+}$  species to that of the leached  $\text{Fe}^{\delta+}$

species leached during the recycle runs ( $\leq 0.5$  mol.%), S400 could increase the efficiency of the  $\cdot\text{OH} \rightarrow \text{SO}_4\cdot^-$  pathway, thus enhancing its recyclability in the degradation of phenol compared to S500-Fe. This was evidenced by the greater  $-r_{\text{PHENOL}, 0}$  values of S400 than those of S500-Fe up to the 4<sup>th</sup> cycle (Figure 2-9B), which indicated that NiO could outperform  $\text{Fe}_2\text{O}_3$  in sustaining the degradation of pollutants with the main use of  $\cdot\text{OH} \rightarrow \text{SO}_4\cdot^-$ . It should be noted that the  $-r_{\text{PHENOL}, 0}$  of S400 at 3 V was far smaller than those of the transition metal sulfides obtained under a comparable environment.[24, 47, 48] However, the metal sulfides were susceptible to severe leaching of metal constituents or irreversible structural deformation, which could yield secondary phases that were inactive during  $\text{H}_2\text{O}_2$  cleavage. Hence, metal sulfides could provide a finite lifespan as  $\cdot\text{OH}$  producers, as evidenced by the noticeable decrease in their  $-r_{\text{PHENOL}, 0}$  values during each of the recycle runs ( $\leq \sim 50\%$  of initial  $-r_{\text{PHENOL}, 0}$  at the 3<sup>rd</sup> cycle). Indeed, all of our experimental results could demonstrate the potential of NiO as an outstanding platform to afford surface  $\text{SO}_4\cdot^-$  species that are highly active in cracking phenol in a heterogeneous and recyclable manners.

## 2.4. Conclusions

This study has investigated the advanced features of  $\text{SO}_4^{2-}$ -functionalized NiO as a platform to afford surface  $\cdot\text{OH}$  producers ( $\text{Ni}^{\delta+}$ ) and  $\text{SO}_4^{\cdot-}$  precursor species ( $\text{SO}_4^{2-}$ ) species, while demonstrating their mechanistic and kinetic functions to prompt the  $\cdot\text{OH} \rightarrow \text{SO}_4^{\cdot-}$  pathway assisted by an electric potential. For this study, NiO was synthesized and subsequently modified with  $\text{SO}_4^{2-}$  to form NiO (S). NiO (S) greatly favored toward the delivery of surface-labile O species and electrons ( $e^-$ ) to the cathode in relation to pristine NiO and therefore could promote  $\text{H}_2\text{O}_2$  productivity. In addition, *in situ*  $\text{NH}_3$  DRIFT spectroscopy and CO-pulse chemisorption provided evidence that NiO (S) could enhance the Lewis acidity of  $\text{Ni}^{\delta+}$  species over NiO, which was also validated by Bader charge calculations. This led to the improved  $\cdot\text{OH}$  productivity of NiO (S) relative to that of NiO during the  $\text{H}_2\text{O}_2$  scission cycle, in which the liberation of  $\cdot\text{OH}$  from the surface could primarily dominate the  $\text{H}_2\text{O}_2$  cleavage as the rate-determining step, as corroborated by DFT calculations on the energetics of the  $\text{H}_2\text{O}_2$  cleavage stages.

NiO (S) could afford  $\text{SO}_4^{2-}$  functionalities, radicalize them via radical transfer from  $\cdot\text{OH}$ , and thereby could oxidatively degrade the recalcitrant (phenol) with the primary use of the supported  $\text{SO}_4^{\cdot-}$  species. The plausibility of the supported  $\text{SO}_4^{\cdot-}$  species and their heterogeneous catalytic nature have been verified by kinetic assessments on the phenol degradation runs in the presence of scavengers, EPR spectroscopy, and filtration runs, respectively. Additional evidence for the radical transfer pathway from  $\cdot\text{OH}$  to  $\text{SO}_4^{\cdot-}$  has been provided using surface charge analysis via DFT calculations, during which  $e^-$  exchange among Ni,  $\text{SO}_4^{2-}$ , and  $\cdot\text{OH}$  would trigger the reaction of ' $\text{SO}_4^{2-} + \cdot\text{OH} + \text{H}^+ \rightarrow \text{SO}_4^{\cdot-} + \text{H}_2\text{O}$ '. The energetics altered during the transformation of  $\text{SO}_4^{2-}$  into  $\text{SO}_4^{\cdot-}$  were also computed and corroborated that the transformation of  $\text{SO}_4^{2-}$  into its corresponding radical was exothermic. This indicated that the radical interconversion cycle did not contain the rate-determining step. It also provided sound evidence that the  $\cdot\text{OH}$  desorption

step could direct the overall  $\cdot\text{OH} \rightarrow \text{SO}_4^{\cdot-}$  pathway toward the degradation of phenol, which was also substantiated by the kinetic comparison between the  $\text{H}_2\text{O}_2$  scission and phenol degradation runs on NiO (S) at various electric potentials.

The temperature used to synthesize NiO (S) was also varied between 300 ° C, 400 ° C, 500 ° C, and 600 ° C. This allowed for the identification of the optimal temperature for Ni (S) via a series of reaction runs. The NiO (S) synthesized at 400 ° C showed the highest efficiency and recyclability during the degradation of phenol among all the NiO (S) catalysts studied, all of which presented more accurate results than those observed for  $\text{SO}_4^{2-}$ -modified  $\text{Fe}_2\text{O}_3$  optimized in our previous study. Albeit demonstrating that the  $\text{Ni}^{\delta+}$  species innate to NiO were promising to expedite  $\cdot\text{OH}$  desorption, which was critical for the acceleration of the  $\cdot\text{OH} \rightarrow \text{SO}_4^{\cdot-}$  pathway, this study poses additional questions on how to reinforce the strength of the metal–O bonds for reducing the amount of metal leaching and how to amend the Lewis acidity of the metal species for furthering  $\cdot\text{OH}$  desorption with the exception of varying the temperatures used to functionalize the catalysts with  $\text{SO}_4^{2-}$  species. Tailoring the Lewis acidity of the metal species included in the  $\text{SO}_4^{2-}$ -functionalized bimetallic oxides is of partial success in expediting the  $\cdot\text{OH} \rightarrow \text{SO}_4^{\cdot-}$  pathway by encouraging the liberation of  $\cdot\text{OH}$  from the catalyst surfaces. This is on-going research being performed in our laboratory.

## Chapter 3

# Tailoring Lewis acidic metals and $\text{SO}_4^{2-}$ functionalities on bimetallic Mn–Fe oxo-spinels to exploit supported $\text{SO}_4^{\cdot -}$ in aqueous pollutant fragmentation

The essence of Chapter 3 has been published in Chemical Engineering Journal. Reprinted with permission from [107].

### 3.1. Introduction

The degradation efficiency of aqueous refractory contaminants is governed by oxidation potential, lifetime, sustainability, and productivity of radicals generated by the heterolytic cleavage of their precursors (*e.g.*,  $\text{H}_2\text{O}_2$  for  $\cdot\text{OH}$ ;  $\text{HSO}_5^-$  and  $\text{S}_2\text{O}_8^{2-}$  for  $\text{SO}_4^{\cdot -}$ ). [108, 109] For instance,  $\cdot\text{OH}$  imparts a strong oxidation potential ( $\sim 2.7$  V); however, its use as an oxidant is often limited because its use as an oxidant because of its short half-life ( $\sim 10^{-3}$   $\mu\text{second}$ ) and the necessity to retain a narrow pH range of 3–5. [33, 110, 111] In addition,  $\text{SO}_4^{\cdot -}$  is deemed as a competitor of  $\cdot\text{OH}$  owing to its appreciable oxidation potential (2.5–3.1 V), long half-life (30–40  $\mu\text{second}$ ) over a wide pH range, and lower vulnerability to the background levels of chemicals present in the water matrix, while offering ample pathways for the degradation of various organic pollutants. [33, 111–115] Nonetheless, the means to regenerate or sustain  $\cdot\text{OH}$  or  $\text{SO}_4^{\cdot -}$  would be demanding to be realized, unless radical precursors are recurrently fed to the aqueous solution containing the pollutant.

To achieve a semi-permanent supply of  $\text{H}_2\text{O}_2$ , two pieces of graphite acting as the anode and cathode can be positioned in contaminated  $\text{H}_2\text{O}$  and exposed to an electric environment under circumneutral pH conditions (Figure 3–1A). [9, 116] This results in  $\text{H}_2\text{O}$  oxidation on or near the anode

via two pathways. One route involves the formation of  $\cdot\text{OH}$ ,  $\text{H}^+$ , and an electron ( $\text{e}^-$ ) via the reaction  $\text{H}_2\text{O} \rightarrow \cdot\text{OH} + \text{H}^+ + \text{e}^-$  (standard potential of 2.72 V), after which  $\cdot\text{OH}$  interplays with the anodic surface to form surface O species ( $\text{O}_\alpha$ ) active in degrading pollutants (known as anodic oxidation).[9, 116, 117] Another route entails the reaction of  $2\text{H}_2\text{O} \rightarrow \text{O}_2 + 4\text{H}^+ + 4\text{e}^-$  to produce  $\text{O}_2$ ,  $\text{H}^+$ , and  $\text{e}^-$  (standard potential of 1.23 V), all of which migrate to the cathode and serve to produce  $\text{H}_2\text{O}_2$  continuously, as far as an electric potential is applied across the electrodes.[117–119] In addition, the cathode can be coated with the catalyst, whose surface contains Lewis acidic metals with oxidation states of 2 or less ( $\text{M}^{\delta+}$ ;  $\delta \leq 2$ ).[9, 116] It was reported that Lewis acidic  $\text{M}^{\delta+}$  is electrophilic and thus can be coordinated to the lone pair electrons of the O atoms of  $\text{H}_2\text{O}_2$  to initially produce  $\text{M}^{\delta+}-\text{H}_2\text{O}_2$ . [42, 45] The  $\text{M}^{\delta+}$  of  $\text{M}^{\delta+}-\text{H}_2\text{O}_2$  then loses one electron for its donation to  $\text{H}_2\text{O}_2$ . This results in the dissection of  $\text{H}_2\text{O}_2$ , by which  $\text{M}^{(\delta+1)+}$  is bound to  $\cdot\text{OH}$  ( $\text{M}^{(\delta+1)+}-\cdot\text{OH}$ ) is formed, while  $\text{OH}^-$  is released to the aqueous environment prior to the liberation of  $\cdot\text{OH}$  from  $\text{M}^{(\delta+1)+}-\cdot\text{OH}$  ( $\text{M}^{\delta+} + \text{H}_2\text{O}_2 \rightarrow \text{M}^{(\delta+1)+} + \text{OH}^- + \cdot\text{OH}$ ; in Figure 3–1B).[119, 120] In conjunction with anodic  $\text{O}_\alpha$ ,  $\cdot\text{OH}$  can also be used to decompose pollutants. Moreover, an ample amount of  $\text{e}^-$  can sustain the recovery of  $\cdot\text{OH}$  producers ( $\text{M}^{\delta+}$ ) via  $\text{M}^{(\delta+1)+}$  reduction with  $\text{e}^-$  (Figure 3–1B).[116, 119] These findings suggest that highly sustainable  $\cdot\text{OH}$  productivity is achievable when using the reactor configuration specified in Figure 3–1A.

Meanwhile, as a method to avoid a periodic supply of  $\text{SO}_4^{\cdot-}$  precursors, we have envisioned to functionalize the catalyst surface with  $\text{SO}_4^{2-}$ , as shown in Figure 3–1C.[25, 39] In Chapter 2, we have validated that  $\text{SO}_4^{2-}$  can be readily radicalized by  $\cdot\text{OH}$  and  $\text{H}^+$  to form  $\text{SO}_4^{\cdot-}$ , which is immobilized on the nickel oxide catalyst surface by using the reactor set-up illustrated in Figure 3–1A ( $\text{SO}_4^{2-} + \cdot\text{OH} + \text{H}^+ \rightarrow \text{SO}_4^{\cdot-} + \text{H}_2\text{O}$ ). [25, 39] Of significance, supported  $\text{SO}_4^{\cdot-}$  can outperform conventional  $\cdot\text{OH}$  in terms of activity, reusability, and stability in the decomposition of contaminants.[25, 39] This, therefore, can



motivate the exploitation of radical inter-conversion from  $\cdot\text{OH}$  to  $\text{SO}_4^{\cdot-}$  under an electric environment (denoted as  $\cdot\text{OH} \rightarrow \text{SO}_4^{\cdot-}$ ).

To deploy the  $\cdot\text{OH} \rightarrow \text{SO}_4^{\cdot-}$  pathway with the aim of prompting the degradation of contaminants, it is imperative to initially grasp the overall elementary stages of the  $\cdot\text{OH} \rightarrow \text{SO}_4^{\cdot-}$  pathway and then expedite the rate-determining step. The  $\cdot\text{OH} \rightarrow \text{SO}_4^{\cdot-}$  pathway comprises of two catalytic cycles to produce  $\cdot\text{OH}$  or supported  $\text{SO}_4^{\cdot-}$ . [25] Again, the  $\cdot\text{OH}$  evolution cycle is featured by  $\text{H}_2\text{O}_2$  adsorption on  $\text{M}^{\delta+}$ , catalytic  $\cdot\text{OH}$  production followed by  $\text{OH}^-$  liberation,  $\cdot\text{OH}$  release from  $\text{M}^{\delta+}$ , and  $\text{M}^{\delta+}$  recovery via  $e^-$  reduction (Figure 3-1B). [25, 47] In particular, the  $\cdot\text{OH}$  desorption stage may compete with the  $\text{M}^{\delta+}$  recovery step for directing the  $\cdot\text{OH}$  production rate, as we suggested earlier. [24, 47] The  $\text{M}^{\delta+}$  recovery step, however, cannot direct the  $\cdot\text{OH}$  evolution cycle because of the abundant quantity of  $e^-$  generated under electric environments. [109, 116, 119] In contrast, the  $\cdot\text{OH}$  desorption step is endothermic, thus dominating the  $\cdot\text{OH}$  evolution cycle as the rate-directing stage. [25, 39] Meanwhile, the surface  $\text{SO}_4^{\cdot-}$  evolution cycle proceeds with the spontaneous formation of  $\text{SO}_4^{2-} - \cdot\text{OH}$  and its exothermic transition to  $\text{SO}_4^{\cdot-} - \text{OH}$  (via  $e^-$  transfer),  $\text{SO}_4^{\cdot-} - \text{H}_2\text{O}$  (via fusion with  $\text{H}^+$ ),  $\text{SO}_4^{\cdot-}$  (via  $\text{H}_2\text{O}$  liberation),  $\text{SO}_4^-$  (\*\*\*; upon contaminant degradation), and  $\text{SO}_4^{2-}$  (via  $e^-$  reduction) (Figure 3-1D), as evidenced by the computation on the surface  $\text{SO}_4^{2-}$  functionality via density-functional theory. [25] Apparently, this can corroborate that the  $\cdot\text{OH}$  desorption step can dominate the  $\cdot\text{OH} \rightarrow \text{SO}_4^{\cdot-}$  route as the rate-determining stage (\* in Figure 3-1B) [25] and suggests the need to locate or further tailor the surface  $\text{M}^{\delta+}$  species to promote the  $\cdot\text{OH}$  desorption.

Iron is cheap, ubiquitous, and readily fuses with  $\text{O}^{2-}$  anions to bear  $\text{Fe}^{\delta+}$  in the resulting oxides. [39, 48] *Rhombohedral*  $\text{Fe}_2\text{O}_3$ , however, is composed of coordinatively-saturated  $\text{Fe}^{3+}$  trapped in *octahedral*  $[\text{FeO}_6]^{9-}$  sub-units only. [121]  $\text{Fe}_2\text{O}_3$ , therefore, should not be active in fragmenting  $\text{H}_2\text{O}_2$ , unless surface defects are formed. Meanwhile, *cubic*  $\text{Fe}_3\text{O}_4$  adopts the inverse spinel

architecture of  $(\text{Fe}^{3+})^{\text{IV}}(\text{Fe}^{2+}\text{Fe}^{3+})^{\text{VI}}\text{O}_4$  (IV for *tetrahedral*: accessible to  $\text{H}_2\text{O}_2$ ; VI for *octahedral*: inaccessible to  $\text{H}_2\text{O}_2$ ), [122, 123] in which *tetrahedral* sites are solely occupied by  $\text{Fe}^{3+}$  ions that are inactive in cleaving  $\text{H}_2\text{O}_2$  (\*\* in Figure 3–1E). Nevertheless,  $\text{Fe}_3\text{O}_4$  was reported to outperform  $\text{Fe}_2\text{O}_3$  due to the inclusion of a greater number of  $\text{Fe}^{\delta+}$  species. [124, 125] This might result from the synthetic conditions that are favorable to generate a greater quantity of surface defects on  $\text{Fe}_3\text{O}_4$  than the number of defects on  $\text{Fe}_2\text{O}_3$ . In addition,  $\text{Fe}_3\text{O}_4$  could improve  $\text{e}^-$  transfer from  $\text{O}^{2-}$  to the adjacent  $\text{Fe}^{3+}$ , resulting in the facile recovery of  $\text{Fe}^{\delta+}$  which is conducive to recurring  $\text{H}_2\text{O}_2$  dissection, as reported elsewhere. [126, 127] Such accelerated  $\text{e}^-$  transfer of  $\text{Fe}_3\text{O}_4$ , however, can be marginal, which is again caused by the abundant quantity of  $\text{e}^-$  produced under electric environments. [109, 116, 119]

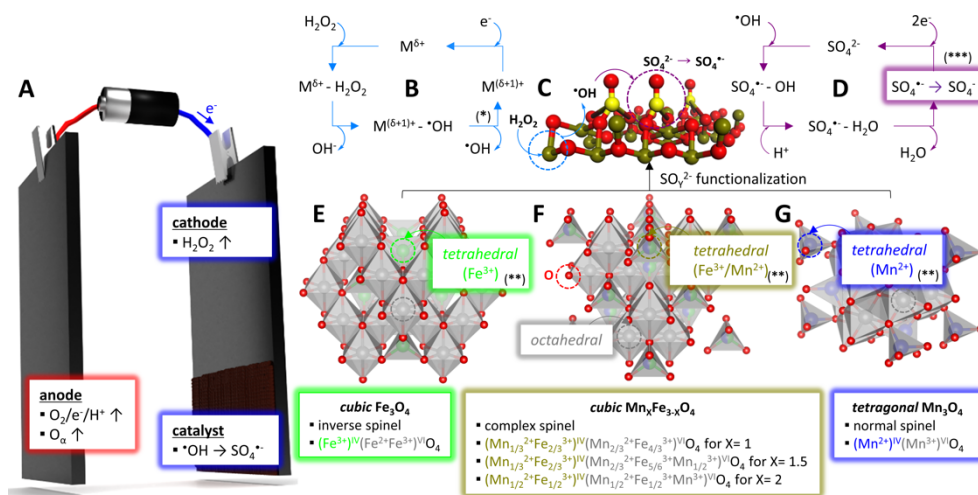


Figure 3–1. Schematic illustrations of the reactor set-up utilized (A), evolution mechanisms of  $\cdot\text{OH}$  (B) and  $\text{SO}_4^{\cdot-}$  (D) on  $\text{SO}_4^{2-}$ -functionalized surfaces (C) for  $\text{Fe}_3\text{O}_4$  (E),  $\text{Mn}_x\text{Fe}_{3-x}\text{O}_4$  (F), and  $\text{Mn}_3\text{O}_4$  (G). The \* symbol in (B) indicates the rate-determining stage of the  $\cdot\text{OH} \rightarrow \text{SO}_4^{\cdot-}$  pathway, whereas the \*\*\* symbol in (D) indicates the elementary stage accounting for the  $\text{SO}_4^{\cdot-}$ -assisted degradation of contaminants. In (E)–(G), the \*\* symbols shown with green, gold, and blue circles denote the  $\text{H}_2\text{O}_2$ -accessible, *tetrahedral* (IV) metal sites present in the catalysts, whereas the grey circles denote the  $\text{H}_2\text{O}_2$ -inaccessible *octahedral* (IV) metal sites present in the catalysts.

Structural inspection of *cubic*  $\text{Fe}_3\text{O}_4$  may suggest its unsuitability as a reservoir of  $\text{H}_2\text{O}_2$  activators. This, however, also suggests the structural modification

of  $\text{Fe}_3\text{O}_4$  to form *cubic*  $\text{M}_x\text{Fe}_{3-x}\text{O}_4$  solid solutions (Figure 3–1F), where the Fe elements are partially substituted by *d*-block metals (M) with similar properties.[128, 129] Herein,  $\text{M}_x\text{Fe}_{3-x}\text{O}_4$  is hypothesized to cause subtle alterations in the electronic characteristics innate to Lewis acidic (or defective)  $\text{Fe}^{\delta+}/\text{M}^{\delta+}$  species, thus potentially tuning the binding strengths of the  $\text{Fe}^{\delta+}/\text{M}^{\delta+}$  species with  $\cdot\text{OH}$  according to the change in the metal compositions (*i.e.*, X values of 0, 1, 1.5, 2, or 3).  $\text{Ni}^{\delta+}$ ,  $\text{Co}^{\delta+}$ , and  $\text{Cu}^{\delta+}$  were demonstrated to prompt  $\cdot\text{OH}$  liberation more effectively than  $\text{Fe}^{\delta+}$  upon modification with  $\text{S}^{2-}$  anions and thereby may be suitable as substituents of Fe in  $\text{M}_x\text{Fe}_{3-x}\text{O}_4$ . [24] However,  $\text{Ni}^{\delta+}$  was reported to reduce  $\cdot\text{OH}$  productivity, in relation to that observed with the  $\text{Fe}^{\delta+}$  of unmodified  $\text{Fe}_3\text{O}_4$ , when forming  $\text{Ni}_x\text{Fe}_{3-x}\text{O}_4$ . [128] In contrast,  $\text{Co}^{\delta+}$  and  $\text{Cu}^{\delta+}$  do construct  $\text{Co}_x\text{Fe}_{3-x}\text{O}_4$  and  $\text{Cu}_x\text{Fe}_{3-x}\text{O}_4$ , both of which showed promising  $\cdot\text{OH}$  productivity.[128, 129] However,  $\text{Co}_x\text{Fe}_{3-x}\text{O}_4$  and  $\text{Cu}_x\text{Fe}_{3-x}\text{O}_4$  could be crystallized under such limited conditions that favored the phase transition or the production of collateral phases.[130, 131]

Although S-modified  $\text{Mn}^{\delta+}$  revealed a lower  $\cdot\text{OH}$  productivity than did the  $\text{Fe}^{\delta+}$  analogue under an electric environment,[24] Mn-modified  $\text{Fe}_3\text{O}_4$  ( $\text{Mn}_x\text{Fe}_{3-x}\text{O}_4$ ) is hypothesized to surpass  $\text{Fe}_3\text{O}_4$  or  $\text{Mn}_3\text{O}_4$  in producing  $\cdot\text{OH}$  owing to several reasons, listed as follows. *Cubic*  $\text{Mn}_3\text{O}_4$  and  $\text{Mn}_x\text{Fe}_{3-x}\text{O}_4$  can construct normal and complex spinel geometries, thereby isolating  $\text{Mn}^{2+}$  species in *tetrahedral* sub-units, which are open to  $\text{H}_2\text{O}_2$  and active in  $\text{H}_2\text{O}_2$  cleavage (\*\* in Figure 3–1F and 3–1G).[122, 123] This is again in contrast to  $\text{Fe}_3\text{O}_4$  which consists of *tetrahedral*  $[\text{FeO}_4]^{5-}$  sub-units that are accessible to  $\text{H}_2\text{O}_2$ , yet, only confine  $\text{Fe}^{3+}$  to being inactive in splitting  $\text{H}_2\text{O}_2$  (\*\* in Figure 3–1E).[132] In addition,  $\text{Mn}_3\text{O}_4$  and  $\text{Mn}_x\text{Fe}_{3-x}\text{O}_4$  were reported to exploit  $\text{Mn}^{2+}$  and  $\text{Mn}^{3+}$  as  $\text{H}_2\text{O}_2$  scissors.[120] Hence,  $\text{Mn}_3\text{O}_4$  and  $\text{Mn}_x\text{Fe}_{3-x}\text{O}_4$  can enhance  $\cdot\text{OH}$  productivity over  $\text{Fe}_3\text{O}_4$ , which only contains (defective)  $\text{Fe}^{2+}$  species, if their synthetic conditions are comparable to provide a similar chance associated with the formation of surface defects.

Noteworthy, *cubic*  $\text{Mn}_3\text{O}_4$  with cell edges of 8.7 Å affords 1 mole of open  $\text{Mn}^{2+}$  per base unit,[133] which allows isotropic access to  $\text{H}_2\text{O}_2$  (kinetic diameter of  $\sim 3.0$  Å).[47, 134]  $\text{Mn}_3\text{O}_4$ , however, is unstable under ambient conditions and readily distorts to transform into a *tetragonal* polymorph (Figure 3–1G);[122, 133] the accessibility of open  $\text{Mn}^{2+}$  to  $\text{H}_2\text{O}_2$  may likely be disruptive because of the reduced cell edges of 5.7 Å. This may reduce the  $\cdot\text{OH}$  productivity of open  $\text{Mn}^{2+}$  in *tetragonal*  $\text{Mn}_3\text{O}_4$  stabilized in electric environments, which is in contrast to the behavior of bimetallic  $\text{Mn}_x\text{Fe}_{3-x}\text{O}_4$  catalysts with structural rigidity in ambient, electric environments. Meanwhile, among the bimetallic  $\text{Mn}_x\text{Fe}_{3-x}\text{O}_4$  catalysts considered,  $\text{Mn}_2\text{Fe}_1\text{O}_4$  is anticipated to reveal the greatest  $\cdot\text{OH}$  productivity. This expectation is based on the largest quantity of  $\text{Mn}^{2+}$  confined in  $\text{H}_2\text{O}_2$ -accessible *tetrahedral* sub-units for  $\text{Mn}_2\text{Fe}_1\text{O}_4$  (Figure 3–1F; 0.5 mole of  $\text{Mn}^{2+}$  for  $\text{Mn}_2\text{Fe}_1\text{O}_4$ ; 0.33 mole of  $\text{Mn}^{2+}$  for  $\text{Mn}_{1.5}\text{Fe}_{1.5}\text{O}_4$  and  $\text{Mn}_1\text{FeO}_4$ )[122, 123] if the bimetallic  $\text{Mn}_x\text{Fe}_{3-x}\text{O}_4$  catalysts are defect-free. Nonetheless, this hypothesis can be unconvincing when contemplating that  $\text{Mn}_x\text{Fe}_{3-x}\text{O}_4$  catalysts are polycrystalline; thus, they have a high likelihood of containing surface defects, some of which will be occupied by  $\text{SO}_4^{2-}$  functionalities post  $\text{SO}_4^{2-}$  modification.

Indeed, the structural examination of the catalysts suggests the benefits of bimetallic  $\text{Mn}_x\text{Fe}_{3-x}\text{O}_4$  over the monometallic analogues in furthering the  $\cdot\text{OH} \rightarrow \text{SO}_4^{\cdot-}$  pathway, yet, also raises the need to regulate the formation of defects across the  $\text{Mn}_x\text{Fe}_{3-x}\text{O}_4$  materials via synthetic strategies. Herein,  $\text{Mn}_x\text{Fe}_{3-x}\text{O}_4$  materials were synthesized under similarly controlled environments to provide the materials with an identical probability associated with the formation of surface defects. Therefore, in this chapter, we pioneered the utilization of bimetallic  $\text{Mn}_x\text{Fe}_{3-x}\text{O}_4$  materials as reservoirs of Lewis acidic Fe/Mn species and  $\text{SO}_4^{2-}$  functionalities, whose surface traits could be tuned by altering the metal compositions (X values of 0–3). The catalyst surfaces were then explored using a group of characterization results including

CO/CO<sub>2</sub> isotherms, *in situ* Diffuse Reflectance Infrared Fourier Transform (DRIFT) spectra, and simulated electron paramagnetic resonance (EPR) spectra to clarifying the Lewis acidities of Fe/Mn, binding configurations of the SO<sub>4</sub><sup>2-</sup> functionalities, and feasibility of the  $\cdot\text{OH} \rightarrow \text{SO}_4^{\cdot-}$  pathway, respectively. These have rarely served in studies on catalytic H<sub>2</sub>O purification, to the best of our knowledge. The catalysts were also compared with regard to their efficiencies in decomposing contaminants by extracting kinetic parameters to locate the X value most adequate to expedite the  $\cdot\text{OH} \rightarrow \text{SO}_4^{\cdot-}$  pathway.

## 3.2. Experimental Section

### 3.2.1. Chemicals

All chemicals were delivered from the vendors and utilized as-received:  $\text{MnCl}_2 \cdot 4\text{H}_2\text{O}$  (JUNSEI, 99.0%),  $\text{FeCl}_3 \cdot 6\text{H}_2\text{O}$  (KANTO, 99.0%),  $\text{CH}_3\text{COONa}$  (Sigma-Aldrich,  $\geq 99.0\%$ ), polyethylene glycol 1000 ( $\text{H}-(\text{O}-\text{CH}_2-\text{CH}_2)_n-\text{OH}$ , Alfa-Aesar), ethylene glycol ( $\text{C}_2\text{H}_6\text{O}_2$ , DAEJUNG, 99.0 %), ethanol ( $\text{C}_2\text{H}_5\text{OH}$ , DAEJUNG, 94.5%), oxalic acid ( $\text{C}_2\text{H}_2\text{O}_4 \cdot 2\text{H}_2\text{O}$ , Sigma-Aldrich,  $\geq 99.0\%$ ),  $\text{FeSO}_4 \cdot 7\text{H}_2\text{O}$  (Sigma-Aldrich,  $\geq 99.0\%$ ),  $\text{NiSO}_4 \cdot 7\text{H}_2\text{O}$  (Sigma-Aldrich,  $\geq 99.0\%$ ), 5,5-dimethyl-1-pyrroline N-oxide ( $\text{C}_6\text{H}_{11}\text{NO}$ , DMPO, Sigma-Aldrich,  $\geq 98.0\%$ ), 2,9-dimethyl-1,10-phenanthroline ( $\text{C}_{14}\text{H}_{12}\text{N}_2$ , Sigma-Aldrich,  $\geq 98.0\%$ ),  $\text{H}_2\text{O}_2$  (DAEJUNG, 30.0 wt. % in  $\text{H}_2\text{O}$ ), phenol ( $\text{C}_6\text{H}_5\text{OH}$ , DAEJUNG, 99.0%), aniline ( $\text{C}_6\text{H}_5\text{NH}_2$ , DAEJUNG, 99.0%), N-Methyl-2-pyrrolidone ( $\text{C}_5\text{H}_9\text{NO}$ , Sigma-Aldrich,  $\geq 99.0\%$ ), poly(vinylidene fluoride) ( $(\text{CH}_2\text{CF}_2)_n$ , average  $M_w \sim 180,000$ , average  $M_n \sim 71,000$ , Sigma-Aldrich),  $\text{Na}_2\text{SO}_4$  (Sigma-Aldrich,  $\geq 99.0\%$ ),  $\text{NaNO}_3$  (Sigma-Aldrich,  $\geq 99.0\%$ ), methanol ( $\text{CH}_3\text{OH}$ , Sigma-Aldrich, 99.8%), acetonitrile ( $\text{C}_2\text{H}_3\text{N}$ , DAEJUNG, 99.8%), Neocuproine ( $\text{C}_{14}\text{H}_{12}\text{N}_2$ , Sigma Aldrich,  $\geq 98.0\%$ ),  $\text{CuSO}_4 \cdot 5\text{H}_2\text{O}$  (Sigma Aldrich,  $\geq 98.0\%$ ), phosphate buffer (SAMCHUN, pH of 7.2), 1,4-benzoquinone ( $\text{C}_6\text{H}_4\text{O}_2$ , Sigma-Aldrich,  $\geq 98.0\%$ ), guaiacol ( $\text{C}_7\text{H}_8\text{O}_2$ , Sigma-Aldrich,  $\geq 99.0\%$ ), catechol ( $\text{C}_6\text{H}_6\text{O}_2$ , Sigma-Aldrich,  $\geq 99.0\%$ ), hydroquinone ( $\text{C}_6\text{H}_6\text{O}_2$ , Sigma-Aldrich,  $\geq 99.0\%$ ), *tert*-butanol ( $\text{C}_4\text{H}_{10}\text{O}$ , TBA, Alfa-aesar, 99.0%), *iso*-propanol ( $\text{C}_3\text{H}_8\text{O}$ , IPA, DAEJUNG,  $\geq 99.5\%$ ), 1,4-dioxane ( $\text{C}_4\text{H}_8\text{O}_2$ , DAEJUNG,  $> 99.0\%$ ), and tetrahydrofuran ( $\text{C}_4\text{H}_8\text{O}$ , THF, DAEJUNG,  $> 99.0\%$ ).  $\text{N}_2$  ( $\geq 99.99\%$ ),  $\text{O}_2$  ( $\geq 99.99\%$ ), 5 %  $\text{SO}_2/\text{N}_2$  ( $\geq 99.99\%$ ), and liquid  $\text{N}_2$  (99.9999%) were also purchased from SHINYANG and used without further purification.

### 3.2.2. Catalysts

$\text{Mn}_x\text{Fe}_{3-x}\text{O}_4$  catalysts with an X value of 0, 1, 1.5, 2, or 3 were solvo-thermally synthesized using the protocol slightly modified based on the work by Y. Li and co-workers.[135] Typically, “A” mmol of  $\text{MnCl}_2 \cdot 4\text{H}_2\text{O}$  dissolved in 160 mL of ethylene glycol was put inside a 200 mL Teflon acid digestion sleeve, mixed with “30-A” mmol of  $\text{FeCl}_3 \cdot 6\text{H}_2\text{O}$ , 3.6 g of  $\text{CH}_3\text{COONa}$ , 1.0 g of  $\text{H}-(\text{O}-\text{CH}_2-\text{CH}_2)_n-\text{OH}$ , and stirred at room temperature for 30 minutes (A of 0 mmol for  $\text{Fe}_3\text{O}_4$ ; 10 mmol for  $\text{Mn}_1\text{Fe}_2\text{O}_4$ ; 15 mmol for  $\text{Mn}_{1.5}\text{Fe}_{1.5}\text{O}_4$ ; 20 mmol for  $\text{Mn}_2\text{Fe}_1\text{O}_4$ ; 30 mmol for  $\text{Mn}_3\text{O}_4$ ). The Teflon sleeve was then located in a stainless steel reactor vessel and heated at 200 ° C for 12 hours prior to being cooled to room temperature. The resulting  $\text{Mn}_x\text{Fe}_{3-x}\text{O}_4$  was collected by vacuum filtration, rinsed thoroughly with 750 mL of de-ionized  $\text{H}_2\text{O}$ , 750 mL of  $\text{C}_2\text{H}_5\text{OH}$ , and dried overnight at 100 ° C.  $\text{Fe}_2\text{O}_3$  (or  $\text{NiO}$ ) catalyst was synthesized according to the protocol we reported previously.[25, 39] Typically, 20 mmol of  $\text{FeSO}_4 \cdot 7\text{H}_2\text{O}$  (or  $\text{NiSO}_4 \cdot 7\text{H}_2\text{O}$ ) dissolved in 100 mL of de-ionized  $\text{H}_2\text{O}$  was mixed with 20 mmol of  $\text{C}_2\text{H}_2\text{O}_4 \cdot 2\text{H}_2\text{O}$ , stirred at 50 ° C for an hour, cooled to room temperature, and vacuum-filtered using 500 mL of de-ionized  $\text{H}_2\text{O}$  and 500 mL of  $\text{C}_2\text{H}_5\text{OH}$ . The resulting synthetic mixture was calcined at 300 ° C for an hour to produce  $\text{Fe}_2\text{O}_3$  (or  $\text{NiO}$ ). The surfaces of the catalysts synthesized herein were then exposed to such a  $\text{N}_2$  stream that contained 500 ppm  $\text{SO}_2$  and 3 vol.%  $\text{O}_2$  at 400 ° C (for  $\text{NiO}$ ) or 500 ° C (for  $\text{Mn}_x\text{Fe}_{3-x}\text{O}_4$  and  $\text{Fe}_2\text{O}_3$ ) for an hour with the ramping rate of 10 ° C  $\text{min}^{-1}$  and the total flow rate of 500 mL  $\text{min}^{-1}$ . This led to the formation of the catalysts, whose surfaces were functionalized with  $\text{SO}_4^{2-}$  species. The  $\text{SO}_4^{2-}$ -modified catalysts are denoted as  $\text{Mn}_x$  for  $\text{Mn}_x\text{Fe}_{3-x}\text{O}_4$ , Fe (S) for  $\text{Fe}_2\text{O}_3$ , and Ni (S) for  $\text{NiO}$ .

### 3.2.3. Characterization techniques

A D8 Advance instrument (Bruker) served to collect X-ray diffraction (XRD) patterns of the catalysts with the use of monochromatic Cu  $K_\alpha$  radiation ( $\lambda = 0.154$  nm), a step size of  $0.02^\circ$  per step, and a scan speed of 2 seconds per step. A ZSX Primus II (Rigaku) was utilized to analyze bulk contents of the catalysts via X-ray fluorescence (XRF) technique. A Titan 80 – 300<sup>TM</sup> electron microscope (FEI) was used to collect high resolution transmission electron microscopy (HRTEM) images and selected area electron diffraction (SAED) patterns of the catalysts at 300 keV. Field emission scanning electron microscope (SEM) images of the catalysts were collected on a JSM-7800F Prime scanning electron microscope (JEOL). Energy-dispersive X-ray spectroscopy (EDX) mapping images of the catalysts were collected on an X-MaxN spectrometer (Oxford) with an acceleration voltage and probe current of 15 kV and 10 pA, respectively. A PHI 5000 VersaProbe was utilized to analyze the surface contents/phases of the catalysts using an X-ray photoelectron (XP) spectroscopy technique with the use of adventitious carbon located at the binding energy of  $\sim 284.6$  eV as a reference. An Autochem II analyzer (Micromeritics) was used to measure the amount of CO adsorbed per gram of the catalysts via CO-pulsed chemisorption technique at  $40^\circ\text{C}$ . An ICS 3000 instrument (Thermo Fisher Scientific) was utilized to measure the amount of metals leached from the catalysts during the reactions via an inductively coupled plasma-atomic absorption spectrometry (ICP-AAS) technique. A NOVA 2200e (Quantachrome Instruments) was used to obtain  $\text{N}_2$  isotherms of the catalysts at  $-196^\circ\text{C}$ . A NOVA 2200e instrument (Quantachrome Instruments) was also used to obtain CO or  $\text{CO}_2$  isotherms of the catalysts at  $-25/-20/-15^\circ\text{C}$  or  $-20/0/20^\circ\text{C}$ . Pore volumes of the catalysts were evaluated using Barrett-Joyner-Halenda (BJH) theory. Surface areas of the catalysts accessible to  $\text{N}_2$  or CO were evaluated using Brunauer – Emmett – Teller (BET) theory, while considering the amounts of gas adsorbed per gram of the catalysts under the partial pressure range of  $0.05 < P/P_0 < 0.3$ .



The CO (or CO<sub>2</sub>) isotherms of the catalysts were fitted to the Toth equation (Eqn. (1)), wherein  $N_a$  and  $N_{a0}$  indicate the amount of CO (or CO<sub>2</sub>) adsorbed ( $\mu\text{mol}_{\text{CO}} \text{g}_{\text{CAT}}^{-1}$  or  $\mu\text{mol}_{\text{CO}_2} \text{g}_{\text{CAT}}^{-1}$ ) and the maximum amount of CO (or CO<sub>2</sub>) adsorbed, respectively.[47, 136–138] In addition, in Eqn. (1),  $c$ ,  $d$ , and  $P$  denote a constant ( $\text{bar}^{-1}$ ), the constant accounting for surface heterogeneity (dimension-less), and the pressure (bar), respectively.[47, 136–138]

$$N_a = N_{a0} \times \frac{c \times P}{(1 + (c \times P)^d)^{\frac{1}{d}}} \quad (1)$$

The Clausius–Clapeyron equation (Eqn. (2)) served to calculate the isosteric heats ( $-Q_{\text{ST}}$ ) of CO (or CO<sub>2</sub>) adsorption for the catalysts. In Eqn. (2),  $T_A$  and  $T_B$  denote the temperatures (K),  $P_A$  and  $P_B$  indicate the pressures (bar) at  $T_A$  and  $T_B$ , and  $R$  indicates the ideal gas constant ( $8.3145 \text{ J mol}^{-1} \text{ K}^{-1}$ ).[47, 136–139]

$$\ln\left(\frac{P_A}{P_B}\right) = \frac{Q_{\text{ST}}}{R} \times \left(\frac{T_A - T_B}{T_A \times T_B}\right) \quad (2)$$

Raman spectra of the catalysts were obtained using a in Via Raman Microscope (Renishaw) equipped with a 532 nm excitation laser, 2400 lines/mm grating, and X 50 objective lens. *In situ* diffuse reflectance Infrared Fourier transform (DRIFT) spectra of the catalysts were obtained using an FT/IR/4200 spectrometer (Jasco).

### 3.2.4. Analytical techniques

An EMX-plus (Bruker) served to observe  $\cdot\text{OH}$  and  $\text{SO}_4^{\cdot-}$  species evolved during the reactions using an electron paramagnetic resonance (EPR) technique with the use of  $\text{C}_6\text{H}_{11}\text{NO}$  (DMPO) as the spin trapping agent.[101, 102, 140, 141] The reaction mixture consisting of 20 mg of the catalyst, 3 mmol of DMPO, 0.3 mmol of  $\text{H}_2\text{O}_2$ , and 5 mL of de-ionized  $\text{H}_2\text{O}$  was shaken vigorously using vortex mixer for 2 minutes. Then, the reaction aliquot (solid and liquid) or the reaction aliquot subjected to the filtration using a  $0.45\ \mu\text{m}$ -sized PES syringe filter (liquid only) was collected from the reaction mixture prior to EPR analysis. The EPR analytical conditions were a center magnetic field of 3435 G, the resonance frequency of 9.64 GHz, the microwave power of 2.95 mW, the modulation amplitude of 1 G, the sweep width of 120 G, and the sweep time of 48 seconds. EPR spectra were also computed using the EasySpin simulation package (version 5.2.28).[101, 140–143] The amount of  $\text{H}_2\text{O}_2$  evolved was quantified using  $\text{C}_{14}\text{H}_{12}\text{N}_2$  method on a UV/VIS spectrometer (Cary 100, Shimadzu) reported elsewhere.[62] Typically, a solution comprising of 1 mL of 0.01 M  $\text{CuSO}_4 \cdot 5\text{H}_2\text{O}$  and 1 mL of 0.01 M  $\text{C}_{14}\text{H}_{12}\text{N}_2$  was mixed with 0.7 mL of de-ionized  $\text{H}_2\text{O}$  only (blank), de-ionized  $\text{H}_2\text{O}$  including 0.1–0.5 mmol  $\text{H}_2\text{O}_2$  (for calibration), or the reaction aliquot (collected during the  $\text{H}_2\text{O}_2$  scission runs). The solution was then mixed with phosphate buffer to adjust adjusting the volume of the resulting solution to 10 mL. The blank and  $\text{H}_2\text{O}_2$  solutions served to construct the calibration curve to relate “the difference of the measured absorbance between the blank and  $\text{H}_2\text{O}_2$  solutions at 454 nm ( $\Delta A_{454}$ )” and “ $\text{H}_2\text{O}_2$  concentration ( $[\text{H}_2\text{O}_2]$ )”, whose slope served to determine  $[\text{H}_2\text{O}_2]$  values of the reaction aliquots taken during  $\text{H}_2\text{O}_2$  scission runs.[62] Conversion of  $\text{H}_2\text{O}_2$  ( $X_{\text{H}_2\text{O}_2}$ ) was calculated according to Eqn. (3), where  $C_{\text{H}_2\text{O}_2,0}$  indicates the initial  $\text{H}_2\text{O}_2$  concentration, and  $C_{\text{H}_2\text{O}_2}$  indicates the  $\text{H}_2\text{O}_2$  concentration measured at a specific reaction time.[24, 39, 47, 48]

$$X_{\text{H}_2\text{O}_2}(\%) = \frac{C_{\text{H}_2\text{O}_2,0} (\text{mol}_{\text{H}_2\text{O}_2}\text{L}^{-1}) - C_{\text{H}_2\text{O}_2} (\text{mol}_{\text{H}_2\text{O}_2}\text{L}^{-1})}{C_{\text{H}_2\text{O}_2,0} (\text{mol}_{\text{H}_2\text{O}_2}\text{L}^{-1})} \times 100 \quad (3)$$

The initial H<sub>2</sub>O<sub>2</sub> fission rate ( $-r_{\text{H}_2\text{O}_2, 0}$ ) was assessed using Eqn. (4), in which  $k_{\text{APP}}$  and  $N_{\text{H}_2\text{O}_2, 0}$  denote the apparent reaction rate constant obtained by fitting the reaction data to the pseudo-1<sup>st</sup>-order kinetic model and the initial H<sub>2</sub>O<sub>2</sub> quantity, respectively.[24, 39, 47, 48]  $N_{\text{CO}, 0.2 \text{ g}}$  denotes the number of CO-accessible surface sites contained per 0.2 g of the catalyst.[24, 39, 47, 48]

$$-r_{\text{H}_2\text{O}_2, 0} (\text{min}^{-1}) = \frac{k_{\text{APP}} (\text{min}^{-1}) \times N_{\text{H}_2\text{O}_2} (\text{mol}_{\text{H}_2\text{O}_2})}{N_{\text{CO}, 0.2 \text{ g}} (\text{mol}_{\text{CO}})} \quad (4)$$

An LC-20A system (Shimadzu) equipped with a Shim-pack GIS C18 column (5  $\mu$  m, 4.6 X 150 mm, Shimadzu), automatic injector (SIL-20A, Shimadzu), pump (LC-20AT, Shimadzu), and UV/VIS detector (SPD-20A, Shimadzu) was utilized to quantify the aqueous model contaminants (phenol or aniline) through reverse phase high performance liquid chromatography (HPLC) technique.[24, 39, 47, 48] Typically, a mixture of methanol and de-ionized H<sub>2</sub>O with a volumetric ratio of 60:40 served as the mobile phase at a constant flow rate of 1.0 mL min<sup>-1</sup> for measuring the concentration of phenol, whereas the mixture of acetonitrile and de-ionized H<sub>2</sub>O with the volumetric ratio of 60:40 served as the mobile phase at the constant flow rate of 1.0 mL min<sup>-1</sup> for measuring the concentration of aniline. The injection volume of the sample was 10  $\mu$  L. Conversion of the contaminant ( $X_{\text{CONTAMINANT}}$ ) was calculated according to Eqn. (5), wherein  $C_{\text{CONTAMINANT}, 0}$  indicates the initial concentration of the contaminant and  $C_{\text{CONTAMINANT}}$  indicates the concentration of the contaminant measured at a specific reaction time.[24, 39, 47, 48]

$$X_{\text{CONTAMINANT}} (\%) = \frac{C_{\text{CONTAMINANT}, 0} (\text{mol}_{\text{CONTAMINANT}} \text{L}^{-1}) - C_{\text{CONTAMINANT}} (\text{mol}_{\text{CONTAMINANT}} \text{L}^{-1})}{C_{\text{CONTAMINANT}, 0} (\text{mol}_{\text{CONTAMINANT}} \text{L}^{-1})} \times 100 \quad (5)$$

The initial degradation rate of the contaminant ( $-r_{\text{CONTAMINANT}, 0}$  or  $-r'_{\text{CONTAMINANT}, 0}$ ) was assessed using Eqn. (6) or Eqn. (7), in which  $k_{\text{APP}}$  and  $N_{\text{CONTAMINANT}, 0}$  denote the apparent reaction rate constant obtained by fitting the reaction data to the pseudo-1<sup>st</sup>-order kinetic model and the initial quantity of contaminant, respectively.[24, 39, 47, 48]  $N_{\text{CO}, 0.2 \text{ g}}$  denotes the number of CO-accessible surface sites contained per 0.2 g of the catalyst.[24,

39, 47, 48]

$$-r_{\text{CONTAMINANT},0} (\text{min}^{-1}) = \frac{k_{\text{APP}} (\text{min}^{-1}) \times N_{\text{CONTAMINANT}} (\text{mol}_{\text{CONTAMINANT}})}{N_{\text{CO},0.2} (\text{mol}_{\text{CO}})} \quad (6)$$

$$-r'_{\text{CONTAMINANT},0} (\text{mol}_{\text{CONTAMINANT}} \text{g}_{\text{CAT}}^{-1} \text{min}^{-1}) = \frac{k_{\text{APP}} (\text{min}^{-1}) \times N_{\text{CONTAMINANT}} (\text{mol}_{\text{CONTAMINANT}})}{0.2 \text{ g}_{\text{CAT}}} \quad (7)$$

The energy barrier ( $E_{\text{BARRIER}}$ ) and pre-factor ( $k_{\text{APP},0}$ ) of the catalyst required to decompose phenol via the  $\cdot\text{OH} \rightarrow \text{SO}_4^{\cdot-}$  pathway were evaluated using the Arrhenius plot of  $\ln(k_{\text{APP}})$  versus  $1/T$  (Eqn. (8)), in which  $k_{\text{APP}}$ ,  $R$ , and  $T$  indicate the apparent reaction rate constant, the ideal gas constant, and the temperature, respectively.[90]

$$\ln(k_{\text{APP}}) = \ln(k_{\text{APP},0}) - \frac{E_{\text{BARRIER}}}{R} \times \left(\frac{1}{T}\right) \quad (8)$$

The carbon or nitrogen contents present in the reaction mixtures were quantified using a total organic carbon contents (TOC) analyzer (TOC-L, Shimadzu) or total nitrogen contents (TN) analyzer (TNM-L, Shimadzu). Mineralization of the pollutant was evaluated by its conversion in terms of carbon ( $X_{\text{CARBON}}$  in Eqn. (9)) or nitrogen ( $X_{\text{NITROGEN}}$  in Eqn. (10)) species. In Eqn. (9) and (10),  $C_{\text{CARBON},0}$  (or  $C_{\text{NITROGEN},0}$ ) and  $C_{\text{CARBON}}$  (or  $C_{\text{NITROGEN}}$ ) denote the initial carbon (or nitrogen) concentration and the carbon (or nitrogen) concentration measured at a specific reaction time, respectively.[47]

$$X_{\text{CARBON},\text{TOC}} (\%) = \frac{C_{\text{CARBON},0} (\text{mol}_{\text{CARBON}} \text{L}^{-1}) - C_{\text{CARBON}} (\text{mol}_{\text{CARBON}} \text{L}^{-1})}{C_{\text{CARBON},0} (\text{mol}_{\text{CARBON}} \text{L}^{-1})} \times 100 \quad (9)$$

$$X_{\text{NITROGEN},\text{TN}} (\%) = \frac{C_{\text{NITROGEN},0} (\text{mol}_{\text{NITROGEN}} \text{L}^{-1}) - C_{\text{NITROGEN}} (\text{mol}_{\text{NITROGEN}} \text{L}^{-1})}{C_{\text{NITROGEN},0} (\text{mol}_{\text{NITROGEN}} \text{L}^{-1})} \times 100 \quad (10)$$

### 3.2.5. Reactions

Reactions were conducted by following the protocol specified in our previous literature resources.[24, 39, 47, 48] Typically, 93 g of N-methyl-2-pyrrolidone and 7 g of poly (vinylidene fluoride) were mixed to form binder solution, whose 0.2 g of which was mixed with 0.2 g of the catalyst to produce a catalyst slurry. The resulting slurry was then coated on a graphite plate acting as the cathode (Groupe Carbone Lorraine, grade 2124) with the area of 3 cm × 4 cm and dried overnight at 110 ° C. Another graphite plate acting as the anode was vertically positioned relative to the cathode with a gap of 3 cm and soaked in a reaction mixture containing 100 mL of de-ionized H<sub>2</sub>O and 0.2 mol of Na<sub>2</sub>SO<sub>4</sub> (supporting electrolyte), in general. The reaction was then initiated by stirring the reaction mixture at 300 rpm and 25 ° C with the occasional use of an electric potential of 1 V (~30 mA), 2 V (~ 24 mA), or 3 V (~ 15 mA). The reaction conditions are specified in the corresponding figure captions and annotations where necessary. H<sub>2</sub>O<sub>2</sub>, phenol, or aniline was quantified by collecting an aliquot (1 mL) from the reaction mixture at a pre-determined time. Typically, 1 mL of the reaction aliquot was quenched with 1 μL of methanol, filtered with a 0.45 μm-sized PES syringe filter (Whatman®), and injected into the HPLC system or TOC or TN analyzer.

### 3.3. Results and Discussion

#### 3.3.1. Generic properties for the catalysts

The solvo-thermal synthetic technique was used to prepare the  $\text{Mn}_x\text{Fe}_{3-x}\text{O}_4$  materials ( $x = 0, 1, 1.5, 2$ , and  $3$ ), wherein identical quantities of sodium acetate and polyethylene glycol were added to regulate the porosities of  $\text{Mn}_x\text{Fe}_{3-x}\text{O}_4$  poly-crystallites that were formed under identical temperature and pressure conditions.[135] This aimed to provide the materials with the comparable probability of forming surface defects, which significantly affects the accessibilities of  $\text{H}_2\text{O}_2$  to the  $\text{Fe}^{2+}/\text{Mn}^{2+}/\text{Mn}^{3+}$  and/or surface  $\text{SO}_4^{2-}$  densities. The crystallographic features of the materials were studied on the basis of their XRD patterns, in which all the bulk facets were indexed accurately to those defined in the Joint Committee on Powder Diffraction Files (JCPDF) of the materials with spinel geometries (Figure 3-2K). Of note, the crystallization of *cubic*  $\text{Mn}_3\text{O}_4$  was attempted, although its favorable phase transition to the *tetragonal* analogue was indispensable under ambient conditions.[122, 133] The *tetragonal*  $\text{Mn}_3\text{O}_4$  lattice is severely deformed to reduce the cell edge in the  $c$  direction relative to that of *cubic*  $\text{Mn}_3\text{O}_4$ :[122, 133] thus, it might likely limit the open  $\text{Mn}^{2+}$  sites in access to  $\text{H}_2\text{O}_2$  during the  $\cdot\text{OH} \rightarrow \text{SO}_4^{\cdot-}$  transformation. This again could raise the necessity to exploit distortion-free, bimetallic *cubic*  $\text{Mn}_x\text{Fe}_{3-x}\text{O}_4$  for prompting the  $\cdot\text{OH} \rightarrow \text{SO}_4^{\cdot-}$  route. Of additional note, the replacement of Fe inherent to the  $\text{Fe}_3\text{O}_4$  using Mn with a larger ionic radius could increase the lattice size of the resulting  $\text{Mn}_x\text{Fe}_{3-x}\text{O}_4$ . This was validated by a greater decrease in the  $2\theta$  values of the facets observed in the XRD pattern of  $\text{Mn}_x\text{Fe}_{3-x}\text{O}_4$  with a larger  $x$  value (*e.g.*, (311) at  $2\theta$  values of  $35.4^\circ \rightarrow 34.9^\circ$ , where  $x$  of  $0 \rightarrow 2$ ). Similar trends were also observed in our previous works on solid solutions of  $\text{Er}_x\text{Ce}_{1-x}\text{VO}_4$ ,  $\text{Co}_x\text{Ni}_{3-x}\text{S}_4$ , and  $\text{Fe}_x\text{Mo}_{2-x}\text{P}$ . [47, 86, 144, 145]  $\text{Mn}_x\text{Fe}_{3-x}\text{O}_4$  surfaces were then modified with  $\text{SO}_4^{2-}$  species with the use of  $\text{SO}_2$  and  $\text{O}_2$  at  $500^\circ\text{C}$ , leading to the creation of  $\text{Mn}_x$  catalysts. A temperature of  $500^\circ\text{C}$  was selected based on our previous work,

demonstrating that iron oxide functionalized with  $\text{SO}_4^{2-}$  at 500 ° C could accelerate  $\cdot\text{OH} \rightarrow \text{SO}_4^{\cdot-}$  in the most proficient manner.[39] SEM images of the catalysts coupled with their EDX mappings served to observe their macroscopic morphological characteristics. The catalysts comprised of 100–200 nm-sized aggregates, wherein oxygen, manganese, iron, or sulfur species were highly dispersed. The catalysts also possessed similar microscopic morphological features, as demonstrated by the HRTEM images which displayed particulates of 100–300 nm in size (Figure 3–2A to 3–2E). The lattice fringes showed distances that could be indexed to the facets of  $\text{Mn}_3\text{O}_4$ ,  $\text{Mn}_2\text{Fe}_1\text{O}_4$ ,  $\text{Mn}_{1.5}\text{Fe}_{1.5}\text{O}_4$ ,  $\text{Mn}_1\text{Fe}_2\text{O}_4$ , and  $\text{Fe}_2\text{O}_3$  for the  $\text{Mn}_3$ ,  $\text{Mn}_2$ ,  $\text{Mn}_{1.5}$ ,  $\text{Mn}_1$ , and  $\text{Mn}_0$  catalysts, respectively, which was in good agreement with the bulk facets of the catalysts found in their XRD patterns. The porosities of the catalysts were also comparable to one another, as corroborated by their surface areas ( $S_{\text{BET}}$ ) of  $15.8 (\pm 5.1) \text{ m}^2 \text{ g}_{\text{CAT}}^{-1}$  and pore volumes ( $V_{\text{BJH}}$ ) of  $0.06 (\pm 0.03) \text{ cm}^3 \text{ g}_{\text{CAT}}^{-1}$  obtained using BET and BJH calculations, respectively. These results suggested that the morphological or textural effects of the catalysts on the  $\cdot\text{OH} \rightarrow \text{SO}_4^{\cdot-}$  could be minimized by regulating their synthetic conditions, as discussed above.

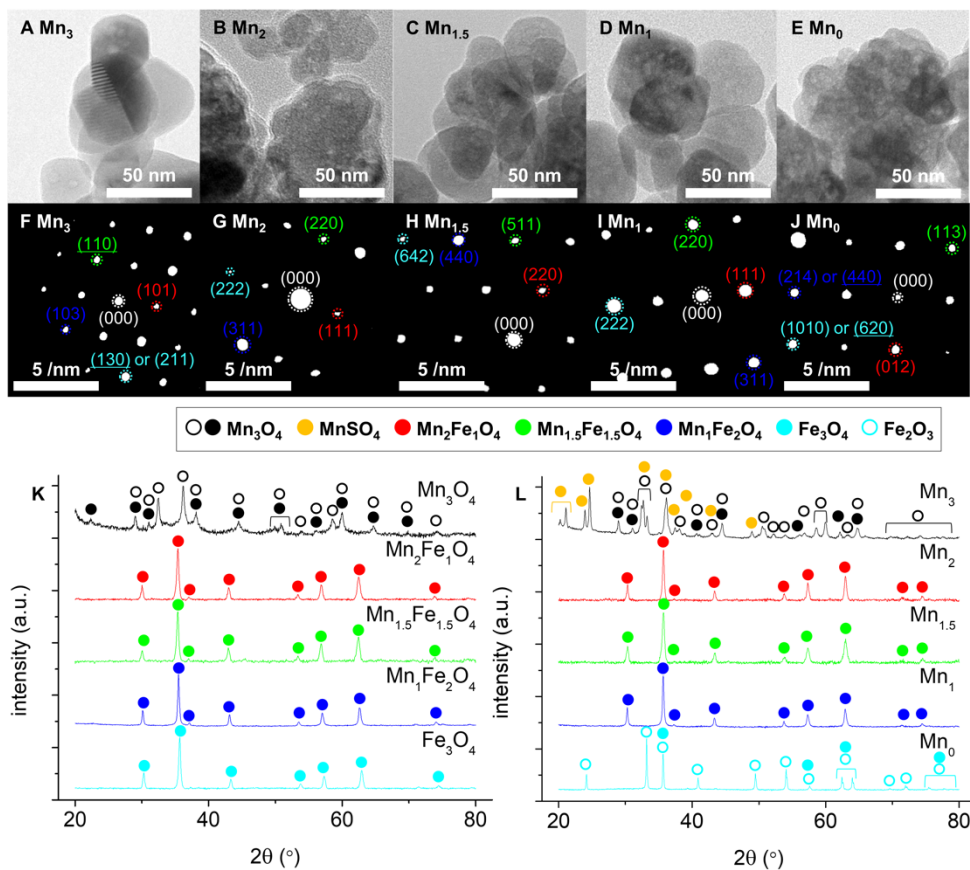


Figure 3-2. HRTEM images ((A)–(E) for  $\text{Mn}_x$ ), SAED patterns ((F)–(J) for  $\text{Mn}_x$ ), and XRD patterns of the catalysts ((K) for  $\text{Mn}_x\text{Fe}_{3-x}\text{O}_4$ ; (L) for  $\text{Mn}_x$ ). In (F)–(J), the surface facets without underlines belong to those of  $\text{Mn}_3\text{O}_4$  (JCPDF No. of 01-075-1560 or 03-065-2776 for (F)),  $\text{Mn}_2\text{Fe}_1\text{O}_4$  (JCPDF No. of 01-075-0035 for (G)),  $\text{Mn}_{1.5}\text{Fe}_{1.5}\text{O}_4$  (JCPDF No. of 01-075-0034 for (H)),  $\text{Mn}_1\text{Fe}_2\text{O}_4$  (JCPDF No. of 00-010-0319 for (I)), and  $\text{Fe}_2\text{O}_3$  (JCPDF No. of 01-080-2377 for (J)). The underlined surface facets belong to those of  $\text{MnSO}_4$  (JCPDF No. of 00-029-0898 for (F)) and  $\text{Fe}_3\text{O}_4$  (JCPDF No. of 01-089-0688 for (J)), respectively.

Nonetheless, the XRD pattern of  $\text{Mn}_0$  exhibited collateral phases that were indexed to those of *rhombohedral*  $\text{Fe}_2\text{O}_3$  (Figure 3-2L), as reported previously.[39]  $\text{Fe}_2\text{O}_3$  facets accompanied by those of  $\text{Fe}_3\text{O}_4$  were consistent to the surface of  $\text{Mn}_0$ , as demonstrated by its SAED pattern showing that the surface facets of  $\text{Mn}_0$  were assigned to those of either  $\text{Fe}_2\text{O}_3$  or  $\text{Fe}_3\text{O}_4$  (Figure 3-2J). This could suggest that the defective  $\text{Fe}^{2+}$  sites of  $\text{Fe}_3\text{O}_4$  were not prominent in expediting  $\cdot\text{OH} \rightarrow \text{SO}_4^{\cdot-}$ , unless otherwise exploited. In addition,  $\text{Mn}_3\text{O}_4$  also experienced drastic structural alterations upon  $\text{SO}_4^{2-}$



modification. This was validated by the XRD (or SAED) pattern of Mn<sub>3</sub> showing the secondary bulk (or surface) facets assigned to those of *orthorhombic* MnSO<sub>4</sub> (Figure 3–2F and 3–2L), wherein the Mn<sup>2+</sup> species are coordinated to six O<sup>2–</sup> anions, thus blocking access to H<sub>2</sub>O<sub>2</sub>.<sup>[146]</sup> In contrast to Mn<sub>0</sub> and Mn<sub>3</sub>, the bimetallic Mn<sub>x</sub> catalysts maintained their *cubic* crystal structure at the bulk/surface levels post SO<sub>4</sub><sup>2–</sup> functionalization, which was again verified by their XRD/SAED patterns (Figure 3–2G to 3–2I and 3–2L). In addition, XRF/EDX mapping and XP spectroscopy techniques were used to inspect the bulk and surface compositions of Mn<sub>1</sub>, Mn<sub>1.5</sub>, and Mn<sub>2</sub>, in which the observed molar ratios of Mn to Fe were in close accordance to those defined in their chemical formula. All the results could suggest that the catalysts were synthesized, as designed.

### 3.3.2. Properties germane to $\cdot\text{OH} \rightarrow \text{SO}_4^{\cdot-}$ for the catalysts

The properties of the catalysts associated with the  $\cdot\text{OH}$  evolution cycle were then investigated. The surface phases of the Mn<sub>x</sub> catalysts were explored using their XP spectra. Their XP spectra in the Mn 2p<sub>3/2</sub> regions were deconvoluted to exhibit three sub-bands centered at the binding energies of ~640.8 eV, ~641.7 eV, and ~642.7 eV, which were assigned to the Mn<sup>2+</sup>, Mn<sup>3+</sup>, and Mn<sup>4+</sup> species, respectively.<sup>[147, 148]</sup> Of interest, the spinel Mn<sub>x</sub> structures should only accommodate the Mn<sup>2+</sup> or Mn<sup>3+</sup> species as tentative H<sub>2</sub>O<sub>2</sub> scission sites,<sup>[122, 123, 149]</sup> as defined in their base units shown in Figure 3–1. However, the Mn<sub>x</sub> surfaces also contained the Mn<sup>4+</sup> species, which were regarded as H<sub>2</sub>O<sub>2</sub>–accessible, defective sites formed in spite of the considerable synthetic regulations in the synthesis of the catalysts. Hence, it was challenging to quantify the H<sub>2</sub>O<sub>2</sub>–accesssible Mn species present in the surfaces from the XP spectra. Meanwhile, the catalysts should only bear the Fe<sup>3+</sup> species in their base units;<sup>[122, 123, 149]</sup> however they also included the defective Fe<sup>2+</sup> species labile to activate H<sub>2</sub>O<sub>2</sub>. This was supported by the XP spectra of the catalysts in the Fe 2p<sub>3/2</sub> domains. These were curve–fitted to

provide two sub-bands centered at the binding energies of  $\sim 710.7$  eV and  $\sim 712.5$  eV, which were indexed to the  $\text{Fe}^{2+}$  and  $\text{Fe}^{3+}$  species, respectively.[150, 151]  $\text{Mn}_0$  exhibited the largest abundance of the  $\text{Fe}^{2+}$  species among the catalysts investigated. Hence,  $\text{Mn}_0$  might show the greatest efficiency in expediting  $\cdot\text{OH} \rightarrow \text{SO}_4^{\cdot-}$  per gram basis, if  $\cdot\text{OH} \rightarrow \text{SO}_4^{\cdot-}$  were primarily dictated by the  $\text{Fe}^{2+}$  species, as was not the case with the bimetallic  $\text{Mn}_x$  catalysts containing surface Fe and Mn species as tentative  $\text{H}_2\text{O}_2$  scission sites. To quantify the surface sites accessible more effectively to  $\text{H}_2\text{O}_2$ , CO served as a model adsorbate because of its kinetic diameter ( $\sim 3.8$  Å), which is similar to that of  $\text{H}_2\text{O}_2$ [47, 134] coupled with its affinity to Lewis acidic  $\text{Fe}^{2+}/\text{Mn}^{2+}/\text{Mn}^{3+}$  (donation of lone pair electrons from the O atom of CO to  $\text{Fe}^{2+}/\text{Mn}^{2+}/\text{Mn}^{3+}$ ). [24, 46, 48] A CO-pulsed chemisorption technique was utilized to measure the numbers of surface sites that are coordinated to CO included per gram of the catalysts ( $N_{\text{CO}}$ ) at near ambient temperature ( $40^\circ\text{C}$ ), which was also used to perform the reactions.[24, 39, 47, 48] The catalysts showed a concave trend in the plot of  $N_{\text{CO}}$  versus X of  $\text{Mn}_x$  (Figure 3-3), while showing the smallest and largest  $N_{\text{CO}}$  values for  $\text{Mn}_{1.5}$  ( $\sim 0.15 \mu\text{mol}_{\text{CO}} \text{g}_{\text{CAT}}^{-1}$ ) and  $\text{Mn}_0$  ( $\sim 0.42 \mu\text{mol}_{\text{CO}} \text{g}_{\text{CAT}}^{-1}$ ), respectively. This indicated that  $\text{Mn}_{1.5}$  and  $\text{Mn}_0$  could provide the smallest and largest efficiencies in prompting  $\cdot\text{OH} \rightarrow \text{SO}_4^{\cdot-}$  transfer per gram of the catalyst, if all Lewis acidic sites had similar intimacy to bind with  $\text{H}_2\text{O}_2$ .

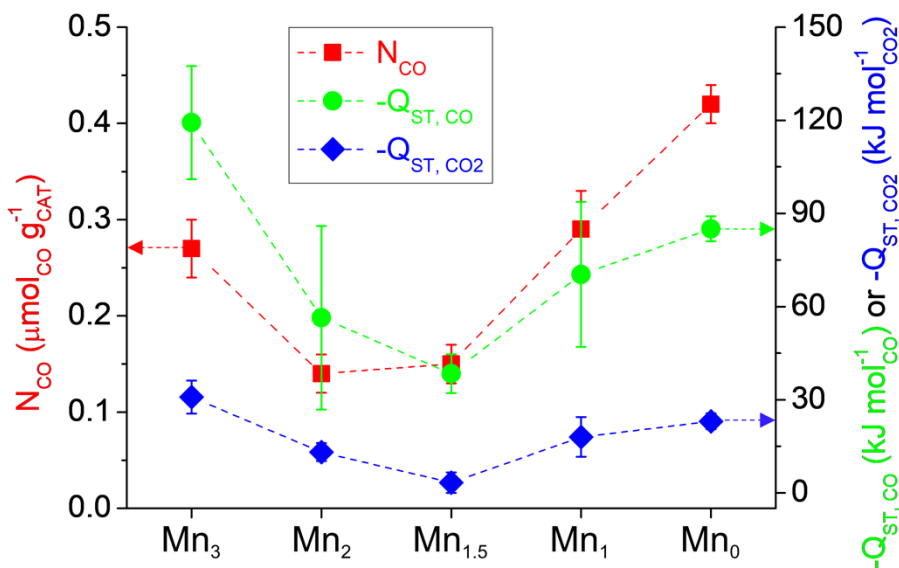


Figure 3-3. Amounts of CO adsorbed per gram of the catalysts measured at 40 ° C ( $N_{CO}$ ). Isosteric heats of CO adsorption ( $-Q_{ST, CO}$ ) and CO<sub>2</sub> adsorption ( $-Q_{ST, CO_2}$ ) for the catalysts measured at -25/-20/-15 ° C and -20/0/20 ° C.

It should be noted that the formation of surface defects was cumbersome to be controlled even with the regulation of the conditions utilized to synthesize or functionalize the catalysts. Hence, for fair comparison, it was necessary to examine the  $\cdot OH \rightarrow SO_4^{\cdot -}$  efficiencies of the catalysts per Lewis acidic site basis (not per-gram basis). Therefore, low-pressure CO isotherms of the catalysts obtained at -25 ° C, -20 ° C, and -15 ° C served to quantify the binding strengths of the surface sites with CO at identical amounts of CO adsorbed (isosteric heat of CO adsorption;  $-Q_{ST, CO}$ ). [47, 136–139] Notably, CO isotherms of the catalyst were not obtainable at or near the reaction temperatures and were only reliable at temperatures  $\leq -15$  ° C. This might result from the limitation of the instrument, for which the  $N_{CO}$  measurements were barely discernible from one another when the relative pressures ( $P/P_0$ ) were altered at temperature  $> -15$  ° C. Nevertheless, the catalysts showed a concave relationship between  $-Q_{ST, CO}$  at near-zero coverage of CO and  $X$  of  $Mn_X$  (Figure 3-3), which was similar to the trend found in the  $N_{CO}$  values for the catalysts. In spite of exhibiting the smallest  $N_{CO}$  value,  $Mn_{1.5}$  showed the

smallest  $-Q_{ST, CO}$  ( $\sim 40 \text{ kJ mol}_{CO}^{-1}$ ) among the studied catalysts ( $\geq \sim 60 \text{ kJ mol}_{CO}^{-1}$  for the other catalysts). Hence, we supposed that  $Mn_{1.5}$  might promote  $\cdot OH$  release from the  $Fe^{2+}/Mn^{2+}/Mn^{3+}$  sites during  $\cdot OH \rightarrow SO_4^{\cdot -}$  transfer, thereby revealing the greatest efficiency in accelerating  $\cdot OH \rightarrow SO_4^{\cdot -}$  per Lewis acidic site.

In addition,  $CO_2$  served as a complementary adsorbate to  $CO$  owing to their similar molecular sizes ( $\sim 3.3 \text{ \AA}$ ) of the two compounds[134] combined with the tendency of  $CO_2$  to coordinate with Lewis acidic metals.[47, 152]  $CO_2$  was reported to also bind with Brönsted acidic  $SO_4^{2-}$  functionalities produced via interactions with  $H^+$  species roaming in the surfaces.[59, 60, 89, 90]  $CO_2$ , however, could strongly interplay with the surface sites; thus, it allowed for obtaining such  $CO_2$  isotherms of the catalysts that were fitted to provide their isosteric heats of  $CO_2$  adsorption near the reaction temperatures ( $-Q_{ST, CO_2}$  at  $-20^\circ \text{C}$ ,  $0^\circ \text{C}$ , and  $20^\circ \text{C}$ ).[24, 39, 47, 48] The trend found in the plot of  $-Q_{ST, CO_2}$  at near-zero coverage of  $CO_2$  versus  $X$  of  $Mn_X$  was also concave (Figure 3-3). In addition, the  $-Q_{ST, CO_2}$  value of  $Mn_{1.5}$  was the smallest among the values of the catalysts studied ( $\sim 3 \text{ kJ mol}_{CO_2}^{-1}$  for  $Mn_{1.5}$ ;  $> 10 \text{ kJ mol}_{CO_2}^{-1}$  for the other catalysts), thereby providing additional evidence to support our claim that  $Mn_{1.5}$  can conduct  $\cdot OH \rightarrow SO_4^{\cdot -}$  in the most efficient fashion by expediting its rate-determining stage ( $\cdot OH$  desorption).

The properties of the catalysts related to the  $SO_4^{\cdot -}$  evolution cycle were explored as follows. The bulk and surface elemental ratios of sulfur to metals innate to the catalysts ( $S/(Mn+Fe)$ ) were investigated via XRF/EDX mapping and XP spectroscopy, respectively.  $Mn_3$  showed the greatest bulk and surface  $S/(Mn+Fe)$  values among the studied catalysts. This was expected because  $Mn_3O_4$  was significantly modified by the  $SO_4^{2-}$  species to produce  $MnSO_4$ , as clarified in the XRD pattern of  $Mn_3$  (Figure 3-2L). In contrast, among the other catalysts, the surface  $S/(Mn+Fe)$  value was highest for  $Mn_{1.5}$ , which might suggest the increased probability of  $\cdot OH$  encountering  $SO_4^{\cdot -}$  supported on  $Mn_{1.5}$  during  $\cdot OH \rightarrow SO_4^{\cdot -}$  per unit time ( $\sim 0.13$  for  $Mn_{1.5}$ ;  $\leq$

~0.11 for the other catalysts in Figure 3-4A). In addition to the  $\text{SO}_4^{2-}$  species, the  $\text{SO}_3^{2-}$  species were also reported to be immobilized on the surface upon modification with  $\text{SO}_2$  and  $\text{O}_2$  at elevated temperatures. Indeed, the catalyst surfaces contained both  $\text{SO}_3^{2-}$  and  $\text{SO}_4^{2-}$  functionalities. This was verified by the Raman spectra of the catalysts at 900–1,200  $\text{cm}^{-1}$ , wherein only the symmetric stretching ( $\nu_1$ ) or asymmetric stretching ( $\nu_3$ ) vibration of the S–O bonds inherent to the  $\text{SO}_3^{2-}/\text{SO}_4^{2-}$  species appeared (Figure 3-4B).[153, 154] This was further supported by the background-subtracted *in situ* DRIFT spectra of the catalysts under the conditions similar to those utilized to generate the  $\text{Mn}_x$  catalysts. ( $\text{SO}_2/\text{O}_2$  at 500 ° C for an hour; details are given in Figure 3-4C caption.) The *in situ* DRIFT spectra of the catalysts exhibited bands, arising from the surface  $\text{SO}_3^{2-}/\text{SO}_4^{2-}$  species with various binding configurations such as *mono*-, *bi*-, and *tri*-dentate arrays, among which the *tri*-dentate  $\text{SO}_4^{2-}$  species were reported vital to prompt the  $\cdot\text{OH} \rightarrow \text{SO}_4^{\cdot-}$  route,[25, 39] as further discussed later. In addition, the relative abundance of surface  $\text{SO}_4^{2-}$  species innate to the catalysts was compared using their XP spectra in the S 2p domains. The XP spectra were curve-fitted to show two sub-bands indexed to  $\text{SO}_3^{2-}$  and  $\text{SO}_4^{2-}$  positioned at the binding energies centered at ~168.4 eV and ~169.5 eV, respectively (Figure 3-4A).[39, 155] Notably,  $\text{Mn}_3$  showed the largest abundance of the  $\text{SO}_4^{2-}$  species (74.7%), which was ascribed to the phase transition to  $\text{MnSO}_4$  during  $\text{SO}_4^{2-}$  functionalization, as stated above. For the other catalysts, the  $\text{Mn}_{1.5}\text{Fe}_{1.5}\text{O}_4$  surface could be the most desired and amicable to  $\text{SO}_4^{2-}$  functionalization without any structural damage. This was corroborated by the greatest abundance of  $\text{SO}_4^{2-}$  species being observed on the surface of  $\text{Mn}_{1.5}$  (62.9% for  $\text{Mn}_{1.5}$ ;  $\leq 54.8\%$  for the others except for  $\text{Mn}_3$ ), in addition to its XRD pattern. This might suggest that  $\text{Mn}_{1.5}$  could enhance the efficiency of  $\cdot\text{OH} \rightarrow \text{SO}_4^{\cdot-}$  per Lewis acidic site over the other catalysts, partially resulting from a high probability for  $\cdot\text{OH}$  to interact with the  $\text{SO}_4^{2-}$  functionalities ( $\text{SO}_4^{\cdot-}$  precursors). The results from the characterization experiments again

suggested that  $\text{Mn}_{1.5}$  could be desirable in activating the  $\cdot\text{OH} \rightarrow \text{SO}_4^{\cdot-}$  pathway primarily due to its Lewis acidic strength, which was the most adequate in dismantling  $\cdot\text{OH}$  from the  $\text{Fe}^{2+}/\text{Mn}^{2+}/\text{Mn}^{3+}$  species and the largest density of supported  $\text{SO}_4^{\cdot-}$  precursors ( $\text{SO}_4^{2-}$ ) without undergoing any structural transitions.

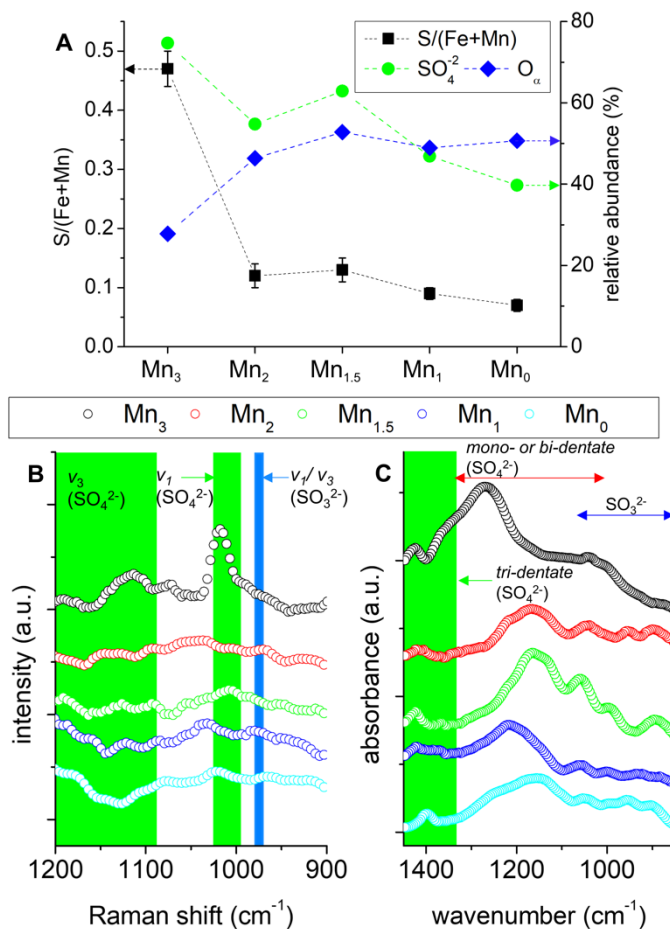


**Figure 3-4.** (A) Elemental ratios of S to metals present in the catalyst surfaces ( $\text{S}/(\text{Mn}+\text{Fe})$ ). Relative abundance of surface  $\text{SO}_4^{2-}$  species present in the catalysts. Surface-mobile O species ( $\text{O}_a$ ) present in the catalyst surfaces. (B) Raman spectra of the catalyst. The bands assigned as symmetric ( $\nu_1$ ) or asymmetric stretching vibration ( $\nu_3$ ) of the S-O bonds for the  $\text{SO}_3^{2-}/\text{SO}_4^{2-}$  species are highlighted with arrows or rectangles. (C) Background-subtracted *in situ* DRIFT spectra of the catalysts. The catalyst surfaces were initially purged with 3 vol.%  $\text{O}_2/\text{N}_2$  at 300 ° C for an hour and subsequently exposed to a  $\text{N}_2$  atmosphere at 500 ° C, in which the spectra of the surfaces were collected as the backgrounds. The backgrounds were then used to correct the spectra of the surfaces exposed to 1,000 ppm  $\text{SO}_2/$  3 vol.%  $\text{O}_2/$   $\text{N}_2$  at 500 ° C for an hour. The bands arising from the  $\text{SO}_3^{2-}$  or  $\text{SO}_4^{2-}$  species with various configurations (*mono*-, *bi*-, or *tri*-dentate) are shown with arrows and rectangle.

### 3.3.3. Kinetics of the $\cdot\text{OH} \rightarrow \text{SO}_4^{\cdot-}$ pathway

The  $\cdot\text{OH} \rightarrow \text{SO}_4^{\cdot-}$  transfers on the catalysts were then explored under such fine-tuned reaction domains as to compare the surface sites in terms of their efficiencies in producing  $\text{H}_2\text{O}_2$ ,  $\cdot\text{OH}$ , and supported  $\text{SO}_4^{\cdot-}$ , or degrading refractory pollutants via kinetic assessments. Phenol and aniline served as model compounds of aqueous pollutants because of their aromatic structures coupled with their  $-\text{OH}/-\text{NH}_2$  functionalities, all of which are of particular challenge to be fragmented upon exposure to severe oxidative conditions.[156, 157] Phenol was utilized to investigate the overall catalytic  $\cdot\text{OH} \rightarrow \text{SO}_4^{\cdot-}$  stages, whereas aniline was used to test the adaptability of the catalysts in decomposing contaminants. Of note, anodic oxidation ( $\text{O}_a$  on the anodic surface) was reported effective in decomposing contaminants to some extent[9, 116] and could be as significant as  $\cdot\text{OH}/\text{SO}_4^{\cdot-}$  in fragmenting contaminants at electric potentials of  $< 1$  V.[24, 25, 39, 47] For rigor, reaction data were thus corrected using backgrounds driven by anodic oxidation prior to extracting the kinetic parameters.[24, 39, 47] Of additional note, the catalysts were drastically dismantled from the cathode surfaces at electric potentials of  $> 3$  V, while leaching significant amounts of ionized metals to aqueous environments.[24, 25, 39, 47] Hence, the electric potentials were dialed in solely in the range of 1–3 V only, for additional rigor.

As an initiator of  $\cdot\text{OH} \rightarrow \text{SO}_4^{\cdot-}$ , the  $\text{H}_2\text{O}_2$  production step was investigated at 1–3 V in the absence of phenol under aqueous, ambient conditions with the use of  $\text{Na}_2\text{SO}_4$  as a supporting electrolyte.[118, 119]  $\text{H}_2\text{O}_2$  can be generated by a  $2e^-$  transfer reaction on the cathode ( $2\text{H}^+ + 2e^- + \text{O}_2 \rightarrow \text{H}_2\text{O}_2$ ),[118, 119] for which greater quantities of  $\text{H}^+$ ,  $e^-$ , and  $\text{O}_2$  are required to prompt  $\text{H}_2\text{O}_2$  production. In this regard, a higher electric potential was desired to yield larger amounts of  $\text{H}^+$ ,  $e^-$ , and  $\text{O}_2$  via anodic  $\text{H}_2\text{O}$  oxidations.[118, 119] This was supported by the greater numbers of  $\text{H}_2\text{O}_2$  ( $N_{\text{H}_2\text{O}_2}$ ) produced during the  $\text{H}_2\text{O}_2$  evolution runs in the absence of the catalysts at higher electric potentials (blank), wherein the increase in electric

potential from 1 V to 3 V increased the  $N_{\text{H}_2\text{O}_2}$  values from  $\sim 0.05 \text{ mmol}_{\text{H}_2\text{O}_2}$  to  $\sim 0.09 \text{ mmol}_{\text{H}_2\text{O}_2}$ . Notably, the blank runs could generate  $\text{H}_2\text{O}_2$  with the main utilization of  $\text{H}^+$ ,  $\text{e}^-$ , and  $\text{O}_2$  obtained via  $\text{H}_2\text{O}$  oxidations with the additional use of  $\text{O}_2$  dissolved in de-ionized  $\text{H}_2\text{O}$ . [25, 39] Hence, the  $N_{\text{H}_2\text{O}_2}$  values obtained during the blank runs at 1–3 V were insufficient to fully account for the  $N_{\text{H}_2\text{O}_2}$  values obtained during catalytic  $\text{H}_2\text{O}_2$  evolution runs, all of which were greater than those of the blank runs by  $0.01\text{--}0.05 \text{ mmol}_{\text{H}_2\text{O}_2}$  and  $0.02\text{--}0.17 \text{ mmol}_{\text{H}_2\text{O}_2}$  at 1 V and 3 V, respectively. The unclarified  $N_{\text{H}_2\text{O}_2}$  quantities, however, could result from the fusion among  $\text{H}^+$ ,  $\text{e}^-$ , and surface-mobile O ( $\text{O}_\alpha$ ) on the catalyst surfaces at the cathode, as we conjectured previously. [25, 39] XP spectra of the catalysts in the O 1s regions were analyzed to determine the relative abundance of the surface O species ( $\text{O}_\alpha$ ) potentially labile to form  $\text{H}_2\text{O}_2$  on or near the cathode. [25, 39] XP spectra were de-convoluted into three sub-bands assigned to lattice O ( $\text{O}_\beta$ ), mobile O ( $\text{O}_\alpha$ ), and the O of chemisorbed  $\text{H}_2\text{O}$  ( $\text{O}'_\alpha$ ), which were located at the binding energies centered at  $\sim 529.8 \text{ eV}$ ,  $\sim 530.6 \text{ eV}$ , and  $\sim 531.9 \text{ eV}$ , respectively. [158, 159] A large abundance of  $\text{O}_\alpha$  species was achieved for  $\text{Mn}_{1.5}$  or Fe-rich analogues ( $\text{Mn}_1$  or  $\text{Mn}_0$ ) in comparison with the those afforded by the other catalysts. This was in exact accordance with the  $\text{H}_2\text{O}_2$  productivities of the catalysts, in which the catalysts with X values of  $\leq 1.5$  showed greater  $N_{\text{H}_2\text{O}_2}$  values than the other catalysts at 1–3 V. In contrast, in the presence of the catalysts,  $N_{\text{H}_2\text{O}_2}$  values rapidly increased and were saturated within 10 minutes of the reaction runs. These were substantially dissimilar to the amounts of phenol consumed in the presence of the catalysts at 1–3 V, which continuously increased up to 8 hours of the reaction runs. In conjunction with the results from our previous works, [24, 25] this provided evidence that the  $\text{H}_2\text{O}_2$  evolution stage should not dominate the  $\cdot\text{OH} \rightarrow \text{SO}_4^{\cdot-}$  cycles as the rate-determining step.

The remaining  $\text{H}_2\text{O}_2$  splitting stages were investigated using control  $\text{H}_2\text{O}_2$  scission runs in the presence of the catalysts. The control runs were performed in a manner identical to the  $\text{H}_2\text{O}_2$  production runs except for excluding the



electric potentials. To simulate the electric potential–assisted, catalytic  $\text{H}_2\text{O}_2$  scission cycles,  $\text{H}_2\text{O}_2$  served as the precursor of  $\cdot\text{OH}$  and was added to the reaction mixtures with the amounts identical to those observed during the  $\text{H}_2\text{O}_2$  production runs (*i.e.*,  $N_{\text{H}_2\text{O}_2}$ ). [24, 25, 39, 47] This provided kinetic data of the catalytic  $\text{H}_2\text{O}_2$  scission control runs, which were corrected with background data (self–decomposition of  $\text{H}_2\text{O}_2$ ), fitted to a pseudo–1<sup>st</sup>–order kinetic model to provide the apparent reaction rate constants, and used to determine the initial  $\text{H}_2\text{O}_2$  scission rates of the catalysts ( $-r_{\text{H}_2\text{O}_2, 0}$ ). [24, 25, 39, 47] Specifically,  $-r_{\text{H}_2\text{O}_2, 0}$  values were obtained by normalizing the numbers of  $\text{H}_2\text{O}_2$  cleaved per unit time with respect to the amounts of Lewis acidic sites inherent to the catalysts. [24, 47] Again, this could minimize the repercussions caused by synthetic artifacts (variable numbers of surface defects) on the  $\text{H}_2\text{O}_2$  fission efficiencies of the catalysts ( $-r_{\text{H}_2\text{O}_2, 0}$ ), as stated above. The resulting  $-r_{\text{H}_2\text{O}_2, 0}$  values were then solely dictated by the Lewis acidic strengths of the metal sites only, [24, 47] which again could direct the  $\cdot\text{OH}$  desorption stage to dominate the whole  $\cdot\text{OH} \rightarrow \text{SO}_4^{\cdot-}$  cycles as the rate–determining step. The  $-r_{\text{H}_2\text{O}_2, 0}$  values of the catalysts at the control runs utilized to simulate the catalytic  $\text{H}_2\text{O}_2$  scission runs at 3 V were compared because 3 V was the upper limit of the varied electric potentials, provided considerable energies acting on the catalyst surfaces, [24, 39, 47] facilitated  $\cdot\text{OH}$  desorption depending on the type of the catalyst surfaces, [24, 25, 39, 47] and therefore could lead to the largest difference among  $-r_{\text{H}_2\text{O}_2, 0}$  values of the catalysts. As anticipated based on a host of characterizations techniques, a convex trend was observed in the plot of  $-r_{\text{H}_2\text{O}_2, 0}$  versus X of  $\text{Mn}_X$  (Figure 3–5A). This was opposite to the concave trends found in the  $-\text{Q}_{\text{ST, CO}}$  and  $-\text{Q}_{\text{ST, CO}_2}$  values for the catalysts (Figure 3–3), which suggested that the Lewis acidic strength of the metal sites innate to the catalysts could be the primary director in activating the  $\cdot\text{OH} \rightarrow \text{SO}_4^{\cdot-}$  cycles. In addition, the bimetallic  $\text{Mn}_X$  catalysts exhibited larger  $-r_{\text{H}_2\text{O}_2, 0}$  values in comparison with  $\text{Mn}_0$  and  $\text{Mn}_3$ , whereas  $\text{Mn}_{1.5}$  showed such  $-r_{\text{H}_2\text{O}_2, 0}$  value that was  $\sim 10$  fold larger than that of  $\text{Mn}_0$  or  $\text{Mn}_3$ . All the results

could provide the rationales associated with the preferential use of bimetallic oxo-spinels over their monometallic counterparts as  $\cdot\text{OH}$  producers.

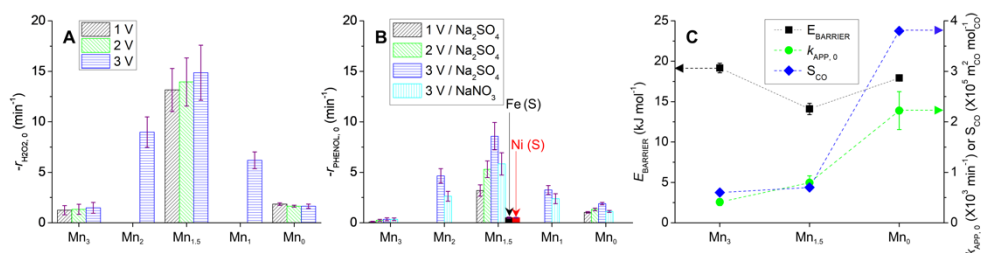


**Figure 3-5.** (A) Background-subtracted initial  $\text{H}_2\text{O}_2$  scission rates ( $-r_{\text{H}_2\text{O}_2,0}$ ) of the catalysts obtained through the control runs to simulate the catalytic  $\text{H}_2\text{O}_2$  scission runs at 1–3 V. (B) Background-subtracted initial phenol degradation rates ( $-r_{\text{PHENOL},0}$ ) of the catalysts with the use of  $\text{Na}_2\text{SO}_4$  or  $\text{NaNO}_3$  as a supporting electrolyte at 1–3 V. (C) Energy barriers ( $E_{\text{BARRIER}}$ ) and pre-factors ( $k_{\text{APP},0}$ ) of the catalysts obtained through phenol degradation runs at 3 V and 25–55 °C. Surface areas per CO-accessible Lewis acidic site innate the catalysts ( $S_{\text{CO}}$ ).

The  $-r_{\text{H}_2\text{O}_2,0}$  values of the catalysts at the control runs used to simulate the catalytic  $\text{H}_2\text{O}_2$  scission runs at 1 V and 2 V were then examined. The sole difference among the control runs was the  $N_{\text{H}_2\text{O}_2}$  values utilized, which allowed for the clarification of whether the  $-r_{\text{H}_2\text{O}_2,0}$  values of the catalysts were affected by the change in the  $N_{\text{H}_2\text{O}_2}$  values. For these control runs,  $\text{Mn}_{1.5}$  was selected owing to its largest  $-r_{\text{H}_2\text{O}_2,0}$  value, whereas monometallic  $\text{Mn}_0$  and  $\text{Mn}_3$  were also adopted for comparison. The  $-r_{\text{H}_2\text{O}_2,0}$  values of  $\text{Mn}_{1.5}$  were  $\sim 10$  times larger than the  $-r_{\text{H}_2\text{O}_2,0}$  values of  $\text{Mn}_0$  and  $\text{Mn}_3$  throughout these control runs (Figure 3-5A), which again suggests the superiority of  $\text{Mn}_{1.5}$  over the other catalysts in prompting  $\cdot\text{OH} \rightarrow \text{SO}_4^{\cdot-}$ . Interestingly, the  $-r_{\text{H}_2\text{O}_2,0}$  values of the catalysts were invariant even with the change in the  $N_{\text{H}_2\text{O}_2}$  values. This suggests that the  $\text{H}_2\text{O}_2$  fission ability of the individual catalyst would be fixed throughout the electric potential-assisted catalytic  $\text{H}_2\text{O}_2$  scission runs at 1–3 V. In addition, the abundant  $e^-$  quantities produced under electric environments made the recovery stage of the Lewis acidic metals via  $e^-$  reduction insignificant. Furthermore, the elementary stages involved in the  $\text{SO}_4^{\cdot-}$  evolution cycle were entirely exothermic and could not dominate the

$\cdot\text{OH} \rightarrow \text{SO}_4^{\cdot-}$  cycle.[25, 39] These left the  $\text{H}_2\text{O}_2$  adsorption and  $\cdot\text{OH}$  desorption as tentative rate-determining stage for the  $\cdot\text{OH} \rightarrow \text{SO}_4^{\cdot-}$ , which was clarified by the other control runs, as discussed below.

The  $\text{SO}_4^{\cdot-}$  supported on the catalysts was an invaluable source in degrading phenol;[25, 39] thus, it was exposed to phenol degradation environments. The conditions used to decompose phenol were identical to those utilized to conduct the electric potential-assisted  $\text{H}_2\text{O}_2$  evolution runs except for the addition of phenol into the reaction mixtures. The initial phenol degradation rates of the catalysts ( $-r_{\text{PHENOL}, 0}$ ) were extracted by a model similar to that used for their  $-r_{\text{H}_2\text{O}_2, 0}$  values.[24, 25, 39, 47] Although the  $-r_{\text{PHENOL}, 0}$  values of the catalysts were smaller than their  $-r_{\text{H}_2\text{O}_2, 0}$  values owing in part to the short lifetime of the  $\cdot\text{OH}$  species which was insufficient to induce  $\cdot\text{OH} \rightarrow \text{SO}_4^{\cdot-}$ , a volcano-shaped trend in the plot of  $-r_{\text{PHENOL}, 0}$  versus X of  $\text{Mn}_x$  was consistent with the degradation of phenol (Figure 3-5B).

Of interest was the smallest  $-r_{\text{PHENOL}, 0}$  value of  $\text{Mn}_3$  among the catalysts, which suggested the importance to avoid severe phase transition during  $\text{SO}_4^{2-}$  functionalization (*i.e.*,  $\text{Mn}_3\text{O}_4 \rightarrow \text{MnSO}_4$ ), as also observed previously on  $\text{Fe}_2\text{O}_3$  and  $\text{NiO}$  modified with  $\text{SO}_4^{2-}$  species.[25, 39] The catalysts other than  $\text{Mn}_3$  showed such a trend of the  $-r_{\text{PHENOL}, 0}$  values as to be opposite to the trends of their  $-\text{Q}_{\text{ST}, \text{CO}}$  and  $-\text{Q}_{\text{ST}, \text{CO}_2}$  values, yet, be concurrent to the trends of their surface  $\text{SO}_4^{2-}$  concentrations (Figure 3-3 and 3-4). Of additional interest was that the  $-r_{\text{PHENOL}, 0}$  value for  $\text{Mn}_{1.5}$  was 3-5 times larger than the  $-r_{\text{PHENOL}, 0}$  values for the other catalysts at electric potentials of at least 1-3 V, whereas  $\text{Mn}_{1.5}$  leached the smallest quantities of metal species during the reaction runs at 3 V (0.06 mol.% for  $\text{Mn}_{1.5}$ ;  $\geq 0.08$  mol.% for the other catalysts). Notably, the  $-r_{\text{PHENOL}, 0}$  value for  $\text{Mn}_{1.5}$  was  $\sim 18$  fold larger than those for  $\text{Fe}_2\text{O}_3$  or  $\text{NiO}$  functionalized with  $\text{SO}_4^{2-}$  at their optimum temperatures (500 ° C for  $\text{Fe}_2\text{O}_3$  denoted as Fe (S);[39] 400 ° C for  $\text{NiO}$  denoted as Ni (S)).[25] All the kinetic results supported our argument that the use of bimetallic oxide as a platform to accommodate  $\text{SO}_4^{\cdot-}$  precursors ( $\text{SO}_4^{2-}$ )

is compelling strategy to promote the degradation efficiency of aqueous recalcitrants.

It should be noted that a quantification of the sulfur leached from the catalysts during the reactions at 3 V was attempted, although it was challenging because of the use of  $\text{Na}_2\text{SO}_4$  as a supporting electrolyte throughout the reaction runs. Hence,  $\text{NaNO}_3$  served as an alternative supporting electrolyte for additional reaction runs at 3 V, when the conditions were identical to those of the reaction runs using the  $\text{Na}_2\text{SO}_4$  electrolyte. The  $-r_{\text{PHENOL},0}$  values of the catalysts were also obtained in addition to the quantities of sulfur leached from the surfaces. The volcano-shaped trend in the plot of  $-r_{\text{PHENOL},0}$  versus X of  $\text{Mn}_x$  was retained even with the use of the  $\text{NaNO}_3$  electrolyte (Figure 3-5B). Meanwhile,  $\text{Mn}_3$  leached 0.12 mol.% of sulfur, whereas the other catalysts leached similar numbers of sulfur (0.03–0.05 mol.%) during the reactions. This might suggest that the degradation of phenol on surface-unbound  $\text{SO}_4^{\cdot-}$  species, produced by  $\cdot\text{OH}$ -mediated radicalization of free  $\text{SO}_4^{2-}$ , could be insignificant. Interestingly, although the catalysts leached lesser amounts of metals ( $\cdot\text{OH}$  producer) upon the alteration of the supporting electrolyte from  $\text{Na}_2\text{SO}_4$  to  $\text{NaNO}_3$ , the  $-r_{\text{PHENOL},0}$  values of the catalysts in the  $\text{NaNO}_3$  electrolyte were smaller than those in the  $\text{Na}_2\text{SO}_4$  counterpart (Figure 3-5B). This could be ascribed to the quenching of  $\text{SO}_4^{2-}$  radicalizer ( $\cdot\text{OH}$ ) by  $\text{NO}_3^-$  when using the  $\text{NaNO}_3$  electrolyte, as reported elsewhere.[160] In addition, this could also be ascribed to the fouling of the anode surface,[161] on which  $\text{H}_2\text{O}$  oxidations were hampered to make the evolution of  $\text{H}^+/\text{O}_2/\text{e}^-$  species used for producing  $\text{H}_2\text{O}_2$  on the cathode be sluggish. This was corroborated by the  $\text{H}_2\text{O}_2$  evolution runs on the catalysts in the  $\text{NaNO}_3$  electrolyte at 3 V, whose  $N_{\text{H}_2\text{O}_2}$  values were approximately half those observed during the  $\text{H}_2\text{O}_2$  evolution runs in the  $\text{Na}_2\text{SO}_4$  analogue at 3 V.

It should be noted that the conclusion concerned with the rate-determining stage of  $\cdot\text{OH} \rightarrow \text{SO}_4^{\cdot-}$  was derived by analysing the  $-r_{\text{PHENOL},0}$  values for  $\text{Mn}_0$ ,

Mn<sub>1.5</sub> and Mn<sub>3</sub> at 1–3 V. Larger electric potentials could exert larger energies on the catalyst surfaces.[24, 25, 39, 47] Hence, if catalytic H<sub>2</sub>O<sub>2</sub> cleavage were the rate-determining stage of  $\cdot\text{OH} \rightarrow \text{SO}_4^{\cdot-}$ , one should observe a retention of the  $-r_{\text{PHENOL}, 0}$  value regardless of the change in the electric potential.[24, 39, 47] In contrast, if H<sub>2</sub>O<sub>2</sub> adsorption or  $\cdot\text{OH}$  desorption were the rate-determining stage of  $\cdot\text{OH} \rightarrow \text{SO}_4^{\cdot-}$ , one should observe a smaller or a larger  $-r_{\text{PHENOL}, 0}$  value at a larger electric potential. [24, 39, 47] As shown in Figure 3–5B, the increase in electric potentials gave rise to the increase in the  $-r_{\text{PHENOL}, 0}$  values for the catalysts, which could provide concrete evidence that the  $\cdot\text{OH}$  desorption stage does dominate the overall  $\cdot\text{OH} \rightarrow \text{SO}_4^{\cdot-}$  cycles.

Indeed, the electric potential was an efficient means to alter the surface energy of the catalyst, thereby tuning the  $\cdot\text{OH}$  liberation stage. However, the electric potential could only be increased up to 3 V to avoid severe release of catalyst particles or their metal constituents during the reactions. Hence, the temperature was considered as an additional measure to adjust the surface energies of the catalysts, whereas Mn<sub>0</sub>, Mn<sub>1.5</sub>, and Mn<sub>3</sub> were selected for the identical reasons discussed above. Additional CO<sub>2</sub> isotherm experiments on the catalysts were carried out at 30~60 °C because the temperature domain of 35~55 °C was selected to conduct the phenol degradation control runs at 3 V, as discussed below. The CO<sub>2</sub> isotherms of the catalysts at 30 °C, 45 °C, and 60 °C were fitted using methods identical to those utilized for fitting their CO<sub>2</sub> isotherms at -20~20 °C. This could provide the  $-Q_{\text{ST}, \text{CO}_2}$  values of Mn<sub>0</sub>, Mn<sub>1.5</sub>, and Mn<sub>3</sub> at near-zero coverage of CO<sub>2</sub> at 30~60 °C, all of which were slightly smaller than the  $-Q_{\text{ST}, \text{CO}_2}$  counterparts at -20~20 °C ( $-Q_{\text{ST}, \text{CO}_2}$  values of  $\sim 30.8 \text{ kJ mol}_{\text{CO}_2}^{-1} \rightarrow \sim 25.0 \text{ kJ mol}_{\text{CO}_2}^{-1}$  for Mn<sub>0</sub>;  $\sim 3.3 \text{ kJ mol}_{\text{CO}_2}^{-1} \rightarrow \sim 1.9 \text{ kJ mol}_{\text{CO}_2}^{-1}$  for Mn<sub>1.5</sub>;  $\sim 23.0 \text{ kJ mol}_{\text{CO}_2}^{-1} \rightarrow \sim 18.6 \text{ kJ mol}_{\text{CO}_2}^{-1}$  for Mn<sub>3</sub> upon the change in the temperature domain of -20~20 °C  $\rightarrow$  30~60 °C). The increase in the temperatures used to adsorb CO<sub>2</sub> on the catalyst surfaces also led to a decline in the amounts of CO<sub>2</sub> adsorbed at  $\sim 1$  bar. All of these results could provide the direct proof that the binding affinity between CO<sub>2</sub> (or  $\cdot\text{OH}$ )

and the Lewis acidic metals was reduced at elevated temperatures, thus expediting CO<sub>2</sub> (or  $\cdot\text{OH}$ ) release from the Lewis acidic Fe<sup>2+</sup>/Mn<sup>2+</sup>/Mn<sup>3+</sup> sites at the higher temperature domain.

It was anticipated that the catalysts conformed to Arrhenius behavior. We thus carried out phenol degradation runs under the conditions identical to those used to perform electric potential–assisted phenol degradation runs at 3 V except that the temperatures were varied from 25 ° C to 35 ° C, 45 ° C, or 55 ° C. Apparently, the increase in the temperatures could favor the liberation of  $\cdot\text{OH}$  from the Lewis acidic sites and subsequently improve the  $-\tau_{\text{PHENOL},0}$  values for the catalysts. The  $k_{\text{APP}}$  values of the catalysts at 25–55 ° C were then utilized to construct the Arrhenius plots of  $\ln k_{\text{APP}}$  versus (1/T) (T: temperature) to extract the pre-factors ( $k_{\text{APP},0}$ ) and energy barriers ( $E_{\text{BARRIER}}$ ) of the catalysts for the  $\cdot\text{OH} \rightarrow \text{SO}_4^{\cdot-}$  pathway, as shown in Figure 3–5C. In addition, the surface area per CO-accessible Lewis acidic site innate to Mn<sub>0</sub>, Mn<sub>1.5</sub>, or Mn<sub>3</sub> (m<sup>2</sup><sub>CO</sub> mol<sub>CO</sub><sup>–1</sup>; denoted as S<sub>CO</sub>) was determined by dividing the CO-accessible BET surface area of the catalyst (m<sup>2</sup><sub>CO</sub> g<sub>CAT</sub><sup>–1</sup>) by the amount of CO adsorbed at ~1 bar and –15 ° C (mol<sub>CO</sub> g<sub>CAT</sub><sup>–1</sup>). The S<sub>CO</sub> values of the catalysts increased considerably when Mn<sub>0</sub> was used (~3.8 X10<sup>5</sup> m<sup>2</sup><sub>CO</sub> mol<sub>CO</sub><sup>–1</sup> for Mn<sub>0</sub>; ~0.7 X10<sup>5</sup> m<sup>2</sup><sub>CO</sub> mol<sub>CO</sub><sup>–1</sup> for the others). This suggested that the Lewis acidic sites included in Mn<sub>0</sub> had a greater chance to interact with H<sub>2</sub>O<sub>2</sub> per unit time than the other catalysts. The trend of the S<sub>CO</sub> values for the catalysts were in partial agreement with the trend of their  $k_{\text{APP},0}$  values, whose magnitudes were ~2.2 X 10<sup>3</sup> min<sup>–1</sup>, ~0.8 X 10<sup>3</sup> min<sup>–1</sup>, and ~0.4 X 10<sup>3</sup> min<sup>–1</sup> for Mn<sub>0</sub>, Mn<sub>1.5</sub>, and Mn<sub>3</sub>, respectively.

Notably, Mn<sub>1.5</sub> provided the second largest values of the surface S/(Fe+Mn) and surface SO<sub>4</sub><sup>2–</sup> concentrations among the Mn<sub>0</sub>, Mn<sub>1.5</sub>, and Mn<sub>3</sub> catalysts (Figure 3–4A). Therefore, the chance of SO<sub>4</sub><sup>2–</sup> innate to Mn<sub>1.5</sub> colliding with  $\cdot\text{OH}$  per unit time might likely be moderate; thus, it could partially contribute to providing the second greatest pre-factor for Mn<sub>1.5</sub>. Meanwhile, the  $E_{\text{BARRIER}}$  values of the catalysts increased in the following order of Mn<sub>1.5</sub> → Mn<sub>0</sub> →

Mn<sub>3</sub>, which demonstrated that bimetallic, equimolar Mn–Fe oxo–spinel required the smallest energy for the liberation of  $\cdot\text{OH}$  species from its Lewis acidic sites. Mn<sub>1.5</sub> did provide the second largest  $k_{\text{APP},0}$  value and the smallest  $E_{\text{BARRIER}}$  value among the catalysts, which corroborated that Mn<sub>1.5</sub> possessed the Lewis acidic sites most conducive to prompt  $\cdot\text{OH} \rightarrow \text{SO}_4^{\cdot-}$  by furthering  $\cdot\text{OH}$  desorption. The amounts of  $\cdot\text{OH}$  species required to effectively radicalize the  $\text{SO}_4^{2-}$  functionalities on the surfaces were considered to present additional proof that Mn<sub>1.5</sub> is the optimized catalyst for the  $\cdot\text{OH} \rightarrow \text{SO}_4^{\cdot-}$  pathways. Hence, the averaged amounts of H<sub>2</sub>O<sub>2</sub> evolved during the H<sub>2</sub>O<sub>2</sub> production runs on the catalysts at 3 V were analyzed along with the H<sub>2</sub>O<sub>2</sub> conversions by the catalysts after an hour of H<sub>2</sub>O<sub>2</sub> scission runs at 3 V. Values of 3 V and an hour were chosen because they caused the largest differences in the  $N_{\text{H}_2\text{O}_2}$  and  $X_{\text{H}_2\text{O}_2}$  values for the catalysts under the reaction–limited domains utilized to extract their  $k_{\text{APP}}$  values. Noteworthy,  $\cdot\text{OH}$  was identified as the major product of H<sub>2</sub>O<sub>2</sub> scission on the surfaces (as opposed to  $\text{O}_2^{\cdot-}$  and  $\cdot\text{OOH}$ ), which was supported by a series of scavenging runs described in the sub–section of 3.3.4 below. This allowed for the presumption that the amounts of  $\cdot\text{OH}$  evolved after an hour of the phenol degradation runs on the catalysts ( $N_{\cdot\text{OH}, 1 \text{ hour}}$ ) was identical to the multiplication of the values of  $N_{\text{H}_2\text{O}_2, 3 \text{ V}}$  and  $X_{\text{H}_2\text{O}_2, 1 \text{ hour}}$ . The bulk sulfur contents of the catalysts used for the reaction (0.2 g of the catalysts;  $N_{\text{S}}$ ) could be then divided by their  $N_{\cdot\text{OH}, 1 \text{ hour}}$  values to determine the efficiencies of the catalysts in  $\cdot\text{OH} \rightarrow \text{SO}_4^{\cdot-}$  (denoted as  $\eta_{\text{RADICALIZATION}}$ ) under the assumption that  $N_{\text{S}}$  fully served to form the surface  $\text{SO}_4^{\cdot-}$  species. Mn<sub>1.5</sub> and Mn<sub>1</sub> provided the greatest  $\eta_{\text{RADICALIZATION}}$  value among the catalysts studied. In addition to the kinetic parameters most desired to proceed with the  $\cdot\text{OH} \rightarrow \text{SO}_4^{\cdot-}$  transfer (*i.e.*,  $E_{\text{BARRIER}}$  and  $k_{\text{APP},0}$ ), the  $\eta_{\text{RADICALIZATION}}$  value of Mn<sub>1.5</sub> apparently proved Mn<sub>1.5</sub> as the optimized catalyst for the  $\cdot\text{OH} \rightarrow \text{SO}_4^{\cdot-}$ .

### 3.3.4. Feasibility of $\cdot\text{OH} \rightarrow \text{SO}_4^{\cdot-}$

Detailed elaboration of  $\cdot\text{OH} \rightarrow \text{SO}_4^{\cdot-}$  on the catalyst surfaces, however, could only remain partially tangible, unless solid proofs were presented with regard to the evolution of  $\cdot\text{OH}$  and/or supported  $\text{SO}_4^{\cdot-}$  species and their functions in fragmenting phenol. It is widely accepted that  $\text{H}_2\text{O}_2$  can be heterolytically cleaved to produce  $\cdot\text{OH}/\text{OH}^-$  through the oxidation of  $\text{Mn}^{2+}/\text{Mn}^{3+}$  or  $\text{Fe}^{2+}$  species via  $e^-$  donation to  $\text{H}_2\text{O}_2$ , [9, 162] whereas  $\text{H}_2\text{O}_2$  is also prone to scission on the catalyst surfaces to generate  $\text{H}_2\text{O}$  and  $1/2\text{O}_2$ , as reported elsewhere. [163–165] Evidently, the reaction of ' $\text{H}_2\text{O}_2 \rightarrow \text{H}_2\text{O} + 1/2\text{O}_2$ ' is highly likely under the reaction environments used in this study. This could be identified in terms of its feasibility with the use of scavengers with distinct rates to quench  $\text{O}_2^{\cdot-}$  during the catalytic phenol degradation runs at 3 V. This suggestion was based on the properties of the  $\text{Mn}^{2+}/\text{Mn}^{3+}$  or  $\text{Fe}^{2+}$  species, both of which tend to donate  $e^-$  to  $\text{O}_2$  for the formation of  $\text{O}_2^{\cdot-}$  ( $\text{Mn}^{2+}/\text{Mn}^{3+} + \text{O}_2 \rightarrow \text{Mn}^{3+}/\text{Mn}^{4+} + \text{O}_2^{\cdot-}$ ;  $\text{Fe}^{2+} + \text{O}_2 \rightarrow \text{Fe}^{3+} + \text{O}_2^{\cdot-}$ ). [9, 162–165] If the production of  $\text{O}_2$  via catalytic  $\text{H}_2\text{O}_2$  scission were phenomenal during the reactions, the quantity of  $\text{O}_2^{\cdot-}$  evolved by the reduction of  $\text{O}_2$  ( $e^-$  acceptance from  $\text{Mn}^{2+}/\text{Mn}^{3+}$  or  $\text{Fe}^{2+}$ ) could be significant. However, the resulting  $\text{O}_2^{\cdot-}$  produced during the reactions could be terminated by the scavengers, leading to a decline in the  $-\tau_{\text{PHENOL},0}$  values for the catalysts, whose magnitudes should be directed by the secondary rate constants of the scavengers in quenching  $\text{O}_2^{\cdot-}$  ( $k_{\text{O}_2, \cdot}$ ). Therefore, the control runs were performed following the identical protocols used to conduct the phenol degradation runs at 3 V with the exception that scavengers such as 1,4-benzoquinone or guaiacol were added to the reaction mixtures. Noteworthily, the amounts of the scavengers utilized for the reactions were twice the possible concentrations of  $\text{O}_2$  present in the reaction mixtures according to the postulates that the amount of  $\text{O}_2$  produced by  $\text{H}_2\text{O}_2$  scission obey the stoichiometry defined by  $\text{H}_2\text{O}_2 \rightarrow \text{H}_2\text{O} + 1/2\text{O}_2$  and that  $\text{O}_2$  dissolved in de-ionized  $\text{H}_2\text{O}$  ( $\sim 0.25 \text{ mmol L}^{-1}$ ) could also serve to generate  $\text{O}_2^{\cdot-}$  on the



$\text{Mn}^{2+}/\text{Mn}^{3+}$  or  $\text{Fe}^{2+}$  species. Meanwhile,  $\text{Mn}_3$  provided the comparable  $-r_{\text{PHENOL}, 0}$  values even with the change in the type of the scavengers utilized; thus it was excluded from the discussion on the scavenging runs. In contrast,  $\text{Mn}_0$  and  $\text{Mn}_{1.5}$  were chosen for the scavenging runs for the identical reasons stated above in conjunction with providing  $-r_{\text{PHENOL}, 0}$  (and  $k_{\text{APP}}$ ) values discernable one another when the type of the scavengers was altered (Figure 3-6A and 3-6C). The catalysts showed the considerable decrease in their  $-r_{\text{PHENOL}, 0}$  values upon the addition of the scavengers because of the quenching of  $\text{O}_2^{\cdot-}$  and/or  $\cdot\text{OH}$ . However, phenol degradation did not halt in the presence of the scavengers tentatively due to the continuous evolution of  $\text{H}_2\text{O}_2$  (precursor of  $\cdot\text{OH}$  or  $\text{O}_2^{\cdot-}$ ) on/near the cathode under electric environments, as discussed above.[118, 119] However, the catalysts declined their  $-r_{\text{PHENOL}, 0}$  values in the following order of ‘without scavenger  $\rightarrow$  1,4-benzoquinone  $\rightarrow$  guaiacol’ (Figure 3-6E). It should be stressed that the trend found in the  $-r_{\text{PHENOL}, 0}$  values for the catalysts was con-current to the increasing trend of the secondary rate constants for the scavengers in terminating  $\cdot\text{OH}$  ( $k_{\cdot\text{OH}}$ ) rather than the trend of their  $k_{\text{O}_2\cdot-}$  values ( $k_{\cdot\text{OH}}$  of  $1.0 \times 10^9 \text{ M}^{-1} \text{ sec}^{-1}$  for 1,4-benzoquinone and  $2.0 \times 10^{10} \text{ M}^{-1} \text{ sec}^{-1}$  for guaiacol;  $k_{\text{O}_2\cdot-}$  of  $1.0 \times 10^9 \text{ M}^{-1} \text{ sec}^{-1}$  for 1,4-benzoquinone and  $2.5 \times 10^3 \text{ M}^{-1} \text{ sec}^{-1}$  for guaiacol).[47] Apparently, this corroborated that  $\text{H}_2\text{O}_2$  could be dissected on the  $\text{Mn}^{2+}/\text{Mn}^{3+}$  or  $\text{Fe}^{2+}$  species to form  $\cdot\text{OH}/\text{OH}^-$  and  $\text{O}_2/\text{H}_2\text{O}$  as the major and minor products, respectively.

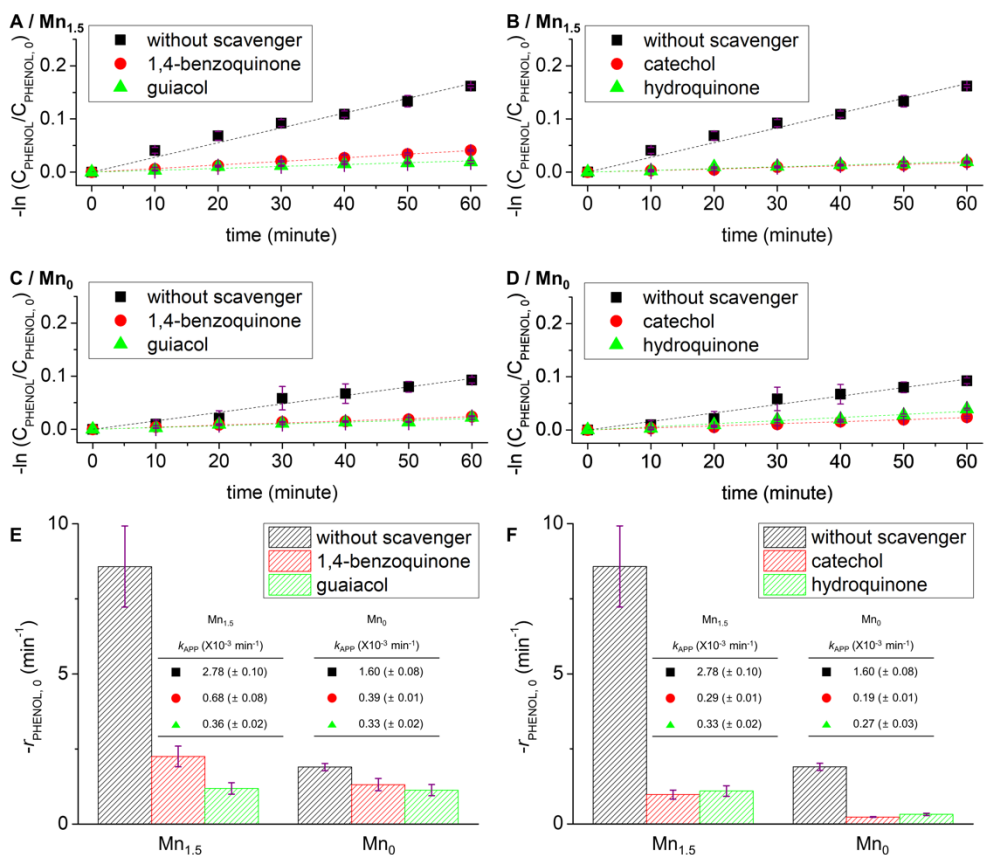


Figure 3-6. Fittings of the reaction data to the pseudo-1<sup>st</sup>-order kinetics model (regression factors of  $\geq 0.94$ ) for the determination of the apparent reaction rate constants ( $k_{\text{APP}}$ ) for Mn<sub>1.5</sub> (A and B) and Mn<sub>0</sub> (C and D) and their background-subtracted initial phenol consumption rates ( $-r_{\text{PHENOL}_0}$ ) in the absence or the presence of a scavenger (1,4-benzoquinone/guaiacol for (E); catechol/hydroquinone for (F)) at 3 V. In (E)–(F), the  $k_{\text{APP}}$  values of the catalysts are displayed in the inset tables with error bars. The reaction data was obtained from background-subtracted degradation profiles of phenol (phenol conversion ( $X_{\text{PHENOL}}$ ) versus time) for the catalysts without or with scavengers at 3 V.

It should be noted that the H<sub>2</sub>O<sub>2</sub> adsorbed on the catalyst surfaces might be oxidized to form H<sup>+</sup> and <sup>•</sup>OOH via e<sup>-</sup> transfer from H<sub>2</sub>O<sub>2</sub> to the Mn<sup>4+</sup> and/or Fe<sup>3+</sup> species, as reported previously by others (Mn<sup>4+</sup>/Fe<sup>3+</sup> + H<sub>2</sub>O<sub>2</sub> → Mn<sup>3+</sup>/Fe<sup>2+</sup> + H<sup>+</sup> + <sup>•</sup>OOH).[42, 166] To verify if <sup>•</sup>OOH was the main product of H<sub>2</sub>O<sub>2</sub> scission on the surfaces, additional scavenging runs on Mn<sub>1.5</sub> or Mn<sub>0</sub> were conducted under conditions identical to those discussed above except for utilizing catechol or hydroquinone with different secondary rate constants to terminate <sup>•</sup>OH and <sup>•</sup>OOH ( $k_{\text{OOH}}$ ). The amounts of scavengers used were

twice those of  $\text{H}_2\text{O}_2$  evolved on the catalysts coupled with their bulk sulfur contents according to the postulates that one mole of  $\text{H}_2\text{O}_2$  served to form two moles of  $\cdot\text{OH}$  or two moles of  $\cdot\text{OOH}$  and that bulk sulfur components served to anchor  $\text{SO}_4^{2-}$  functionalities on the surfaces. Again, the decrease in the  $-r_{\text{PHENOL}, 0}$  (and  $k_{\text{APP}}$ ) values on  $\text{Mn}_{1.5}$  and  $\text{Mn}_0$  was obvious when the scavengers were added to the reaction mixtures (Figure 3–6B and 3–6D), yet, were comparable even with the change in the kind of the scavengers (Figure 3–6F). This was not in alignment with the trend of the  $k_{\cdot\text{OOH}}$  values for the scavengers, which differ by three orders of magnitude ( $1.7 \times 10^7 \text{ M}^{-1} \text{ sec}^{-1}$  of hydroquinone;  $4.7 \times 10^4 \text{ M}^{-1} \text{ sec}^{-1}$  for catechol). Meanwhile, the  $-r_{\text{PHENOL}, 0}$  values in the presence of the scavengers conformed to their  $k_{\cdot\text{OH}}$  values, which are similar each other ( $5.2 \times 10^9 \text{ M}^{-1} \text{ sec}^{-1}$  of hydroquinone;  $1.1 \times 10^{10} \text{ M}^{-1} \text{ sec}^{-1}$  for catechol). All the results of the scavenging runs provided evidence that  $\text{H}_2\text{O}_2$  scission on the catalysts afforded  $\cdot\text{OH}$  as the major product rather than  $\text{O}_2^{\cdot-}$  or  $\cdot\text{OOH}$ .

Additional control runs were carried out using the reaction mixtures that only comprised  $\text{Mn}_x$ ,  $\text{H}_2\text{O}_2$ , and de-ionized  $\text{H}_2\text{O}$ , while utilizing DMPO ( $\text{C}_6\text{H}_{11}\text{NO}$ ) as a spin trapper of  $\cdot\text{OH}$  and  $\text{SO}_4^{\cdot-}$ . [101, 103, 140, 141] EPR spectroscopy was then utilized to confirm the presence of  $\cdot\text{OH}$  and supported  $\text{SO}_4^{\cdot-}$  species in the reaction mixtures (solid (catalyst) + liquid) or reaction solutions (liquid) for the catalysts except for  $\text{Mn}_3$  because of its vigorous, uncontrollable reaction with an excess amount of  $\text{H}_2\text{O}_2$  (Figure 3–7). The EPR spectra of the reaction mixtures were featured by large quartet signals with intensity ratios of 1:2:2:1 and the hyperfine splitting constants of  $a(^{14}\text{N}) = a(^1\text{H}) = \sim 14.8 \text{ G}$ . [101] This indicated that  $\cdot\text{OH}$  species adducted by DMPO to form DMPO–OH were present in the reaction mixtures. In addition, DMPO–OH was oxidized by  $\cdot\text{OH}$  to form HDMPO–OH as a by-product, which also appeared in the EPR spectra of the reaction mixtures. [140, 141] Furthermore, the EPR spectra of the reaction mixtures also showed sextet signals with hyperfine splitting constants of  $a(^{14}\text{N}) = \sim 13.8 \text{ G}$  and

$a(^1\text{H}) = \sim 9.5$  G. This validated that  $\text{SO}_4^{\bullet -}$  species adducted by DMPO to form  $\text{DMPO-SO}_4^-$  were also present in the reaction mixtures.[101]

Meanwhile, the three S-O bonds of the  $\text{SO}_4^{2-}$  functionalities were coordinated to the catalyst surfaces via *tri*-dentate configurations, which was again corroborated by their *in situ* DRIFT spectra under  $\text{SO}_2/\text{O}_2$  atmosphere, as discussed above (Figure 3-4C). This was also demonstrated by our previous computational works to demonstrate that  $\text{SO}_4^{2-}$  is of energetically favorable in ligating with  $\text{Fe}_2\text{O}_3$  and  $\text{NiO}$  surfaces via *tri*-dentate array.[25, 39] It was also likely that the supported  $\text{SO}_4^{2-}$  species were radicalized by  $\cdot\text{OH}$  to form supported  $\text{SO}_4^{\bullet -}$  analogues, whose free S-O bond was in turn bound to DMPO to form  $\text{DMPO-SO}_4^-$  anchored on the catalyst surfaces.[39] If these hypotheses held impeccably, the EPR spectra of the reaction solutions (not reaction mixtures) should only show the signals assigned to  $\text{DMPO-OH}$  or  $\text{HDMPO-OH}$ , whereas the signals assigned to  $\text{DMPO-SO}_4^-$  should be missing because  $\text{SO}_4^{\bullet -}$  precursors ( $\text{SO}_4^{2-}$ ) were bound to the catalyst surfaces. However, the EPR spectra of the reaction solutions for the catalysts showed  $\text{DMPO-OH}$ ,  $\text{HDMPO-OH}$ , and  $\text{DMPO-SO}_4^-$  (Figure 3-7). It should be noted that the simulated EPR spectra of  $\text{DMPO-OH}$ ,  $\text{HDMPO-OH}$ , and  $\text{DMPO-SO}_4^-$  [101-103, 140-143] were superimposed with the experimental EPR spectra, revealing good agreement, as shown in Figure 3-7. This could validate the accurate assignment of the signals observed in the EPR spectra. Importantly, this study aims to decompose phenol with the main use of the  $\text{SO}_4^{\bullet -}$  species supported on the catalyst surfaces. However, the results of the EPR experiments did pose the likelihood that unsupported  $\text{SO}_4^{\bullet -}$  or  $\cdot\text{OH}$  might roam in the reaction mixtures and contribute toward decomposing phenol.

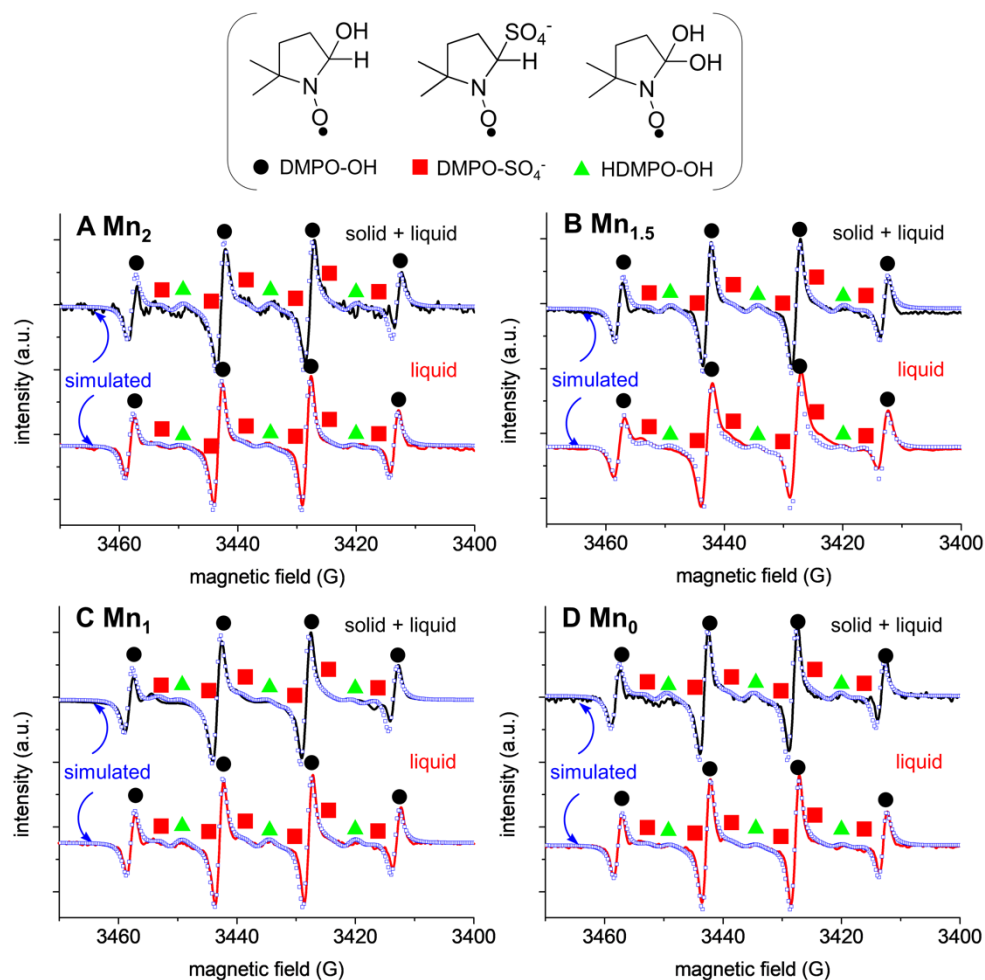


Figure 3-7. EPR spectra of intact reaction aliquots (solid (catalyst) + liquid; black lines) or reaction aliquots subjected to the filtration (liquid; red lines) for the catalyst: (A) Mn<sub>2</sub>, (B) Mn<sub>1.5</sub>, (C) Mn<sub>1</sub>, and (D) Mn<sub>0</sub>. Black circles, red squares, and green triangles denote DMPO-OH, DMPO-SO<sub>4</sub><sup>-</sup>, and HDMPO-OH adducts, respectively. Blue squares indicate simulated EPR spectra.

To elucidate the significance of phenol degradation by unsupported SO<sub>4</sub><sup>-</sup> species, we performed filtration runs, whose conditions were comparable to those utilized to conduct the electric potential-assisted phenol degradation runs at 3 V. Exceptions existed for these reactions such as the substitution of the catalyst-uncoated (bare) cathode for a catalyst-coated one together with vacuum filtration of the reaction mixtures after an hour of the reaction runs. The resulting reaction solutions were then immediately used to soak the bare anode and cathode and were further monitored in regard to the conversions

of phenol ( $X_{\text{PHENOL}}$ ) up to 8 hours (Figure 3–8). The blank run (without catalyst) could fragment phenol primarily via anodic oxidation and showed the  $X_{\text{PHENOL}}$  value of  $\sim 18.6 (\pm 2.2) \%$  at 1–8 hours of the reaction runs. Filtration runs in the presence of the catalysts showed such  $X_{\text{PHENOL}}$  values with magnitudes similar to that of the blank run during an identical period of the reaction runs (1–8 hours). This could provide solid evidence related to the insignificance of unsupported  $\text{SO}_4^{\cdot -}$  species in decomposing phenol, thereby leaving  $\cdot\text{OH}$  and supported  $\text{SO}_4^{\cdot -}$  species as tentative main sources utilized for fragmenting phenol.

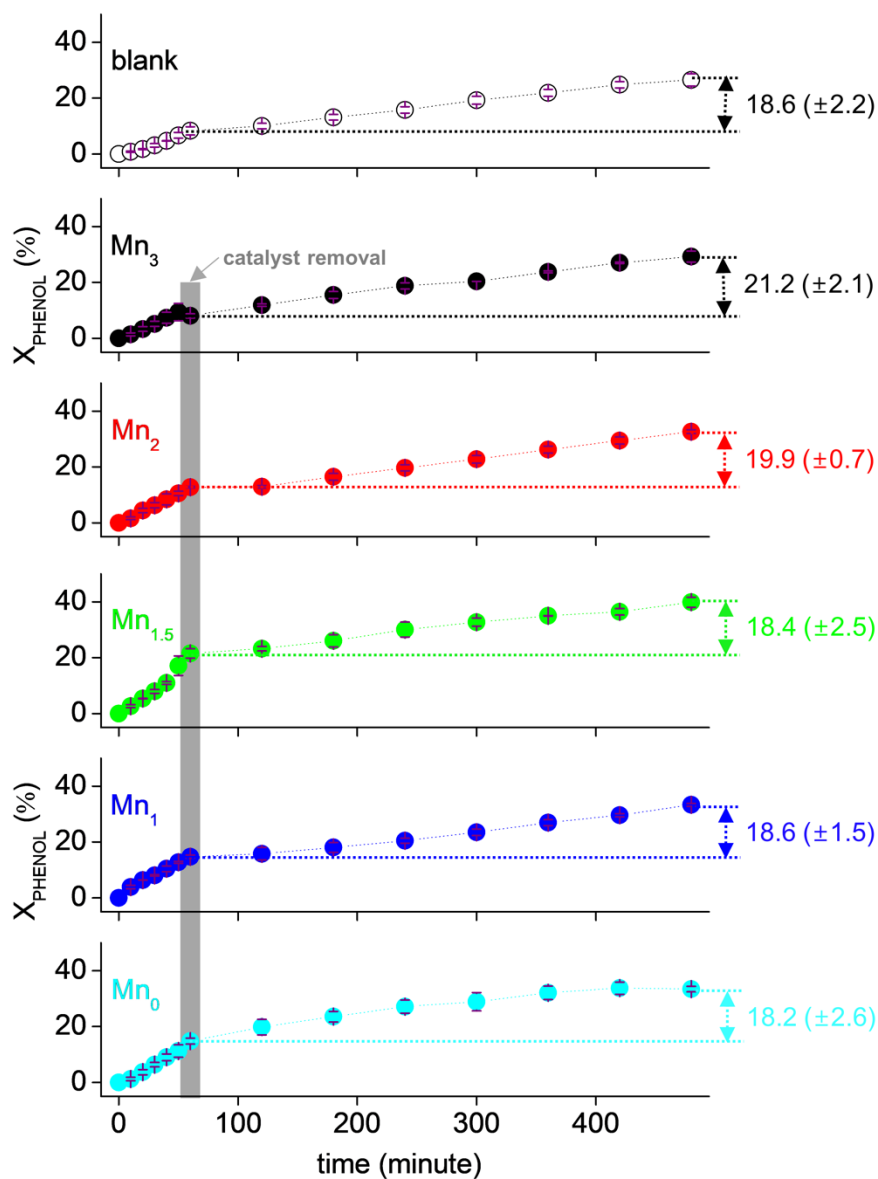


Figure 3–8. Degradation profiles of phenol (phenol conversion ( $X_{\text{PHENOL}}$ ) versus time) in the absence (blank) or the presence of the catalysts at 3 V. Cathodes coated with the catalyst were removed after an hour of the reaction runs (shown with a grey rectangle) and was exchanged with catalyst–uncoated analogues. Reaction conditions: 0.2 g of catalyst with diameters ( $d$ ) of  $< 50 \mu\text{m}$ ; 0.2 mol of  $\text{Na}_2\text{SO}_4$ ; 100 mL of de-ionized  $\text{H}_2\text{O}$ ; 0.1 mmol of phenol;  $25^\circ\text{C}$ ; and 300 rpm.

To compare the relative significance of  $\cdot\text{OH}$  and supported  $\text{SO}_4^{\cdot-}$  in decomposing phenol, scavenging runs were performed under such environments that were identical to those used to perform catalytic phenol degradation runs at 3 V except for mixing the reaction mixtures with

scavengers (Figure 3–9). *Tert*-butanol (TBA), 1, 4-dioxane, *iso*-propanol (IPA), and tetrahydrofuran (THF) served as scavengers because their secondary rate constants in terminating  $\cdot\text{OH}$  ( $k_{\cdot\text{OH}}$ ) and  $\text{SO}_4^{\cdot-}$  ( $k_{\text{SO}_4^{\cdot-}}$ ) are dissimilar to one another. Notably, the amounts of scavengers utilized for the scavenging runs were determined according to two major assumptions. One presumption was that one mole of  $\text{H}_2\text{O}_2$  was cleaved homolytically to provide two moles of  $\cdot\text{OH}$ , albeit the Lewis acidic site typically splits  $\text{H}_2\text{O}_2$  heterolytically. The second presumption was that the bulk sulfur components of the catalysts were exploited to form surface  $\text{SO}_4^{2-}$  functionalities. Of note,  $\text{Mn}_0$  and  $\text{Mn}_{1.5}$  were chosen for the scavenging runs for the identical reasons discussed above. Of additional note, we hypothesized that  $\text{Mn}_0$  and  $\text{Mn}_{1.5}$  could degrade phenol with the primary use of the supported  $\text{SO}_4^{\cdot-}$  species. For comparison,  $\text{Fe}_3\text{O}_4$  and  $\text{Mn}_{1.5}\text{Fe}_{1.5}\text{O}_4$  (precursors of  $\text{Mn}_0$  and  $\text{Mn}_{1.5}$  respectively) were also utilized as controls for the scavenging runs because these catalysts could fragment phenol with the main utilization of  $\cdot\text{OH}$  generated via catalytic  $\text{H}_2\text{O}_2$  scission on Lewis acidic metals.

In the case of  $\text{Mn}_{1.5}$  and  $\text{Mn}_{1.5}\text{Fe}_{1.5}\text{O}_4$  (Figure 3–9A, 3–9C, and 3–9E), the  $-r_{\text{PHENOL}, 0}$  values of  $\text{Mn}_{1.5}\text{Fe}_{1.5}\text{O}_4$  decreased in the following order of ‘without scavenger  $\rightarrow$  TBA  $\rightarrow$  IPA  $\rightarrow$  1,4-dioxane  $\rightarrow$  THF’, whose sequence was in exact line with the increasing trend of the  $k_{\cdot\text{OH}}$  values for the scavengers ( $3.8\text{--}7.6 \times 10^8 \text{ M}^{-1} \text{ sec}^{-1}$  for TBA;  $1.9 \times 10^9 \text{ M}^{-1} \text{ sec}^{-1}$  for IPA;  $3.1 \times 10^9 \text{ M}^{-1} \text{ sec}^{-1}$  for 1,4-dioxane;  $4.0 \times 10^9 \text{ M}^{-1} \text{ sec}^{-1}$  for THF). Meanwhile, the  $-r_{\text{PHENOL}, 0}$  values of  $\text{Mn}_{1.5}$  decreased in the following order of ‘without scavenger  $\rightarrow$  TBA  $\rightarrow$  1,4-dioxane  $\rightarrow$  IPA  $\rightarrow$  THF’, which was in accurate accordance with the increasing order of the  $k_{\text{SO}_4^{\cdot-}}$  values for the scavengers ( $4.0\text{--}9.1 \times 10^5 \text{ M}^{-1} \text{ sec}^{-1}$  for TBA;  $7.3 \times 10^7 \text{ M}^{-1} \text{ sec}^{-1}$  for 1,4-dioxane;  $8.2 \times 10^7 \text{ M}^{-1} \text{ sec}^{-1}$  for IPA;  $2.8 \times 10^8 \text{ M}^{-1} \text{ sec}^{-1}$  for THF). This strongly suggested that  $\text{Mn}_{1.5}$  and  $\text{Mn}_{1.5}\text{Fe}_{1.5}\text{O}_4$  could exploit supported  $\text{SO}_4^{\cdot-}$  and  $\cdot\text{OH}$  as the main decomposer of phenol, respectively.



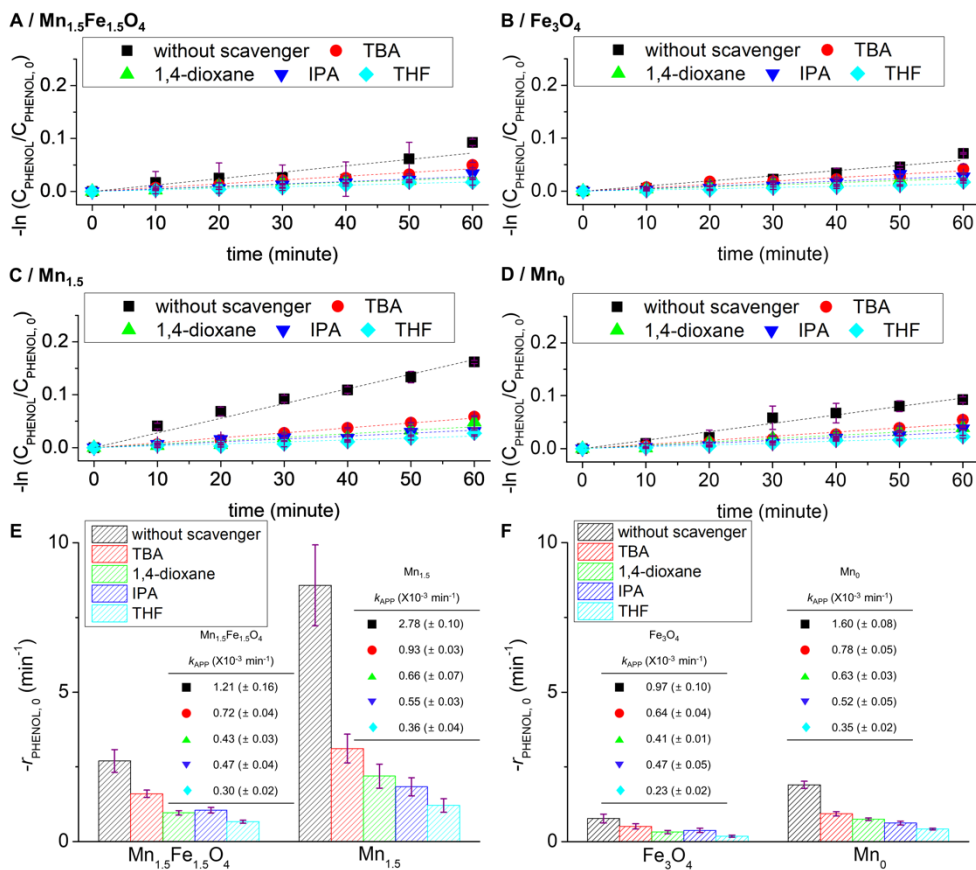


Figure 3-9. Fittings of the reaction data to the pseudo-1<sup>st</sup>-order kinetics model (regression factors of  $\geq 0.87$ ) for the determination of the apparent reaction rate constants ( $k_{\text{APP}}$ ) for  $\text{Mn}_{1.5}\text{Fe}_{1.5}\text{O}_4$  (A),  $\text{Fe}_3\text{O}_4$  (B),  $\text{Mn}_{1.5}$  (C), and  $\text{Mn}_0$  (D) and their background-subtracted initial phenol consumption rates ( $-r_{\text{PHENOL},0}$ ) in the absence or the presence of scavenger (TBA, 1,4-dioxane, IPA, or THF) at 3 V (E) and (F)). In (E)–(F), the  $k_{\text{APP}}$  values of the catalysts are displayed in the inset tables with error bars. The reaction data was obtained from background-subtracted degradation profiles of phenol (phenol conversion ( $X_{\text{PHENOL}}$ ) versus time) for the catalysts without or with scavengers at 3 V.

In addition, the amount of scavenger utilized during the scavenging runs on  $\text{Mn}_{1.5}$  (0.8 mmol) was approximately twice that of  $\text{Mn}_{1.5}\text{Fe}_{1.5}\text{O}_4$  (0.34 mmol). Nonetheless, the  $-r_{\text{PHENOL},0}$  values of  $\text{Mn}_{1.5}$  were consistently larger than those of  $\text{Mn}_{1.5}\text{Fe}_{1.5}\text{O}_4$  when using the identical scavengers (Figure 3-9E). If  $\text{Mn}_{1.5}$  deployed  $\cdot\text{OH}$  as the main source in fragmenting phenol, the  $-r_{\text{PHENOL},0}$  values of  $\text{Mn}_{1.5}$  should be similar to or even far smaller than those of  $\text{Mn}_{1.5}\text{Fe}_{1.5}\text{O}_4$  when exposed to the identical scavengers, which again was not the case for the  $-r_{\text{PHENOL},0}$  values of  $\text{Mn}_{1.5}$  and  $\text{Mn}_{1.5}\text{Fe}_{1.5}\text{O}_4$  in the presence of scavengers.

This again could corroborate the insignificance of  $\cdot\text{OH}$  in degrading phenol on  $\text{Mn}_{1.5}$ . Furthermore, the  $-r_{\text{PHENOL},0}$  values of  $\text{Mn}_{1.5}$  and  $\text{Mn}_{1.5}\text{Fe}_{1.5}\text{O}_4$  were differed by  $\leq \sim 7.4 \text{ min}^{-1}$  and  $\leq \sim 2.0 \text{ min}^{-1}$ , respectively, in the presence of scavengers (Figure 3-9E). This was in great alignment with the differences of the  $k_{\text{SO}_4^{\cdot-}}$  and  $k_{\cdot\text{OH}}$  values for the scavengers ( $\leq \sim 10^3 \text{ M}^{-1} \text{ sec}^{-1}$  for  $k_{\text{SO}_4^{\cdot-}}$ ;  $\leq \sim 10 \text{ M}^{-1} \text{ sec}^{-1}$  for  $k_{\cdot\text{OH}}$ ). The trends of the  $-r_{\text{PHENOL},0}$  values for  $\text{Mn}_0$  and  $\text{Fe}_3\text{O}_4$  in the presence of scavengers were identical to those found in the scavenging runs on  $\text{Mn}_{1.5}$  and  $\text{Mn}_{1.5}\text{Fe}_{1.5}\text{O}_4$ , as shown in Figure 3-9B, 3-9D, and 3-9F. All of these results could prove the statement that the  $\text{SO}_4^{2-}$ -modified  $\text{Mn}_x$  catalysts do accelerate the  $\cdot\text{OH} \rightarrow \text{SO}_4^{\cdot-}$  and deploy supported  $\text{SO}_4^{\cdot-}$  as the prime agent in the degradation of phenol.

### 3.3.5. Practicability of $\cdot\text{OH} \rightarrow \text{SO}_4^{\cdot-}$

The investigations on the phenol degradation efficiencies of the catalysts per Lewis acidic site was central to deeply understand the vitalness of the supported  $\text{SO}_4^{\cdot-}$  and  $\cdot\text{OH} \rightarrow \text{SO}_4^{\cdot-}$  kinetics. However, the catalysts were not studied in terms of their practical applicability, wherein the phenol degradation efficiencies of the catalysts per mass basis could be greatly informative. Hence,  $\text{Mn}_0$ ,  $\text{Mn}_{1.5}$ , and  $\text{Mn}_3$  were exposed to phenol degradation environments at 3 V multiple times, throughout which the catalysts coated on the cathode were rinsed solely with de-ionized  $\text{H}_2\text{O}$  only and dried at  $110^\circ \text{C}$  prior to conducting the next recycle runs. The number of moles of phenol consumed per unit time per gram of the catalysts (denoted as  $-r'_{\text{PHENOL},0}$ ) were calculated with background corrections during each of the recycle runs in order to contrast their reusability in phenol degradation (Figure 3-10A). All the catalysts exhibited a decrease in their  $-r'_{\text{PHENOL},0}$  values throughout each of the recycle runs. However,  $\text{Mn}_3$  provided minute  $-r'_{\text{PHENOL},0}$  values of  $\leq 0.1 \mu\text{mol}_{\text{PHENOL}} \text{g}_{\text{CAT}}^{-1} \text{min}^{-1}$  up to the 4<sup>th</sup> cycle and terminate its lifetime as a phenol decomposer from the 5<sup>th</sup> cycle, as evidenced by its  $-r'_{\text{PHENOL},0}$  values of  $\sim 0 \mu\text{mol}_{\text{PHENOL}} \text{g}_{\text{CAT}}^{-1} \text{min}^{-1}$ . This could have resulted from

the severe leaching of the  $\cdot\text{OH}$  producers ( $\text{Mn}^{2+}/\text{Mn}^{3+}$ ) innate to  $\text{Mn}_3$  throughout the recycle runs (0.11–0.18 mol.%). In addition,  $\text{Mn}_0$  showed such  $-r'_{\text{PHENOL}, 0}$  values that were approximately half of those observed for  $\text{Mn}_{1.5}$  up to the 2<sup>nd</sup> cycle, which further plummeted from the 3<sup>rd</sup> cycle, and were one tenth of the  $-r'_{\text{PHENOL}, 0}$  value for  $\text{Mn}_{1.5}$  at the 5<sup>th</sup> cycle. This was likely due to the leaching of  $\text{Fe}^{2+}$  components ( $\cdot\text{OH}$  producer) during the recycle runs, where the amounts of Fe leached from  $\text{Mn}_0$  were larger than those of Fe/Mn released from  $\text{Mn}_{1.5}$  up to the 2<sup>nd</sup> run (0.08–0.11 mol.% for  $\text{Mn}_0$ ; 0.05–0.06 mol.% for  $\text{Mn}_{1.5}$ ), thus hindering the occurrence of  $\cdot\text{OH} \rightarrow \text{SO}_4^{\cdot-}$  on the  $\text{Mn}_0$  surface. Meanwhile, although the  $\text{Mn}_{1.5}$  surface leached the smallest quantities of  $\cdot\text{OH}$  producers ( $\text{Mn}^{2+}/\text{Mn}^{3+}/\text{Fe}^{2+}$ ) among the catalysts up to the 2<sup>nd</sup> cycle,  $\text{Mn}_{1.5}$  showed moderate leaching of the metals, which was comparable to those of  $\text{Mn}_0$  during the remaining cycles ( $\leq 0.05$  mol.%). This was likely caused by the inclusion of Mn species in the  $\text{Mn}_{1.5}$  architecture, whose Mn components were less tolerant against the leaching during the recycle runs in comparison with the Fe counterparts. This was supported by the continuous decrease in the bulk molar ratios of Mn to Fe innate to  $\text{Mn}_{1.5}$  during the recycle runs (Mn/Fe of 0.92  $\rightarrow$  0.79 via XRF), which was in good agreement with the surface concentration ratios of Mn to Fe species inherent to  $\text{Mn}_{1.5}$  (Mn/Fe of 1.01  $\rightarrow$  0.89 via XP spectroscopy). The liberation of Mn species from  $\text{Mn}_{1.5}$  during the recycle runs also led to the evolution of the sulfur element, as evidenced by the XRD patterns of the used  $\text{Mn}_{1.5}$  catalysts showing bulk facets indexed to those of *monoclinic* sulfur (Figure 3–11F). Nonetheless, the surfaces of the used  $\text{Mn}_{1.5}$  catalysts exhibited diffractions that were indexed to those of  $\text{Mn}_{1.5}\text{Fe}_{1.5}\text{O}_4$  rather than those of elemental sulfur (Figure 3–11A to 3–11E). This suggested that  $\text{Mn}_{1.5}$  can retain a catalytic phase that promotes the production of the  $\cdot\text{OH}$  species used for sustaining the  $\cdot\text{OH} \rightarrow \text{SO}_4^{\cdot-}$  pathway on the surface scale. This allowed for the recyclable utilization of  $\text{Mn}_{1.5}$ , albeit  $\text{Mn}_{1.5}$  showed a moderate decrease in the  $-r'_{\text{PHENOL}, 0}$  values throughout each of the recycle runs (Figure 3–10A). Again,

the results of the recycle runs provided evidence associated with the appreciable recyclability of Mn<sub>1.5</sub> in fragmenting phenol.

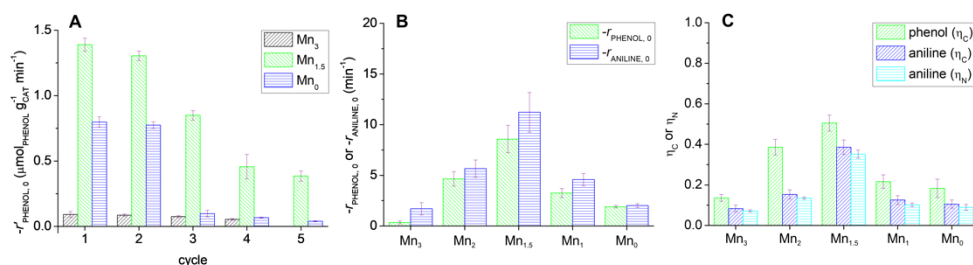


**Figure 3-10.** (A) Background-subtracted initial phenol degradation rates ( $-r_{\text{PHENOL},0}$ ) of the catalysts obtained through recycle runs at 3 V. (B) Background-subtracted initial degradation rates of phenol/aniline ( $-r_{\text{PHENOL},0}/-r_{\text{ANILINE},0}$ ) for the catalysts at 3 V. (C) Mineralization efficiencies (selectivities to CO<sub>A</sub> ( $\eta_{\text{C}}$ ; A=1 or 2) or NO<sub>A</sub>/N<sub>2</sub>O ( $\eta_{\text{N}}$ )) for the catalysts obtained after 8 hours of the reaction runs in the absence of an electric potential. Reaction conditions of (C): 0.2 g of catalyst with diameters ( $d$ ) of  $< 50 \mu\text{m}$ ; 0.2 mol of Na<sub>2</sub>SO<sub>4</sub>; 100 mL of de-ionized H<sub>2</sub>O; 0.1 mmol of phenol/aniline; 30 mmol of H<sub>2</sub>O<sub>2</sub>; 25 °C; and 300 rpm.

Aniline then served as a model compound to represent NH<sub>2</sub>-functionalized aromatic contaminants and therefore was exposed to degradation environments.[156, 157] Experimental conditions were comparable to those utilized to degrade phenol in the presence of the catalysts at 3 V, whereas their initial aniline degradation rates ( $-r_{\text{ANILINE},0}$ ) were calculated using the method analogous to that of  $-r_{\text{PHENOL},0}$ . [24, 39, 47] The degradation of phenol (C<sub>6</sub>H<sub>5</sub>-OH) and aniline (C<sub>6</sub>H<sub>5</sub>-NH<sub>2</sub>) by the supported SO<sub>4</sub><sup>•-</sup> species might be initiated by ring opening and -NH<sub>2</sub> oxidation to populate -OH and ring fragments in the reaction mixtures, respectively. This was postulated based on the literature resources to deal with the clarify the <sup>•</sup>OH-mediated degradation pathways of phenol/aniline.[100, 167, 168] Meanwhile, supported SO<sub>4</sub><sup>•-</sup> might preferentially oxidize -NH<sub>2</sub> rather than attack the ring due possibly to the energetic favor achieved during -NH<sub>2</sub> oxidation in comparison with ring oxidation, as reported in the literatures.[100, 167, 168] However, this was in partial line with the  $-r_{\text{ANILINE},0}$  values of the catalysts, which were similar to or slightly larger than the  $-r_{\text{PHENOL},0}$  values (Figure 3-

10B). This suggested that the affinity of Lewis acidic metals to the  $-OH$  or  $-NH_2$  groups of phenol or aniline respectively, might rely on the type of the catalysts employed. Nevertheless,  $Mn_{1.5}$  provided the largest  $-r_{ANILINE, 0}$  value among the studied catalysts, which demonstrated the adaptability of  $Mn_{1.5}$  in decomposing refractory contaminants.

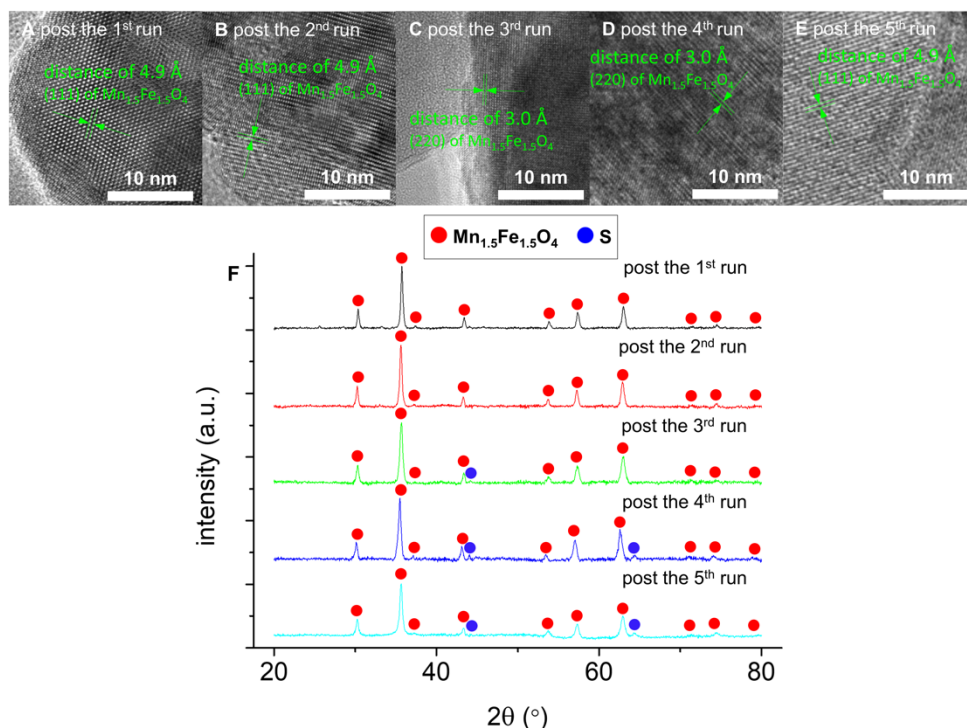


**Figure 3–11.** HRTEM images of the used  $Mn_{1.5}$  catalysts ((A) post the 1<sup>st</sup> run; (B) post the 2<sup>nd</sup> run; (C) post the 3<sup>rd</sup> run; (D) post the 4<sup>th</sup> run; and (E) post the 5<sup>th</sup> run) and their XRD patterns (F). In (A)–(E), the distances of the lattice fringes for the used  $Mn_{1.5}$  catalysts were measured and assigned to the surface facets of  $Mn_{1.5}Fe_{1.5}O_4$  (JCPDF No. of 01–075–0034). See the contents marked in green. In (F), the solid red and blue circles indicate the diffractions indexed to those of  $Mn_{1.5}Fe_{1.5}O_4$  and sulfur (JCPDF No. of 01–074–2106), respectively.

The organic components of phenol and aniline that remained after experiencing  $\cdot\text{OH} \rightarrow \text{SO}_4^{\cdot-}$  for a certain amount of time were finally assessed via TOC (for phenol/aniline) and TN (for aniline) techniques.[47] For this investigation, the catalysts were exposed to ambient, electric potential-free conditions, most of which were identical to those used for degrading aniline at 3 V, whereas 30 mmol of  $\cdot\text{OH}$  precursor ( $\text{H}_2\text{O}_2$ ) was vigorously mixed with the catalysts vigorously. Notably, the electrodes were inadequate because carbon species were leached from the electrodes in the presence of  $\text{H}_2\text{O}_2$ , possibly resulting from their erosion by  $\text{O}_\alpha$  oxidation (anodic oxidation).[47] The two backgrounds, namely, the adsorption of phenol/aniline on the catalyst surfaces and the oxidation of phenol/aniline by  $\text{H}_2\text{O}_2$  (not  $\cdot\text{OH}$ ) were not negligible and were therefore used to correct the reaction data. The conversions (X) of phenol/aniline after 8 hours of the reaction runs on the catalysts were then assessed via HPLC and TOC/TN analysis to obtain ratios of  $X_{\text{CARBON, TOC}}$  to  $X_{\text{HPLC}}$  ( $\eta_C$ ) or ratios of  $X_{\text{NITROGEN, TN}}$  to  $X_{\text{HPLC}}$  ( $\eta_N$ ), each of which indicated the selectivities of the catalysts to  $\text{CO}_A$  ( $\eta_C$ ;  $A=1$  or  $2$ ) or  $\text{NO}_A/\text{N}_2\text{O}$  ( $\eta_N$ ) during the degradation of contaminants (*i.e.*, mineralization efficiencies in Figure 3–10C). The  $\eta_C$  values of the catalysts were larger for the decomposition of phenol than those for the degradation of aniline. This might be attributed to the degradation pathway of aniline, which was more complicated and lengthier than that of phenol, as reported elsewhere.[100, 167, 168] Nonetheless,  $\text{Mn}_{1.5}$  revealed the greatest  $\eta_C$  and  $\eta_N$  values among the studied catalysts, which again could corroborate the superiority of  $\text{Mn}_{1.5}$  over the other catalysts in its adaptability and practical degradation of recalcitrant pollutants.

### 3.4. Conclusions

This study has pioneered the use of bimetallic oxo-spinel  $\text{Mn}_x\text{Fe}_{3-x}\text{O}_4$  as a striking reservoir of Lewis acidic metals and  $\text{SO}_4^{2-}$  species acting as  $\cdot\text{OH}$  producers and surface  $\text{SO}_4^{\cdot-}$  precursors in prompting the  $\cdot\text{OH} \rightarrow \text{SO}_4^{\cdot-}$  pathway. The  $\text{Mn}_x\text{Fe}_{3-x}\text{O}_4$  materials were chosen based on a host of rationales and exposed to thermal gas media including  $\text{SO}_2/\text{O}_2$  to anchor  $\text{SO}_4^{2-}$  functionalities on the surfaces. The composition of the metals innate to the resulting  $\text{Mn}_x$  catalysts ( $x$  of 0–3) was verified as the prime descriptor to regulate the Lewis acidic strengths ( $-\text{Q}_{\text{ST}}$ ) of the metals and the surface  $\text{SO}_4^{2-}$  concentrations desired for the  $\cdot\text{OH} \rightarrow \text{SO}_4^{\cdot-}$  route. The catalysts revealed a concave trend in the Lewis acidic strength of the metals versus the  $x$  of  $\text{Mn}_x$  with the minimum located at an equimolar metal composition ( $x \sim 1.5$ ). This was corroborated by the results of the  $\text{CO}/\text{CO}_2$  isotherm experiments and suggested that  $\text{Mn}_{1.5}$  could lower the energy required to dismantle  $\cdot\text{OH}$  from the surface, thus prompting the rate-determining stage ( $\cdot\text{OH}$  desorption) of the  $\cdot\text{OH} \rightarrow \text{SO}_4^{\cdot-}$ . In addition, the catalysts exhibited a volcano-shaped trend in the plot of  $\text{SO}_4^{2-}$  concentration versus  $x$  of  $\text{Mn}_x$  with the maximum placed at  $x \sim 1.5$  (except for  $\text{Mn}_3$ ). This suggested that  $\text{Mn}_{1.5}$  could provide the surface  $\text{SO}_4^{2-}$  species with a greater probability to interact with  $\cdot\text{OH}$  per unit time in comparison with the other catalysts. Therefore,  $\text{Mn}_{1.5}$  improved the productivity of the supported  $\text{SO}_4^{\cdot-}$  species used for degrading aqueous refractory aromatics.

The efficiencies of the  $\cdot\text{OH} \rightarrow \text{SO}_4^{\cdot-}$  cycles for the catalysts were then tested by performing the control runs utilized to decompose aqueous phenol in the presence of an electric potentials. Indeed, the catalysts did accelerate the  $\cdot\text{OH} \rightarrow \text{SO}_4^{\cdot-}$  pathway, as evidenced by their EPR spectra demonstrating the presence of  $\cdot\text{OH}$  and  $\text{SO}_4^{\cdot-}$  under aqueous environments analogous to those of the reaction runs. The role of supported  $\text{SO}_4^{\cdot-}$  as the primary decomposer of phenol was also substantiated by the filtration runs or scavenging runs, each of which could substantiate the insignificance of unsupported  $\text{SO}_4^{\cdot-}$  or

$\cdot\text{OH}$  in degrading phenol. Of note, the kinetics of the  $\cdot\text{OH} \rightarrow \text{SO}_4\cdot^-$  on the catalysts were also assessed via control runs to provide compelling proof that  $\cdot\text{OH}$  release from the surfaces is the rate-determining step. In addition,  $\text{Mn}_{1.5}$  provided the smallest energy barrier in desorbing  $\cdot\text{OH}$  and the second greatest collision frequency (pre-factor) between  $\text{H}_2\text{O}_2$  and the Lewis acidic metals or between  $\cdot\text{OH}$  and  $\text{SO}_4^{2-}$ , thus achieving the greatest initial phenol consumption rate ( $-r_{\text{PHENOL},0}$ ) among the catalysts. Of additional note, the  $-r_{\text{PHENOL},0}$  of  $\text{Mn}_{1.5}$  was  $\sim 20$  times larger than those of the  $\text{SO}_4^{2-}$ -functionalized  $\text{Fe}_2\text{O}_3$  and  $\text{NiO}$  catalysts, which we reported previously. Consequently,  $\text{Mn}_{1.5}$  could provide the greatest reusability, adaptability, and mineralization efficiency in degrading recalcitrant pollutants among all the catalysts we discovered so far.



## Chapter 4

# Deciphering evolution pathway of supported $\text{NO}_3^\cdot$ enabled via radical transfer from $^\cdot\text{OH}$ to surface $\text{NO}_3^-$ functionalized on $\text{MnO}_2$ for oxidative degradation of aqueous contaminants

The essence of Chapter 4 has been published in JACS Au. Reprinted with permission from [18].

### 4.1. Introduction

Radical-enabled oxidative fragmentation of aqueous electron ( $\text{e}^-$ )-rich moieties is primarily dictated by the radical's traits such as the lifespan (half-life,  $t_{1/2}$ ), electro-philicity (standard reduction potential,  $E_0$ ), and resistance to background radical scavengers present in  $\text{H}_2\text{O}$  matrices (*e.g.*,  $\text{HCO}_3^-$ ,  $\text{CO}_3^{2-}$ , and  $\text{Cl}^-$ , *etc.*). [109, 169] The  $^\cdot\text{OH}$  is deemed as an omnipotent radical and exploited owing to its large  $E_0$  value (2.7 V), yet, it is short-lived ( $t_{1/2}$  of  $< 1 \mu\text{second}$ ) and vulnerable to background scavengers, thereby revealing noticeable efficiencies in degrading contaminants only under a restricted pH span of 3–5. [111, 115, 170–172] Meanwhile,  $\text{SO}_4^{\cdot-}$  is comparable to  $^\cdot\text{OH}$  in terms of  $E_0$  (2.6 V), but is longer-lived ( $t_{1/2}$  of  $\sim 35 \mu\text{second}$ ), and shows a greater tolerance to quenching by backgrounds than  $^\cdot\text{OH}$  over a wide pH range. [111, 115] Thus,  $\text{SO}_4^{\cdot-}$  is garnered as an alternative to  $^\cdot\text{OH}$ . As an additional substitute for  $^\cdot\text{OH}$ ,  $\text{NO}_3^\cdot$  has gained attractions because of its  $E_0$  ( $\sim 2.4$  V) and  $t_{1/2}$  ( $\sim 60 \mu\text{second}$ ) values along with its lesser propensity to accept  $\text{e}^-$  from background scavengers in compared to  $^\cdot\text{OH}$  and  $\text{SO}_4^{\cdot-}$ . [111, 173]  $\text{NO}_2^\cdot$  was reported to react with ozone ( $\text{O}_3$ ) to evolve  $\text{NO}_3^\cdot$  in the absence of sunlight ( $\text{NO}_2^\cdot + \text{O}_3 \rightarrow \text{NO}_3^\cdot + \text{O}_2$ ), yet, exhibits a moderate secondary rate constant ( $k$ ) of  $2.1 \times 10^4 \text{ M}^{-1} \text{ sec}^{-1}$  and can be viable only after

the issues concerning low  $O_3$  solubility in an aqueous medium coupled with  $NO_2^\cdot$  isolation/transportation are resolved.[174] In contrast, aqueous  $NO_3^-$  can be converted to  $NO_3^\cdot$  via pulse radiolysis ( $NO_3^- \rightarrow NO_3^\cdot + e^-$ ), for which the  $e^-$  source should be highly accelerated up to a wavelength of  $\leq \sim 10^{-2}$  nm in the presence of a radio-active element (U and Pu).[175, 176] Alternatively, aqueous  $NO_3^-$  can be subjected to flash photolysis in the presence of a high-power light source (*e.g.*, excimer ( $h\nu$ ) with a wavelength ( $\lambda$ ) of  $\sim 200$  nm), leading to the generation of  $^\cdot OH$  via  $NO_3^- + H^+ + h\nu \rightarrow NO_2^\cdot + ^\cdot OH$ . [177, 178] In addition,  $^\cdot OH$  formation is enabled by heterolytic  $H_2O_2$  scission using a Lewis acidic  $d$ -block metal ion (liquid-phase  $M^{\delta+}$ ;  $M$ : metal;  $\delta$ : 2 or 3) or metal oxide (solid-phase  $M^{\delta+}$ ) as a catalyst, whose details are discussed below.[179] Notably, the resulting  $^\cdot OH$  produced via catalysis (or photolysis) can radicalize  $NO_3^-$  to produce  $NO_3^\cdot$  ( $NO_3^- + ^\cdot OH \rightarrow NO_3^\cdot + OH^-$ ;  $^\cdot OH \rightarrow NO_3^\cdot$ ) with a  $k$  of  $1.4 \times 10^8 \text{ M}^{-1} \text{ sec}^{-1}$  (or  $5.0 \times 10^5 \text{ M}^{-1} \text{ sec}^{-1}$ ) utilizing  $HNO_3$  (or  $NaNO_3$ ) as a  $NO_3^-$  shuttle.[180, 181] The use of  $HNO_3$ , however, drastically acidifies the aqueous medium to a pH of 0–1,[180, 181] thus tentatively resulting in severe leaching of  $M^{\delta+}$  species from the metal oxide. Moreover, the utilization of  $NaNO_3$  can release basic  $Na^+$  ions, which poison  $H_2O_2$  activators ( $M^{\delta+}$ ) via coordination.[59, 182] Thus,  $HNO_3$  (or  $NaNO_3$ ) can only incur a finite number of utilization for  $M^{\delta+}$  species ionized or embedded on metal oxides as  $H_2O_2$  scissors ( $^\cdot OH$  producer) for activating  $^\cdot OH \rightarrow NO_3^\cdot$ . Indeed, the  $^\cdot OH \rightarrow NO_3^\cdot$  route is barely deployed because of the grand demands on catalytic (or photolytic)  $^\cdot OH$  evolution.

Nonetheless,  $NO_3^-$  is photo-sensitive and thereby also functions as the precursors of  $NO_2^\cdot$  and  $NO^\cdot$ . [183] In general,  $NO_3^-$  is dissociated into  $NO_2^-$  ( $NO_3^- \rightarrow NO_2^- + 1/2O_2$ ) or transforms into  $NO_2^\cdot$  ( $NO_3^- \rightarrow NO_2^\cdot + O^{\cdot-}$ ) upon  $h\nu$  excitation ( $\lambda$  of  $< 250$  nm), while evolving  $^\cdot OH$  ( $O^{\cdot-} + H_2O \rightarrow ^\cdot OH + OH^-$ ). [183, 184] In turn,  $^\cdot OH$  acts as a  $NO_2^-$ -attacking radical to generate additional  $NO_2^\cdot$  via  $NO_2^- + ^\cdot OH \rightarrow NO_2^\cdot + OH^-$  ( $^\cdot OH \rightarrow NO_2^\cdot$ ) with a large  $k$  of  $1.0 \times 10^{10} \text{ M}^{-1} \text{ sec}^{-1}$ . [183] However,  $NO_2^\cdot$  possesses moderate  $E_0$

(1.0 V) and small  $t_{1/2}$  (1.4  $\mu$  second) values and therefore cannot be as efficient as  $\text{NO}_3^\cdot$  in degrading pollutants.[185, 186] Interestingly,  $\text{NO}_2^\cdot$  experiences further dissection into  $\text{O}^{\cdot-}$  and  $\text{NO}$ .[183] Despite having a long lifetime ( $t_{1/2}$  of  $10^7 \mu$  second),  $\text{NO}^\cdot$  is inactive in degrading contaminants ( $E_0$  of  $-0.4$  V).[187, 188] In addition,  $\text{NO}^\cdot$  functions as a  $^\cdot\text{OH}$  sink ( $\text{NO}^\cdot + ^\cdot\text{OH} \rightarrow \text{HNO}_2$ ),[183, 189] thereby reducing the probability associated with  $\text{NO}_2^\cdot$  production via  $^\cdot\text{OH} \rightarrow \text{NO}_2^\cdot$ . Apparently, the  $^\cdot\text{OH} \rightarrow \text{NO}_2^\cdot$  route is kinetically favorable, yet, imparts  $\text{NO}_2^\cdot$  with a moderate oxidizing power and is disruptive owing to the presence of  $\text{NO}^\cdot$  used to quench  $^\cdot\text{OH}$ .

Inspection of previous studies concerning  $\text{NO}_3^\cdot/\text{NO}_2^\cdot/\text{NO}^\cdot$  boosts the preferential usage of  $\text{NO}_3^\cdot$  as a pollutant degrader over the other two radicals and motivates us to envisage a novel route to readily form, sustain, and exploit aqueous  $\text{NO}_3^\cdot$  under circum-neutral pH and alkali metal-free environments. We previously envisioned a unique  $^\cdot\text{OH} \rightarrow$  supported  $\text{SO}_4^{\cdot-}$  ( $\text{SO}_4^{\cdot-}_{\text{SUP}}$ ) pathway under an  $e^-$ -abundant electric condition, for which  $\text{SO}_4^{2-}$  functionalities are anchored on  $d$ -block metal oxide surfaces (*e.g.*,  $\text{Fe}_2\text{O}_3$ ,  $\text{NiO}$ , and Fe-substituted  $\text{Mn}_3\text{O}_4$ ) to expedite  $\text{H}_2\text{O}_2$  scission and radical transfer from  $^\cdot\text{OH}$  to supported  $\text{SO}_4^{2-}$  ( $\text{SO}_4^{2-}_{\text{SUP}}$ ) via a series of elementary steps (Figure 4-1A and 4-1C).[25, 39, 107] Initially, a lone pair of electrons on  $\text{H}_2\text{O}_2$  binds with a Lewis acidic surface  $\text{M}^{\delta+}$  species ( $\text{Fe}^{2+}$ ,  $\text{Ni}^{2+}$ , or  $\text{Mn}^{2+/3+}$ ) to produce  $\text{M}^{\delta+} \cdots \text{H}_2\text{O}_2$  prior to heterolytic  $\text{H}_2\text{O}_2$  splitting to form surface  $\text{M}^{(\delta+1)+} \cdots ^\cdot\text{OH}$  and surface-unbound  $^\cdot\text{OH}$  (Figure 4-1A). [25, 39, 107]  $\text{M}^{(\delta+1)+} \cdots ^\cdot\text{OH}$  then desorbs  $^\cdot\text{OH}$ , by which  $\text{SO}_4^{\cdot-}$  productivity via the  $^\cdot\text{OH} \rightarrow \text{SO}_4^{\cdot-}_{\text{SUP}}$  route is directed. This indicates that the  $^\cdot\text{OH}$  desorption stage dominates the overall  $^\cdot\text{OH} \rightarrow \text{SO}_4^{\cdot-}_{\text{SUP}}$  route as the rate-determining step (red arrow in Figure 4-1A).[25, 39, 107] Finally, the  $\text{M}^{(\delta+1)+}$  on the surface is reduced to  $\text{M}^{\delta+}$  via  $e^-$  reduction for recycling the  $\text{H}_2\text{O}_2$  scission cycle.[25, 39, 107] Meanwhile, surface-unbound  $^\cdot\text{OH}$  migrates to and interacts with the  $\text{SO}_4^{2-}_{\text{SUP}}$  functionality and undergoes the transitions from  $\text{SO}_4^{2-} \cdots ^\cdot\text{OH}$  and  $\text{SO}_4^{\cdot-} \cdots \text{OH}^-$  to  $\text{SO}_4^{\cdot-}$  upon the release of  $\text{OH}^-$  to

the aqueous medium ( $\text{SO}_4^{2-}/\text{SO}_4^{\cdot-}$  in exchange for  $\text{NO}_3^-/\text{NO}_3^{\cdot}$  in Figure 4-1C).[25, 39, 107]  $\text{SO}_4^{\cdot-}_{\text{SUP}}$  can radicalize or destabilize the contaminant via  $e^-$  exchange prior to the recovery of  $\text{SO}_4^{2-}$  for reactivating radical interconversion of  $\cdot\text{OH} \leftrightarrow \text{SO}_4^{\cdot-}_{\text{SUP}}$ . [25, 39, 107] Of note,  $\cdot\text{OH} \rightarrow \text{SO}_4^{\cdot-}_{\text{SUP}}$  can be activated at a circum-neutral pH of 5.5–7.0 with the exclusion of  $\text{M}^{\delta+}$  poisons (alkali metals).[25, 39, 107] Of additional note,  $\text{SO}_4^{\cdot-}_{\text{SUP}}$  can outperform conventional  $\cdot\text{OH}$  in decomposing contaminant in an efficient/recyclable fashion.[25, 39, 107]

Herein, we postulated that  $\text{NO}_3^-$  functionalities can be grafted on a metal oxide in proximity to surface  $\text{M}^{\delta+}$  species, substitute for  $\text{SO}_4^{2-}$  functionalities, and do activate the  $\cdot\text{OH} \rightarrow$  supported  $\text{NO}_3^{\cdot}$  ( $\text{NO}_3^{\cdot}_{\text{SUP}}$ ) route (Figure 4-1C). It should be stressed that  $\text{H}_2\text{O}_2$  can be continuously generated and fed to the surface  $\text{M}^{\delta+}/\text{M}^{(\delta+1)+}$  species for  $\text{H}_2\text{O}_2$  scission/ $\text{M}^{\delta+}$  recovery in the presence of an electric potential.[25, 39, 107] Nonetheless, this study rules out the utilization of an electric environment and serves an excess amount of  $\text{H}_2\text{O}_2$  as the  $\cdot\text{OH}$  precursor to substantiate the tangibility of  $\cdot\text{OH} \rightarrow \text{NO}_3^{\cdot}_{\text{SUP}}$  by simplifying the reaction environments. Moreover, even with the absence of an abundant amount of  $e^-$  generated under an electric condition, surface  $\text{M}^{\delta+}$  species can be readily recovered via alternative pathways.[190, 191] For instance,  $\text{M}^{(\delta+1)+}$  is bound to  $\text{H}_2\text{O}_2$  to form  $\text{M}^{(\delta+1)+} \cdot \cdot \cdot \text{H}_2\text{O}_2$ , which in turn dissects  $\text{H}_2\text{O}_2$  via  $e^-$  donation from  $\text{H}_2\text{O}_2$  to  $\text{M}^{(\delta+1)+}$ , leading to the recovery of  $\text{M}^{\delta+}$  with the emission of a proton ( $\text{H}^+$ ) and  $\cdot\text{OOH}$  to the aqueous medium (Figure 4-1A).[190, 191] Moreover,  $\cdot\text{OOH}$  can be further cleaved to  $\text{H}^+$  and  $\text{O}_2^{\cdot-}$ . The  $\text{O}_2^{\cdot-}$  species is then coordinated to  $\text{M}^{(\delta+1)+}$  to form  $\text{M}^{(\delta+1)+} \cdot \cdot \cdot \text{O}_2^{\cdot-}$ , where  $e^-$  is transferred from  $\text{O}_2^{\cdot-}$  to  $\text{M}^{(\delta+1)+}$  to recover  $\text{M}^{\delta+}$  with the liberation of  $\text{O}_2$  (Figure 4-1A).[190, 191] Furthermore, in this part of the study,  $\text{H}_2\text{O}_2$  also served in this study to minimize the separation of  $\text{NO}_3^-$  species from the surface. This is because  $\text{NO}_3^-$  intrinsically possesses low binding affinity to the surface[192, 193] and thereby might be detached easily from the surface if the surface were heated by an electric energy. This

raises the need to select the metal oxide properly to afford a large amount of  $\text{NO}_3^-$  functionalities on its surface. Importantly, given the exothermic nature of  $\cdot\text{OH} \rightarrow \text{SO}_4^{\cdot-}{}_{\text{SUP}}$  or  $\cdot\text{OH} \rightarrow \text{NO}_3^{\cdot}{}_{\text{SUP}}$  in the aqueous medium,[25, 39, 107, 180, 181]  $\cdot\text{OH} \rightarrow \text{NO}_3^{\cdot}{}_{\text{SUP}}$  was presumed to be energetically favorable.

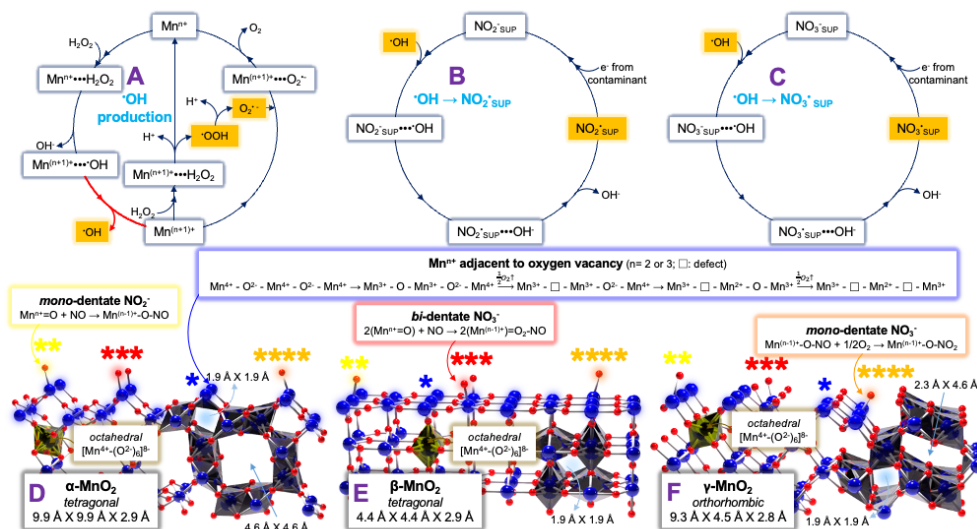


Figure 4-1. Schematic representation of (A)  $\text{H}_2\text{O}_2$  scission cycle on surface  $\text{Mn}^{n+}$  species ( $n= 2$  or  $3$ ) and radical transfer from surface-unbound  $\cdot\text{OH}$  to  $\text{NO}_2^-$  or  $\text{NO}_3^-$  species supported on  $\alpha\text{-}/\beta\text{-}/\gamma\text{-MnO}_2$  surfaces ( $\text{NO}_2^{\cdot}{}_{\text{SUP}}$  or  $\text{NO}_3^{\cdot}{}_{\text{SUP}}$ ), leading to the production of supported  $\text{NO}_2^{\cdot}$  ( $\text{NO}_2^{\cdot}{}_{\text{SUP}}$  in B) or  $\text{NO}_3^{\cdot}$  ( $\text{NO}_3^{\cdot}{}_{\text{SUP}}$  in C) utilized for degrading aqueous pollutants. Illustration of porous architectures for  $\alpha\text{-MnO}_2$  (D),  $\beta\text{-MnO}_2$  (E), and  $\gamma\text{-MnO}_2$  (F), whose surfaces afford  $\text{NO}_2^-$  or  $\text{NO}_3^-$  species with various binding configurations. In (D)–(F), \* denotes defective Mn species accessible to  $\text{H}_2\text{O}_2$ , whereas \*\*, \*\*\*, and \*\*\*\* indicate labile O species allowing for the formation of *mono*-dentate  $\text{NO}_2^-$ , *bi*-dentate  $\text{NO}_3^-$ , and *mono*-dentate  $\text{NO}_3^-$  on  $\alpha\text{-}/\beta\text{-}/\gamma\text{-MnO}_2$  surfaces.

Overall, the surface should favor  $\text{NO}_3^-$  adsorption, contain a large quantity of Lewis acidic  $\text{M}^{\delta+}$  species with the strengths desired to desorb  $\cdot\text{OH}$  to lower the energy barrier of the tentative rate-determining stage for  $\cdot\text{OH} \rightarrow \text{NO}_3^{\cdot}{}_{\text{SUP}}$ . Mn oxides are classified as one of reducible oxides with structural flexibility,[194, 195] by which  $\text{Mn}^{4+}$  (or  $\text{Mn}^{3+}$ ) readily accepts  $e^-$  from the adjacent  $\text{O}^{2-}$ , liberates oxygen, and transforms into defective, Lewis acidic  $\text{Mn}^{3+}$  (or  $\text{Mn}^{2+}$ ;  $\text{Mn}^{n+}$ ;  $n= 2$  or  $3$ ),[196] as highlighted with the blue box in Figure 4-1.  $\text{Mn}^{n+}$  can be in access to  $\text{H}_2\text{O}_2$  and cleave  $\text{H}_2\text{O}_2$  to evolve  $\cdot\text{OH}$ .

Meanwhile, a portion of  $\text{Mn}^{n+}$  species may act as anchoring spots of  $\text{NO}_Y^-$  ( $Y=2$  or  $3$ ) formed via chemical fusion of  $\text{NO}/\text{O}_2$  on or near the  $\text{Mn}^{n+}$  species, as reported previously.[197, 198] In addition, labile oxygens ( $\text{O}_\alpha$ ) bound to the surface  $\text{Mn}^{n+}$  species are also prone to bind with  $\text{NO}/\text{O}_2$  and generate  $\text{NO}_2^-/\text{NO}_3^-$  functionalities with a *mono*- or *bi*-dentate configuration along with the reductive transition of  $\text{Mn}^{n+}$  to  $\text{Mn}^{(n-1)+}$ .[199, 200] (See boxes highlighted in yellow/red/orange in Figure 4-1.) It should be noted that  $\text{NO}_2^-$  functionalities can be radicalized via  $\cdot\text{OH} \rightarrow \text{NO}_2^{\cdot}\text{_{SUP}}$  route (Figure 4-1B), yet, cannot be desirable in decomposing contaminants owing to the demerits of  $\text{NO}_2^{\cdot}$  stated above.[183, 185, 186, 201] Nevertheless, these can suggest the merits of Mn oxides in activating  $\cdot\text{OH} \rightarrow \text{NO}_3^{\cdot}\text{_{SUP}}$  and poses the necessity to select the Mn oxide suitable to disperse  $\text{Mn}^{n+}/\text{O}_\alpha$  species with the desired properties. Mn species are multi-valent in nature ( $\text{Mn}^{2+}/\text{Mn}^{3+}/\text{Mn}^{4+}$ ) and therefore offer a variety of architectures including  $\text{MnO}$ ,  $\text{Mn}_3\text{O}_4$ ,  $\text{Mn}_2\text{O}_3$ , and  $\text{MnO}_2$ . Among them,  $\text{MnO}_2$  was reported to provide the largest quantities of  $\text{O}_\alpha$  and/or  $\text{Mn}^{n+}$  species,[202, 203] and was thus chosen in this part of the study. Notably,  $\text{MnO}_2$  offers a series of polymorphs such as  $\alpha$ -/ $\beta$ -/ $\gamma$ -/ $\delta$ -/ $\varepsilon$ -/ $\lambda$ - $\text{MnO}_2$ , wherein  $\delta$ -/ $\varepsilon$ -/ $\lambda$ - $\text{MnO}_2$  are meta-stable under aqueous or ambient environments[204, 205] and thus, they are excluded in this study. The  $\alpha$ -/ $\beta$ - and  $\gamma$ - $\text{MnO}_2$  polymorphs are defined by crystal systems of *tetragonal* and *orthorhombic* crystal systems, respectively, across which *octahedral*  $[\text{Mn}^{4+}-(\text{O}^{2-})_6]^{8-}$  motifs could provide  $\text{H}_2\text{O}_2$ -inaccessible  $\text{Mn}^{4+}$  species only if  $\alpha$ -/ $\beta$ -/ $\gamma$ - $\text{MnO}_2$  were defect-free (Figure 4-1D to 4-1F). [202-205] However, poly-crystalline  $\alpha$ -/ $\beta$ -/ $\gamma$ - $\text{MnO}_2$  can be deformed to possess meso-porosities and ample  $\text{Mn}^{n+}/\text{O}_\alpha$  species,[206, 207] whose numbers and strengths are presumably distinct due to the difference in their cell edges, albeit with identical cell angle of  $90^\circ$ . Of interest,  $\alpha$ -/ $\beta$ -/ $\gamma$ - $\text{MnO}_2$  bear  $1.9 \text{ \AA} \times 1.9 \text{ \AA}$ -sized tunnels inaccessible to  $\text{H}_2\text{O}_2$ ,  $\text{NO}_2^-$ , and  $\text{NO}_3^-$  ( $2.3$ - $2.9 \text{ \AA}$  in Figure 4-1D to 4-1F).[202-207] Of interest, this holds true in  $\beta$ - $\text{MnO}_2$  with a single tunnel of  $1.9 \text{ \AA} \times 1.9 \text{ \AA}$ , yet, should be re-considered

in  $\alpha$ -/ $\gamma$ -MnO<sub>2</sub>. Both  $\alpha$ - and  $\gamma$ -MnO<sub>2</sub> provide additional tunnels with the sizes of 4.6 Å X 4.6 Å and 2.3 Å X 4.6 Å, respectively, into which H<sub>2</sub>O<sub>2</sub> and NO<sub>3</sub><sup>-</sup> can be diffused (Figure 4-1D to 4-1F).[202-207] It may be reasonable to conjecture that  $\alpha$ -MnO<sub>2</sub> has pores with the biggest size, which are the most amicable for H<sub>2</sub>O<sub>2</sub> and NO/O<sub>2</sub> to diffuse into the Mn<sup>n+</sup> and O <sub>$\alpha$</sub>  species present in the pores; thus, they may exhibit the highest efficiencies for the production of  $\cdot$ OH and NO<sub>3</sub> $\cdot$  among the  $\alpha$ -/ $\beta$ -/ $\gamma$ -MnO<sub>2</sub> polymorphs considered. The hypothesis stated above, however, could be valid only when the numbers/strengths of Mn<sup>n+</sup>/O <sub>$\alpha$</sub>  species were alike across  $\alpha$ -/ $\beta$ -/ $\gamma$ -MnO<sub>2</sub>. Of significance, this hypothesis could be coupled with the textural traits of  $\alpha$ -/ $\beta$ -/ $\gamma$ -MnO<sub>2</sub>, which regulation is challenging even after amending the synthetic methodologies. This highly suggests that NO<sub>3</sub> $\cdot$  productivities on NO<sub>3</sub><sup>-</sup>-functionalized  $\alpha$ -/ $\beta$ -/ $\gamma$ -MnO<sub>2</sub> should be tested under diffusion-free environments and compared in terms of site basis rather than gram or area basis for rigorous comparison.

Again, in order to compensate for the aforementioned demerits of unsupported  $\cdot$ OH/SO<sub>4</sub><sup>-</sup> $\cdot$ /NO $\cdot$ /NO<sub>2</sub> $\cdot$ /NO<sub>3</sub> $\cdot$  as a decomposer of pollutants, it is necessary to discover a unique yet easy way to produce and sustain NO<sub>3</sub> $\cdot$  species. This study first reports the viability and impact of  $\cdot$ OH  $\rightarrow$  NO<sub>3</sub> $\cdot$ <sub>SUP</sub> to generate NO<sub>3</sub> $\cdot$ <sub>SUP</sub> deployed for contaminants' degradation, for which  $\alpha$ -/ $\beta$ -/ $\gamma$ -MnO<sub>2</sub> serve as platforms to accommodate Mn<sup>n+</sup>/O <sub>$\alpha$</sub> . The  $\alpha$ -/ $\beta$ -/ $\gamma$ -MnO<sub>2</sub> polymorphs and their NO<sub>3</sub><sup>-</sup>-modified analogues were synthesized for comparison and subjected to spectroscopic analysis (EPR and XANES) and DFT calculations to simulate and corroborate the plausibility of H<sub>2</sub>O<sub>2</sub> splitting and  $\cdot$ OH  $\rightarrow$  NO<sub>3</sub> $\cdot$ <sub>SUP}. In addition, the catalysts were examined by degrading a model compound of aqueous pollutants (phenol) and/or textile wastewater. Furthermore, kinetics of  $\cdot$ OH  $\rightarrow$  NO<sub>3</sub> $\cdot$ <sub>SUP} on the catalysts were assessed to elaborate the significance of their geometric differences on the properties of Mn<sup>n+</sup>, NO<sub>3</sub><sup>-</sup>, and NO<sub>3</sub> $\cdot$  along with the extraction of the kinetic parameters.</sub></sub>

## 4.2. Experimental Section

### 4.2.1. Chemicals

All chemicals were delivered from the vendors and used without further purifications:  $\text{MnCl}_2 \cdot 4\text{H}_2\text{O}$  (Sigma-Aldrich,  $\geq 99.0\%$ ),  $\text{KMnO}_4$  (Sigma-Aldrich,  $99.0\%$ ),  $\text{MnSO}_4 \cdot \text{H}_2\text{O}$  (Sigma-Aldrich,  $\geq 99.0\%$ ),  $(\text{NH}_4)_2\text{S}_2\text{O}_8$  (JUNSEI,  $99.0\%$ ), ethanol ( $\text{C}_2\text{H}_5\text{OH}$ , DAEJUNG,  $94.5\%$ ),  $\text{FeSO}_4 \cdot 7\text{H}_2\text{O}$  (Sigma-Aldrich,  $\geq 99.0\%$ ),  $\text{NiSO}_4 \cdot 7\text{H}_2\text{O}$  (Sigma-Aldrich,  $\geq 99.0\%$ ), oxalic acid ( $\text{C}_2\text{H}_2\text{O}_4 \cdot 2\text{H}_2\text{O}$ , Sigma-Aldrich,  $\geq 99.0\%$ ), 5,5-dimethyl-1-pyrroline N-oxide ( $\text{C}_6\text{H}_{11}\text{NO}$ , DMPO, Sigma-Aldrich,  $\geq 98.0\%$ ), 2,9-dimethyl-1,10-phenanthroline (Neocuproine,  $\text{C}_{14}\text{H}_{12}\text{N}_2$ , Sigma-Aldrich,  $\geq 98.0\%$ ),  $\text{H}_2\text{O}_2$  (DAEJUNG, 30.0 wt.% in  $\text{H}_2\text{O}$ ), phenol ( $\text{C}_6\text{H}_5\text{OH}$ , DAEJUNG,  $99.0\%$ ), methanol ( $\text{CH}_3\text{OH}$ , Sigma-Aldrich,  $99.8\%$ ),  $\text{CuSO}_4 \cdot 5\text{H}_2\text{O}$  (Sigma-Aldrich,  $\geq 98.0\%$ ), phosphate buffer (SAMCHUN, pH of 7.2), 1,4-benzoquinone ( $\text{C}_6\text{H}_4\text{O}_2$ , Sigma-Aldrich,  $\geq 98.0\%$ ), guaiacol ( $\text{C}_7\text{H}_8\text{O}_2$ , Sigma-Aldrich,  $\geq 99.0\%$ ), catechol ( $\text{C}_6\text{H}_6\text{O}_2$ , Sigma-Aldrich,  $\geq 99.0\%$ ), hydroquinone ( $\text{C}_6\text{H}_6\text{O}_2$ , Sigma-Aldrich,  $\geq 99.0\%$ ), tert-butanol ( $\text{C}_4\text{H}_{10}\text{O}$ , TBA, Alfa-aesar,  $99.0\%$ ), 1,4-dioxane ( $\text{C}_4\text{H}_8\text{O}_2$ , DAEJUNG,  $> 99.0\%$ ), tetrahydrofuran ( $\text{C}_4\text{H}_8\text{O}$ , THF, DAEJUNG,  $> 99.0\%$ ), textile wastewater (DYETEC, TOC of  $52.7 (\pm 0.4) \text{ mmol}_{\text{CARBON}} \text{ L}^{-1}$ ; TN of  $5.6 (\pm 0.1) \text{ mmol}_{\text{NITROGEN}} \text{ L}^{-1}$ ; pH of  $11.0 (\pm 0.5)$ ), and  $\text{H}_2\text{SO}_4$  (KANTO CHEMICAL CO.,  $96.0\%$ ). Air ( $\geq 99.99\%$ ),  $\text{N}_2$  ( $\geq 99.999\%$ ), Ar ( $\geq 99.999\%$ ), He ( $\geq 99.999\%$ ), CO ( $\geq 99.999\%$ ),  $\text{CO}_2$  ( $\geq 99.999\%$ ), 5 vol. %  $\text{NH}_3/\text{N}_2$  ( $\geq 99.99\%$ ), 5 vol. %  $\text{NO}/\text{N}_2$  ( $\geq 99.99\%$ ), 5 vol. %  $\text{SO}_2/\text{N}_2$  ( $\geq 99.99\%$ ), 3 vol. %  $\text{O}_2/\text{Ar}$  ( $\geq 99.99\%$ ), 3 vol. %  $\text{O}_2/\text{N}_2$  ( $\geq 99.99\%$ ), 10 vol. %  $\text{H}_2/\text{Ar}$  ( $\geq 99.99\%$ ), and liquid  $\text{N}_2$  ( $99.9999\%$ ) were purchased from SHINYANG and used as-received.



#### 4.2.2. Catalysts

The catalysts were synthesized via hydro-thermal techniques, whose protocols were slightly modified based on those reported elsewhere.[109, 169] For the synthesis of  $\alpha$ -MnO<sub>2</sub>, 20 mmol of MnCl<sub>2</sub> • 4H<sub>2</sub>O, 20 mmol of KMnO<sub>4</sub>, and 200 mL of de-ionized H<sub>2</sub>O were placed into a 250 mL Teflon acid digestion sleeve, stirred at room temperature for 30 minutes, placed in a stainless steel reactor vessel, exposed to hydro-thermal conditions at 160 ° C for 6 hours, and cooled to room temperature. The resulting  $\alpha$ -MnO<sub>2</sub> was collected via vacuum filtration, rinsed with 750 mL of de-ionized H<sub>2</sub>O and 750 mL of ethanol, and dried overnight at 90 ° C. In addition, for the synthesis of  $\beta$ - or  $\gamma$ -MnO<sub>2</sub>, 32 mmol of MnSO<sub>4</sub> • H<sub>2</sub>O, 32 mmol of (NH<sub>4</sub>)<sub>2</sub>S<sub>2</sub>O<sub>8</sub>, and 160 mL of de-ionized H<sub>2</sub>O were placed into a 250 mL Teflon acid digestion sleeve, stirred at room temperature for 30 minutes, placed in a stainless steel reactor vessel, and exposed to hydro-thermal conditions at 140 ° C for 12 hours (for  $\beta$ -MnO<sub>2</sub>) or at 90 ° C for 12 hours (for  $\gamma$ -MnO<sub>2</sub>) prior to being cooled to room temperature. The resulting  $\beta$ - or  $\gamma$ -MnO<sub>2</sub> was collected via vacuum filtration, rinsed with 750 mL of de-ionized H<sub>2</sub>O and 750 mL of ethanol, and dried overnight at 90 ° C. The surface of  $\alpha$ -,  $\beta$ -, or  $\gamma$ -MnO<sub>2</sub> was then modified by NO/O<sub>2</sub>, as follows: Typically, 1 g of  $\alpha$ -,  $\beta$ -, or  $\gamma$ -MnO<sub>2</sub> was loaded in a quartz reactor, placed inside a tube furnace, and exposed to a N<sub>2</sub>-balanced feed gas stream consisting of 5,000 ppm NO and 3 vol. % O<sub>2</sub> at 150 ° C for an hour with a ramping rate of 10 ° C min<sup>-1</sup> and the total flow rate of 500 mL min<sup>-1</sup>. This resulted in the production of NO<sub>Y</sub><sup>-</sup>-functionalized  $\alpha$ -,  $\beta$ -, or  $\gamma$ -MnO<sub>2</sub>, each of which is denoted as  $\alpha$ -MnO<sub>2</sub>-N,  $\beta$ -MnO<sub>2</sub>-N, or  $\gamma$ -MnO<sub>2</sub>-N (Y=2 or 3), respectively. Moreover, Fe<sub>2</sub>O<sub>3</sub> and NiO were synthesized and modified by SO<sub>2</sub>/O<sub>2</sub> by following the procedures reported in our previous papers.[111, 115, 170] Typically, 20 mmol of FeSO<sub>4</sub> • 7H<sub>2</sub>O (or NiSO<sub>4</sub> • 7H<sub>2</sub>O), 20 mmol of C<sub>2</sub>H<sub>2</sub>O<sub>4</sub> • 2H<sub>2</sub>O, and 100 mL of de-ionized H<sub>2</sub>O were stirred at 50 ° C for an hour, cooled to room temperature, and vacuum-filtered using 750 mL of

de-ionized H<sub>2</sub>O and 750 mL of ethanol. The resulting synthetic mixture was calcined at 300 ° C for an hour to produce Fe<sub>2</sub>O<sub>3</sub> (or NiO). Next, 1 g of Fe<sub>2</sub>O<sub>3</sub> (or NiO) was then loaded in a quartz reactor, placed inside a tube furnace, and exposed to a N<sub>2</sub>-balanced feed gas stream composed of 500 ppm SO<sub>2</sub> and 3 vol. % O<sub>2</sub> at 400 ° C for an hour (for NiO) or at 500 ° C for an hour (for Fe<sub>2</sub>O<sub>3</sub>) with the ramping rate of 10 ° C min<sup>-1</sup> and the total flow rate of 500 mL min<sup>-1</sup>. This led to the generation of SO<sub>4</sub><sup>2-</sup>-functionalized Fe<sub>2</sub>O<sub>3</sub> or NiO, each of which is denoted as Fe<sub>2</sub>O<sub>3</sub>-S or NiO-S, respectively.

#### 4.2.3. Characterizations

A D8 Advance instrument (Bruker) was implemented to collect X-ray diffraction (XRD) patterns of the catalysts using monochromatic Cu K<sub>α</sub> radiation (wavelength of 1.54 Å) at the step size and the scan speed of 0.02° per step and 2 seconds per step, respectively. A ZSX Primus II (Rigaku) and a FLASH 2000 (Thermo Fisher Scientific) were utilized to acquire bulk compositional information of the catalysts via X-ray fluorescence (XRF) and elemental analysis (EA) technique, respectively. A Titan 80-300™ electron microscope (FEI) was used to collect high resolution transmission electron microscopy (HRTEM) images and selected area electron diffraction (SAED) patterns of the catalysts at 300 keV. An Inspect F50 microscope (FEI) was implemented to collect scanning electron microscopy (SEM) images of the catalysts at 10 kV. A in Via Raman Microscope system (Renishaw) equipped with 532 nm excitation laser, 2400 lines/mm grating, and X 50 objective lens was implemented to acquire surface concentrations of the oxygen vacancies inherent to the catalysts with a resolution of 0.3 cm<sup>-1</sup>. A PHI 5000 Versa Probe instrument (Ulvac-Phi) was implemented to acquire the information of surface compositions and phases for the catalysts via X-ray photoelectron spectroscopy (XPS) technique with the resolution of 0.05 eV, while using an adventitious carbon peak with the binding energy centered at ~284.6 eV as a reference. The XP spectra were deconvoluted using Gaussian function. An

Autochem II instrument (Micromeritics) was implemented to quantify the amounts of CO-accessible sites included per gram of the catalysts via CO-pulsed chemisorption technique at 40 ° C.[111, 115, 170–173] In addition, an Autochem II instrument (Micromeritics) was also utilized to collect H<sub>2</sub> temperature-programmed reduction (H<sub>2</sub>-TPR) profiles of the catalysts (H<sub>2</sub> thermal conductivity detection (TCD) signal versus temperature) at 50~800 ° C. Typically, the catalyst surfaces were purged with 3 vol.% O<sub>2</sub>/Ar at 110 ° C for an hour, cooled to 50 ° C under an Ar, and heated to 800 ° C under 10 vol.% H<sub>2</sub>/Ar with the ramping rate of 10 ° C min<sup>-1</sup>. The H<sub>2</sub>-TPR profiles were deconvoluted using Gaussian function. An ICS 3000 system (Thermo Fisher Scientific) and a total nitrogen content (TN) analyzer (TNM-L, Shimadzu) were implemented to quantify the amounts of metal and nitrogen species leached from the catalysts during the reaction runs via inductively coupled plasma (ICP) and TN technique, respectively. A 10D (XAS KIST) beamline in Pohang Light Source was used to collect the X-ray absorption near edge structure (XANES) spectra of the catalysts in the top-up mode at the energy, the storage current, and the resolution of 3 GeV, 250 mA, and 0.2 eV, respectively, under an ultra-high vacuum (~10<sup>-9</sup> mmHg).[111] The XANES spectra were deconvoluted using Gaussian function. A NOVA 2200e instrument (Quantachrome Instruments) was implemented to collect N<sub>2</sub> isotherms, CO isotherms, and CO<sub>2</sub> isotherms of the catalysts at -196 ° C, -30 ° C, and -20~20 ° C, respectively. N<sub>2</sub>-accessible pore volumes of the catalysts were assessed using Barrett-Joyner-Halenda (BJH) theory. N<sub>2</sub>- or CO-accessible surface areas of the catalysts were evaluated using Brunauer-Emmett-Teller (BET) theory with the consideration of the amounts of N<sub>2</sub> or CO adsorbed per gram of the catalysts under the partial pressure range (P/P<sub>0</sub>) of 0.05~0.3. CO<sub>2</sub> isotherms of the catalysts were fitted using the Toth equation, wherein N<sub>CO<sub>2</sub></sub> and A indicate the amount of CO<sub>2</sub> adsorbed per gram of the catalyst ( $\mu\text{mol}_{\text{CO}_2}\text{ g}_{\text{CAT}}^{-1}$ ) and the maximum amount of CO<sub>2</sub> adsorbed per gram of the catalyst ( $\mu\text{mol}_{\text{CO}_2}\text{ g}_{\text{CAT}}^{-1}$ ),

respectively.[170, 173–175] In addition, B, C, and P denote the constant (bar<sup>-1</sup>), the constant accounting for surface heterogeneity (dimensionless), and the pressure (bar), respectively.

$$N_{\text{CO}_2} = A \times \frac{B \times P}{(1 + (B \times P)^C)^{\frac{1}{C}}} \quad (\text{S1})$$

The Clausius–Clapeyron equation was then utilized to determine the isosteric heats of CO<sub>2</sub> adsorption ( $-Q_{\text{ST, CO}_2}$ ) for the catalysts.[170, 173–176] In Equation (S2), T<sub>1</sub> and T<sub>2</sub> denote the temperatures (K), whereas P<sub>1</sub>/P<sub>2</sub> and R indicate the pressures (bar) at T<sub>1</sub>/T<sub>2</sub> and the ideal gas constant (8.3145 J mol<sup>-1</sup> K<sup>-1</sup>).

$$\ln\left(\frac{P_1}{P_2}\right) = \frac{Q_{\text{ST, CO}_2}}{R} \times \left(\frac{T_1 - T_2}{T_1 \times T_2}\right) \quad (\text{S2})$$

An FT/IR/is20 Fourier transform infrared spectrometer (Omnic) equipped with a KBr optics and a mercury–cadmium–telluride (MCT) detector was implemented to collect background–subtracted in situ diffuse reflectance infrared Fourier transform (DRIFT) spectra of the catalysts with a resolution of 4 cm<sup>-1</sup>. Typically, the catalyst was placed in a reaction cell (Harrick Scientific), purged with 3 vol.% O<sub>2</sub>/N<sub>2</sub> at 110 ° C for an hour, and cooled to 50 ° C (or heated to 150 ° C) under a N<sub>2</sub> for the subtraction of the background spectra under a N<sub>2</sub> from the DRIFT spectra of the catalyst under a dynamic feed gas stream composed of NH<sub>3</sub> or NO/O<sub>2</sub>. The catalyst was then exposed to a N<sub>2</sub>–balanced feed gas stream composed of 1,000 ppm NH<sub>3</sub> at 50 ° C or 1,000 ppm NO/3 vol.% O<sub>2</sub> at 150 ° C for collecting in situ DRIFT spectra, whose analytical conditions are also detailed in the figure captions. An EMX–plus (Bruker) was implemented to observe the evolution of ·OH, ·OOH, O<sub>2</sub>·<sup>-</sup>, NO<sub>2</sub>· (supported), or NO<sub>3</sub>· (supported) during the H<sub>2</sub>O<sub>2</sub> scission runs on the catalysts via electron paramagnetic resonance (EPR) technique, for which C<sub>6</sub>H<sub>11</sub>NO (DMPO) served as a spin trapping agent for the radical species stated above.[177–180] Typically, a reaction mixture composed of 2 mg of the catalyst, 3 mmol of DMPO, 0.3 mmol of H<sub>2</sub>O<sub>2</sub>, and 1 mL of de–ionized H<sub>2</sub>O was shaken vigorously with the use of vortex for 2 minutes. A reaction aliquot collected from the reaction mixture (solid (catalyst)

+ liquid) or from the reaction mixture filtered using a 0.45  $\mu\text{m}$ -sized PES syringe filter (*i.e.*, reaction solution (liquid)) served to collect EPR spectra at the center magnetic field, the resonance frequency, the microwave power, the modulation amplitude, the sweep width, and the sweep time of 3435 G, 9.64 GHz, 2.95 mW, 1 G, 120 G, and 48 seconds, respectively.[111, 170] In addition, EPR spectra of the catalyst were also collected at the resonance frequency, the microwave power, and the modulation amplitude of 9.64 GHz, 1 mW, and 10 G, respectively. Furthermore, EPR spectra were simulated using the EasySpin software package (version 5.2.28).

#### 4.2.4. Computations

The CAMbridge Serial Total Energy Package (CASTEP) program in Materials Studio was first utilized to construct the (110) facet for  $\alpha$ -,  $\beta$ -, or  $\gamma$ - $\text{MnO}_2$  with a cell size of 2 X 2 X 2 and the vacuum gap of 15 Å. In the geometric optimization of  $\alpha$ -,  $\beta$ -, or  $\gamma$ - $\text{MnO}_2$ , a plane-wave basis set coupled with the ultra-soft pseudopotential and Perdew-Burke-Ernzerhof (PBE) generalized gradient approximation (GGA) functional were used.[59, 182] The total system energy convergence, the force on the atom, the maximum stress, the maximal displacement, and the cut-off energy were regulated to  $2.0 \times 10^{-6}$  eV atom<sup>-1</sup>,  $5.0 \times 10^{-2}$  eV,  $1.0 \times 10^8$  Pa,  $2.0 \times 10^{-3}$  Å, and  $3.0 \times 10^2$  eV, respectively. In contrast, the self-consistent calculation of the irreducible Brillion k point  $7 \times 7 \times 1$  was produced by the program automatically with the Broyden-Fletcher-Goldfarb-Shanno (BFGS) algorithm used for geometry optimization and surface relaxation. To compute the interactions between the  $\text{NO}_3^-$  (or  $\text{NO}_3^\cdot$ ) species and the surface on the (110) facet for  $\alpha$ - $\text{MnO}_2$ , the cluster approach was harnessed by initially cutting the (110) facet on or near the  $\alpha$ - $\text{MnO}_2$  surface before the  $\text{NO}_3^-$  (or  $\text{NO}_3^\cdot$ ) species settled on the  $\alpha$ - $\text{MnO}_2$  surface. Noteworthily, given the calculations reported in a group of previous papers,[115, 183, 184] the cluster approach, using local electronic wave functions, was anticipated to provide

the Coulombic electron energies of  $\text{NO}_3^-$  and  $\text{NO}_3^\cdot$  molecules, more efficiently and reliably than the use of plane wave functions. Hence, the coordinates of the surface (110) facet for  $\alpha\text{-MnO}_2$  were utilized, whereas additional optimization combined with frequency calculations for  $\text{NO}_3^-$  or  $\text{NO}_3^\cdot$  relaxed on the fixed model structure of  $\alpha\text{-MnO}_2$  were conducted using the Gaussian 16 package.[185] In addition, the B3LYP functional was implemented with the LANL2DZ basis set for Mn and a 6-31G\* basis set for N, O, and C (Figure 4–8).

#### 4.2.5. Reactions

Typically, 0.2 g of the catalyst was initially placed into 100 mL of de-ionized  $\text{H}_2\text{O}$  (pH of 7.0) and stirred at 300 rpm and 25 ° C for 3 minutes prior to being mixed with 30 mmol of  $\text{H}_2\text{O}_2$  for initiating  $\text{H}_2\text{O}_2$  scission. Next, 0.7 mL of the reaction aliquot was collected from the reaction mixture at a specific reaction time, quenched with 1  $\mu\text{L}$  of methanol, filtered using a 0.45  $\mu\text{m}$ -sized PES syringe filter (Whatman®), and mixed with  $\text{CuSO}_4 \cdot 5\text{H}_2\text{O}$ ,  $\text{C}_{14}\text{H}_{12}\text{N}_2$ , and phosphate buffer to determine the  $\text{H}_2\text{O}_2$  concentration via the  $\text{C}_{14}\text{H}_{12}\text{N}_2$  method. (See the details in the Analysis section.) Phenol decomposition runs were performed following the procedures identical to those used to conduct the  $\text{H}_2\text{O}_2$  scission runs, except for using 100 mL de-ionized  $\text{H}_2\text{O}$  to dissolve 0.1 mmol of phenol (pH of 7.0). Subsequently, 1.0 mL of the reaction aliquot was collected from the reaction mixture at a specific reaction time, quenched with 1  $\mu\text{L}$  of methanol, and filtered using a 0.45  $\mu\text{m}$ -sized PES syringe filter to analyze the phenol concentration through reverse phase high performance liquid chromatography (HPLC) method, whose details are found in analysis section. In addition, 10.0 mL of a reaction aliquot was taken from a reaction mixture after 480 minutes of reaction run, and filtered using a 0.20  $\mu\text{m}$ -sized mixed cellulose ester filter (HYUNDAI Micro Co., LTD) to determine the carbon concentration by the total organic carbon content (TOC) method. Meanwhile, textile wastewater was vacuum-

filtered using a 1.2  $\mu\text{m}$ -sized GF/C filter (Whatman®) to remove the suspended solids before the pH of the resulting filtrate was adjusted to 7.0 ( $\pm 0.1$ ) with the use of  $\text{H}_2\text{SO}_4$ . Next, 2 g of the catalyst was placed into 200 mL of the filtrate and stirred at 300 rpm and 25 ° C for 3 minutes prior to being mixed with 150 mmol of  $\text{H}_2\text{O}_2$  for initiating textile wastewater degradation. Finally, 10.0 mL of the reaction aliquot was collected from the reaction mixture at a specific reaction time and filtered using a 0.20  $\mu\text{m}$ -sized mixed cellulose ester filter to analyze the carbon and nitrogen concentrations using TOC/TN methods.

#### 4.2.6. Analysis

A UV/Vis spectrometer (Cary 100, Shimadzu) was implemented to quantify the amounts of  $\text{H}_2\text{O}_2$  included in the reaction mixtures during the  $\text{H}_2\text{O}_2$  scission runs using the  $\text{C}_{14}\text{H}_{12}\text{N}_2$  method, whose protocols were reported elsewhere.[170, 186] Typically, a solution consisting of 1 mL of 0.01 M  $\text{CuSO}_4 \cdot 5\text{H}_2\text{O}$  and 1 mL of 0.01 M  $\text{C}_{14}\text{H}_{12}\text{N}_2$  was added to 0.7 mL of de-ionized  $\text{H}_2\text{O}$  for the blank solution, 0.7 mL of de-ionized  $\text{H}_2\text{O}$  with 0.1–50.0 mmol  $\text{H}_2\text{O}_2$  for the  $\text{H}_2\text{O}_2$  calibration solution, or 0.7 mL of a reaction aliquot (mixed with 1  $\mu\text{L}$  of methanol) for the analytical solution. The solutions stated above were then mixed with phosphate buffer to regulate the total volume of the final solutions to 10 mL. The blank and  $\text{H}_2\text{O}_2$  calibration solutions were used to construct the calibration curve of “the difference in absorbance between the blank and  $\text{H}_2\text{O}_2$  calibration solutions at 454 nm ( $\Delta A_{454}$ )” versus “ $\text{H}_2\text{O}_2$  concentration ( $C_{\text{H}_2\text{O}_2}$ )”. The plot of  $\Delta A_{454}$  versus  $C_{\text{H}_2\text{O}_2}$  provided the slope utilized to determine the  $C_{\text{H}_2\text{O}_2}$  values of the analytical solutions. Conversion of  $\text{H}_2\text{O}_2$  ( $X_{\text{H}_2\text{O}_2}$ ) was calculated using Equation (S3), in which  $C_{\text{H}_2\text{O}_2, 0}$  and  $C_{\text{H}_2\text{O}_2}$  denote the initial  $\text{H}_2\text{O}_2$  concentration and the  $\text{H}_2\text{O}_2$  concentration at a specific reaction time, respectively.[111, 115, 170–173]

$$X_{\text{H}_2\text{O}_2} (\%) = \frac{C_{\text{H}_2\text{O}_2, 0} (\text{mol}_{\text{H}_2\text{O}_2} \text{L}^{-1}) - C_{\text{H}_2\text{O}_2} (\text{mol}_{\text{H}_2\text{O}_2} \text{L}^{-1})}{C_{\text{H}_2\text{O}_2, 0} (\text{mol}_{\text{H}_2\text{O}_2} \text{L}^{-1})} \times 100 \quad (\text{S3})$$

The initial  $\text{H}_2\text{O}_2$  scission rate ( $-r_{\text{H}_2\text{O}_2, 0}$ ) of the catalyst was assessed using

Equation (S4), in which  $N_{H_2O_2, 0}$  and  $k_{APP}$  indicate the initial  $H_2O_2$  quantity and the apparent reaction rate constant (slope of  $-\ln (C_{H_2O_2}/ C_{H_2O_2, 0})$  versus time), respectively.[111, 115, 170–173] In addition,  $N_{CO, 0.2 g}$  indicates the amount of CO-accessible surface Mn species included in 0.2 g of the catalyst.

$$-r_{H_2O_2, 0} (min^{-1}) = \frac{k_{APP} (min^{-1}) \times N_{H_2O_2} (mol_{H_2O_2})}{N_{CO, 0.2 g} (mol_{CO})} \quad (S4)$$

A LC-20A system (Shimadzu) equipped with a Shim-pack GIS C18 column (5  $\mu m$ , 4.6 X 150 mm, Shimadzu), an automatic injector (SIL-20A, Shimadzu), a pump (LC-20AT, Shimadzu), and an UV/Vis detector (SPD-20A, Shimadzu) was implemented to quantify phenol through reverse phase HPLC technique.[111, 115, 170–173] Typically, a mixture of methanol and de-ionized  $H_2O$  with the volumetric ratio of 6:4 served as the mobile phase at the flow rate of 1.0 mL  $min^{-1}$  for quantifying the phenol concentrations, whereas the injection volume of the sample was  $10^{-5}$  L. Conversion of phenol ( $X_{PHENOL}$ ) was calculated using Equation (S5), in which  $C_{PHENOL, 0}$  and  $C_{PHENOL}$  denotes the initial phenol concentration and the phenol concentration at a specific reaction time, respectively.[111, 115, 170–173]

$$X_{PHENOL} (\%) = \frac{C_{PHENOL, 0} (mol_{PHENOL} L^{-1}) - C_{PHENOL} (mol_{PHENOL} L^{-1})}{C_{PHENOL, 0} (mol_{PHENOL} L^{-1})} \times 100 \quad (S5)$$

The initial phenol decomposition rate ( $-r_{PHENOL, 0}$  or  $-r'_{PHENOL, 0}$ ) was assessed using Equation (S6) or Equation (S7), in which  $N_{PHENOL, 0}$  and  $k_{APP}$  indicate the initial phenol quantity and the apparent reaction rate constant (slope of  $-\ln (C_{PHENOL}/ C_{PHENOL, 0})$  versus time), respectively.[111, 115, 170–173]

$$-r_{PHENOL, 0} (min^{-1}) = \frac{k_{APP} (min^{-1}) \times N_{PHENOL, 0} (mol_{PHENOL})}{N_{CO, 0.2 g} (mol_{CO})} \quad (S6)$$

$$-r'_{PHENOL, 0} (mol_{PHENOL} g_{CAT}^{-1} min^{-1}) = \frac{k_{APP} (min^{-1}) \times N_{PHENOL, 0} (mol_{PHENOL})}{0.2 g_{CAT}} \quad (S7)$$

The energy barrier ( $E_{BARRIER}$ ) and pre-factor ( $k_{APP, 0}$ ) of the catalyst needed to dissect  $H_2O_2$  or decompose phenol were assessed using the Arrhenius plot of  $\ln (k_{APP})$  versus  $1/T$  (Equation (S8)), where  $k_{APP}$ , R, and T denote the apparent reaction rate constant, the ideal gas constant, and the temperature, respectively.[170, 187, 188]

$$\ln (k_{APP}) = \ln (k_{APP, 0}) - \frac{E_{BARRIER}}{R} \times \left( \frac{1}{T} \right) \quad (S8)$$

A TOC analyzer (TOC-L, Shimadzu) and a TN analyzer were utilized to



quantify the carbon and nitrogen components of the reaction mixtures. Mineralization of phenol or textile wastewater was assessed by conversions with regard to carbon ( $X_{\text{CARBON}}$  in Equation (S9)) or nitrogen species ( $X_{\text{NITROGEN}}$  in Equation (S10)) species, in which  $C_{\text{CARBON},0}$  (or  $C_{\text{NITROGEN},0}$ ) and  $C_{\text{CARBON}}$  (or  $C_{\text{NITROGEN}}$ ) denote the initial carbon (or nitrogen) concentration and the carbon (or nitrogen) concentration at a specific reaction time, respectively.[170, 173]

$$X_{\text{CARBON}} (\%) = \frac{C_{\text{CARBON},0} (\text{mol}_{\text{CARBON}} \text{L}^{-1}) - C_{\text{CARBON}} (\text{mol}_{\text{CARBON}} \text{L}^{-1})}{C_{\text{CARBON},0} (\text{mol}_{\text{CARBON}} \text{L}^{-1})} \times 100 \quad (\text{S9})$$

$$X_{\text{NITROGEN}} (\%) = \frac{C_{\text{NITROGEN},0} (\text{mol}_{\text{NITROGEN}} \text{L}^{-1}) - C_{\text{NITROGEN}} (\text{mol}_{\text{NITROGEN}} \text{L}^{-1})}{C_{\text{NITROGEN},0} (\text{mol}_{\text{NITROGEN}} \text{L}^{-1})} \times 100 \quad (\text{S10})$$

The initial degradation rate of textile wastewater ( $-r_{\text{C}}$ ,  $-r'_{\text{C}}$ ,  $-r_{\text{N}}$ , or  $-r'_{\text{N}}$ ) was assessed using Equations (S11)–(S14), in which  $N_{\text{CARBON},0}$  (or  $N_{\text{NITROGEN},0}$ ) and  $k_{\text{APP}}$  indicate the initial carbon (or nitrogen) quantity and the apparent reaction rate constant, respectively.[111, 115, 170–173] In addition,  $N_{\text{CO},2\text{g}}$  indicates the amount of CO-accessible surface Mn sites included in 2 g of the catalyst.

$$-r_{\text{C}} (\text{min}^{-1}) = \frac{k_{\text{APP}} (\text{min}^{-1}) \times N_{\text{CARBON}} (\text{mol}_{\text{CARBON}})}{N_{\text{CO},2\text{g}} (\text{mol}_{\text{CO}})} \quad (\text{S11})$$

$$-r'_{\text{C}} (\text{mol}_{\text{CARBON}} \text{g}_{\text{CAT}}^{-1} \text{min}^{-1}) = \frac{k_{\text{APP}} (\text{min}^{-1}) \times N_{\text{CARBON}} (\text{mol}_{\text{CARBON}})}{2 \text{ g}_{\text{CAT}}} \quad (\text{S12})$$

$$-r_{\text{N}} (\text{min}^{-1}) = \frac{k_{\text{APP}} (\text{min}^{-1}) \times N_{\text{NITROGEN}} (\text{mol}_{\text{NITROGEN}})}{N_{\text{CO},2\text{g}} (\text{mol}_{\text{CO}})} \quad (\text{S13})$$

$$-r'_{\text{N}} (\text{mol}_{\text{NITROGEN}} \text{g}_{\text{CAT}}^{-1} \text{min}^{-1}) = \frac{k_{\text{APP}} (\text{min}^{-1}) \times N_{\text{NITROGEN}} (\text{mol}_{\text{NITROGEN}})}{2 \text{ g}_{\text{CAT}}} \quad (\text{S14})$$

## 4.3. Results and Discussion

### 4.3.1. Properties of $\alpha$ -/ $\beta$ -/ $\gamma$ -MnO<sub>2</sub>

One of our primary goals was to validate the advantages of  $\cdot\text{OH} \rightarrow \text{NO}_3^{\cdot\text{SUP}}$  on  $\text{NO}_Y^-$ -functionalized  $\alpha$ -/ $\beta$ -/ $\gamma$ -MnO<sub>2</sub> (denoted as  $\alpha$ -/ $\beta$ -/ $\gamma$ -MnO<sub>2</sub>-N; Y= 2 or 3) in degrading aqueous contaminants relative to  $\cdot\text{OH}$  production on  $\alpha$ -/ $\beta$ -/ $\gamma$ -MnO<sub>2</sub>. Hence,  $\alpha$ -/ $\beta$ -/ $\gamma$ -MnO<sub>2</sub> were first isolated via hydrothermal synthesis, during which multiple, equimolar Mn precursors of the  $\text{Mn}^{2+}/\text{MnO}_4^-$  or  $\text{Mn}^{2+}$  oxidant of  $(\text{NH}_4)_2\text{S}_2\text{O}_8$  served to preferentially crystallize  $\alpha$ -/ $\beta$ -/ $\gamma$ -MnO<sub>2</sub> architectures at 90–160 °C.[208, 209] The porosities of  $\alpha$ -/ $\beta$ -/ $\gamma$ -MnO<sub>2</sub> were analyzed via N<sub>2</sub> isotherm techniques, by which  $\alpha$ -/ $\beta$ -/ $\gamma$ -MnO<sub>2</sub> were verified to possess diverse BET surface areas ( $S_{\text{BET}}$ ) of 10–160 m<sup>2</sup> g<sub>CAT</sub><sup>-1</sup> and BJH pore volumes ( $V_{\text{BJH}}$ ) of 0.1–0.2 cm<sup>3</sup> g<sub>CAT</sub><sup>-1</sup> with  $\beta$ -MnO<sub>2</sub> being almost non-porous. This suggested that the amounts of  $\text{Mn}^{n+}/\text{O}_\alpha$  species exposed to the H<sub>2</sub>O<sub>2</sub>/NO<sub>Y</sub><sup>-</sup> precursor (NO/O<sub>2</sub>) were severely limited in  $\beta$ -MnO<sub>2</sub>, thereby potentially resulting in the smallest  $\cdot\text{OH} \rightarrow \text{NO}_3^{\cdot\text{SUP}}$  efficiency on  $\beta$ -MnO<sub>2</sub>-N per gram basis. Conversely,  $\alpha$ -/ $\gamma$ -MnO<sub>2</sub> showed moderate  $S_{\text{BET}}$  values of  $\geq 50$  m<sup>2</sup> g<sub>CAT</sub><sup>-1</sup>, including that they might have larger quantities of  $\text{Mn}^{n+}/\text{O}_\alpha$  species (NO<sub>Y</sub><sup>-</sup>-anchoring spot) available to conduct  $\cdot\text{OH} \rightarrow \text{NO}_3^{\cdot\text{SUP}}$  compared to  $\beta$ -MnO<sub>2</sub>. Nevertheless, the  $\cdot\text{OH} \rightarrow \text{NO}_3^{\cdot\text{SUP}}$  efficiencies on  $\alpha$ -/ $\gamma$ -MnO<sub>2</sub>-N per gram basis could be directed by the number of moles of  $\text{Mn}^{n+}$  species were present in the pores with sizes of  $\geq 2.7 (\pm 0.2)$  Å (kinetic diameter of H<sub>2</sub>O<sub>2</sub>[25]). This was because  $\cdot\text{OH} \rightarrow \text{NO}_3^{\cdot\text{SUP}}$  can be initiated by catalytic H<sub>2</sub>O<sub>2</sub> cleavage on the  $\text{Mn}^{n+}$  species. These results suggested that the  $\cdot\text{OH} \rightarrow \text{NO}_3^{\cdot\text{SUP}}$  efficiencies on  $\alpha$ -/ $\beta$ -/ $\gamma$ -MnO<sub>2</sub>-N could be drastically affected by their textural features or diffusional artifacts originating from H<sub>2</sub>O<sub>2</sub>. This again justified the necessity to evaluate the  $\cdot\text{OH} \rightarrow \text{NO}_3^{\cdot\text{SUP}}$  efficiencies per site basis under diffusion-free environments to precisely investigate the geometrical effect of  $\alpha$ -/ $\beta$ -/ $\gamma$ -MnO<sub>2</sub>-N on the  $\cdot\text{OH} \rightarrow \text{NO}_3^{\cdot\text{SUP}}$  efficiencies. Interestingly,  $\alpha$ -/ $\beta$ -/ $\gamma$ -MnO<sub>2</sub> lacked micro-porosities. Micro-porosities

were anticipated to be observed across the catalysts, as conjectured based on their tunnel sizes illustrated in Figure 4-1D to 4-1F. These might be due in part to the hydrothermal synthetic technique utilized or structural collapse of the  $\alpha$ -/ $\beta$ -/ $\gamma$ -MnO<sub>2</sub> hosts upon the removal of the guest synthetic solvents, as reported elsewhere.[210, 211] Nonetheless, this could indicate that a significant portion of Mn<sup>n+</sup>/O<sub>α</sub> species was deposited in the pores with sizes of  $\geq 20$  Å, thereby helping improve the access of the NO<sub>3</sub>·<sub>SUP</sub> species on  $\alpha$ -/ $\beta$ -/ $\gamma$ -MnO<sub>2</sub>-N to phenol with a size of  $\sim 6.7$  Å[212] or textile wastewater. Bulk crystallographic features of  $\alpha$ -/ $\beta$ -/ $\gamma$ -MnO<sub>2</sub> were explored using their XRD patterns, where the diffractions were in close alignment with those simulated for *tetragonal*  $\alpha$ -/ $\beta$ -MnO<sub>2</sub> and *orthorhombic*  $\gamma$ -MnO<sub>2</sub> with no collateral diffractions assigned. Bulk structural characteristics of the catalysts were maintained on their surfaces. This was proved by the SAED patterns of the catalysts, wherein all spots were indexed to those simulated for  $\alpha$ -/ $\beta$ -/ $\gamma$ -MnO<sub>2</sub> (Figure 4-2G to 4-2I). Morphological traits of the catalysts were then inspected using their HRTEM images, in which  $\alpha$ -/ $\beta$ -/ $\gamma$ -MnO<sub>2</sub> were composed of 1–5 μm-sized chunks (Figure 4-2A to 4-2C) with the lattice fringes (*d*) of 1.4 Å, 3.1 Å, and 2.3 Å, respectively (Figure 4-2D to 4-2F). These were assigned to surface facets of (002) for *tetragonal*  $\alpha$ -MnO<sub>2</sub>, (110) for *tetragonal*  $\beta$ -MnO<sub>2</sub>, and (400) for *orthorhombic*  $\gamma$ -MnO<sub>2</sub>, respectively, all of which were also indexed in the SAED patterns of the catalysts. All the analytic results suggested that  $\alpha$ -/ $\beta$ -/ $\gamma$ -MnO<sub>2</sub> were bulk/surface phase-pure, synthesized as targeted, and could be such platforms as to bear Mn<sup>n+</sup>/O<sub>α</sub> species for ·OH → NO<sub>3</sub>·<sub>SUP</sub>.

Numbers and strengths of Lewis acidic Mn<sup>n+</sup> (n=2 or 3) species (Lewis acidities) are pivotal to prompt ·OH production, whose rate-determining stage could be ·OH desorption from the Mn<sup>n+</sup> species, as discussed in the Introduction. Hence, surface traits of  $\alpha$ -/ $\beta$ -/ $\gamma$ -MnO<sub>2</sub> were investigated using the XPS technique. The resultant XP spectra exhibited two broad bands in the Mn 2p<sub>3/2</sub> and Mn 2p<sub>1/2</sub> domains. These bands stated above were de-

convoluted to provide three sub-bands with binding energies centered at  $\sim 640.3$  eV,  $\sim 641.3$  eV, and  $\sim 642.3$  eV in the Mn 2p<sub>3/2</sub> domains, each of which could be respectively assigned to the Mn<sup>2+</sup>, Mn<sup>3+</sup>, and Mn<sup>4+</sup> species with a separation of 12.0 eV from those present in the Mn 2p<sub>1/2</sub> domains.[213]

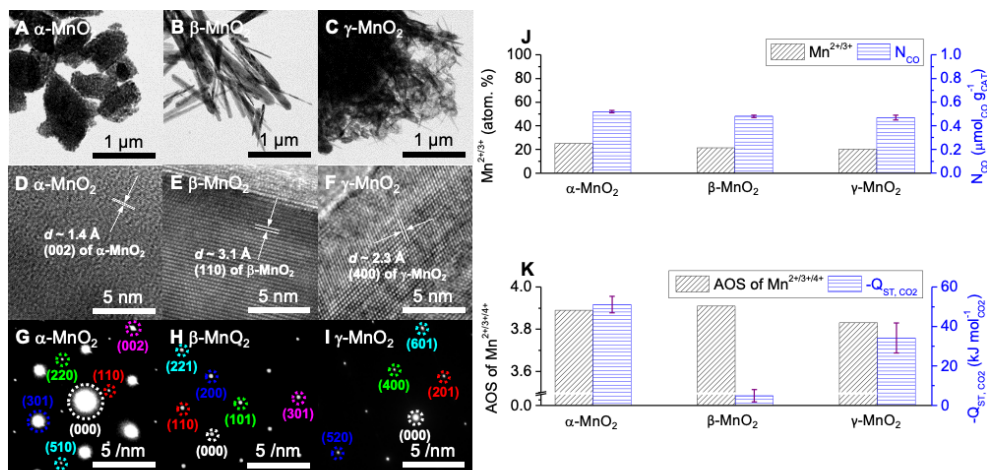


Figure 4-2. HRTEM images of  $\alpha$ -MnO<sub>2</sub> (A and D),  $\beta$ -MnO<sub>2</sub> (B and E), and  $\gamma$ -MnO<sub>2</sub> (C and F). In (D)–(F), lattice fringes with  $d$  values of 1.4 Å, 3.1 Å and 2.3 Å are indexed to (002), (110), and (400) facets for *tetragonal*  $\alpha$ -MnO<sub>2</sub> (JCPDF No. of 01-072-1982), *tetragonal*  $\beta$ -MnO<sub>2</sub> (JCPDF No. of 00-024-0735), and *orthorhombic*  $\gamma$ -MnO<sub>2</sub> (JCPDF No. of 01-082-2169), respectively. SAED patterns of  $\alpha$ -MnO<sub>2</sub> (G),  $\beta$ -MnO<sub>2</sub> (H), and  $\gamma$ -MnO<sub>2</sub> (I), where dots indicate surface facets assigned to those of  $\alpha$ -,  $\beta$ -, or  $\gamma$ -MnO<sub>2</sub>. (J) Atomic concentrations of Mn<sup>2+</sup>/Mn<sup>3+</sup> species present in or near the catalyst surfaces and the amounts of CO-accessible Mn species included per gram of the catalysts (N<sub>CO</sub>). (K) average oxidation states (AOS) of Mn<sup>2+</sup>/Mn<sup>3+</sup>/Mn<sup>4+</sup> species present in or near the catalyst surfaces and the isosteric heats of CO<sub>2</sub> adsorption ( $-Q_{ST, CO_2}$ ) for the catalysts at small CO<sub>2</sub> coverages ( $\sim 5.1$  μmol g<sub>CAT</sub><sup>-1</sup> for  $\alpha$ -MnO<sub>2</sub> and  $\gamma$ -MnO<sub>2</sub>;  $\sim 3.7$  μmol g<sub>CAT</sub><sup>-1</sup> for  $\beta$ -MnO<sub>2</sub>).

Again, the Mn<sup>n+</sup> species adjacent to the oxygen vacancies were defective: thus, they can bind with H<sub>2</sub>O<sub>2</sub>,[196] as discussed earlier. However, the relative abundances of the surface Mn<sup>n+</sup> species were similar for all the catalysts (20.3–25.2% in Figure 4-2J). In addition, CO, which is comparable to H<sub>2</sub>O<sub>2</sub> in size (3.2 Å),[214] can only bind with Lewis acidic species, and therefore served as a probe to quantify the amounts of Lewis acidic sites included in one gram of  $\alpha$ -/ $\beta$ -/ $\gamma$ -MnO<sub>2</sub> (N<sub>CO</sub>) using CO-pulsed chemisorption technique at 40 ° C (near ambient temperature).[25, 39, 107] The N<sub>CO</sub> values

of the catalysts retained similar magnitudes ( $\sim 0.5 \mu\text{mol}_{\text{CO}} \text{g}_{\text{CAT}}^{-1}$ ) and were in good agreement with their surface  $\text{Mn}^{n+}$  concentrations. The relative abundance of surface  $\text{Mn}^{n+}$  defects innate to the catalysts was further inspected using their Raman spectra, by which oxygen vacancies vicinal to the  $\text{Mn}^{n+}$  species were quantifiable using the locations/intensities of the bands centered at Raman shifts of  $628.7\text{--}630.2 \text{ cm}^{-1}$ . These bands could result from symmetric stretching vibrations of the Mn–O bonds innate to the *octahedral*  $[\text{Mn}^{4+}(\text{O}^{2-})_6]^{8-}$  sub-units for the  $\alpha\text{--}/\beta\text{--}/\gamma\text{--}\text{MnO}_2$  architectures.[215, 216] These bands, however, were alike in terms of their locations and intensities, which suggested similar concentrations of oxygen vacancies ( $\text{Mn}^{n+}$  species) across the catalysts.[215, 216] EPR spectra of the catalysts were also collected at  $-223^\circ \text{C}$  to quantify the concentrations of oxygen vacancies included in the catalysts with improved amplitude and resolution. The resulting EPR spectra revealed symmetric signals with  $g$ -factor values of  $2.004\text{--}2.007$ , which could originate from free electrons trapped in the paramagnetic oxygen vacancies adjacent to the  $\text{Mn}^{n+}$  species inherent to the catalysts.[213, 217] Interestingly, the EPR signal of  $\gamma\text{--}\text{MnO}_2$  was broader than those of  $\alpha\text{--}/\beta\text{--}\text{MnO}_2$ , which was caused by the transition of magnetic properties for  $\gamma\text{--}\text{MnO}_2$  from para-magnetism to antiferro-magnetism at  $\leq -181^\circ \text{C}$ . [218] Nonetheless, the areas under the EPR signals of  $\alpha\text{--}/\beta\text{--}\text{MnO}_2$  were comparable and thus further corroborated the similar concentrations of oxygen vacancies included in  $\alpha\text{--}/\beta\text{--}\text{MnO}_2$ . [213, 217] Apparently, the XP/Raman/EPR spectra of the catalysts provide evidence that the geometrical difference among  $\alpha\text{--}/\beta\text{--}/\gamma\text{--}\text{MnO}_2$  could hardly diversify the quantities of the Lewis acidic  $\text{Mn}^{n+}$  species included per gram of the catalysts. This, however, provided an impetus to explore the  $\text{H}_2\text{O}_2$  scission efficiencies per site basis, whose  $\cdot\text{OH}$  productivities could be mainly dictated by the Lewis acidic strengths of the surface  $\text{Mn}^{n+}$  sites. In this regard, XP spectra of  $\alpha\text{--}/\beta\text{--}/\gamma\text{--}\text{MnO}_2$  in the Mn 3s regimes were explored. The XP spectra were de-convoluted to provide two sub-bands,[200, 219] with a peak splitting

( $\Delta E_{\text{BINDING ENERGY}}$ ) was 4.50 eV, 4.48 eV, or 4.55 eV for  $\alpha$ -,  $\beta$ -, or  $\gamma$ - $\text{MnO}_2$ , respectively. The  $\Delta E_{\text{BINDING ENERGY}}$  values could be converted to average oxidation state (AOS) of the surface Mn species using the relationship of  $\text{AOS} = 8.956 - 1.126 \times \Delta E_{\text{BINDING ENERGY}}$ . [200, 219] The AOS values of  $\alpha$ -/ $\beta$ -/ $\gamma$ - $\text{MnO}_2$  were  $\geq 3.8$ , which was expected given the surface concentrations of  $\text{Mn}^{4+}$  species ( $\geq \sim 75.0\%$ ) for the catalysts. However, the AOS of  $\gamma$ - $\text{MnO}_2$  (3.83) was smaller than those of  $\alpha$ -/ $\beta$ - $\text{MnO}_2$  ( $\sim 3.90$ ), which suggests the lowest Lewis acidic strength of  $\text{Mn}^{n+}$  species inherent to  $\gamma$ - $\text{MnO}_2$  (Figure 4-2K). In addition to the similarity in size observed for the  $\text{H}_2\text{O}_2$ , CO, and  $\text{CO}_2$  molecules (3.3 Å), [134] the lone pair of  $e^-$  present in  $\text{CO}_2$  can be coordinated to the Lewis acidic metals; [47, 107] thus, it served as an additional probe to quantify the Lewis acidic strengths of the  $\text{Mn}^{n+}$  species inherent to the surfaces. For this purpose,  $\text{CO}_2$  isotherms of the catalysts were collected at  $-20^\circ\text{C}$  to  $20^\circ\text{C}$  (near ambient temperature) and subjected to Toth fittings in order to extract the isosteric heats of  $\text{CO}_2$  adsorption for the catalysts ( $-Q_{\text{ST}, \text{CO}_2}$ ) at a near-zero coverage of  $\text{CO}_2$  with the use of the Clausius–Clapeyron equation. [220, 221] Interestingly, the  $-Q_{\text{ST}, \text{CO}_2}$  values of  $\beta$ - $\text{MnO}_2$  was  $\sim 5.0 \text{ kJ mol}_{\text{CO}_2}^{-1}$  (Figure 4-2K). This might be ascribed to the low porosity of  $\beta$ - $\text{MnO}_2$  ( $\sim 10 \text{ m}^2 \text{ g}_{\text{CAT}}^{-1}$ ) amicable to enhance the lateral  $\text{CO}_2 \cdots \text{CO}_2$  interactions rather than the  $\text{CO}_2 \cdots \text{Mn}^{n+}$  interactions [47, 222] and therefore, it remained challenging to accurately quantify the  $\text{CO}_2 \cdots \text{Mn}^{n+}$  interactions through  $-Q_{\text{ST}, \text{CO}_2}$ . However, the  $-Q_{\text{ST}, \text{CO}_2}$  value of  $\gamma$ - $\text{MnO}_2$  ( $\sim 42.9 \text{ kJ mol}_{\text{CO}_2}^{-1}$ ) was smaller than that of  $\alpha$ - $\text{MnO}_2$  ( $\sim 51.1 \text{ kJ mol}_{\text{CO}_2}^{-1}$ ). In conjunction with the AOS values, the  $-Q_{\text{ST}, \text{CO}_2}$  values highly suggested that Lewis acidic  $\text{Mn}^{n+}$  species could be the most desirable in expediting  $\cdot\text{OH}$  desorption, when being deposited on the  $\gamma$ - $\text{MnO}_2$  surface. Noteworthy, the lone  $e^-$  pair innate to  $\text{CO}_2$  can also bind with the proton of the surface Brönsted acidic sites ( $-\text{OH}$ ), as reported previously. [223, 224] Indeed,  $\alpha$ -/ $\beta$ -/ $\gamma$ - $\text{MnO}_2$  surfaces afforded Brönsted acidic (*B*) and Lewis acidic (*L*) sites, as supported by their background-subtracted, *in situ* DRIFT

spectra. *B/L* bands resulting from asymmetric or symmetric stretching (or bending) vibrations of the N–H bonds of NH<sub>3</sub> coordinated to *B/L* sites were developed under an NH<sub>3</sub> atmosphere at 50 °C (near ambient temperature).[59, 90, 200, 225, 226] Nevertheless, the areas under the *L* bands were greater than those of the *B* bands across the catalysts. This could indicate that the  $-Q_{ST, CO_2}$  values of the catalysts mainly originated from CO<sub>2</sub> • • • Mn<sup>n+</sup> interactions, although the contributions of the CO<sub>2</sub> • • • *B* interactions to the  $-Q_{ST, CO}$  values could not be ruled out entirely. Nevertheless, AOS and  $-Q_{ST, CO_2}$  analysis on  $\alpha$ –/ $\beta$ –/ $\gamma$ –MnO<sub>2</sub> could aid in establishing the hierarchy with regard to the Lewis acidic strengths of the Mn<sup>n+</sup> species adequate to desorb •OH, to be in the following order of  $\alpha$ –MnO<sub>2</sub> ~  $\beta$ –MnO<sub>2</sub> <  $\gamma$ –MnO<sub>2</sub>.

In contrast, the surface area of Lewis acidic Mn<sup>n+</sup> species (*S*<sub>CO</sub>) can be closely related to the frequency of H<sub>2</sub>O<sub>2</sub> • • • Mn<sup>n+</sup> collisions, thereby directing the pre-factor (*k*<sub>APP, 0</sub>) of the catalyst in H<sub>2</sub>O<sub>2</sub> scission or the •OH-mediated pollutant degradation run, as we suggested in previous studies.[107, 200] Hence, the *S*<sub>CO</sub> (*S*<sub>BET, CO</sub> divided by *N*<sub>CO</sub>) values of the catalysts were quantified using their CO isotherms, all of which provided CO-accessible BET surface areas (*S*<sub>BET, CO</sub>) along with the amounts of CO adsorbed per gram of the catalysts at 1 bar (*N*<sub>CO</sub>).[107, 200] It should be noted that the CO<sub>2</sub> isotherm experiments could also provide the *S*<sub>CO<sub>2</sub></sub> values of the catalysts analogous to their *S*<sub>CO</sub> counterparts, yet, were not considered owing to CO<sub>2</sub> adsorption on the Brönsted acidic sites. We attempted to collect CO isotherms of the catalysts at near-ambient temperature. However, the CO isotherms revealed minute differences in terms of the *S*<sub>BET, CO</sub> and *N*<sub>CO</sub> values throughout the catalysts range at temperatures ≥ –20 °C due to the limitation of the instrument used[107] (not shown) and therefore were collected at –30 °C only. The *S*<sub>CO</sub> values of the catalysts increased in the following order of  $\gamma$ –MnO<sub>2</sub> (~3.0 X 10<sup>5</sup> m<sub>CO</sub><sup>2</sup> mol<sub>CO</sub><sup>–1</sup>) <  $\alpha$ –MnO<sub>2</sub> (~3.9 X 10<sup>5</sup> m<sub>CO</sub><sup>2</sup> mol<sub>CO</sub><sup>–1</sup>) <  $\beta$ –MnO<sub>2</sub> (~6.6 X 10<sup>5</sup> m<sub>CO</sub><sup>2</sup> mol<sub>CO</sub><sup>–1</sup>). This suggested that  $\beta$ –MnO<sub>2</sub> might be

the most desirable in producing  $\cdot\text{OH}$  among the studied catalysts, in spite of its greatest intimacy with  $\cdot\text{OH}$  (evidenced by AOS analysis).

#### 4.3.2. $\text{H}_2\text{O}_2$ scission kinetics on $\alpha$ -/ $\beta$ -/ $\gamma$ - $\text{MnO}_2$

$\text{H}_2\text{O}_2$  scission/pollutant degradation runs on the catalysts were then conducted at 25 ° C. Of note, it was reported that  $\text{H}_2\text{O}_2$  can be dissected on surface-unbound  $\text{Mn}^{2+}$  and  $\text{Mn}^{3+}$  to produce  $\cdot\text{OH}$  and regenerate  $\text{Mn}^{2+}$  with moderate  $k$  values of  $\sim 1.3 \times 10^1 \text{ M}^{-1} \text{ sec}^{-1}$  and  $\sim 2.8 \times 10^3 \text{ M}^{-1} \text{ sec}^{-1}$ , respectively.[190, 191] Moreover, in spite of having a longer lifespan ( $t_{1/2}$  of  $2.0 \times 10^6 \mu\text{second}$ ),  $\cdot\text{OOH}$  possesses a lower electro-philicity ( $E_0$  of 1.8 V) than that of  $\cdot\text{OH}$ .[48, 190, 191] Thus,  $\cdot\text{OOH}$  might not likely serve to fragment the contaminant (Figure 4-1A). Of additional note,  $\cdot\text{OOH}$  can also be cleaved to form  $\text{O}_2\cdot^-$  with the smallest electro-philicity among the radicals considered ( $E_0$  of -0.2 V).[190, 191, 227] Given the reaction of  $\text{Mn}^{3+}$  (surface-unbound) +  $\text{O}_2\cdot^- \rightarrow \text{Mn}^{2+}$  (surface-unbound) +  $\text{O}_2$  with a large  $k$  of  $\sim 7.0 \times 10^7 \text{ M}^{-1} \text{ sec}^{-1}$ ,[191]  $\text{O}_2\cdot^-$  might be utilized to recover surface  $\text{Mn}^{n+}$  species, as illustrated in Figure 4-1A. The potential functions of  $\cdot\text{OH}/\text{H}_2\text{O}_2/\cdot\text{OOH}/\text{O}_2\cdot^-$  depicted above could suggest their vitalness in decomposing the pollutant (via  $\cdot\text{OH}$ ) and/or regenerating surface  $\text{Mn}^{n+}$  species (via  $\text{H}_2\text{O}_2$  or  $\cdot\text{OOH}/\text{O}_2\cdot^-$ ). This thus rationalized the use of an excess amount of  $\text{H}_2\text{O}_2$  (30 mmol) relative to that of the  $\text{Mn}^{n+}$  species inherent to the catalyst ( $\sim 0.5 \mu\text{mol}_{\text{CO}} \text{ g}_{\text{CAT}}^{-1}$ ) throughout the reaction runs.

Of additional note,  $\text{H}_2\text{O}_2$  can experience self-decomposition under aqueous environments to evolve  $\cdot\text{OOH}/\text{O}_2\cdot^-$  even in the absence of the catalysts[25, 39, 107, 228] and therefore should be regarded as backgrounds. Thus, the reaction data were corrected using backgrounds and fitted using the pseudo-1<sup>st</sup>-order kinetic model to extract the apparent reaction rate constants of the catalysts ( $k_{\text{APP}}$ ).[25, 39, 107] Moreover, the change in the type of  $\text{MnO}_2$  polymorphs did not alter their  $N_{\text{CO}}$  values, yet, did vary their  $-\text{Q}_{\text{ST, CO}_2}$  values along with the AOS values of the surface Mn species. This indicated that  $\text{H}_2\text{O}_2$



scission efficiencies on the catalysts could rely mainly on the Lewis acidic strengths of the  $\text{Mn}^{n+}$  species. Therefore, the initial  $\text{H}_2\text{O}_2$  scission rates of the catalysts were evaluated from a site basis and defined as the amounts of  $\text{H}_2\text{O}_2$  cleaved per CO-accessible Lewis acidic site per unit time ( $-r_{\text{H}_2\text{O}_2, 0}$  in Equation (S4)).[25, 39, 107] The  $-r_{\text{H}_2\text{O}_2, 0}$  values of  $\alpha$ -/ $\beta$ - $\text{MnO}_2$  were comparable ( $\sim 25 \text{ min}^{-1}$ ), yet, were smaller than that of  $\gamma$ - $\text{MnO}_2$  ( $\sim 35 \text{ min}^{-1}$  in Figure 4-3A), which indicated that  $\text{Mn}^{n+}$  species innate to  $\gamma$ - $\text{MnO}_2$  possessed Lewis acidic strength most desirable to generate  $\cdot\text{OH}/\cdot\text{OOH}/\text{O}_2\cdot^-$ . The trend found in the  $-r_{\text{H}_2\text{O}_2, 0}$  values of  $\alpha$ -/ $\beta$ -/ $\gamma$ - $\text{MnO}_2$  was in exact and partial alignments with those found in the AOS values of surface Mn species and  $-Q_{\text{ST, CO}_2}$  values of the catalysts, respectively. All the results were gathered to demonstrate that  $\text{Mn}^{n+}$  species with smaller Lewis acidic strengths could accelerate  $\cdot\text{OH}$  desorption (rate-determining step) more efficiently and thus resulted in a higher  $-r_{\text{H}_2\text{O}_2, 0}$  of the catalyst, as also proven in our previous studies on the  $\cdot\text{OH} \rightarrow \text{SO}_4\cdot^-_{\text{SUP}}$  route for NiO and Fe-modified  $\text{Mn}_3\text{O}_4$ . [25, 107] The evolution of  $\cdot\text{OH}/\cdot\text{OOH}/\text{O}_2\cdot^-$  during catalytic  $\text{H}_2\text{O}_2$  dissection on  $\alpha$ -/ $\beta$ -/ $\gamma$ - $\text{MnO}_2$  was apparent. This was evidenced by the EPR spectra of reaction mixtures and solutions collected upon the filtration of the reaction mixtures, whose compositions were identical to those used to perform  $\text{H}_2\text{O}_2$  scission runs except for adding DMPO as a spin trapper of  $\cdot\text{OH}/\cdot\text{OOH}/\text{O}_2\cdot^-$ .

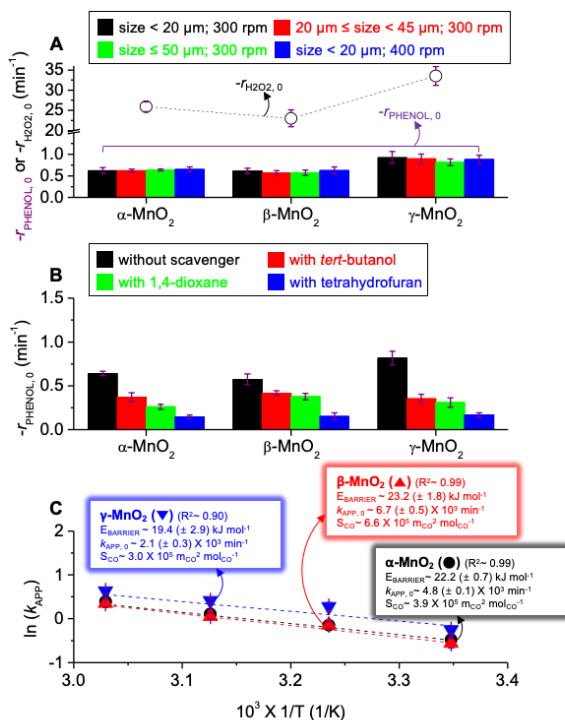


**Figure 4-3.** (A) Background-subtracted initial  $\text{H}_2\text{O}_2$  scission rates ( $-r_{\text{H}_2\text{O}_2,0}$ ) and initial phenol decomposition rates ( $-r_{\text{PHENOL},0}$ ) of  $\alpha$ -,  $\beta$ -, or  $\gamma$ - $\text{MnO}_2$ , for which particle size or stirring speed was varied during phenol decomposition runs. (B) Change in  $-r_{\text{PHENOL},0}$  values for  $\alpha$ -,  $\beta$ -, or  $\gamma$ - $\text{MnO}_2$  in the absence or the presence of quencher (*tert*-butanol, 1,4-dioxane, or tetrahydrofuran) (C) Arrhenius plots ( $\ln(k_{\text{APP}})$ ) versus  $10^3/T$  for  $\alpha$ -,  $\beta$ -, or  $\gamma$ - $\text{MnO}_2$ , whose apparent reaction rate constants ( $k_{\text{APP}}$ ) were obtained from phenol decomposition runs at 25~55 ° C. Reaction conditions: 0.2 g of the catalysts with the sizes of  $\leq 50 \mu\text{m}$  ( $\text{H}_2\text{O}_2$  scission (A), (B), and (C)) or  $< 20 \mu\text{m}/20\text{--}45 \mu\text{m}/\leq 50 \mu\text{m}$  (phenol decomposition (A)); 100 mL of de-ionized  $\text{H}_2\text{O}$ ; 30 mmol of  $\text{H}_2\text{O}_2$ ; 0 mmol ( $\text{H}_2\text{O}_2$  scission (A)) or 0.1 mmol of phenol (phenol decomposition (A), (B), and (C)); 0 mmol ((A) and (C)) or 60 mmol of quencher (B); pH of 7.0; 25 ° C (A and B) or 25~55 ° C (C); 300 rpm ( $\text{H}_2\text{O}_2$  scission (A), (B), and (C)) or 400 rpm (phenol decomposition (A)).

It was reported that DMPO can be rapidly coordinated to  $\cdot\text{OH}$  or  $\cdot\text{OOH}$  for its transition to DMPO-OH or DMPO-OOH adducts (Figure 4-4A), whose lifetimes are sufficiently long enough to be detected and are thus qualitatively analyzed through EPR spectroscopy experiments.[229, 230] Interestingly, DMPO can also bind with  $\text{O}_2^{\cdot-}$  to produce the DMPO- $\text{O}_2$  intermediate, which in turn interacts with  $\text{H}^+$  in the aqueous medium to finally transform into the DMPO-OOH adduct, as reported elsewhere.[231] Indeed,

the EPR spectra revealed large quartet signals with hyperfine splitting constants of 14.8 G for  $a(^{14}\text{N})/a(^1\text{H})$  and intensity ratios of 1:2:2:1,[229, 230] which typically indicated the presence of DMPO-OH (black squares in Figure 4-4B to 4-4D). In addition, the EPR spectra also exhibited sextet signals with hyperfine splitting constants of 14.4 G and 11.2 G for  $a(^{14}\text{N})$  and  $a(^1\text{H})$ , respectively,[229, 230] which could demonstrate the presence of DMPO-OOH (red circles in Figure 4-4B to 4-4D). Of importance, EPR spectroscopy was reported to be particular challenging for the precise quantification of multiple paramagnetic adducts, owing to overlap and/or broadness of their spectral signals.[232-234] Hence, although the relative abundance of DMPO-OH (80-95%) and DMPO-OOH (5-20%) is quantifiable upon the simulation of the EPR spectra, it should only be utilized for rough comparison. Of additional importance, the EPR spectra observed and simulated did show good agreement post the inclusion of DMPO-OOH species in the simulated EPR spectra, albeit with their small relative abundance. This suggested that the evolution of  $\cdot\text{OOH}$  might be as phenomenal as that of  $\cdot\text{OH}$  during catalytic  $\text{H}_2\text{O}_2$  scission. Interestingly, in spite of the challenge associated with the accurate quantification of the adducts, the EPR spectra of reaction mixtures (solid (catalyst) + liquid) were comparable to those of reaction solutions (liquid; Figure 4-4B to 4-4D). This could indicate that  $\cdot\text{OH}/\cdot\text{OOH}/\text{O}_2^{\cdot-}$  species were mostly present in reaction solutions and thereby demonstrated the liberation of  $\cdot\text{OH}/\cdot\text{OOH}/\text{O}_2^{\cdot-}$  species from the catalyst surfaces to liquid phases, as depicted in Figure 4-1A.

Meanwhile, phenol is one of aromatics with -OH functionality, both of which are particularly arduous to be fragmented under aqueous medium.[25, 39, 107] Therefore, phenol was utilized as a model compound of aqueous contaminants. Phenol decomposition runs on the catalysts were conducted under the identical conditions to those utilized to perform  $\text{H}_2\text{O}_2$  scission runs except for adding 0.1 mmol of phenol to reaction mixtures. It should be stressed that phenol adsorption on  $\alpha$ -/ $\beta$ -/ $\gamma$ - $\text{MnO}_2$  surfaces was not trivial

and was as considerable as phenol degradation mediated by  $\cdot\text{OH}/\cdot\text{OOH}/\text{O}_2^{\cdot-}$  evolved via  $\text{H}_2\text{O}_2$  self-decomposition (not shown). Hence, phenol adsorption on the catalyst surfaces was also deemed as backgrounds utilized for correcting reaction data. This could provide initial phenol decomposition rates of the catalysts ( $-r_{\text{PHENOL}, 0}$  in Equation (S6)), whose definition was analogous to that of  $-r_{\text{H}_2\text{O}_2, 0}$ . [25, 39, 107]

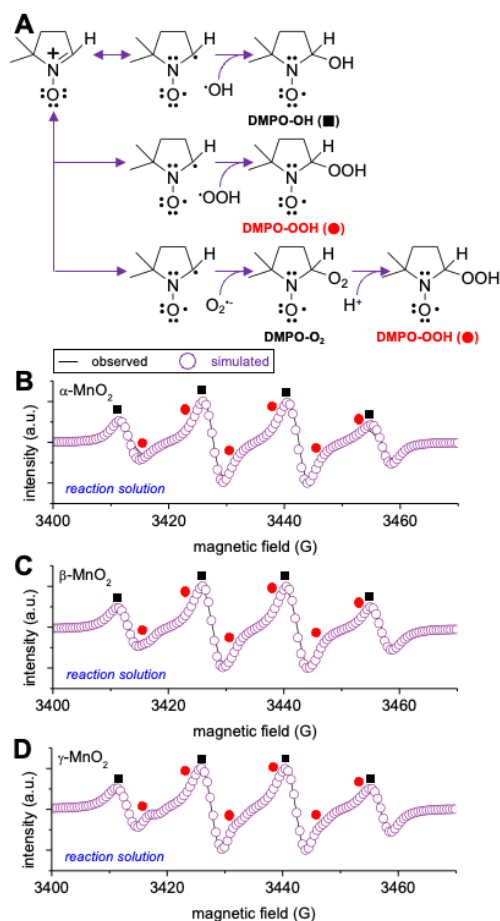


**Figure 4-4.** (A) Formation mechanisms of DMPO-OH and DMPO-OOH adducts. EPR spectra of reaction aliquots (liquid) taken from reaction mixtures (solid (catalyst) + liquid) that underwent filtration using a  $0.45\ \mu\text{m}$ -sized PES syringe (B-D). Reaction mixtures included DMPO as a spin trapper for  $\cdot\text{OH}/\cdot\text{OOH}/\text{O}_2^{\cdot-}$  and  $\alpha\text{-MnO}_2$  (B),  $\beta\text{-MnO}_2$  (C), or  $\gamma\text{-MnO}_2$  (D) as a catalyst. In (B)-(D), black solid lines and empty purple circles indicate raw and simulated EPR spectra, respectively. Black solid squares and red solid circles indicate DMPO-OH and DMPO-OOH adducts, respectively, whose relative abundance was simulated and exhibited in (B)-(D). Reaction mixture: 2 mg of the catalyst with the sizes of  $\leq 50\ \mu\text{m}$ ; 1 mL of de-ionized  $\text{H}_2\text{O}$ ; 0.3 mmol of  $\text{H}_2\text{O}_2$ ; 3 mmol of DMPO; pH of 7.0;  $25^\circ\text{C}$ ; vortex for 2 minutes.

It should be also emphasized that to rigorously assess the  $-r_{\text{PHENOL},0}$  values (activities) of the catalysts, it is imperative to ensure the  $-r_{\text{PHENOL},0}$  values are evaluated under reaction-limited regimes, in which the  $-r_{\text{PHENOL},0}$  values are not affected or directed by diffusional artifacts,[235, 236] such as the transport of phenol (or  $\cdot\text{OH}$ ) from aqueous phase to  $\text{NO}_3\cdot$  (or  $\text{NO}_3^-$ ) grafted on exterior surfaces of the catalysts (denoted as external diffusion) and the transport of phenol (or  $\cdot\text{OH}$ ) from exterior surfaces of the catalysts to  $\text{NO}_3\cdot$  (or  $\text{NO}_3^-$ ) anchored inside the catalyst pores (denoted as inter-(or intra-)particle diffusion; internal diffusion).[25] In this regard, SEM analysis of the catalysts were performed to evaluate their particle sizes, most of which were  $\leq 50\ \mu\text{m}$ . Hence, the catalysts were sieved to vary their particle sizes of  $< 20\ \mu\text{m}$ ,  $20\text{--}45\ \mu\text{m}$ , or  $\leq 50\ \mu\text{m}$  and subjected to phenol degradation runs to inspect the significance of internal diffusional artifacts on the  $-r_{\text{PHENOL},0}$  values.[25] In addition, the stirring speed of the reaction mixtures during phenol degradation runs was also altered to investigate the significance of external diffusional artifacts on the  $-r_{\text{PHENOL},0}$  values (300 rpm or 400 rpm).[25] The resulting  $-r_{\text{PHENOL},0}$  values of the catalysts, however, were invariant even with the alteration of the reaction conditions mentioned above (catalyst particle sizes or stirring speeds). This could provide evidence that  $-r_{\text{PHENOL},0}$  values were evaluated under diffusion-free environments. In addition,  $-r_{\text{PHENOL},0}$  values of the catalysts were smaller than those of the corresponding  $-r_{\text{H}_2\text{O}_2,0}$  counterparts, which was due possibly to short lifetime of  $\cdot\text{OH}$  or  $\text{O}_2\cdot^-$  (Figure 4-3A). Nonetheless, the trends found in  $-r_{\text{H}_2\text{O}_2,0}$  and  $-r_{\text{PHENOL},0}$  values for the catalysts were identical (*i.e.*,  $-r_{\text{PHENOL},0}$  of  $\sim 0.6\ \text{min}^{-1}$  for  $\alpha\text{-MnO}_2$ ;  $\sim 0.8\ \text{min}^{-1}$  for  $\gamma\text{-MnO}_2$ ). Moreover,  $\gamma\text{-MnO}_2$  leached moderate amount of Mn species after 8 hours of phenol decomposition runs ( $\sim 2.5\ \text{mol.}\%$  for  $\alpha\text{-MnO}_2$ ;  $\sim 0.1\ \text{mol.}\%$  for  $\beta\text{-MnO}_2$ ;  $\sim 0.5\ \text{mol.}\%$  for  $\gamma\text{-MnO}_2$ ). All of the results helped suggest that  $\text{Mn}^{n+}$  species innate to  $\gamma\text{-MnO}_2$  could desorb  $\cdot\text{OH}$  most proficiently.

Our claim stated above could be partially convincing, unless the solid proof

on the role of  $\cdot\text{OH}$  as the main degrade of phenol were presented. In this regard, a series of scavengers with distinct secondary rate constants in quenching  $\cdot\text{OH}$  ( $k_{\cdot\text{OH}}$ ) were selected such as *tert*-butanol ( $\sim 6.0 \times 10^8 \text{ M}^{-1} \text{ sec}^{-1}$ ), 1,4-dioxane ( $\sim 3.1 \times 10^9 \text{ M}^{-1} \text{ sec}^{-1}$ ), and tetrahydrofuran ( $\sim 4.0 \times 10^9 \text{ M}^{-1} \text{ sec}^{-1}$ ). The conditions utilized for scavenging runs were identical to those used to perform phenol decomposition runs, except for adding scavengers, whose quantities were twice that of  $\text{H}_2\text{O}_2$  utilized.[25, 39, 107] It was expected that  $-r_{\text{PHENOL},0}$  of a catalyst decreased upon the addition of a scavenger. However,  $-r_{\text{PHENOL},0}$  should be higher in the presence of a scavenger with a smaller  $k_{\cdot\text{OH}}$ , if the phenol degradation were primarily directed by  $\cdot\text{OH}$ . The reduction of  $-r_{\text{PHENOL},0}$  values for  $\alpha$ -/ $\beta$ -/ $\gamma$ - $\text{MnO}_2$  was more pronounced in the following order of ‘with *tert*-butanol  $\rightarrow$  with 1,4-dioxane  $\rightarrow$  with tetrahydrofuran’, which was concurrent to the hierarchy on the  $k_{\cdot\text{OH}}$  values for the scavengers (Figure 4-3B). This suggested that  $\cdot\text{OH}$  could function as the main degrader of phenol upon  $\text{H}_2\text{O}_2$  splitting on  $\alpha$ -/ $\beta$ -/ $\gamma$ - $\text{MnO}_2$  surfaces. In addition, *tert*-butanol was reported to barely quench  $\cdot\text{OOH}$  ( $k_{\cdot\text{OOH}}$  of  $\sim 7.1 \times 10^1 \text{ M}^{-1} \text{ sec}^{-1}$ ) or  $\text{O}_2^{\cdot-}$  and thereby should not decline  $-r_{\text{PHENOL},0}$  of a catalyst if  $\cdot\text{OOH}$  or  $\text{O}_2^{\cdot-}$  acted as a major decomposer of phenol. However, the reduction of  $-r_{\text{PHENOL},0}$  values was substantial across the catalysts in the presence of *tert*-butanol, which could corroborate that  $\cdot\text{OOH}$  or  $\text{O}_2^{\cdot-}$  was hardly exploited to decompose phenol with  $\alpha$ -/ $\beta$ -/ $\gamma$ - $\text{MnO}_2$  in use as catalysts. In addition to the nature of  $\text{O}_2^{\cdot-}$  almost inactive in decomposing phenol,[237] scavenging runs could provide concrete evidence that  $\cdot\text{OH}$  was deployed to fragment phenol. In addition to EPR spectra of the catalysts validating the evolution of  $\cdot\text{OOH}$  and/or  $\text{O}_2^{\cdot-}$  during  $\text{H}_2\text{O}_2$  scission runs (Figure 4-4), scavenging runs validated that  $\cdot\text{OOH}$  and/or  $\text{O}_2^{\cdot-}$  were major species acting as a reductant of  $\text{M}^{(\delta+1)+}$  for the recovery of  $\text{M}^{\delta+}$ . Additional control runs were performed to inspect if  $\text{Mn}^{n+}$  species could produce  $\cdot\text{OH}$  via heterogeneous catalytic scission of  $\text{H}_2\text{O}_2$ . The reaction conditions were identical to those utilized to perform phenol decomposition

runs except for vacuum filtration of reaction mixtures to collect reaction solutions after an hour of reaction runs. Phenol conversions ( $X_{\text{PHENOL}}$ ) of the resulting reaction solutions then kept being monitored up to 8 hour of reaction runs.[25, 39, 107] In addition,  $\text{H}_2\text{O}_2$  self-decomposition run in the absence of the catalyst was conducted and monitored with regard to  $X_{\text{PHENOL}}$  values up to 8 hours, for comparison.  $\text{H}_2\text{O}_2$  self-decomposition run showed the increase in  $X_{\text{PHENOL}}$  values of 4.3 ( $\pm 0.5$ ) % at 1–8 hours ( $\Delta X_{\text{PHENOL, BLANK}}$ ), which could be attributed to  $\cdot\text{OOH}$  or  $\text{O}_2^{\cdot-}$  indispensably evolved, as reported previously.[25, 39, 107, 228] Interestingly,  $\Delta X_{\text{PHENOL, BLANK}}$  obtained during  $\text{H}_2\text{O}_2$  self-decomposition run was in similar magnitude to  $\Delta X_{\text{PHENOL}}$  values obtained during filtration runs at 1–8 hours (5.2 ( $\pm 0.8$ ) % for  $\alpha$ - $\text{MnO}_2$ ; 4.3 ( $\pm 0.4$ ) % for  $\beta$ - $\text{MnO}_2$ ; 4.7 ( $\pm 1.2$ ) % for  $\gamma$ - $\text{MnO}_2$ ). This clearly indicated that unsupported, leached  $\text{Mn}^{n+}$  species tentatively present in reaction solutions did play a marginal role in producing  $\cdot\text{OH}$  used to decompose phenol. Filtration runs validated that  $\alpha$ -/ $\beta$ -/ $\gamma$ - $\text{MnO}_2$  could degrade phenol with the main use of  $\cdot\text{OH}$  species generated via heterogeneous catalytic  $\text{H}_2\text{O}_2$  scission on surface  $\text{Mn}^{n+}$  species.

Again,  $-r_{\text{H}_2\text{O}_2, 0}/-r_{\text{PHENOL}, 0}$  values of  $\alpha$ -/ $\beta$ -/ $\gamma$ - $\text{MnO}_2$  could increase at a higher temperature. This was because a larger heat energy was delivered to the catalyst surface and helped overcoming the energy barrier ( $E_{\text{BARRIER}}$ ) required to desorb  $\cdot\text{OH}$  from surface  $\text{Mn}^{n+}$  species at a greater temperature.[25, 39, 107] This indicated that the reactions should conform to Arrhenius behavior.[25, 39, 107] Hence, additional control runs were performed identically to phenol decomposition runs except for altering the temperatures from 25 ° C to 55 ° C, at which  $k_{\text{APP}}$  values of the catalysts were obtained. The resulting  $k_{\text{APP}}$  values served to establish Arrhenius plots of  $\ln(k_{\text{APP}})$  versus  $1/T$  for the catalysts, whose slopes and y-intercepts were used to extract kinetic parameters of  $E_{\text{BARRIER}}$  values and pre-factors ( $k_{\text{APP}, 0}$ ), respectively (Figure 4–3C).[25, 39, 107]  $E_{\text{BARRIER}}$  values of the catalysts increased in the following order of  $\gamma$ - $\text{MnO}_2$  ( $\sim 19.7 \text{ kJ mol}^{-1}$ ) <  $\alpha$ - $\text{MnO}_2$  ~

$\beta$ -MnO<sub>2</sub> ( $\sim 22.7$  kJ mol<sup>-1</sup>). This was in close line with the hierarchy of Lewis acidic strengths identified via AOS of Mn species and  $-Q_{ST, CO_2}$  values for the catalysts (Figure 4-2K). This again demonstrated that  $\cdot OH$  desorption could dominate H<sub>2</sub>O<sub>2</sub> scission cycle on  $\alpha$ -/ $\beta$ -/ $\gamma$ -MnO<sub>2</sub>. In addition,  $k_{APP, 0}$  values of the catalysts increased in the following sequence of  $\gamma$ -MnO<sub>2</sub> ( $\sim 2.3 \times 10^3$  min<sup>-1</sup>) <  $\alpha$ -MnO<sub>2</sub> ( $\sim 4.8 \times 10^3$  min<sup>-1</sup>) <  $\beta$ -MnO<sub>2</sub> ( $\sim 6.7 \times 10^3$  min<sup>-1</sup>), which was in exact agreement with the hierarchy found in their  $S_{CO}$  values, as discussed above. This also indicated that  $\beta$ -MnO<sub>2</sub> surface provided the greatest probability for H<sub>2</sub>O<sub>2</sub> to collide with Mn<sup>n+</sup> per unit time. Nonetheless,  $\gamma$ -MnO<sub>2</sub> showed the greatest  $-r_{PHENOL, 0}$  values throughout all temperatures considered, which clarified that small Lewis acidic strength of Mn<sup>n+</sup> species was pivotal to achieve high  $\cdot OH$  productivity on  $\alpha$ -/ $\beta$ -/ $\gamma$ -MnO<sub>2</sub> surfaces via H<sub>2</sub>O<sub>2</sub> scission.

#### 4.3.3. Properties of $\alpha$ -/ $\gamma$ -MnO<sub>2</sub>-N

$\alpha$ -/ $\beta$ -/ $\gamma$ -MnO<sub>2</sub> were subjected to NO<sub>Y</sub><sup>-</sup> functionalization to form  $\alpha$ -/ $\beta$ -/ $\gamma$ -MnO<sub>2</sub>-N upon their exposure to NO/O<sub>2</sub> stream for an hour, for which NO concentration and temperature were adjusted to 5,000 ppm and 150 ° C through the optimization for achieving the greatest quantities of N species deposited on the resulting  $\alpha$ -/ $\gamma$ -MnO<sub>2</sub>-N surfaces. Interestingly,  $\beta$ -MnO<sub>2</sub> surface was attempted to be modified with NO<sub>Y</sub><sup>-</sup> species under a variety of conditions, yet, could not afford NO<sub>Y</sub><sup>-</sup> functionalities. Again, this could be due in part to small porosity of  $\beta$ -MnO<sub>2</sub>, by which Mn<sup>n+</sup> and O <sub>$\alpha$</sub>  species were in limited access to NO<sub>Y</sub><sup>-</sup> and NO/O<sub>2</sub> even under an optimized environment used to settle down NO<sub>Y</sub><sup>-</sup> functionalities in  $\alpha$ -/ $\gamma$ -MnO<sub>2</sub> surfaces. The properties of  $\alpha$ -/ $\gamma$ -MnO<sub>2</sub>-N were characterized using a host of techniques and compared with those of  $\alpha$ -/ $\gamma$ -MnO<sub>2</sub>. Crystallographic and morphological traits of  $\alpha$ -/ $\gamma$ -MnO<sub>2</sub> were unchanged post their modification with NO<sub>Y</sub><sup>-</sup> species. This was evidenced by XRD patterns, SAED patterns, and lattice fringes ( $d$ ) in HRTEM images of  $\alpha$ -/ $\gamma$ -MnO<sub>2</sub>-N,



whose details were illustrated in figure captions. Conversely,  $S_{\text{BET}}$  and  $V_{\text{BJH}}$  values of  $\alpha$ -/ $\gamma$ - $\text{MnO}_2$ -N were smaller than those of  $\alpha$ -/ $\gamma$ - $\text{MnO}_2$  by 10–20  $\text{m}^2 \text{g}_{\text{CAT}}^{-1}$  and  $\sim 0.1 \text{ cm}^3 \text{g}_{\text{CAT}}^{-1}$ , as clarified by  $\text{N}_2$  isotherm experiments. This could be ascribed to the occupation of  $\text{NO}_Y^-$  functionalities inside the pores of  $\alpha$ -/ $\gamma$ - $\text{MnO}_2$ -N.

In addition, the amounts of Lewis acidic sites present in  $\alpha$ -/ $\gamma$ - $\text{MnO}_2$  decreased post  $\text{NO}_Y^-$  functionalization. This was corroborated by deconvoluted XP spectra of  $\alpha$ -/ $\gamma$ - $\text{MnO}_2$  and  $\alpha$ -/ $\gamma$ - $\text{MnO}_2$ -N in the Mn 2p domains,[213] where relative abundance of  $\text{Mn}^{n+}$  species were reduced from 25.2% to 18.0% for  $\alpha$ - $\text{MnO}_2$  and from 20.3% to 16.5% for  $\gamma$ - $\text{MnO}_2$  post the modification with  $\text{NO}_Y^-$  functionalities (Figure 4–5A). This was in close agreement with CO-pulsed chemisorption analysis of the catalysts,[25, 39, 107] wherein  $\text{N}_{\text{CO}}$  values were also declined from  $\sim 0.5 \mu\text{mol}_{\text{CO}} \text{g}_{\text{CAT}}^{-1}$  to  $\sim 0.4 \mu\text{mol}_{\text{CO}} \text{g}_{\text{CAT}}^{-1}$  for  $\alpha$ -/ $\gamma$ - $\text{MnO}_2$  after  $\text{NO}_Y^-$  functionalization (Figure 4–5A). Raman spectra of  $\alpha$ -/ $\gamma$ - $\text{MnO}_2$ -N also revealed the bands with Raman shifts centered at  $631.5 \text{ cm}^{-1}$  and  $632.0 \text{ cm}^{-1}$ , respectively, whose intensities were similar to those of  $\alpha$ -/ $\gamma$ - $\text{MnO}_2$ , whereas locations were blue-shifted relative to those of  $\alpha$ -/ $\gamma$ - $\text{MnO}_2$  ( $628.7 \text{ cm}^{-1}$  for  $\alpha$ - $\text{MnO}_2$ ;  $630.2 \text{ cm}^{-1}$  for  $\gamma$ - $\text{MnO}_2$ ). This could indicate the reduction of oxygen vacancies upon the functionalization of  $\alpha$ -/ $\gamma$ - $\text{MnO}_2$  with  $\text{NO}_Y^-$  species, leading to enhanced symmetric stretching vibrations of Mn–O bonds of  $[\text{Mn}^{4+}-(\text{O}^{2-})_6]^{8-}$  sub-units for  $\alpha$ -/ $\gamma$ - $\text{MnO}_2$ -N architectures.[215, 216] Moreover, this was in close alignment with the EPR spectra of  $\alpha$ -/ $\gamma$ - $\text{MnO}_2$ -N collected at  $-223^\circ \text{C}$ , in which  $g$ -factor values were almost unchanged even post  $\text{NO}_Y^-$  functionalization (2.004). The areas under the EPR signals for  $\alpha$ -/ $\gamma$ - $\text{MnO}_2$ -N were reduced markedly in comparison with those of  $\alpha$ -/ $\gamma$ - $\text{MnO}_2$ , which resulted from the decrease in the concentrations of oxygen vacancies innate to  $\alpha$ -/ $\gamma$ - $\text{MnO}_2$  architectures modified with  $\text{NO}_Y^-$  species.[213, 217] All of the analytic results stated above could corroborate that in addition to  $\text{O}_\alpha$  species allowing for an access to  $\text{NO}/\text{O}_2$ ,  $\text{Mn}^{n+}$  species on  $\alpha$ -/ $\gamma$ - $\text{MnO}_2$

could be also grafted by gaseous  $\text{NO}_Y^-$  species that were formed in proximity to  $\text{Mn}^{n+}$  sites during the synthesis of  $\alpha$ -/ $\gamma$ - $\text{MnO}_2$ -N, which was also suggested and computed elsewhere.[197–200] Of importance, the amounts of Lewis acidic sites were comparable across the catalysts subjected to  $\text{NO}_Y^-$  modification, which again posed the need to compare  $-r_{\text{H}_2\text{O}_2, 0}/-r_{\text{PHENOL}, 0}$  values of  $\alpha$ -/ $\gamma$ - $\text{MnO}_2$ -N per site basis for clarifying their geometrical effect on  $\cdot\text{OH} \rightarrow \text{NO}_3 \cdot_{\text{SUP}}$  route.

Furthermore, Lewis acidic strengths of  $\text{Mn}^{n+}$  species inherent to  $\alpha$ -/ $\gamma$ - $\text{MnO}_2$  were also altered in such a way as to improve  $\cdot\text{OH}$  desorption from  $\text{Mn}^{n+}$  species upon  $\text{NO}_Y^-$  modification. This was substantiated by XP spectra of the catalysts in the Mn 3s domains,[200, 219] in which  $\Delta E_{\text{BINDING ENERGY}}$  values of  $\alpha$ - and  $\gamma$ - $\text{MnO}_2$  increased by  $\sim 0.35$  eV and  $\sim 0.25$  eV post  $\text{NO}_Y^-$  functionalization. This led to the decrease in the resulting AOS values of surface Mn species of 3.89 for  $\alpha$ - $\text{MnO}_2 \rightarrow 3.51$  for  $\alpha$ - $\text{MnO}_2$ -N and 3.83 for  $\gamma$ - $\text{MnO}_2 \rightarrow 3.55$  for  $\gamma$ - $\text{MnO}_2$ -N (Figure 4–5B). This was also in close line with  $-Q_{\text{ST}, \text{CO}_2}$  values of the catalysts obtained via  $\text{CO}_2$  isotherm experiments.[220, 221] Interestingly,  $\alpha$ - $\text{MnO}_2$  showed a greater decrease in  $-Q_{\text{ST}, \text{CO}_2}$  from  $\sim 51.1 \text{ kJ mol}_{\text{CO}_2}^{-1}$  to  $\sim 24.7 \text{ kJ mol}_{\text{CO}_2}^{-1}$  at a near-zero coverage of  $\text{CO}_2$  post  $\text{NO}_Y^-$  modification in comparison with that of  $\gamma$ - $\text{MnO}_2$  ( $\sim 42.9 \text{ kJ mol}_{\text{CO}_2}^{-1}$  for  $\gamma$ - $\text{MnO}_2$ ;  $\sim 36.2 \text{ kJ mol}_{\text{CO}_2}^{-1}$  for  $\gamma$ - $\text{MnO}_2$ -N), as depicted in Figure 4–5B. The analytic results on Lewis acidic strengths for the catalysts highly suggested that  $\alpha$ - $\text{MnO}_2$ -N could outperform  $\gamma$ - $\text{MnO}_2$ -N in cleaving  $\text{H}_2\text{O}_2$  (or producing  $\cdot\text{OH}$ ), thus degrading phenol better than  $\gamma$ - $\text{MnO}_2$ -N based on a higher efficiency to produce  $\text{NO}_3 \cdot_{\text{SUP}}$  species.

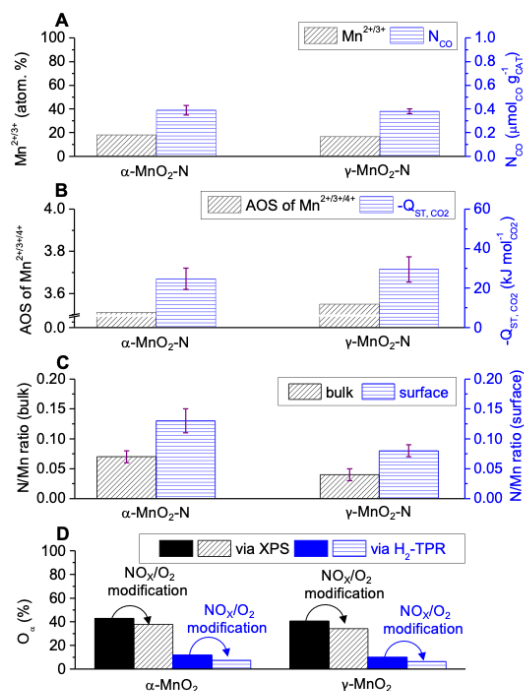


**Figure 4-5.** (A) Atomic concentrations of Mn<sup>2+</sup>/Mn<sup>3+</sup> species present in or near the surfaces of  $\alpha$ -MnO<sub>2</sub>-N and  $\gamma$ -MnO<sub>2</sub>-N and their N<sub>CO</sub> values. (B) AOS values of Mn<sup>2+</sup>/Mn<sup>3+</sup>/Mn<sup>4+</sup> species present in or near the surfaces of  $\alpha$ -MnO<sub>2</sub>-N and  $\gamma$ -MnO<sub>2</sub>-N and their -Q<sub>ST, CO2</sub> values with small CO<sub>2</sub> coverages (~5.1 μmol g<sub>CAT</sub><sup>-1</sup> for  $\alpha$ -MnO<sub>2</sub>-N and  $\gamma$ -MnO<sub>2</sub>-N). (C) Molar ratios of N to Mn (N/Mn) innate to  $\alpha$ -MnO<sub>2</sub>-N and  $\gamma$ -MnO<sub>2</sub>-N analyzed via XRF/EA (for bulk) and XP spectroscopy (XPS; for surface). (D) Relative abundance of labile O species (O<sub>α</sub>) inherent to  $\alpha$ -MnO<sub>2</sub>,  $\alpha$ -MnO<sub>2</sub>-N,  $\gamma$ -MnO<sub>2</sub>, and  $\gamma$ -MnO<sub>2</sub>-N analyzed via XPS and H<sub>2</sub>-TPR.

It should be stressed that N<sub>CO</sub> values of  $\alpha$ -/ $\gamma$ -MnO<sub>2</sub> (~0.5 μmol<sub>CO</sub> g<sub>CAT</sub><sup>-1</sup>) were reduced to show ~0.4 μmol<sub>CO</sub> g<sub>CAT</sub><sup>-1</sup> upon NO<sub>Y</sub><sup>-</sup> modification. This again could suggest that NO<sub>Y</sub><sup>-</sup> functionalities were anchored on  $\alpha$ -/ $\gamma$ -MnO<sub>2</sub>-N based on the interplays between Mn<sup>n+</sup> and gaseous NO<sub>Y</sub><sup>-</sup> species. Meanwhile, the formation of surface NO<sub>Y</sub><sup>-</sup> species based on the interactions between NO/O<sub>2</sub> and O<sub>α</sub> species was left unclarified, thus being inspected using XPS and H<sub>2</sub>-TPR experiments. XP spectra of the catalysts in the O 1s regimes showed a broad band, which was de-convoluted into three sub-bands assigned to lattice O (O<sub>β</sub>), O chemically-susceptible (O<sub>α</sub>), and O of H<sub>2</sub>O chemisorbed (O'<sub>α</sub>) with binding energies centered at ~529.8 eV, ~530.6

eV, and  $\sim 531.9$  eV, respectively.[107, 200]  $\beta$ -MnO<sub>2</sub> with  $S_{\text{BET}}$  of  $\sim 10 \text{ m}^2 \text{ g}_{\text{CAT}}^{-1}$  provided the smallest concentration of surface  $\text{O}_\alpha$  species ( $\sim 30\%$ ) among  $\alpha$ -/ $\beta$ -/ $\gamma$ -MnO<sub>2</sub>. Therefore,  $\beta$ -MnO<sub>2</sub> surface could be barely modified by  $\text{NO}_\text{Y}^-$  species and showed negligible N contents. This was evidenced by EA/XPS analytic results, all of which showed background level of N compositions ( $\sim 0$ ) in the resulting  $\beta$ -MnO<sub>2</sub>-N (not shown). We thus did not explore the properties of  $\beta$ -MnO<sub>2</sub>-N. In contrast,  $\alpha$ -/ $\gamma$ -MnO<sub>2</sub> with  $S_{\text{BET}}$  values of  $\geq \sim 50 \text{ m}^2 \text{ g}_{\text{CAT}}^{-1}$  afforded larger concentrations of surface  $\text{O}_\alpha$  species ( $\geq 40.6\%$ ) than  $\beta$ -MnO<sub>2</sub>. Indeed,  $\alpha$ -/ $\gamma$ -MnO<sub>2</sub> reduced their surface  $\text{O}_\alpha$  concentrations by 5.0–6.5% during  $\text{NO}_\text{Y}^-$  functionalization (Figure 4–5D). This indicated that  $\text{O}_\alpha$  species could bind with NO/O<sub>2</sub> and acted as an additional source used to immobilize  $\text{NO}_\text{Y}^-$  species on  $\alpha$ -/ $\gamma$ -MnO<sub>2</sub> surfaces.

As a complementary technique of XPS, H<sub>2</sub>-TPR experiments were performed to collect the profiles of H<sub>2</sub> consumption versus temperature for the catalysts. H<sub>2</sub>-TPR profiles showed a broad band over a wide temperature range of 50–800 ° C. This could be de-convoluted into four sub-bands with temperatures centered at  $\sim 215$  ° C,  $\sim 300$  ° C,  $\sim 385$  ° C, and  $\sim 465$  ° C, each of which could result from  $\text{O}_\alpha$  species and reductive transition of  $\text{Mn}^{4+} \rightarrow \text{Mn}^{3+}$ ,  $\text{Mn}^{3+} \rightarrow \text{Mn}^{2+/3+}$ ,  $\text{Mn}^{2+/3+} \rightarrow \text{Mn}^{2+}$ . [200, 238] The areas under the sub-bands assigned to  $\text{O}_\alpha$  species were quantified for the catalysts and utilized to grasp their  $\text{O}_\alpha$  concentrations.  $\beta$ -MnO<sub>2</sub> contained negligible  $\text{O}_\alpha$  contents ( $\sim 1.9\%$ ), which was in agreement with the analytic result on XPS experiment discussed above. Conversely,  $\alpha$ -/ $\gamma$ -MnO<sub>2</sub> included  $\text{O}_\alpha$  contents of 10–12% and utilized  $\text{O}_\alpha$  components of 3.5–4.5% for synthesizing  $\alpha$ -/ $\gamma$ -MnO<sub>2</sub>-N (Figure 4–5D), which again could originate from the fusion between  $\text{O}_\alpha$  and NO/O<sub>2</sub> to immobilize  $\text{NO}_\text{Y}^-$  species on the surfaces. Apparently, CO-pulsed chemisorption, XPS, and H<sub>2</sub>-TPR experiments demonstrated that the generation of  $\text{NO}_\text{Y}^-$  functionalities on  $\alpha$ -/ $\gamma$ -MnO<sub>2</sub> surfaces was of great likelihood and could originate from multiple sources such as  $\text{Mn}^{n+}/\text{NO}_\text{Y}^-$  and

$O_\alpha/NO/O_2$ .

In this regard, EA/XRF (bulk) and XPS (surface) technique served to better quantify the amounts of  $NO_Y^-$  species on  $\alpha$ -/ $\gamma$ - $MnO_2$ -N surfaces with the use of their N contents (Figure 4-5C). The molar ratios of N to Mn (N/Mn) innate to  $\alpha$ - $MnO_2$ -N were twice and  $\sim 1.5$  times those inherent to  $\gamma$ - $MnO_2$ -N in the bulk and surface scale, respectively. This highly suggested that the generation of  $NO_3^{\bullet SUP}$  species could be more efficient in  $\alpha$ - $MnO_2$ -N surface than  $\gamma$ - $MnO_2$ -N surface per unit time, if  $\cdot OH$  productivity of  $\alpha$ - $MnO_2$ -N were similar to or greater than that of  $\gamma$ - $MnO_2$ -N. It should be also stressed that binding configurations of  $NO_Y^-$  functionalities and their populations on  $\alpha$ -/ $\gamma$ - $MnO_2$ -N surfaces are essential factors to consider and therefore were analyzed via DRIFT and XPS/XANES spectroscopy, respectively. Background-subtracted *in situ* DRIFT spectra of  $\alpha$ -/ $\gamma$ - $MnO_2$  were collected by exposing the surfaces to  $NO/O_2$  stream at  $150^\circ C$  for an hour to simulate the conditions utilized to functionalize  $\alpha$ -/ $\gamma$ - $MnO_2$  surfaces with  $NO_Y^-$  species (Figure 4-6A).[200] The catalysts showed large bands, which resulted from N-O bond of  $NO_3^-$  coordinated to  $Mn^{n+}/O_\alpha$  with *mono*- or *bi*-dentate configuration.[200] The catalysts also exhibited bands, originating from N-O bond of  $NO_2^-$  bound to  $Mn^{n+}/O_\alpha$  with minute intensities.[200] The area under *in situ*  $NO/O_2$ -DRIFT spectrum of  $\alpha$ - $MnO_2$  was greater than that of  $\gamma$ - $MnO_2$ . This corroborated that  $\alpha$ - $MnO_2$  surface had a greater inclination to be modified by  $NO_Y^-$  species than  $\gamma$ - $MnO_2$ , which was also in close alignment with N/Mn ratios of  $\alpha$ -/ $\gamma$ - $MnO_2$ -N elucidated above (Figure 4-5C). XP spectra of  $\alpha$ -/ $\gamma$ - $MnO_2$ -N in the N 1s domains were further explored via de-convolution to reveal two sub-bands with binding energies centered at  $\sim 407.4$  eV and  $\sim 403.6$  eV, each of which was assigned to surface  $NO_3^-$  and  $NO_2^-$  species (Figure 4-6B and 4-6D).[239] The XP spectral results in the N 1s domains suggested that  $\alpha$ - $MnO_2$ -N surface could provide a higher  $NO_3^-$  concentration (80.2%) than  $\gamma$ - $MnO_2$ -N counterpart (49.6%). However, the XPS results discussed above did show

low ‘signal to noise’ ratios due possibly to low concentrations of surface N species (Figure 4–5C) and thus were only partially convincing.

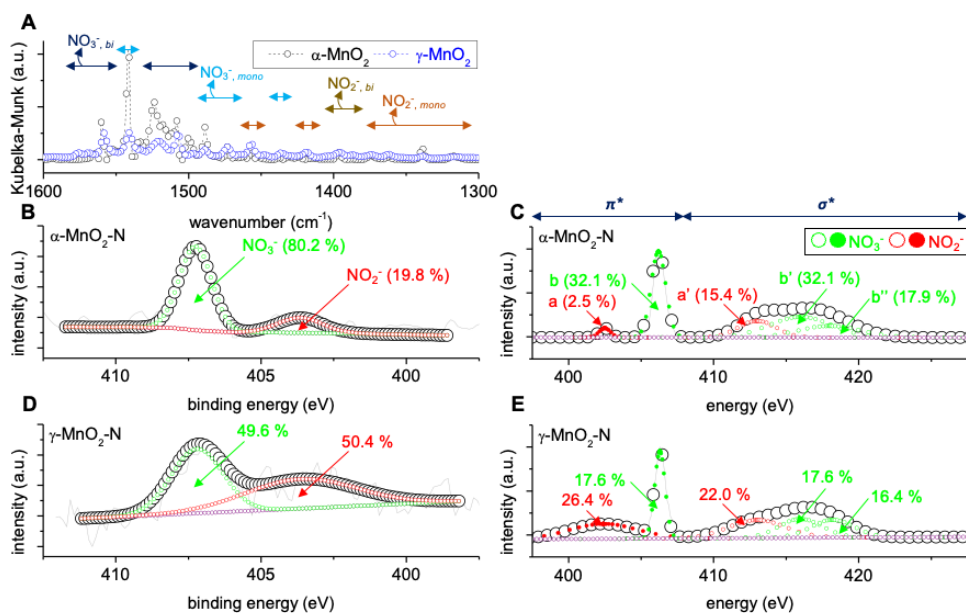


Figure 4–6. (A) Background-subtracted, *in situ* NO/O<sub>2</sub>-DRIFT spectra of  $\alpha$ -MnO<sub>2</sub> and  $\gamma$ -MnO<sub>2</sub> at 150 ° C. The surfaces were initially purged with 3 vol. % O<sub>2</sub>/N<sub>2</sub> at 110 ° C for an hour prior to the collection of their background signals under a N<sub>2</sub> at 150 ° C. The spectra of the catalysts were then recorded under 1,000 ppm NO/3 vol. % O<sub>2</sub>/N<sub>2</sub> at 150 ° C for an hour upon the subtraction of the background signals. The ramping rate and total flow rate were 10 ° C min<sup>-1</sup> and 200 mL min<sup>-1</sup>, respectively. In (A), NO<sub>2</sub><sup>-</sup> and NO<sub>3</sub><sup>-</sup> indicate vibrations of N–O bonds of NO<sub>2</sub><sup>-</sup> and NO<sub>3</sub><sup>-</sup> coordinated to the surface with distinct binding configuration of *mono*- (denoted as *mono*) or *bi*-dentate (denoted as *bi*). XP spectra of  $\alpha$ -MnO<sub>2</sub>-N (B) and  $\gamma$ -MnO<sub>2</sub>-N (D) in the N 1s domains. In (B) and (D), grey solid lines and black empty circles indicate raw and fitted XP spectra, respectively, whereas purple empty circles denote backgrounds. Numbers shown with arrows denote relative abundance of surface NO<sub>2</sub><sup>-</sup>/NO<sub>3</sub><sup>-</sup> species innate to the catalysts. XANES spectra of  $\alpha$ -MnO<sub>2</sub>-N (C) and  $\gamma$ -MnO<sub>2</sub>-N (E) at the N K-edges, in which  $\pi^*$  (a and b) and  $\sigma^*$  resonances (a', b', and b'') of surface NO<sub>2</sub><sup>-</sup>/NO<sub>3</sub><sup>-</sup> species were observed at photon energies of  $\leq 407$  eV and  $> 407$  eV, respectively.

Hence, XANES at the N K-edges also served as an alternative to accurately quantify surface NO<sub>Y</sub><sup>-</sup> concentrations innate to  $\alpha$ -/ $\gamma$ -MnO<sub>2</sub>-N. The XANES curves were divided into two domains of  $\pi^*$  and  $\sigma^*$  resonance at photon energies of  $\leq 407$  eV and  $> 407$  eV, respectively.[240, 241] Intense bands found in  $\pi^*$  resonance was de-convoluted into NO<sub>2</sub><sup>-</sup> (a in Figure 4–

6C and 4–6E) and  $\text{NO}_3^-$  (b in Figure 4–6C and 4–6E) with photon energies centered at 402.5 eV and 406.2 eV, respectively.[240, 241]  $\text{NO}_2^-$  and  $\text{NO}_3^-$  were caused by electronic transition of  $1s \rightarrow 2b_1$  and  $1s \rightarrow 2a_2''$ , respectively,[240, 241] with the latter area being larger in  $\alpha\text{-MnO}_2\text{-N}$  (32.1% relative to 2.5%) compared to  $\gamma\text{-MnO}_2\text{-N}$  (17.6% relative to 26.4%). Additional intense bands found in  $\sigma^*$  resonance were also de-convoluted into  $\text{NO}_2^-$  (a' in Figure 4–6C and 4–6E) and  $\text{NO}_3^-$  (b' and b'' in Figure 4–6C and 4–6E) with photon energies centered at 413.0 eV and 416.0 eV/418.1 eV, respectively.[240, 241]  $\text{NO}_2^-$  and  $\text{NO}_3^-$  were caused by electronic excitation to empty orbitals of  $1s \rightarrow 7a_1/5b_2$  and  $1s \rightarrow 5a_1'/5e_1'$ , respectively,[240, 241] with the latter area again being greater in  $\alpha\text{-MnO}_2\text{-N}$  (50.0% relative to 15.4%) compared to  $\gamma\text{-MnO}_2\text{-N}$  (34.0% relative to 22.0%). XP and XANES spectra provided sound evidence that  $\alpha\text{-MnO}_2\text{-N}$  provided a higher concentration of  $\text{NO}_3^-$  than  $\gamma\text{-MnO}_2\text{-N}$ . When considering that  $\text{NO}_2^\cdot$  is less electro-philic and shorter-lived than  $\text{NO}_3^\cdot$ , [185, 186, 201]  $\alpha\text{-MnO}_2\text{-N}$  could potentially degrade phenol better than  $\gamma\text{-MnO}_2\text{-N}$  by having a higher chance to evolve  $\text{NO}_3^\cdot\text{_{SUP}}$  species via  $^\cdot\text{OH} \rightarrow \text{NO}_3^\cdot\text{_{SUP}}$  route. Overall,  $\alpha\text{-MnO}_2\text{-N}$  was anticipated to outperform  $\gamma\text{-MnO}_2\text{-N}$  in degrading phenol because of multiple merits including smaller Lewis acidic strength of  $\text{Mn}^{n+}$  species for promoting  $^\cdot\text{OH}$  desorption (potential rate-determining stage of  $^\cdot\text{OH} \rightarrow \text{NO}_3^\cdot\text{_{SUP}}$  route) and larger N contents/higher  $\text{NO}_3^-$  concentration for furthering the collisions between  $^\cdot\text{OH}$  and  $\text{NO}_3^\cdot\text{_{SUP}}$  species per unit time.

#### 4.3.4. Viability of $\cdot\text{OH} \rightarrow \text{NO}_3^\cdot$ on $\alpha$ -/ $\gamma$ - $\text{MnO}_2\text{-N}$

EPR spectra of reaction mixtures and solutions were then inspected to identify a group of radicals generated such as  $\cdot\text{OH}$ ,  $\cdot\text{OOH}/\text{O}_2^{\cdot-}$ , and  $\text{NO}_Y^\cdot$  <sub>SUP</sub> under such environments that could mimic  $\cdot\text{OH} \rightarrow \text{NO}_Y^\cdot$  <sub>SUP</sub> on  $\alpha$ -/ $\gamma$ - $\text{MnO}_2\text{-N}$  with the inclusion of DMPO as a spin trapper. (see the details in Figure 4–7 caption.)

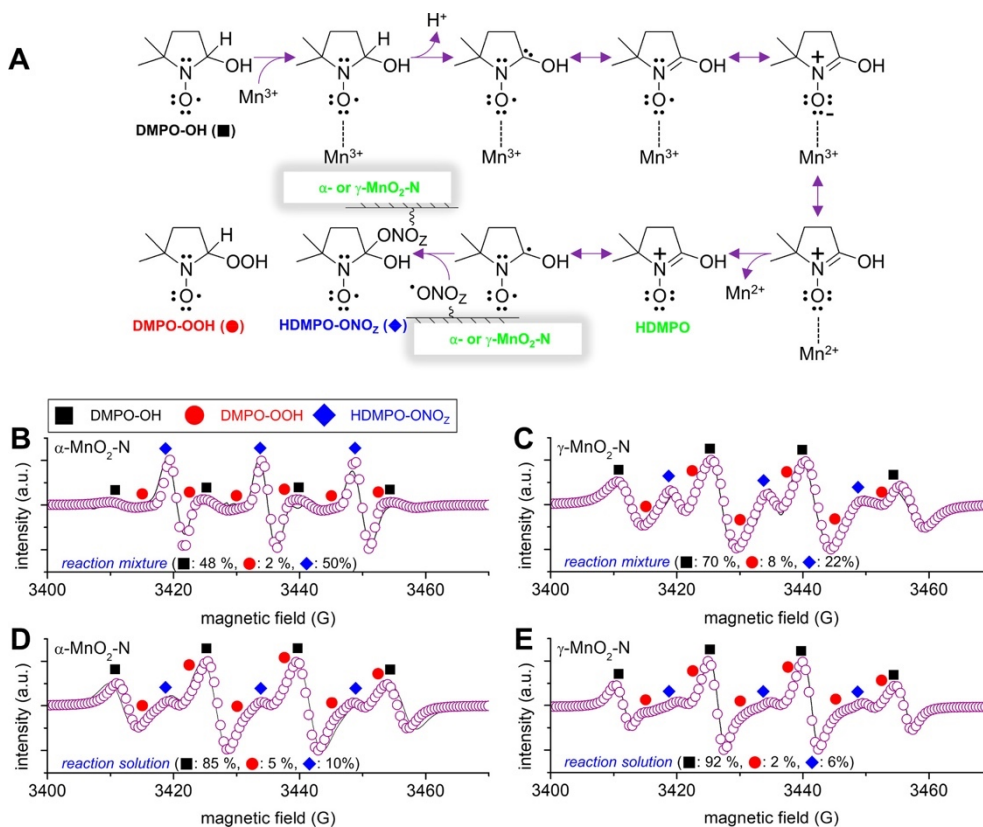


Figure 4–7. (A) Formation mechanisms of HDMPO–ONO<sub>Z</sub> adduct (Z = 1 or 2). EPR spectra of reaction aliquots taken from reaction mixtures (solid (catalyst) + liquid; B and C) or reaction solutions (liquid; D and E). Reaction mixtures contained DMPO as a spin trapper for  $\cdot\text{OH}/\cdot\text{OOH}/\text{O}_2^{\cdot-}/\text{NO}_2^\cdot$  <sub>SUP</sub>/NO<sub>3</sub><sup>·</sup> <sub>SUP</sub> and  $\alpha$ -MnO<sub>2</sub>-N (B and D) or  $\gamma$ -MnO<sub>2</sub>-N (C and E) as a catalyst. Reaction solutions were obtained from the filtration of reaction mixtures using a 0.45  $\mu\text{m}$ -sized PES syringe (D and E). In (B)–(E), black solid lines and empty purple circles indicate raw and simulated EPR spectra, respectively. Black solid squares, red solid circles, and blue solid diamonds indicate DMPO–OH, DMPO–OOH, and HDMPO–ONO<sub>Z</sub> adducts, respectively, whose relative abundance was simulated and exhibited in (B)–(E). Reaction mixture: 2 mg of the catalyst with the sizes of  $\leq 50 \mu\text{m}$ ; 1 mL of de-ionized H<sub>2</sub>O; 0.3 mmol of H<sub>2</sub>O<sub>2</sub>; 3 mmol of DMPO; pH of 7.0; 25 ° C; vortex for 2 minutes.



Of note, given the literatures on the transition of DMPO upon its coordination to  $\text{Fe}^{3+}$ , [242] a series of steps were proposed to account for the production of  $\text{NO}_Y \cdot_{\text{SUP}}$  species. Catalytic  $\text{H}_2\text{O}_2$  scission on surface  $\text{Mn}^{n+}$  sites initially form  $\cdot\text{OH}$  species, some of which can migrate into supported  $\text{NO}_Y^-$  functionalities to generate  $\text{NO}_Y \cdot_{\text{SUP}}$  species. In addition, the remaining  $\cdot\text{OH}$  species are also coordinated to DMPO to produce DMPO–OH adducts (black squares in Figure 4–7A). [101, 229, 230] Furthermore, catalytic  $\text{H}_2\text{O}_2$  scission on surface  $\text{Mn}^{n+}$  sites also produce  $\cdot\text{OOH}/\text{O}_2 \cdot^-$  species, both of which are also adducted by DMPO to form DMPO–OOH (red circles in Figure 4–7A), [101, 229–231] as illustrated in Figure 4–4. Meanwhile, DMPO–OH adducts provide lone  $e^-$  pair of O species allowing for the coordination to surface  $\text{Mn}^{3+}$  species, liberate  $\text{H}^+$ , exchange  $e^-$  with vicinal  $\text{Mn}^{3+}$  species for their reduction to  $\text{Mn}^{2+}$  analogues, and are detached from the resulting  $\text{Mn}^{2+}$  species. This can lead to the evolution of surface–unbound HDMPO adduct, as highlighted with green in Figure 4–7A. The resulting HDMPO species are finally bound to  $\text{NO}_Y \cdot_{\text{SUP}}$  species ( $\text{ONO}_Z \cdot$  on  $\alpha\text{--}/\gamma\text{--MnO}_2\text{--N}$  in Figure 4–7A, where  $Z=1$  or  $2$ ) to evolve HDMPO– $\text{ONO}_Z$  species supported on  $\alpha\text{--}/\gamma\text{--MnO}_2\text{--N}$  surfaces (blue diamonds in Figure 4–7A).

Of additional note, a number of six–membered spin adducts, where  $-\text{H}$  on  $\beta$ –carbon is replaced by  $-\text{CH}_3$ , were reported to reveal hyperfine splitting constants ( $a(^{14}\text{N})$ ) of 16.1–17.3 G in their EPR spectra. The spin adducts stated above also exhibited trio signals with the intensity ratios of 1:1:1, as might be the case with supported HDMPO– $\text{ONO}_Z$ . In addition, it was also found in previous literatures on spin adducts with partial structural similarity to supported HDMPO– $\text{ONO}_Z$  that a greater decrease in  $a(^{14}\text{N})$  was observed in a five–membered spin adduct, in which a bulkier substituent was replaced for  $-\text{H}$  on  $\beta$ –carbon,  $-\text{H}$  on  $\gamma/\gamma'$ –carbons, or  $-\text{CH}_3$  on  $\beta'$ –carbon. Hence, HDMPO– $\text{ONO}_Z$  species bound to ‘bulky  $\alpha\text{--}/\gamma\text{--MnO}_2\text{--N}$ ’ were envisaged to show  $a(^{14}\text{N})$  of  $\sim 14.7$  G, in addition to assuming  $a(^1\text{H})$  of  $\sim 1.1$  G for  $-\text{H}$  on  $\gamma$ –carbon. Indeed, the signals originating from DMPO–OH, DMPO–

OOH, and supported HDMPO-ONO<sub>Z</sub> were detected throughout the EPR spectra (Figure 4-7B to 4-7E). This did indicate that the evolution of NO<sub>Y</sub><sup>•</sup><sub>SUP</sub> on  $\alpha$ -/ $\gamma$ -MnO<sub>2</sub>-N was of great plausibility via  $\cdot\text{OH} \rightarrow \text{NO}_Y^{\bullet}\text{_{SUP}}$  route. The predicted EPR signals of supported HDMPO-ONO<sub>Z</sub> were then coupled with those of DMPO-OH/DMPO-OOH and utilized to simulate the EPR spectra. Again, the consideration of DMPO-OOH was imperative to attain good fits between EPR spectra observed and simulated, despite relative abundance of DMPO-OOH is only 2-8% across the simulated EPR spectra. In addition, although EPR spectra can only allow for rough comparison of relative abundance among paramagnetic species detected/simulated,[232-234] the intensities of signals assigned to supported HDMPO-ONO<sub>Z</sub> species were more pronounced in the EPR spectra of reaction mixtures (solid (catalyst) + liquid; 22-50%) compared to those of the corresponding reaction solutions (liquid; 6-10%), as shown in Figure 4-7. This indicated that HDMPO-ONO<sub>Z</sub> species were present in  $\alpha$ -/ $\gamma$ -MnO<sub>2</sub>-N surfaces, which could also provide sound evidence concerning the evolution of NO<sub>Y</sub><sup>•</sup><sub>SUP</sub> species via  $\cdot\text{OH} \rightarrow \text{NO}_Y^{\bullet}\text{_{SUP}}$ . It should be noted that reaction solutions also exhibited signals assigned to supported HDMPO-ONO<sub>Z</sub> species. This could be due to the inclusion of  $\alpha$ -/ $\gamma$ -MnO<sub>2</sub>-N particulates with sizes of  $< 0.45 \mu\text{m}$  in reaction mixtures because a  $0.45 \mu\text{m}$ -sized PES syringe served to isolate reaction solutions from reaction mixtures. Again, the EPR spectral results substantiated that  $\cdot\text{OH} \rightarrow \text{NO}_Y^{\bullet}\text{_{SUP}}$  route on  $\alpha$ -/ $\gamma$ -MnO<sub>2</sub>-N surfaces was highly tangible. The feasibility of  $\cdot\text{OH} \rightarrow \text{NO}_3^{\bullet}\text{_{SUP}}$  route was further investigated via DFT calculations with thermodynamic energy analysis on supported NO<sub>3</sub><sup>-</sup> (or NO<sub>3</sub><sup>•</sup>) species via cluster model.[39] Herein, NO<sub>3</sub><sup>•</sup> (or NO<sub>3</sub><sup>-</sup>) was chosen because of its merits over NO<sub>2</sub><sup>•</sup> in terms of reduction potential and lifetime,[185, 186, 201] as stated above. On the other hand, (110) facet was selected due to its thermodynamic stability and ubiquity across  $\alpha$ -/ $\beta$ -/ $\gamma$ -MnO<sub>2</sub> architectures. Initially, gaseous NO<sub>3</sub><sup>-</sup> was attempted to be intercalated into the pores normal to (110) facets for relaxed  $\alpha$ -/ $\beta$ -/ $\gamma$ -MnO<sub>2</sub> structure

models. The diffusion of  $\text{NO}_3^-$  species into the pores of  $\text{MnO}_2$ , however, was readily achievable in  $\alpha\text{-MnO}_2$  architecture, thus rationalizing the selection of  $\alpha\text{-MnO}_2$  for further calculations. The surface-terminated (110) facet of  $\alpha\text{-MnO}_2$  was then subjected to the removal of an O atom coordinated to two surface Mn species and optimized. This led to the creation of two Mn defects utilized to interact with an O atom of  $\text{NO}_3^-$ , as shown in Figure 4-8A. The energy required for two O atoms of  $\text{NO}_3^-$  to bind with defective Mn species (blue dashed circles in Figure 4-8) was highly exothermic, as evidenced by calculated adsorption energy of  $-3.0 \times 10^3 \text{ kJ mol}^{-1}$  ( $\Delta E_{\text{NO}_3^- \text{ ADSORPTION}} = E_{\text{NO}_3^- \text{ ON } \alpha\text{-MnO}_2\text{-N}} - (E_{\text{NO}_3^-} + E_{\alpha\text{-MnO}_2})$ ). It was also identified via calculations that  $\text{NO}_3^-$  could settle down in the surface-terminated (110) facet for  $\alpha\text{-MnO}_2$  via bridging *bi*-dentate configuration in the most stable fashion, while leaving an O atom highly active in degrading pollutants. This could be coupled with *in situ*  $\text{NO}/\text{O}_2$ -DRIFT spectral results on  $\alpha\text{-}/\gamma\text{-MnO}_2$  (Figure 4-6A), in which the bands originating from surface  $\text{NO}_3^-$  species with *bi*-dentate arrays were more pronounced in  $\alpha\text{-MnO}_2$  surface, thereby deriving the tentative conclusion that  $\alpha\text{-MnO}_2\text{-N}$  outperformed  $\gamma\text{-MnO}_2\text{-N}$  in accelerating  $\cdot\text{OH} \rightarrow \text{NO}_3^{\cdot \text{ SUP}}$  per unit time.

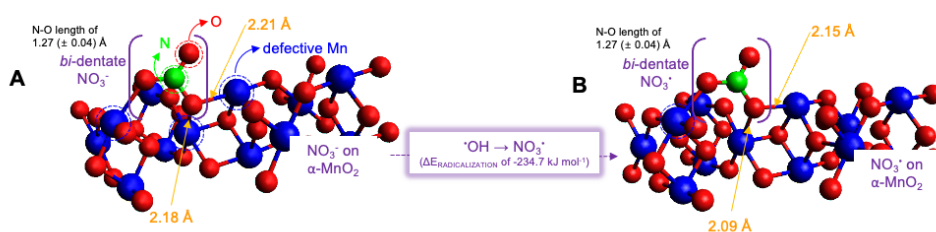


Figure 4-8. Computed surface (110) facet of  $\alpha\text{-MnO}_2$  with defective Mn species (shown with blue dashed circles) coordinated to  $\text{NO}_3^-$  (A) or  $\text{NO}_3^{\cdot}$  (B) via *bi*-dentate configurations.

Of interest, the length of N-O bonds for surface-unbound  $\text{NO}_3^-$  was calculated to  $1.44 \text{ \AA}$ , yet, was reduced to  $\sim 1.27 \text{ \AA}$  upon the adsorption of  $\text{NO}_3^-$  on  $\alpha\text{-MnO}_2$  and retained during the radicalization of  $\text{NO}_3^-$  on  $\alpha\text{-MnO}_2\text{-N}$  upon structural relaxation (Figure 4-8B). This indicated  $e^-$

extraction from supported  $\text{NO}_3^-$  could incur only a little structural deformation in the resulting  $\text{NO}_3^\cdot$  SUP. This also suggested  $^\cdot\text{OH} \rightarrow \text{NO}_3^\cdot$  SUP could be highly favorable, which was in partial line with rapid  $^\cdot\text{OH}$ -mediated radicalization of  $\text{NO}_3^-$  ion ( $^\cdot\text{OH} \rightarrow \text{NO}_3^\cdot$ ) with a  $k$  of  $\sim 10^5$ – $10^8 \text{ M}^{-1} \text{ sec}^{-1}$ . [180, 181] Of additional interest, the radicalization of supported  $\text{NO}_3^-$  could shorten the lengths of N–O bonds bound to defective Mn species from 2.18–2.21 Å to 2.09–2.15 Å. This highly suggested that  $\text{NO}_3^\cdot$  species could be coordinated to  $\alpha\text{-MnO}_2$  more rigidly than  $\text{NO}_3^-$  counterparts. Indeed, the energy released for the radicalization of  $\text{NO}_3^-$  on  $\alpha\text{-MnO}_2\text{-N}$  was computed to unveil  $234.7 \text{ kJ mol}^{-1}$  ( $\Delta E_{\text{RADICALIZATION}} \sim (E_{\text{NO}_3^\cdot \text{ on } \alpha\text{-MnO}_2\text{-N}} + E_{\text{OH}^\cdot}) - (E_{\text{NO}_3^- \text{ on } \alpha\text{-MnO}_2\text{-N}} + E_{\text{OH}^\cdot})$ ) in Figure 4–8).

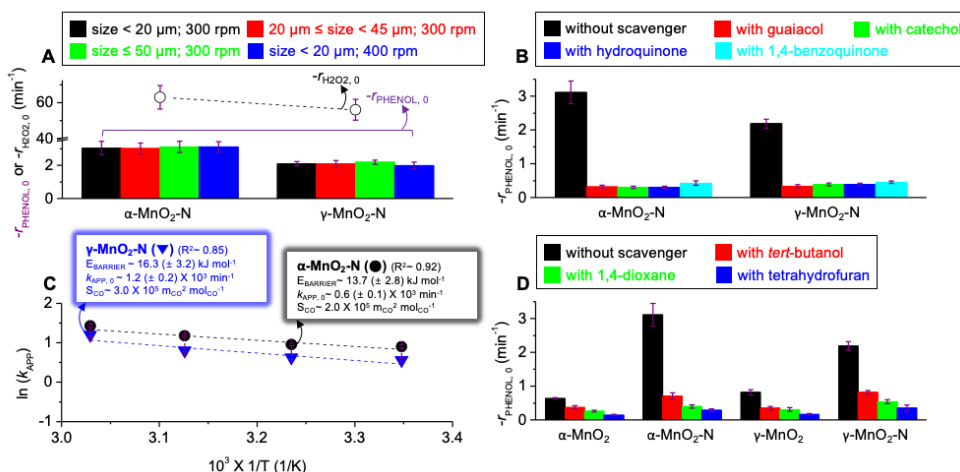


Figure 4–9. (A) Background-subtracted  $-r_{\text{H}_2\text{O}_2,0}$  and  $-r_{\text{PHENOL},0}$  values of  $\alpha\text{-MnO}_2\text{-N}$  and  $\gamma\text{-MnO}_2\text{-N}$ , for which particle size or stirring speed was varied during phenol decomposition runs. Change in  $-r_{\text{PHENOL},0}$  values for the catalysts in the absence or the presence of quencher (guaiacol, catechol, hydroquinone, or 1,4-benzoquinone for B; *tert*-butanol, 1,4-dioxane, or tetrahydrofuran for D) (C) Arrhenius plots ( $\ln(k_{\text{APP}})$  versus  $10^3/T$ ) for  $\alpha\text{-MnO}_2\text{-N}$  and  $\gamma\text{-MnO}_2\text{-N}$ , whose apparent reaction rate constants ( $k_{\text{APP}}$ ) were obtained from phenol decomposition runs at 25–55 ° C. Reaction conditions: 0.2 g of the catalysts with the sizes of  $\leq 50 \mu\text{m}$  ( $\text{H}_2\text{O}_2$  scission (A), (B), (C), and (D)) or  $< 20 \mu\text{m}/20\text{--}45 \mu\text{m}/\leq 50 \mu\text{m}$  (phenol decomposition (A)); 100 mL of de-ionized  $\text{H}_2\text{O}$ ; 30 mmol of  $\text{H}_2\text{O}_2$ ; 0 mmol ( $\text{H}_2\text{O}_2$  scission (A)) or 0.1 mmol of phenol (phenol decomposition (A), (B), (C), and (D)); quencher of 0 mmol ((A) and (C)), 60.0 mmol for  $\alpha\text{-MnO}_2$  and  $\gamma\text{-MnO}_2$ , 60.2 mmol for  $\alpha\text{-MnO}_2\text{-N}$ , and 60.1 mmol for  $\gamma\text{-MnO}_2\text{-N}$  ((B), and (D)); pH of 7.0; 25 ° C ((A), (B), and (D)) or 25–55 ° C (C); 300 rpm ( $\text{H}_2\text{O}_2$  scission (A), (B), (C), and (D)) or 400 rpm (phenol decomposition (A)).

In conjunction with the EPR spectral results discussed above, the calculation results could prove that the formation of  $\text{NO}_3^{\bullet}\text{_{SUP}}$  species was of substantial energetic favor. In addition to our validation that  $\cdot\text{OH}$  desorption was the rate-determining step of  $\text{H}_2\text{O}_2$  scission cycle on  $\alpha\text{-}/\beta\text{-}/\gamma\text{-MnO}_2$ , exothermic nature of  $\text{NO}_3^{\bullet}\text{_{SUP}}$  production could also prove that  $\cdot\text{OH}$  desorption from  $\alpha\text{-}/\gamma\text{-MnO}_2\text{-N}$  was the rate-determining stage of  $\cdot\text{OH} \rightarrow \text{NO}_3^{\bullet}\text{_{SUP}}$  route which  $\text{H}_2\text{O}_2$  scission cycle is part of. This was in close alignment with the conclusion derived in our previous studies concerning  $\cdot\text{OH} \rightarrow \text{SO}_4^{\bullet-}\text{_{SUP}}$  route, where  $\cdot\text{OH}$  desorption was endothermic and thus directed the overall  $\cdot\text{OH} \rightarrow \text{SO}_4^{\bullet-}\text{_{SUP}}$  route as the rate-determining step, whereas  $\text{SO}_4^{\bullet-}\text{_{SUP}}$  formation was exothermic.[25, 107]

#### 4.3.5. $\cdot\text{OH} \rightarrow \text{NO}_3^{\bullet}$ kinetics on $\alpha\text{-}/\gamma\text{-MnO}_2\text{-N}$

$\text{H}_2\text{O}_2$  scission/phenol decomposition runs on  $\alpha\text{-}/\gamma\text{-MnO}_2\text{-N}$  were then performed identically to those on  $\alpha\text{-}/\beta\text{-}/\gamma\text{-MnO}_2$ , whereas the resulting  $-r_{\text{H}_2\text{O}_2, 0}/-r_{\text{PHENOL}, 0}$  values were corrected using backgrounds specified above.[25, 39, 107]  $-r_{\text{H}_2\text{O}_2, 0}$  values of  $\alpha\text{-}/\gamma\text{-MnO}_2\text{-N}$  were 1.5–2.5 fold higher than those of  $\alpha\text{-}/\gamma\text{-MnO}_2$  (Figure 4–9A). This could validate the merit of  $\text{NO}_Y^-$  functionalities potentially acting as  $e^-$  donators to vicinal  $\text{Mn}^{n+}$  species, which could in turn weaken their Lewis acidic strengths, resulting in the promotion of  $\cdot\text{OH}$  desorption efficiency per unit time. In addition,  $-r_{\text{H}_2\text{O}_2, 0}$  of  $\alpha\text{-MnO}_2\text{-N}$  was  $\sim 10 \text{ min}^{-1}$  greater than that of  $\gamma\text{-MnO}_2\text{-N}$  ( $\sim 55 \text{ min}^{-1}$ ). This might suggest  $\alpha\text{-MnO}_2\text{-N}$  enhance  $\cdot\text{OH} \rightarrow \text{NO}_3^{\bullet}\text{_{SUP}}$  efficiency over  $\gamma\text{-MnO}_2\text{-N}$ , as also anticipated based on AOS values of surface Mn species and  $-\text{Q}_{\text{ST}, \text{CO}_2}$  values for  $\alpha\text{-}/\gamma\text{-MnO}_2\text{-N}$ .

$-r_{\text{PHENOL}, 0}$  values of  $\alpha\text{-}/\gamma\text{-MnO}_2\text{-N}$  were also assessed with the variation of catalyst particle sizes and/or stirring speeds to ensure negligible effects of internal/external diffusions on  $-r_{\text{PHENOL}, 0}$  values (Figure 4–9A).[25] Similar to  $-r_{\text{PHENOL}, 0}$  values of  $\alpha\text{-}/\beta\text{-}/\gamma\text{-MnO}_2$  (Figure 4–3A),  $-r_{\text{PHENOL}, 0}$  values of

$\alpha$ -/ $\gamma$ -MnO<sub>2</sub>-N were invariant even with the change in reaction conditions mentioned above. This indicated that the interactions between H<sub>2</sub>O<sub>2</sub> and Mn<sup>n+</sup>,  $\cdot$ OH and supported NO<sub>3</sub><sup>-</sup>, NO<sub>3</sub> $\cdot$ <sub>SUP</sub> and phenol were not limited by diffusional artifacts across the catalysts. In addition to exothermic nature of radical interconversion stages on  $\cdot$ OH  $\leftrightarrow$  NO<sub>3</sub> $\cdot$ <sub>SUP</sub> elucidated via DFT calculations, this could leave  $\cdot$ OH desorption as the rate-determining stage of overall  $\cdot$ OH  $\rightarrow$  NO<sub>3</sub> $\cdot$ <sub>SUP</sub> route for  $\alpha$ -/ $\gamma$ -MnO<sub>2</sub>-N. Of significance,  $-r_{\text{PHENOL}, 0}$  values of  $\alpha$ -/ $\gamma$ -MnO<sub>2</sub>-N were 2.5–5.0 fold higher than those of  $\alpha$ -/ $\gamma$ -MnO<sub>2</sub> (Figure 4–9A), which demonstrated that NO<sub>3</sub> $\cdot$ <sub>SUP</sub> could outperform conventional  $\cdot$ OH in degrading phenol. Although  $\alpha$ -/ $\gamma$ -MnO<sub>2</sub>-N barely leached N species ( $\leq 10^{-4}$  mol.%) after 8 hours of reaction runs,  $\alpha$ -MnO<sub>2</sub>-N lost Mn species markedly ( $\sim 5.2$  mol.%) compared to  $\gamma$ -MnO<sub>2</sub>-N ( $\sim 0.1$  mol.%). This posed the need of synthetic amendment used to reduce Mn leaching from  $\alpha$ -MnO<sub>2</sub>-N surface. Nonetheless,  $-r_{\text{PHENOL}, 0}$  of  $\alpha$ -MnO<sub>2</sub>-N was  $\sim 1.0 \text{ min}^{-1}$  higher than that of  $\gamma$ -MnO<sub>2</sub>-N and showed the largest  $-r_{\text{PHENOL}, 0}$  among the catalysts studied. This suggested that  $\alpha$ -MnO<sub>2</sub> could be most suitable to desorb  $\cdot$ OH and afford surface NO<sub>3</sub><sup>-</sup> species, which were combined to improve  $\cdot$ OH  $\rightarrow$  NO<sub>3</sub> $\cdot$ <sub>SUP</sub> efficiency on  $\alpha$ -MnO<sub>2</sub>-N, as also supported by computations, EA/XRF, XPS, XANES experiments, *etc.*

Filtration runs on  $\alpha$ -/ $\gamma$ -MnO<sub>2</sub>-N were carried out following the identical protocols to those used to conduct filtration runs on  $\alpha$ -/ $\beta$ -/ $\gamma$ -MnO<sub>2</sub>, whose details were discussed above.[25, 39, 107] Again, the objective of filtration runs was to verify the significance of surface-unbound, leached Mn species ( $\cdot$ OH producer) present in reaction solutions on phenol degradation performance. Thus,  $\Delta X_{\text{PHENOL}}$  values of reaction solutions (liquid) were evaluated at 1–8 hours of reaction runs upon their separation from reaction mixtures (solid (catalyst) + liquid) via vacuum filtration after an hour of reaction runs.  $\Delta X_{\text{PHENOL}}$  of reaction solution in the absence of the catalyst was  $4.3 (\pm 0.5) \% (\Delta X_{\text{PHENOL}, \text{BLANK}})$ , which again primarily resulted from H<sub>2</sub>O<sub>2</sub>

self-decomposition.[25, 39, 107, 228]  $\Delta X_{\text{PHENOL, BLANK}}$  value was comparable to  $\Delta X_{\text{PHENOL}}$  value of reaction solution separated from reaction mixture including  $\alpha\text{-MnO}_2\text{-N}$  (5.3 ( $\pm$  0.6) %) or  $\gamma\text{-MnO}_2\text{-N}$  (4.3 ( $\pm$  1.0) %). This did suggest that  $\alpha\text{-MnO}_2\text{-N}$  (or  $\gamma\text{-MnO}_2\text{-N}$ ) could decompose phenol with the main use of  $\text{NO}_3^{\cdot\text{SUP}}$  species instead of surface-unbound  $^{\cdot}\text{OH}$  tentatively produced via  $\text{H}_2\text{O}_2$  scission on leached Mn species, albeit the amount of Mn species leached from  $\alpha\text{-MnO}_2\text{-N}$  was not trivial.

To clearly identify the major degrader of phenol on  $\alpha\text{-}/\gamma\text{-MnO}_2\text{-N}$ , scavenging runs were performed identically to those on  $\alpha\text{-}/\beta\text{-}/\gamma\text{-MnO}_2$  .[25, 39, 107] The quantities of quenchers used during the reactions were around twice the amounts of  $\text{H}_2\text{O}_2$  coupled with N species of the catalysts present in reaction mixtures.[25, 39, 107] Guaiacol, catechol, hydroquinone, or 1,4-benzoquinone served as a quencher to terminate  $^{\cdot}\text{OH}$ ,  $^{\cdot}\text{OOH}$ ,  $\text{O}_2^{\cdot-}$ ,  $\text{NO}_3^{\cdot\text{SUP}}$ , or  $\text{NO}_2^{\cdot\text{SUP}}$  with a wide range of secondary rate constants in terminating the radicals stated above. If the prime degrader of phenol were  $\text{NO}_2^{\cdot\text{SUP}}$ ,  $-r_{\text{PHENOL}, 0}$  values of  $\alpha\text{-}/\gamma\text{-MnO}_2\text{-N}$  should be maintained even with the addition of hydroquinone ( $k_{\text{NO}_2^{\cdot\text{SUP}}}$  of  $0\text{ M}^{-1}\text{ sec}^{-1}$ ) into reaction mixtures. However,  $\alpha\text{-}/\gamma\text{-MnO}_2\text{-N}$  reduced their  $-r_{\text{PHENOL}, 0}$  values markedly in the presence of hydroquinone (Figure 4-9B), which allowed for the conclusion that  $\text{NO}_2^{\cdot\text{SUP}}$  functioned as minor species in decomposing phenol. In addition, hydroquinone ( $k_{^{\cdot}\text{OOH}}$  of  $1.7 \times 10^7\text{ M}^{-1}\text{ sec}^{-1}$ ) can terminate  $^{\cdot}\text{OOH}$  around  $\sim 10^3$  faster than catechol ( $k_{^{\cdot}\text{OOH}}$  of  $4.7 \times 10^4\text{ M}^{-1}\text{ sec}^{-1}$ ).  $-r_{\text{PHENOL}, 0}$  values of  $\alpha\text{-}/\gamma\text{-MnO}_2\text{-N}$  stayed under similar magnitudes upon the change in the type of scavengers from catechol to hydroquinone (Figure 4-9B), which indicated that the function of  $^{\cdot}\text{OOH}$  as the main phenol decomposer was highly unlikely. Furthermore, the difference in terminating  $\text{O}_2^{\cdot-}$  was quite dissimilar across the scavengers utilized, as evidenced by the difference in their  $k_{\text{O}_2^{\cdot-}}$  values of  $\sim 6$  orders of magnitude. Hence, if  $\text{O}_2^{\cdot-}$  were the prime decompose of phenol,  $-r_{\text{PHENOL}, 0}$  values of  $\alpha\text{-}/\gamma\text{-MnO}_2\text{-N}$  should be significantly distinct and decrease in the following

order of guaiacol ( $2.5 \times 10^3 \text{ M}^{-1} \text{ sec}^{-1}$ )  $\rightarrow$  catechol ( $2.7 \times 10^5 \text{ M}^{-1} \text{ sec}^{-1}$ )  $\rightarrow$  hydroquinone ( $1.7 \times 10^7 \text{ M}^{-1} \text{ sec}^{-1}$ )  $\rightarrow$  1,4-benzoquinone ( $1.0 \times 10^9 \text{ M}^{-1} \text{ sec}^{-1}$ ). Nonetheless,  $-r_{\text{PHENOL}, 0}$  values of  $\alpha$ -/ $\gamma$ - $\text{MnO}_2$ -N varied by less than an order of magnitude only, regardless of altering the type of scavengers utilized (Figure 4-9B), which validated that  $\text{O}_2^{\cdot -}$  acted as minor species in degrading phenol. This left  $\cdot\text{OH}$  or  $\text{NO}_3^{\cdot \text{SUP}}$  as the tentative main degrader of phenol. It should be noted that guaiacol, catechol, and hydroquinone could be barely distinct in quenching  $\cdot\text{OH}$  or  $\text{NO}_3^{\cdot \text{SUP}}$  species because their  $k_{\cdot\text{OH}}$  or  $k_{\text{NO}_3^{\cdot \text{SUP}}}$  values only differ by less than an order of magnitude.

Therefore, *tert*-butanol, 1,4-dioxane, or tetrahydrofuran served as additional quenchers to identify the prime decomposer of phenol by monitoring their effects on  $-r_{\text{PHENOL}, 0}$  values for  $\alpha$ -/ $\gamma$ - $\text{MnO}_2$ -N, whereas  $-r_{\text{PHENOL}, 0}$  values of  $\alpha$ -/ $\gamma$ - $\text{MnO}_2$  were also presented in Figure 4-9D for comparison with those of  $\alpha$ -/ $\gamma$ - $\text{MnO}_2$ -N. It was found that  $-r_{\text{PHENOL}, 0}$  values of  $\alpha$ -/ $\gamma$ - $\text{MnO}_2$  were reduced in the following order of *tert*-butanol  $\rightarrow$  1,4-dioxane  $\rightarrow$  tetrahydrofuran, which was in exact agreement with the increasing trend of  $k_{\cdot\text{OH}}$  or  $k_{\text{NO}_3^{\cdot \text{SUP}}}$  values for the quenchers utilized (Figure 4-9D). Of note,  $k_{\cdot\text{OH}}$  of *tert*-butanol, 1,4-dioxane, or tetrahydrofuran was  $10^2$ – $10^4$  fold larger than its  $k_{\text{NO}_3^{\cdot \text{SUP}}}$  counterpart. Hence, if  $\cdot\text{OH}$  were the main degrader of phenol,  $-r_{\text{PHENOL}, 0}$  of  $\alpha$ - or  $\gamma$ - $\text{MnO}_2$ -N could be of similar magnitude to or even smaller than that of  $\alpha$ - or  $\gamma$ - $\text{MnO}_2$  in the presence of the quencher mentioned above. However,  $-r_{\text{PHENOL}, 0}$  of  $\alpha$ - or  $\gamma$ - $\text{MnO}_2$ -N was always higher than that of  $\alpha$ - or  $\gamma$ - $\text{MnO}_2$  in the presence of the identical scavenger (Figure 4-9D). This suggested that  $\text{NO}_3^{\cdot \text{SUP}}$  species could play a major role in degrading phenol on  $\alpha$ -/ $\gamma$ - $\text{MnO}_2$ -N. Of additional note,  $-r_{\text{PHENOL}, 0}$  values of  $\alpha$ -/ $\gamma$ - $\text{MnO}_2$  in the presence of scavengers ( $\Delta -r_{\text{PHENOL}, 0}$ ) only differed by  $0.5$ – $0.7 \text{ min}^{-1}$ , which was highly anticipated given the difference among  $k_{\cdot\text{OH}}$  values of the scavengers used (less than an order of magnitude). Conversely,  $\Delta -r_{\text{PHENOL}, 0}$  of  $\alpha$ -/ $\gamma$ - $\text{MnO}_2$ -N was  $1.8$ – $2.8 \text{ min}^{-1}$  and far larger than that of  $\alpha$ -/ $\gamma$ - $\text{MnO}_2$  (Figure 4-9D). Considering the difference among



$k_{\text{NO}_3}$ . values of the scavengers utilized (3 orders of magnitude), one could conclude that  $\text{NO}_3 \cdot_{\text{SUP}}$  species were the prime degrader of phenol.

Arrhenius plots of  $\alpha$ -/ $\gamma$ - $\text{MnO}_2$ -N were finally constructed to compare their kinetic parameters (Figure 4-9C).[25, 39, 107] Again, Lewis acidic strength of  $\text{Mn}^{n+}$  species inherent to  $\alpha$ - $\text{MnO}_2$ -N was smaller than that innate to  $\gamma$ - $\text{MnO}_2$ -N. Thus,  $\alpha$ - $\text{MnO}_2$ -N was expected to accelerate the rate-determining stage ( $\cdot\text{OH}$  desorption) more readily than  $\gamma$ - $\text{MnO}_2$ -N. Indeed, this could be corroborated by smaller  $E_{\text{BARRIER}}$  of  $\alpha$ - $\text{MnO}_2$ -N ( $\sim 13.2 \text{ kJ mol}^{-1}$ ) compared to that of  $\gamma$ - $\text{MnO}_2$ -N ( $\sim 16.8 \text{ kJ mol}^{-1}$ ).

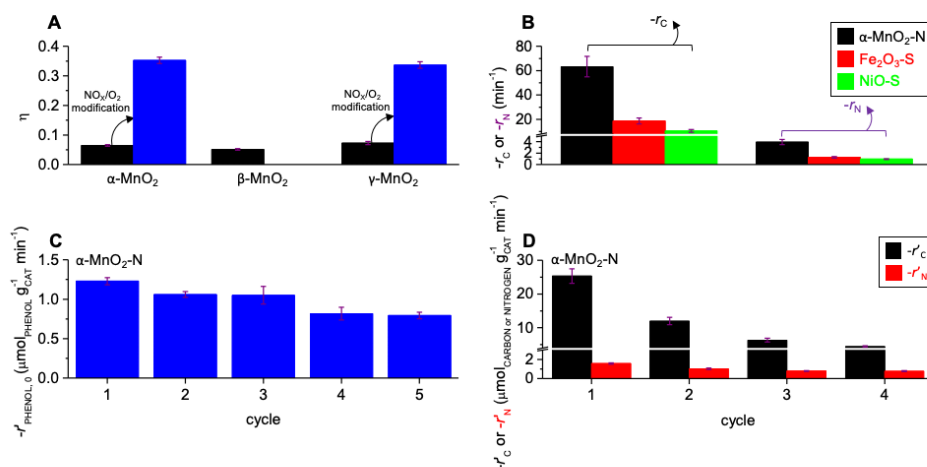


**Figure 4-10.** (A) Mineralization efficiencies ( $\eta$ ) of the catalysts in decomposing phenol (B) Background-subtracted initial degradation rates of textile wastewater for  $\alpha$ - $\text{MnO}_2$ -N,  $\text{Fe}_2\text{O}_3$ -S, and NiO-S in terms of carbon ( $-r_c$ ) or nitrogen component ( $-r_n$ ). (C) Background-subtracted initial phenol decomposition rates ( $-r_{\text{PHENOL}, 0}$ ) for as-synthesized (1<sup>st</sup> cycle) or used  $\alpha$ - $\text{MnO}_2$ -N catalysts (2<sup>nd</sup>~5<sup>th</sup> cycles). (D) Background-subtracted initial degradation rates of textile wastewater ( $-r_c$  and  $-r_n$ ) for as-synthesized (1<sup>st</sup> cycle) or used  $\alpha$ - $\text{MnO}_2$ -N catalysts (2<sup>nd</sup>~4<sup>th</sup> cycles). Reaction conditions for (C): 0.2 g of  $\alpha$ - $\text{MnO}_2$ -N (as-synthesized or used) with the sizes of  $\leq 50 \mu\text{m}$ ; 100 mL of de-ionized  $\text{H}_2\text{O}$ ; 30 mmol of  $\text{H}_2\text{O}_2$ ; 0.1 mmol of phenol; pH of 7.0; 25 ° C; 300 rpm. Reaction conditions for (B) and (D): 2 g of the catalysts (as-synthesized or used) with the sizes of  $\leq 50 \mu\text{m}$ ; 200 mL of textile wastewater undergoing vacuum-filtration with 1.2  $\mu\text{m}$  GF/C filter paper; 150 mmol of  $\text{H}_2\text{O}_2$ ; pH of 7.0; 25 ° C; 300 rpm.

Meanwhile, the collision frequency between  $\text{H}_2\text{O}_2$  and  $\text{Mn}^{n+}$  could be greater in  $\gamma$ - $\text{MnO}_2$ -N in comparison with  $\alpha$ - $\text{MnO}_2$ -N. This could be evidenced by a larger surface area of Lewis acidic  $\text{Mn}^{n+}$  species innate to  $\gamma$ - $\text{MnO}_2$ -N

( $S_{\text{CO}}$  of  $\sim 3.0 \times 10^5 \text{ m}_{\text{CO}}^2 \text{ mol}_{\text{CO}}^{-1}$ ) than that of  $\alpha\text{-MnO}_2\text{-N}$  ( $S_{\text{CO}}$  of  $\sim 2.0 \times 10^5 \text{ m}_{\text{CO}}^2 \text{ mol}_{\text{CO}}^{-1}$ ). Conversely,  $\alpha\text{-MnO}_2\text{-N}$  could enhance the collision frequency between  $\cdot\text{OH}$  and  $\text{NO}_3^-$  over  $\gamma\text{-MnO}_2\text{-N}$ , as supported by a greater N contents (via EA/XRF/XPS) and a larger concentration of  $\text{NO}_3^-$  relative to that of  $\text{NO}_2^-$  (via XPS/XANES) in conjunction with a higher  $\cdot\text{OH}$  productivity (via  $-r_{\text{H}_2\text{O}_2, 0}$ ). However, pre-factor ( $k_{\text{APP}, 0}$ ) of  $\gamma\text{-MnO}_2\text{-N}$  ( $\sim 1.6 \times 10^3 \text{ min}^{-1}$ ) was larger than that of  $\alpha\text{-MnO}_2\text{-N}$  ( $\sim 0.5 \times 10^3 \text{ min}^{-1}$ ). This suggested that  $\text{H}_2\text{O}_2 \cdot \cdot \cdot \text{Mn}^{n+}$  interactions could outweigh  $\cdot\text{OH} \cdot \cdot \cdot \text{NO}_3^-$  counterparts in improving the recurrence of  $\cdot\text{OH} \rightarrow \text{NO}_3 \cdot_{\text{SUP}}$  per unit time. Nonetheless,  $-r_{\text{PHENOL}, 0}$  values of  $\alpha\text{-MnO}_2\text{-N}$  were consistently greater than those of  $\gamma\text{-MnO}_2\text{-N}$  throughout all temperature domains considered. This made it persuasive that the core in promoting  $\cdot\text{OH} \rightarrow \text{NO}_3 \cdot_{\text{SUP}}$  route is to facilitate  $\cdot\text{OH}$  desorption for lowering  $E_{\text{BARRIER}}$  and that  $\alpha\text{-MnO}_2$  geometry is the optimum to exploit  $\cdot\text{OH} \rightarrow \text{NO}_3 \cdot_{\text{SUP}}$  route upon  $\text{NO}_3^-$  functionalization.

#### 4.3.6. Merits of $\text{NO}_3^{\cdot\text{SUP}}$ over $\cdot\text{OH}/\text{SO}_4^{\cdot\text{SUP}}$

$\text{NO}_3^{\cdot\text{SUP}}$  on  $\alpha\text{-}/\gamma\text{-MnO}_2\text{-N}$  did reveal a higher  $-r_{\text{PHENOL}, 0}$  than  $\cdot\text{OH}$  liberated from  $\alpha\text{-}/\gamma\text{-MnO}_2$ , albeit  $\alpha\text{-}/\gamma\text{-MnO}_2\text{-N}$  leached a larger or comparable quantity of Mn species compared to  $\alpha\text{-}/\gamma\text{-MnO}_2$ . Hence, the advantage of  $\text{NO}_3^{\cdot\text{SUP}}$  over conventional  $\cdot\text{OH}$  was further explored using the conversion (X) ratios of  $X_{\text{CARBON}}$  to  $X_{\text{PHENOL}}$  ( $X_{\text{CARBON}}/X_{\text{PHENOL}}$  analyzed via TOC/HPLC techniques in Equations (S10) and (S5)).[47, 107] This corresponded to mineralization efficiencies of the catalysts ( $\eta$ ) to assess the portions of phenol that underwent mineralization after 8 hours of reaction runs (Figure 4-10A).[47, 107]  $\eta$  values of  $\alpha\text{-}/\gamma\text{-MnO}_2\text{-N}$  ( $\sim 0.35$ ) were 5-7 fold larger than those of  $\alpha\text{-}/\beta\text{-}/\gamma\text{-MnO}_2$  ( $< 0.1$ ), thereby corroborating that  $\text{NO}_3^{\cdot\text{SUP}}$  outperformed conventional  $\cdot\text{OH}$  in the mineralization of phenol.  $\alpha\text{-}/\gamma\text{-MnO}_2\text{-N}$  exhibited comparable  $\eta$  values, yet, could be distinct in terms of Lewis acidic strength of  $\text{Mn}^{n+}$  ( $\cdot\text{OH}$  producer), concentration of  $\text{NO}_3^-$  ( $\text{NO}_3^{\cdot\text{SUP}}$  precursor),  $-r_{\text{PHENOL}, 0}$ , and  $E_{\text{BARRIER}}$ , leading to the conclusion that  $\alpha\text{-MnO}_2$  could be better than  $\gamma\text{-MnO}_2$  in bearing  $\text{Mn}^{n+}/\text{NO}_3^-$  species and deploying  $\cdot\text{OH} \rightarrow \text{NO}_3^{\cdot\text{SUP}}$  route upon  $\text{NO}_3^-$  functionalization.  $\alpha\text{-MnO}_2\text{-N}$  was thus subjected to phenol decomposition multiple times to test the recyclability of  $\text{NO}_3^{\cdot\text{SUP}}$  species, for which  $\alpha\text{-MnO}_2\text{-N}$  was rinsed with de-ionized  $\text{H}_2\text{O}$  and dried prior to performing next recycle run. In addition, phenol decomposition efficiencies were evaluated per mass basis to diagnose the practicability of  $\alpha\text{-MnO}_2\text{-N}$  ( $-r'_{\text{PHENOL}, 0}$  in Equation (S7)).  $-r'_{\text{PHENOL}, 0}$  of  $\alpha\text{-MnO}_2\text{-N}$  was  $\sim 1.2 \mu\text{mol}_{\text{PHENOL}} \text{g}_{\text{CAT}}^{-1} \text{min}^{-1}$  at the 1<sup>st</sup> cycle, yet, steadily decreased to  $\sim 0.6 \mu\text{mol}_{\text{PHENOL}} \text{g}_{\text{CAT}}^{-1} \text{min}^{-1}$  at the 5<sup>th</sup> cycle (Figure 4-10C). This could suggest moderate recyclability of  $\alpha\text{-MnO}_2\text{-N}$  (or  $\text{NO}_3^{\cdot\text{SUP}}$ ) in degrading phenol. In the meantime, the amount of Mn species leached from  $\alpha\text{-MnO}_2\text{-N}$  was also moderate and varied dynamically such as  $\sim 5.2 \text{ mol.}\%$ ,  $\sim 0.8 \text{ mol.}\%$ ,  $\sim 1.4 \text{ mol.}\%$ , and  $\sim 5.2 \text{ mol.}\%$  at the 1<sup>st</sup>, 2<sup>nd</sup>/3<sup>rd</sup>, 4<sup>th</sup>, and 5<sup>th</sup> cycle, respectively, with negligible quantities of N species leached ( $\leq 10^{-4} \text{ mol.}\%$ ). However, the trend

found in the amounts of  $\cdot\text{OH}$  producer (Mn) or  $\text{NO}_3\cdot$  precursor (N) leached from  $\alpha\text{-MnO}_2\text{-N}$  during recycle run was discrepant to the trend found in its  $-r'_{\text{PHENOL},0}$  values observed. In conjunction with the result on the filtration run of  $\alpha\text{-MnO}_2\text{-N}$ , this could suggest that phenol degradation on  $\alpha\text{-MnO}_2\text{-N}$  could be mainly directed by  $\text{NO}_3\cdot_{\text{SUP}}$  species.

To further demonstrate the significance of  $\text{NO}_3\cdot_{\text{SUP}}$  species in degrading phenol throughout each of the recycle runs, XRF/EA and XPS techniques served to inspect bulk and surface molar ratios of N to Mn (N/Mn) for the used catalysts. Bulk N/Mn values of the catalysts ( $0.06 (\pm 0.01)$ ) were retained even post experiencing multiple phenol degradation runs. This was in exact alignment with surface N/Mn counterparts of the catalysts exhibiting  $0.14 (\pm 0.02)$  throughout the recycle runs. Meanwhile, surface  $\text{NO}_3^-$  concentrations of the used catalysts were also explored using their XP spectra in the N 1s domains, in which relative abundance of  $\text{NO}_3^-$  species were alike throughout the recycle runs (78.8–80.2%). These were combined with minute leaching of N contents from the used catalysts to suggest high likelihood of surface  $\text{NO}_3^-$  species radicalized by  $\cdot\text{OH}$  to produce  $\text{NO}_3\cdot_{\text{SUP}}$  species during the recycle runs. In contrast,  $\text{N}_{\text{CO}}$  values of the (used) catalysts were continuously declined post each of the recycle runs ( $\sim 0.39 \mu\text{mol}_{\text{CO}} \text{g}_{\text{CAT}}^{-1}$  for pristine  $\rightarrow \sim 0.16 \mu\text{mol}_{\text{CO}} \text{g}_{\text{CAT}}^{-1}$  after the 4<sup>th</sup> cycle). This were in agreement with XP spectra of the (used) catalysts in the Mn 2p<sub>3/2</sub> regimes, where surface concentration of  $\text{Mn}^{2+/3+}$  species were steadily declined ( $\sim 14.7\%$  for pristine  $\rightarrow \sim 8.6\%$  after the 4<sup>th</sup> cycle). This could highly suggest that the evolution of  $\text{NO}_3\cdot_{\text{SUP}}$  species can be sustainable during multiple recycle runs, yet, is limited by  $\cdot\text{OH}$  species produced via catalytic  $\text{H}_2\text{O}_2$  scission. This raised the need to tune the synthetic conditions for dispersing ample  $\text{H}_2\text{O}_2$  activators ( $\text{Mn}^{2+/3+}$ ) on  $\alpha\text{-MnO}_2\text{-N}$  surface.

Textile wastewater with initial TOC, TN, and pH values of  $\sim 53 \text{ mmol}_{\text{CARBON}} \text{L}^{-1}$ ,  $\sim 6 \text{ mmol}_{\text{NITROGEN}} \text{L}^{-1}$ , and  $\sim 11$  further served to compare the practicability of  $\alpha\text{-MnO}_2\text{-N}$  along with  $\text{SO}_4^{2-}$ -functionalized  $\text{Fe}_2\text{O}_3$  ( $\text{Fe}_2\text{O}_3\text{-}$

S) and NiO (NiO-S), whose synthetic protocols were optimized to enable  $\cdot\text{OH} \rightarrow \text{SO}_4^{\cdot-}\text{SUP}$  route and utilize  $\text{SO}_4^{\cdot-}\text{SUP}$  as the main degrader of phenol.[25, 39, 107] Notably, textile wastewater was initially subjected to vacuum-filtration to eliminate suspended solids ( $\geq 1.2 \mu\text{m}$ ) acting as notorious poisons of catalyst surfaces,[243, 244] whereas pH of textile wastewater was set to  $\sim 7$  using  $\text{H}_2\text{SO}_4$  for the removal of  $\text{CO}_3^{2-}/\text{HCO}_3^-$  ions functioning as  $\cdot\text{OH}$  scavenger.[245, 246] Textile wastewater degradation runs on  $\alpha\text{-MnO}_2\text{-N}$ ,  $\text{Fe}_2\text{O}_3\text{-S}$ , and  $\text{NiO-S}$  were conducted to evaluate their initial degradation rates ( $-r_{\text{C}}/-r_{\text{N}}$  in Equations (S11) and (S12)).  $-r_{\text{C}}/-r_{\text{N}}$  values were defined as the moles of C/N contents consumed per Lewis acidic site per unit time upon the correction using backgrounds such as  $\text{H}_2\text{O}_2$  self-decomposition and pollutants' adsorption.[25, 39, 107] Importantly,  $\text{NO}_3^{\cdot}\text{SUP}$  was demonstrated to degrade textile wastewater far more efficiently than  $\text{SO}_4^{\cdot-}\text{SUP}$ . This was evidenced by  $-r_{\text{C}}$  ( $\sim 65 \text{ min}^{-1}$ ) and  $-r_{\text{N}}$  values ( $\sim 4 \text{ min}^{-1}$ ) of  $\alpha\text{-MnO}_2\text{-N}$ , both of which were higher than those of  $\text{Fe}_2\text{O}_3\text{-S}$  and  $\text{NiO-S}$  ( $-r_{\text{C}}$  values of  $\leq \sim 20 \text{ min}^{-1}$ ;  $-r_{\text{N}}$  values of  $\leq \sim 1 \text{ min}^{-1}$  in Figure 4-10B), while similarly leaching metal components during half an hour of reaction runs ( $\leq \sim 0.5 \text{ mol.}\%$ ). This could prove the superiority of  $\text{NO}_3^{\cdot}\text{SUP}$  relative to  $\text{SO}_4^{\cdot-}\text{SUP}$  in decomposing real wastewater. Finally,  $\alpha\text{-MnO}_2\text{-N}$  was exposed to degradation environments of textile wastewater multiple times to examine its recyclability with the use of initial degradation rates assessed per mass basis ( $-r'_{\text{C}}/-r'_{\text{N}}$  in Equations (S13) and (S14)). The resulting  $-r'_{\text{C}}/-r'_{\text{N}}$  values of  $\alpha\text{-MnO}_2\text{-N}$  were gradually reduced to show a sixth and half of their initial values at the 4<sup>th</sup> cycle (Figure 4-10D), respectively. This could be due in part to suspended solids ( $< 1.2 \mu\text{m}$ ) present in textile wastewater subjected to vacuum filtration, which were continuously accumulated on/near  $\text{Mn}^{n+}$  and  $\text{NO}_3^-$  species throughout each of the recycle runs, resulting in severe decline in their access to  $\text{H}_2\text{O}_2$  and  $\cdot\text{OH}$ /phenol, respectively, at the 4<sup>th</sup> cycle. This could be partially substantiated by the continuous decrease in  $\text{N}_{\text{CO}}$  values of the (used) catalysts throughout each of the recycle runs ( $\sim 0.39 \mu\text{mol}_{\text{CO}} \text{ g}_{\text{CAT}}^{-1}$

<sup>1</sup> for pristine;  $\sim 0.20 \mu\text{mol}_{\text{CO}} \text{g}_{\text{CAT}}^{-1}$  after the 1<sup>st</sup> cycle;  $\sim 0.13 \mu\text{mol}_{\text{CO}} \text{g}_{\text{CAT}}^{-1}$  after the 2<sup>nd</sup> cycle;  $\sim 0.11 \mu\text{mol}_{\text{CO}} \text{g}_{\text{CAT}}^{-1}$  after the 3<sup>rd</sup> cycle). Nevertheless,  $\alpha$  – MnO<sub>2</sub>–N leached negligible quantities of Mn species from the 2<sup>nd</sup> cycle (for 30 minutes;  $\sim 0.5 \text{ mol.}\%$  and  $\sim 0.1 \text{ mol.}\%$  at the 1<sup>st</sup> and the 2<sup>nd</sup>–4<sup>th</sup> cycles). A series of reaction runs were gathered to derive the conclusion that in comparison with conventional  $\cdot\text{OH}$  and  $\text{SO}_4^{\cdot-}\text{SUP}$ ,  $\text{NO}_3^{\cdot}\text{SUP}$  is particularly promising as the decomposer of refractory aqueous contaminants.

## 4.4. Conclusions

This study has exploited polymorphic  $\text{MnO}_2$  as a platform to bear Lewis acidic  $\text{Mn}^{2+/3+}$  species and  $\text{NO}_3^-$  functionalities on the surfaces.  $\text{Mn}^{2+/3+}$  species served to cleave  $\text{H}_2\text{O}_2$  for the production of surface-unbound  $\cdot\text{OH}$  species, which in turn could interact with  $\text{NO}_3^-$  functionalities in proximity, enabled radical interconversion of  $\cdot\text{OH} \leftrightarrow \text{NO}_3\cdot$  (or denoted as  $\cdot\text{OH} \rightarrow \text{NO}_3\cdot$ ), resulting in the evolution of supported  $\text{NO}_3\cdot$  ( $\text{NO}_3\cdot_{\text{SUP}}$ ) species deployed to fragment aqueous pollutants (phenol or textile wastewater).

$\alpha$ -/ $\beta$ -/ $\gamma$ - $\text{MnO}_2$  polymorphs provide distinct structural traits. Hence,  $\alpha$ -/ $\beta$ -/ $\gamma$ - $\text{MnO}_2$  poly-crystallites synthesized herein were hypothesized to afford defective  $\text{Mn}^{2+/3+}$  species with diverse Lewis acidic strengths, which are vital to direct the rate-determining step ( $\cdot\text{OH}$  desorption) of  $\text{H}_2\text{O}_2$  scission cycle and initial reaction rates in cleaving  $\text{H}_2\text{O}_2$  ( $-r_{\text{H}_2\text{O}_2, 0}$ ) or decomposing phenol ( $-r_{\text{PHENOL}, 0}$ ). Indeed,  $\text{Mn}^{2+/3+}$  species inherent to  $\alpha$ -/ $\beta$ -/ $\gamma$ - $\text{MnO}_2$  acted as major species in cleaving  $\text{H}_2\text{O}_2$ , resulting in the liberation of  $\cdot\text{OH}/\cdot\text{OOH}/\text{O}_2\cdot^-$  into aqueous environments, as evidenced by EPR spectra observed/simulated. Of note, filtration runs corroborated that surface-unbound  $\text{Mn}^{2+/3+}$  species leached from  $\alpha$ -/ $\beta$ -/ $\gamma$ - $\text{MnO}_2$  surfaces did function as minor species in producing  $\cdot\text{OH}/\cdot\text{OOH}/\text{O}_2\cdot^-$ , among which  $\cdot\text{OH}$  was identified to primarily decompose phenol, as substantiated by scavenging runs. Of additional note,  $\text{Mn}^{2+/3+}$  species innate to  $\gamma$ - $\text{MnO}_2$  were verified to possess the smallest Lewis acidic strengths, thus exhibiting the greatest  $-r_{\text{H}_2\text{O}_2, 0}$  and  $-r_{\text{PHENOL}, 0}$  values among  $\alpha$ -/ $\beta$ -/ $\gamma$ - $\text{MnO}_2$ .

Meanwhile,  $\alpha$ -/ $\beta$ -/ $\gamma$ - $\text{MnO}_2$  surfaces might exhibit high affinity to  $\text{NO}_3^-$  species and therefore were modified by  $\text{NO}/\text{O}_2$  to immobilize surface  $\text{NO}_3^-$  functionalities on  $\alpha$ -/ $\gamma$ - $\text{MnO}_2$ , denoted as  $\alpha$ -/ $\gamma$ - $\text{MnO}_2\text{-N}$ . It should be stressed that  $\beta$ - $\text{MnO}_2$  barely underwent the modification with  $\text{NO}_3^-$  species due to its small pore size, as also demonstrated by DFT calculations, thus being excluded for further inspection. XPS and  $\text{CO}_2$  isotherm experiments provided evidence that  $\text{Mn}^{2+/3+}$  species innate to  $\alpha$ -/ $\gamma$ - $\text{MnO}_2\text{-N}$  were less

Lewis acidic than those inherent to  $\alpha$ -/ $\gamma$ -MnO<sub>2</sub>, thus enhancing  $-r_{\text{H}_2\text{O}_2, 0}$  values for  $\alpha$ -/ $\gamma$ -MnO<sub>2</sub>-N. In addition,  $\alpha$ -MnO<sub>2</sub>-N provided smaller Lewis acidity than  $\gamma$ -MnO<sub>2</sub>-N and thus could expedite the rate-determining stage of  $\cdot\text{OH} \rightarrow \text{NO}_3\cdot$  route ( $\cdot\text{OH}$  desorption) better than  $\gamma$ -MnO<sub>2</sub>-N. This was demonstrated by a smaller energy barrier needed to enable  $\cdot\text{OH} \rightarrow \text{NO}_3\cdot$  route for  $\alpha$ -MnO<sub>2</sub>-N in comparison with that for  $\gamma$ -MnO<sub>2</sub>-N.

On the other hand,  $\alpha$ -MnO<sub>2</sub> imparted Mn<sup>2+/3+</sup> and labile O, both of which were more adequate to disperse NO<sub>3</sub><sup>-</sup> functionalities compared to those of  $\gamma$ -MnO<sub>2</sub>. This led to higher N contents (via EA/XRF and XPS) and higher NO<sub>3</sub><sup>-</sup> concentration (via XPS/XANES) in the resulting  $\alpha$ -MnO<sub>2</sub>-N in comparison with  $\gamma$ -MnO<sub>2</sub>-N, all of which again could allow for the tentative conclusion that  $\alpha$ -MnO<sub>2</sub> is the optimum architecture to proceed with  $\cdot\text{OH} \rightarrow \text{NO}_3\cdot$  route upon NO<sub>3</sub><sup>-</sup> functionalization. Apparently,  $\cdot\text{OH} \rightarrow \text{NO}_3\cdot$  route could be activated by  $\alpha$ -/ $\gamma$ -MnO<sub>2</sub>-N surfaces to generate  $\cdot\text{OH}/\cdot\text{OOH}/\text{O}_2^{\cdot-}/\text{NO}_2^{\cdot\text{SUP}}/\text{NO}_3^{\cdot\text{SUP}}$ , as substantiated by EPR spectra observed/simulated. Of significance, the formation of NO<sub>3</sub><sup>·SUP</sup> via radical transfer from  $\cdot\text{OH}$  to NO<sub>3</sub><sup>-</sup> was highly tangible and exothermic across  $\alpha$ -/ $\gamma$ -MnO<sub>2</sub>-N surfaces, as proved by EPR spectra observed/simulated and DFT calculations, respectively. Of additional significance, NO<sub>3</sub><sup>·SUP</sup> on  $\alpha$ -/ $\gamma$ -MnO<sub>2</sub>-N played a major role in decomposing phenol, as validated by scavenging and filtration runs.

Overall,  $\alpha$ -MnO<sub>2</sub>-N outperformed  $\gamma$ -MnO<sub>2</sub>-N in decomposing phenol and textile wastewater with the prime utilization of NO<sub>3</sub><sup>·SUP</sup> species. The efficiency of NO<sub>3</sub><sup>·SUP</sup> on  $\alpha$ -MnO<sub>2</sub>-N in decomposing phenol or textile wastewater was higher than those of conventional  $\cdot\text{OH}$  and/or supported SO<sub>4</sub><sup>·-</sup> species generated via radical interconversion of  $\cdot\text{OH} \leftrightarrow \text{SO}_4^{\cdot-}$  on Fe<sub>2</sub>O<sub>3</sub> or NiO we discovered previously. This study has demonstrated the impact of NO<sub>3</sub><sup>·SUP</sup> as a potent degrader of aqueous contaminants, yet, opens an additional study on how to increase the amount of NO<sub>3</sub><sup>·SUP</sup> precursors (NO<sub>3</sub><sup>-</sup>) deposited on the catalyst surface.



# Chapter 5

## Deploying radical inter-transition from $\cdot\text{OH}$ to supported $\text{NO}_3\cdot$ on *mono*-dentate $\text{NO}_3^-$ -modified $\text{ZrO}_2$ to sustain fragmentation of aqueous contaminants

The essence of Chapter 5 has been published in Separation and Purification Technology. Reprinted with permission from [247].

### 5.1. Introduction

*Tetragonal/monoclinic*  $\text{ZrO}_2$  polymorphs are chemically robust[248, 249] and consist of  $[(\text{Zr}^{4+})-(\text{O}^{2-})_8]^{12-}/[(\text{Zr}^{4+})-(\text{O}^{2-})_7]^{10-}$  sub-units, whose  $\text{Zr}^{4+}$  cations *octa*-fold/*hepta*-fold connected to  $\text{O}^{2-}$  anions are coordinatively-saturated and confined in  $\text{Zr}^{4+}-\text{O}^{2-}-\text{Zr}^{4+}-\text{O}^{2-}-\text{Zr}^{4+}$  channels.[250, 251] Of interest is the alteration of electronic feature for  $\text{Zr}^{4+}-\text{O}^{2-}-\text{Zr}^{4+}-\text{O}^{2-}-\text{Zr}^{4+}$  channels on  $\text{ZrO}_2$  surface terminated. Albeit with non-reducibility and void d-orbitals of  $\text{Zr}^{4+}$  cations, these cations can be defective upon the loss of vicinal  $\text{O}^{2-}$  anions.[196, 251, 252] This can create Lewis acidic surface  $\text{Zr}^{4+}\cdot$  ( $\text{LA}_\text{I}$  in Figure 5-1A) and/or  $\cdot\text{Zr}^{4+}$  ( $\text{LA}_\text{II}$  in Figure 5-1A) species with  $\text{O}^{2-}$  species being reduced to form  $\text{O}^{\cdot-}$  analogues bound to adjacent  $\text{Zr}^{4+}$  cations ( $*$  in Figure 5-1A), where  $\cdot$  denotes a free electron trapped in surface  $\text{Zr}^{4+}$  cation.[196, 251, 252] For instance, *monoclinic*  $\text{ZrO}_2$  terminated on major surface facets can bear  $\text{Zr}^{4+}$  species with coordination numbers of 7 (closed), 6 ( $\text{LA}_\text{I}$ ), and 5 or less ( $\text{LA}_\text{II}$ ).[196, 251, 252] Of additional interest is distinct adsorptive properties of  $\text{LA}_\text{I}$  and  $\text{LA}_\text{II}$ .  $\text{LA}_\text{I}$  interacts with unpaired electron of a reactive molecule through the formation of covalent bond ( $\text{NO}$ ,  $\text{NO}_2$ , and  $\cdot\text{OH}$ ),[253, 254] whereas  $\text{LA}_\text{II}$  binds with lone electron pairs of a reactive molecule through the generation of coordinative bond ( $\text{CO}$ ,  $\text{CO}_2$ ,  $\text{NH}_3$ , and  $\text{H}_2\text{O}_2$ ) in addition to enabling to form covalent bonds with

NO/NO<sub>2</sub>/ $\cdot$ OH.[252–255] Moreover, surface  $\text{Zr}^{4+}\text{--O}^{2-}\text{--Zr}^{4+}\text{--O}^{2-}\text{--Zr}^{4+}$  channels adsorb/dissociate H<sub>2</sub>O spontaneously under aqueous environments to evolve H<sup>+</sup> and OH<sup>−</sup>, which are bound to surface O<sup>2−</sup> and LA<sub>II</sub>, respectively, and generate two Brönsted acidic sites (BA in Figure 5–1A).[256–259] It is also feasible that O $\cdot^-$  bound to surface Zr<sup>4+</sup> cation (\* in Figure 5–1A) interplays with aqueous hydrogen (H $\cdot$ ) to yield BA site.[256–259] It should be stressed that H and O atoms of BA sites can bind with O atom of CO<sub>2</sub> and H atom of H<sub>2</sub>O<sub>2</sub>, respectively.[256, 257, 260] Meanwhile, the transition of LA<sub>II</sub> to BA via dissociative H<sub>2</sub>O adsorption[256–259] makes it unavoidable that ZrO<sub>2</sub> surface is BA-rich, LA<sub>II</sub>-limited, and thereby should possess weak affinity to H<sub>2</sub>O for reducing additional loss of LA<sub>II</sub> sites via H<sub>2</sub>O adsorption/dissociation.

Our discussions mentioned earlier pose tentative merits of ZrO<sub>2</sub> as an activator for aqueous-phase catalysis directed by LA<sub>II</sub>/BA sites with LA<sub>II</sub> leaching to an aqueous phase evaded. Homolytic H<sub>2</sub>O<sub>2</sub> dissection (H<sub>2</sub>O<sub>2</sub>→2 $\cdot$ OH) is mediated by BA and LA<sub>II</sub> sites ( $\cdot$ Zr<sup>4+</sup> $\cdot$ ,  $\cdot$ Nb<sup>5+</sup> $\cdot$ ,  $\cdot$ Ta<sup>5+</sup> $\cdot$ , *etc.*),[261–263] whereas  $\cdot$ OH species evolved can radicalize/destabilize aqueous refractory pollutants mineralized to yield H<sub>2</sub>O/CO<sub>2</sub>.[9, 42] Notably, homolytic H<sub>2</sub>O<sub>2</sub> dissection provides ample advantages over heterolytic H<sub>2</sub>O<sub>2</sub> counterpart mediated by reducible, Lewis acidic metals (H<sub>2</sub>O<sub>2</sub>+e<sup>−</sup>→ $\cdot$ OH+OH<sup>−</sup>; e<sup>−</sup> provided from Fe<sup>2+</sup>, Ni<sup>2+</sup>, Mn<sup>2+/3+</sup>, *etc.*)[25, 39, 107] such as higher  $\cdot$ OH productivity, no need to regenerate metals via e<sup>−</sup> (electron) reduction, negligible metal leaching, *etc.*[261–263] We thus revisited and inspected homolytic H<sub>2</sub>O<sub>2</sub> dissection on ZrO<sub>2</sub> with regard to its kinetics, energetics, and rate-determining step,[264] while proposing elementary stages of H<sub>2</sub>O<sub>2</sub> adsorption, H<sub>2</sub>O<sub>2</sub> distortion, H<sub>2</sub>O<sub>2</sub> scission, and  $\cdot$ OH desorption (Figure 5–1B).[256, 257, 262, 264] Initially, H atoms of H<sub>2</sub>O<sub>2</sub> interplay with O atoms of BA sites for exothermic H<sub>2</sub>O<sub>2</sub> adsorption on the surface.[256, 257, 262, 264] Surface H<sub>2</sub>O<sub>2</sub> species then experience endothermic distortion, whose energy required can decrease under such

environments that hydrogen bonds between H atoms of  $\text{H}_2\text{O}_2$  and O atoms of BA sites are rigid (BA strength;  $E_{\text{BA}} \downarrow$ ), while  $\text{LA}_{\text{II}}$  site vicinal to BA sites possesses high coordinative affinity to lone electron pairs of  $\text{H}_2\text{O}_2$  ( $\text{LA}_{\text{II}}$  strength;  $E_{\text{LA}} \uparrow$ ). [256, 257, 262, 264] The surface  $\text{H}_2\text{O}_2$  species twisted did undergo exothermic scission to generate two  $\cdot\text{OH}$  species, whose O atoms are covalent-bonded to  $\text{LA}_{\text{II}}$  sites, whereas H atoms are hydrogen-bonded to O atoms of BA sites. [256, 257, 262, 264] Two surface  $\cdot\text{OH}$  species finally experience endothermic desorption, whose facilitation is achievable by elevating  $E_{\text{BA}}$  (deprotonation  $\uparrow$ ) and  $E_{\text{LA}}$  (electron-sharing tendency  $\downarrow$ ) of BA/ $\text{LA}_{\text{II}}$  sites. [253, 254, 264] Of significance,  $\cdot\text{OH}$  desorption is verified as the rate-directing stage, [264] which suggests the necessity to escalate  $E_{\text{BA}}/E_{\text{LA}}$  values of BA/ $\text{LA}_{\text{II}}$  sites for reducing energy barrier ( $E_{\text{BARRIER}}$ ) of homolytic  $\text{H}_2\text{O}_2$  dissection. Moreover, its collision frequency can be escalated by enlarging the area of BA or  $\text{LA}_{\text{II}}$  site ( $S_{\text{BA}}$  or  $S_{\text{LA}}$ ) given that larger  $S_{\text{BA}}$  and  $S_{\text{LA}}$  values can promote the interplays of  $\text{BA} \cdots \text{H}_2\text{O}_2$  for  $\text{H}_2\text{O}_2$  adsorption and  $\text{LA}_{\text{II}} \cdots \text{H}_2\text{O}_2$  for  $\text{H}_2\text{O}_2$  distortion, respectively. [256, 257, 262, 264] In our previous study, Lewis basic N/S dopants acting as electron donors were located near  $\text{LA}_{\text{II}}$ /BA sites of  $\text{ZrO}_2$  particulates dispersed on carbon scaffolds. [264] This was in success to improve  $E_{\text{BA}}/S_{\text{BA}}$  values of  $\text{ZrO}_2$  clusters modified with N/S dopants, yet, declined their  $E_{\text{LA}}/S_{\text{LA}}$  values. [264] Herein, we suggested the use of  $\text{NO}_Y^-$  species ( $Y=2$  or  $3$ ) as modifiers of  $\text{ZrO}_2$  surface for elevating its  $E_{\text{BA}}$ ,  $E_{\text{LA}}$ ,  $S_{\text{BA}}$ , or  $S_{\text{LA}}$  with an aim to promote homolytic  $\text{H}_2\text{O}_2$  dissection efficiency ( $\cdot\text{OH}$  productivity). Based on literatures concerning  $\text{NO}_Y^-$  adsorption on metal oxide surfaces, [18, 200, 225] it was speculated that under low thermal energies ( $\leq 150^\circ\text{C}$ ),  $\text{O}^{\cdot-}$  bound to surface  $\text{Zr}^{4+}$  cation (\* in Figure 5-1A) can initially interplay with NO to form  $\text{NO}_2^-$  supported on  $\text{ZrO}_2$  ( $\text{NO}_2^-_{\text{SUP}}$  in Figure 5-1A), which in turn can react with  $\text{O}_2$  co-fed to produce supported  $\text{NO}_3^-$  ( $\text{NO}_3^-_{\text{SUP}}$  in Figure 5-1A). The evolution of  $\text{NO}_2^-_{\text{SUP}}$  functionalities is imperative, yet, can be beneficial owing to electronic trait of  $\text{NO}_2^-$  acting as an electron acceptor. [265] Hence,  $\text{NO}_2^-_{\text{SUP}}$  species may

withdraw electrons from proximal  $LA_{II}$  sites and potentially elevate their  $E_{LA}$  values. Furthermore,  $NO_3^-$  acts as an electron donator[266] and therefore is expected to elevate  $E_{BA}/S_{BA}$  values of  $ZrO_2$  surface modified with  $NO_3^-_{SUP}$  functionalities, which is conjectured given our study concerning  $ZrO_2$  particulates on N/S-doped carbons,[264] as depicted above. Interestingly,  $NO_3^-_{SUP}$  was reported to reveal peculiar trait to elevate  $E_{LA}$  of surface  $Zr^{4+}$  site in proximity[267] and thus can allow for our speculation concerning the increase in  $E_{LA}$  of  $ZrO_2$  surface modified with  $NO_3^-_{SUP}$  functionalities.

Again,  $ZrO_2$  surface exposed to aqueous conditions is  $BA$ -rich yet  $LA_{II}$ -limited[256–259] and thereby should not be further damaged by  $NO_Y^-_{SUP}$  and  $H_2O$ , both of which possess lone electron pairs and may bind with  $LA_{II}$  sites through the formation of coordinative bonds.[252, 255] Nonetheless, the distances between two  $Zr^{4+}$  cations innate to  $Zr^{4+}-O^{2-}-Zr^{4+}$  channels ( $d_{Zr-Zr}$ ) for  $ZrO_2$  polymorphs are 3.4–3.6 Å.[250, 251] The  $d_{Zr-Zr}$  values can be maintained even post the loss of  $O^{2-}$  anion positioned at the middle of  $Zr^{4+}-O^{2-}-Zr^{4+}$  channels due possibly to structural robustness of  $ZrO_2$ . [248, 249] Importantly, the  $d_{Zr-Zr}$  values are greater than kinetic diameters of  $NO_Y^-$  species (2.3–2.4 Å)[268] and thereby can hardly allow O atoms of  $NO_Y^-_{SUP}$  species to interact with adjacent  $LA_{II}$  sites. This makes it sound that  $NO_Y^-_{SUP}$  species are anchored on  $ZrO_2$  surface preferentially via *mono*-dentate array (Figure 5–1A), while avoiding  $NO_Y^-_{SUP}$ -mediated loss of  $LA_{II}$  sites through the formation of *bi*-dentate  $NO_Y^-_{SUP}$  species. Furthermore, steric hindrance imparted by *mono*-dentate  $NO_Y^-_{SUP}$  species may also limit the access of  $H_2O$  to adjacent  $LA_{II}$  sites and may help them intact post the exposure of  $NO_Y^-_{SUP}$ -modified  $ZrO_2$  ( $ZrO_2-N$ ) to wet environments. Overall,  $ZrO_2-N$  is predicted to provide plentiful merits in enhancing homolytic  $H_2O_2$  dissection efficiency over  $ZrO_2$  by lowering  $E_{BARRIER}$  ( $NO_3^-_{SUP}$  for  $E_{BA}/E_{LA} \uparrow$ ;  $NO_2^-_{SUP}$  for  $E_{LA} \uparrow$ )[264, 265, 267] or elevating pre-factor ( $k_{APP,0}$ ;  $NO_3^-_{SUP}$  for  $S_{BA} \uparrow$ )[264] with the minimization of  $LA_{II}$  loss (*mono*-dentate  $NO_Y^-_{SUP}$ [250, 251, 268] coupled with its steric hindrance  $\uparrow$ ).

It should be emphasized that  $\text{NO}_Y^-$  (unsupported) can be rapidly radicalized by  $\cdot\text{OH}$  to yield  $\text{OH}^-$  and  $\text{NO}_Y\cdot$  ( $\cdot\text{OH}\rightarrow\text{NO}_Y\cdot$ ) with secondary rate constants ( $k$ ) of  $10^5\text{--}10^8\text{ M}^{-1}\text{ sec}^{-1}$  for  $\text{NO}_3\cdot$  and  $\sim 10^{10}\text{ M}^{-1}\text{ sec}^{-1}$  for  $\text{NO}_2\cdot$ . [180, 181, 183] In particular,  $\text{NO}_3\cdot$  outweighs  $\text{NO}_2\cdot$  in terms of half-life ( $t_{1/2}$  of  $\sim 60\text{ }\mu\text{seconds}$  for  $\text{NO}_3\cdot$ ;  $\sim 1\text{ }\mu\text{second}$  for  $\text{NO}_2\cdot$ ) and ability to radicalize a contaminant via  $e^-$  elimination (standard reduction potential ( $E_0$ ) of  $\sim 2.4\text{ V}$  for  $\text{NO}_3\cdot$ ;  $\sim 1.0\text{ V}$  for  $\text{NO}_2\cdot$ ). [111, 185, 201, 269] Moreover, despite a high  $E_0$  ( $\sim 2.7\text{ V}$ ) of  $\cdot\text{OH}$ ,  $\text{NO}_3\cdot$  can substitute for  $\cdot\text{OH}$  because  $\text{NO}_3\cdot$  has a greater resistance to be quenched by itself ( $t_{1/2}$  of  $\sim 10^{-3}\text{ }\mu\text{second}$  for  $\cdot\text{OH}$ ) or by ubiquitous aqueous scavengers ( $\text{CO}_3^{2-}$ ,  $\text{Cl}^-$ , etc.) compared to  $\cdot\text{OH}$ . [111, 173] Nevertheless,  $\text{NO}_3\cdot$  typically requires a radioactive element, hard-to-isolate  $\text{NO}_2\cdot$ , or nitric acid for its evolution via radiolysis/photolysis. [18] However, we substantiated that  $\text{NO}_3\cdot_{\text{SUP}}$  can be readily yielded, sustained, and regenerated via radical transfer from  $\cdot\text{OH}$  to  $\text{NO}_3^-_{\text{SUP}}$  ( $\cdot\text{OH}\rightarrow\text{NO}_3\cdot_{\text{SUP}}$ ). [18] Elementary stages of  $\cdot\text{OH}\rightarrow\text{NO}_3\cdot_{\text{SUP}}$  were proposed such as  $\text{NO}_3^-_{\text{SUP}} \cdots \cdot\text{OH}$  formation,  $\text{NO}_3\cdot_{\text{SUP}} \cdots \text{OH}^-$  formation,  $\text{OH}^-$  desorption, and  $\text{NO}_3^-_{\text{SUP}}$  recovery from  $\text{NO}_3\cdot_{\text{SUP}}$  via  $e^-$  acceptance (Figure 5–1C). [18] All the stages were verified exothermic and energetically favorable on  $\text{MnO}_2$  functionalized with  $\text{NO}_3^-_{\text{SUP}}$  species ( $\alpha\text{-MnO}_2\text{-N}$ ), on which  $\cdot\text{OH}\rightarrow\text{NO}_3\cdot_{\text{SUP}}$  was proved to outperform  $\cdot\text{OH}$  in degrading phenol or mineralizing textile wastewater. [18]

Herein, we hypothesized that  $\cdot\text{OH}\rightarrow\text{NO}_3\cdot_{\text{SUP}}$  can also be viable on  $\text{ZrO}_2\text{-N}$  surface. Overall  $\cdot\text{OH}\rightarrow\text{NO}_3\cdot_{\text{SUP}}$  route is comprised of  $\text{H}_2\text{O}_2$  dissection (Figure 5–1B) and  $\cdot\text{OH}\rightarrow\text{NO}_3\cdot_{\text{SUP}}$  (Figure 5–1C) cycles and can be initiated with  $\text{H}_2\text{O}_2$  fed to the catalyst. Of significance, overall  $\cdot\text{OH}\rightarrow\text{NO}_3\cdot_{\text{SUP}}$  route can be dictated by endothermic  $\cdot\text{OH}$  desorption stage, at which  $\text{ZrO}_2\text{-N}$  can outperform  $\text{ZrO}_2$  based on ample rationales stated earlier, thus potentially showing improved efficiencies in contaminant degradation and/or mineralization. Of additional significance,  $\cdot\text{OH}$  initially radicalizes phenol (contaminant) via  $\cdot\text{OH}$  addition to produce dihydroxy-cyclohexadienyl

radical or via  $\text{H}^\bullet$  abstraction to form phenoxyl radical, whereas dihydroxy-cyclohexadienyl radical is dehydrated to also transform into phenoxyl radical.[114, 270, 271] Phenoxyl radical was reported to be polymerized via couplings to produce oligomeric compounds functioning as surface poisons ( $\text{ZrO}_2$  reusability  $\downarrow$ ).[264, 272] In contrast, the evolution of  $\text{NO}_3^\bullet_{\text{SUP}}$  via  $\cdot\text{OH} \rightarrow \text{NO}_3^\bullet_{\text{SUP}}$  cycle was indeed recurrent, as evidenced by noticeable contaminant degradation rates on  $\alpha\text{-MnO}_2\text{-N}$ . [18] Notably,  $\text{NO}_3^\bullet_{\text{SUP}}$  may initiate phenol degradation via  $\text{NO}_3^\bullet_{\text{SUP}}$  addition or  $\text{H}^\bullet$  abstraction to generate  $\text{NO}_3^-_{\text{SUP}}$  coordinated to monohydroxy-cyclohexadienyl radical or  $\text{HNO}_3_{\text{SUP}}$ , either of which cannot serve to recur  $\cdot\text{OH} \rightarrow \text{NO}_3^\bullet_{\text{SUP}}$  cycle, thus leading to severe decrease in phenol degradation efficiency on  $\text{NO}_3^\bullet_{\text{SUP}}$ . This leaves electron transfer as feasible initial phenol degradation route on  $\text{NO}_3^\bullet_{\text{SUP}}$  for the production of monohydroxy-cyclohexadienyl radical. Noteworthily, electron transfer route was reported to reduce/evade the generation of oligomeric compounds (poisons) on the catalyst surface ( $\text{ZrO}_2\text{-N}$  reusability  $\uparrow$ ). [270] Moreover,  $\alpha\text{-MnO}_2\text{-N}$  leached Mn species significantly under aqueous phases and possessed *bi*-dentate  $\text{NO}_3^-_{\text{SUP}}$  with only one O atom available to the radicalization via  $\cdot\text{OH} \rightarrow \text{NO}_3^\bullet_{\text{SUP}}$ . [18] *Bi*-dentate  $\text{NO}_3^-_{\text{SUP}}$  also incurred the loss of  $\text{H}_2\text{O}_2$  disector ( $\text{Mn}^{2+/3+}$ ) via its coordination to  $\text{NO}_3^-_{\text{SUP}}$ , [18] thus reducing heterolytic  $\text{H}_2\text{O}_2$  dissection efficiency. This can be in contrast to  $\text{ZrO}_2\text{-N}$ , whose *mono*-dentate  $\text{NO}_3^-_{\text{SUP}}$  imparts two O atoms deployed to the radicalization via  $\cdot\text{OH} \rightarrow \text{NO}_3^\bullet_{\text{SUP}}$  (orange circles in Figure 5-1C) in tandem with minute Zr leaching under aqueous phases. This study validated/highlighted the merits concerning the use of  $\text{NO}_3^-_{\text{SUP}}$  functionality on non-reducible  $\text{ZrO}_2$  as a decomposer of aqueous refractory pollutants via microscopy, spectroscopy, chemisorption, and computation techniques alongside with a host of control runs/kinetic assessments under regulated environments.

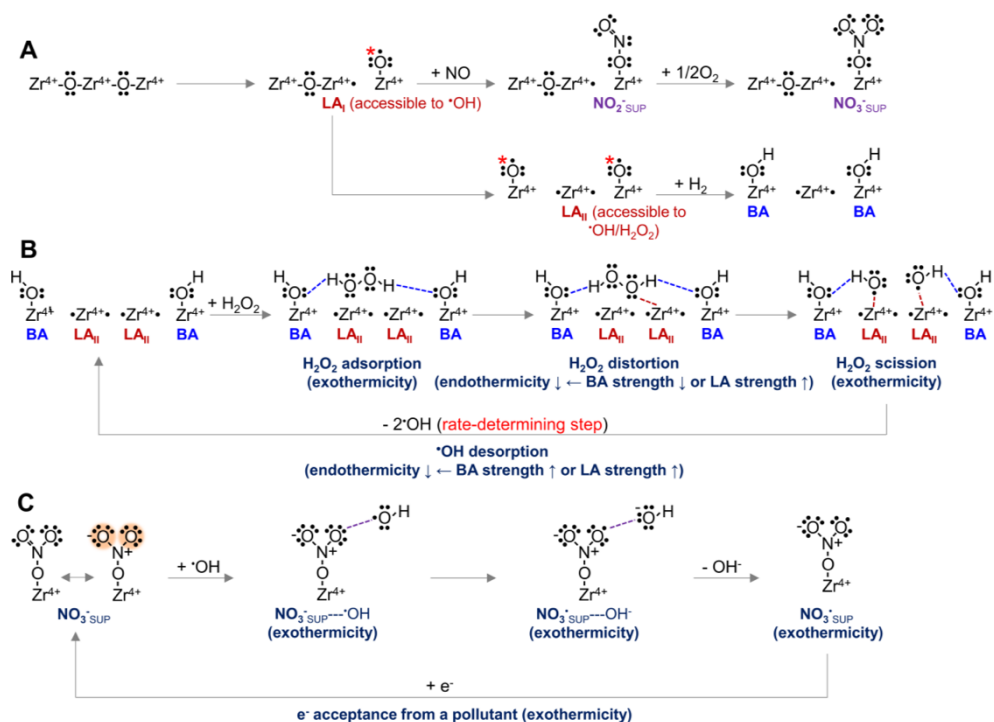


Figure. 5–1. (A) Illustration of  $\text{ZrO}_2$  surface composed of  $\text{Zr}^{4+}-\text{O}^{2-}-\text{Zr}^{4+}-\text{O}^{2-}-\text{Zr}^{4+}$  channels, where non-reducible, coordinatively-saturated  $\text{Zr}^{4+}$  cations are inter-connected to  $\text{O}^{2-}$  anions.  $\text{Zr}^{4+}$  cation located at the middle of  $\text{Zr}^{4+}-\text{O}^{2-}-\text{Zr}^{4+}-\text{O}^{2-}-\text{Zr}^{4+}$  channel is disconnected from one and two  $\text{O}^{2-}$  anions in proximity, leading to the production of Lewis acidic  $\cdot\text{Zr}^{4+}$  ( $\text{LA}_\text{I}$ ) and  $\cdot\text{Zr}^{4+}\cdot$  ( $\text{LA}_\text{II}$ ) open to  $\cdot\text{OH}$  and  $\cdot\text{OH}/\text{H}_2\text{O}_2$ , respectively. Meanwhile,  $\text{O}^{\cdot-}$  bound to  $\text{Zr}^{4+}$  (\*) reacts with  $\text{NO}/\text{NO}$  coupled with oxygen ( $1/2\text{O}_2$ ) to generate supported  $\text{NO}_2^{\cdot-}$  ( $\text{NO}_2^{\cdot-}\text{SUP}$ )/ $\text{NO}_3^{\cdot-}$  ( $\text{NO}_3^{\cdot-}\text{SUP}$ ) or interplays with hydrogen roaming on the surface ( $\text{H}^{\cdot}$ ;  $1/2\text{H}_2$ ) to yield Brønsted acidic  $-\text{OH}$  ( $\text{BA}$ ). (B) Proposed elementary steps of homolytic  $\text{H}_2\text{O}_2$  dissection on  $\text{ZrO}_2$  surface mediated by  $\text{LA}_\text{II}$  and  $\text{BA}$ :  $\text{H}_2\text{O}_2$  adsorption,  $\text{H}_2\text{O}_2$  distortion,  $\text{H}_2\text{O}_2$  scission, and  $\cdot\text{OH}$  desorption, wherein  $\cdot\text{OH}$  desorption stage dictates the efficiency of homolytic  $\text{H}_2\text{O}_2$  dissection as the rate-determining step. (C) Proposed elementary steps of radical transfer from  $\cdot\text{OH}$  to  $\text{NO}_3^{\cdot-}\text{SUP}$  to yield supported  $\text{NO}_3^{\cdot-}$  ( $\text{NO}_3^{\cdot-}\text{SUP}$ ) on  $\text{ZrO}_2$  surface, where surface-unbound oxygens of  $\text{NO}_3^{\cdot-}\text{SUP}$  (highlighted with orange circles) interact with  $\cdot\text{OH}$  for bearing radicals, whereas  $\text{NO}_3^{\cdot-}\text{SUP}$  is recovered to  $\text{NO}_3^{\cdot-}\text{SUP}$  via electron ( $e^-$ ) acceptance from a pollutant (denoted as electron transfer).

## 5.2. Methods

### 5.2.1. Catalysts

Zirconium oxide ( $\text{ZrO}_2$ ) and that modified with  $\text{NO}_2^-/\text{NO}_3^-$  functionalities ( $\text{ZrO}_2\text{-N}$ ) were synthesized using the protocols we reported elsewhere with minor modifications.[248, 249] Typically, 20 mmol of  $\text{ZrOCl}_2 \cdot 8\text{H}_2\text{O}$  (Kanto, 99.0%) was dissolved in 50 mL of de-ionized  $\text{H}_2\text{O}$ , mixed with 40 mmol of  $\text{C}_2\text{H}_2\text{O}_4 \cdot 2\text{H}_2\text{O}$  (oxalic acid dihydrate, Junsei, 99.5–100.2%) dissolved in 50 mL of de-ionized  $\text{H}_2\text{O}$ , stirred at 50 ° C for half an hour, subjected to rotary evaporation for the elimination of  $\text{H}_2\text{O}$ , dried at 70 ° C for 18 hours, and calcined at 400 ° C for 2 hours with a ramping rate of 5 ° C  $\text{min}^{-1}$ . [248, 249] This led to the formation of  $\text{ZrO}_2$ . In addition, 1 g of  $\text{ZrO}_2$  was loaded in a quartz reactor, situated in a tube furnace, and exposed to 5,000 ppm  $\text{NO}/3$  vol.%  $\text{O}_2/\text{N}_2$  stream at 100 ° C for an hour with a ramping rate of 10 ° C  $\text{min}^{-1}$  and a total flow rate of 500 mL  $\text{min}^{-1}$ . [250] This resulted in the generation of  $\text{ZrO}_2\text{-N}$ .

### 5.2.2. Characterizations

A Regulus 8230 (Hitachi) and a Titan 80–300<sup>TM</sup> (FEI) served to acquire scanning electron microscopy (SEM) and high-resolution transmission electron microscopy (HRTEM) images of the catalysts at 15 kV and 300 keV, respectively, post their surfaces were purged under vacuum. An Ultim max 170 (Oxford) was utilized to acquire energy-dispersive X-ray spectroscopy (EDX) mapping images of the catalysts at 15 kV. A D8 Advance (Bruker) served to acquire X-ray diffraction (XRD) patterns of the catalysts with the utilization of monochromatic  $\text{Cu K}_\alpha$  radiation ( $\lambda = 1.54 \text{ \AA}$ ) under analytic conditions of the step size and the scan speed of 0.02° per step and 2 seconds per step, respectively. A PHI 5000 Versa Probe (Ulvac-Phi) served to acquire X-ray photoelectron (XP) spectra of the catalysts with the resolution of 0.1 eV post their surfaces were purged under vacuum. XP spectra were curve-fitted using Gaussian functions, whereas binding energies of the resulting sub-



bands were corrected using an adventitious carbon band with a binding energy centered at  $\sim 284.6$  eV. A ZSX Primus II (Rigaku) and a FLASH 2000 (Thermo Fisher Scientific) served to quantify Zr and N contents included in the catalysts via X-ray fluorescence (XRF) and elemental analysis (EA) techniques, respectively. An iCAP 6500 duo (Thermo Fisher Scientific) and a total organic nitrogen (TN) analyzer served to quantify Zr and N contents leached from the catalyst surfaces during reaction runs via inductively coupled plasma–optical emission spectroscopy (ICP–OES) and TN techniques, respectively. A NOVA 2200e (Quantachrome Instruments) and a BELSORP–MAX (MicrotracBEL) served to acquire  $N_2$  isotherms (at  $-196^\circ\text{C}$ )/CO isotherms (at  $0/20/40^\circ\text{C}$ )/CO $_2$  isotherms (at  $0/20/40^\circ\text{C}$ ) and H $_2$ O isotherms (at  $20/30/40^\circ\text{C}$ ) for the catalysts, respectively, post their surfaces were purged under vacuum at  $100^\circ\text{C}$ . [196, 248–255]  $N_2$ /CO/CO $_2$ –accessible surfaces areas ( $S_{\text{BET}, N_2/\text{CO}/\text{CO}_2}$ ) and  $N_2$ –accessible pore volumes ( $V_{\text{BJH}, N_2}$ ) of the catalysts were assessed using Brunauer–Emmett–Teller (BET) and Barrett–Joyner–Halenda (BJH) methods, respectively. [196, 248–255] The numbers of  $N_2$ /CO/CO $_2$  adsorbed ( $N_{N_2/\text{CO}/\text{CO}_2}$ ) at partial pressure ( $P/P_0$ ) domains of 0.05–0.30 were implemented to acquire  $S_{\text{BET}, N_2/\text{CO}/\text{CO}_2}$  values of the catalysts. [196, 248–255] Surface areas of CO/CO $_2$ –accessible sites ( $S_{\text{CO}/\text{CO}_2}$ ) for the catalysts were evaluated by dividing  $S_{\text{BET}, \text{CO}/\text{CO}_2}$  values by  $N_{\text{CO}/\text{CO}_2}$  ones at  $P/P_0$  of  $\sim 1.0$  under the assumption that lateral interactions among CO (or CO $_2$ ) molecules adsorbed on the surfaces are negligible. [196, 248–255] H $_2$ O/CO/CO $_2$  isotherms were simulated using Toth equation (Equation S1), in which A indicates the maximum amount of H $_2$ O/CO/CO $_2$  adsorbed on the catalyst per a gram basis ( $\text{mol}_{\text{H}_2\text{O}/\text{CO}/\text{CO}_2} \text{g}_{\text{CAT}}^{-1}$ ), whereas B and C indicate the coefficients directed by the catalyst surface ( $\text{bar}^{-1}$ ) and its heterogeneity (unitless), respectively. [196, 248–255] Note in H $_2$ O isotherms of the catalysts that the numbers of H $_2$ O adsorbed on the surfaces could be analyzed under  $P/P_0$  domains of 0–0.8 and 0–0.4 at  $30^\circ\text{C}$  and  $40^\circ\text{C}$ , respectively, owing to the instrumental limitations, thereby only allowing for the simulation of H $_2$ O

isotherms for the catalysts under  $P/P_0$  regimes of 0–0.4 at 20–40 ° C.

$$N_{H2O/CO/CO2} = A \times \frac{B \times P}{(1 + (B \times P)^2)^{1/2}} \quad (S1)$$

Isosteric heats of  $H_2O/CO/CO_2$  adsorption at near-zero surface coverages ( $E_{H2O/CO/CO2}$ ) were assessed using Clausius–Clapeyron equation (Equation S2), where  $P_A/P_B$  and  $R$  indicate the pressures (bar) at temperatures of  $T_A/T_B$  (K) and the ideal gas constant ( $8.3145 \text{ J mol}^{-1} \text{ K}^{-1}$ ), respectively.[196, 248–255]

$$\ln \left( \frac{P_A}{P_B} \right) = \frac{E_{H2O/CO/CO2}}{R} \times \left( \frac{T_A - T_B}{T_A \times T_B} \right) \quad (S2)$$

An Autochem II (Micromeritics) equipped with an on-line mass spectrometer (HPR20, Hiden Analytical) served to acquire  $NH_3$  temperature-programmed desorption ( $NH_3$ -TPD) profiles (signal of  $NH_3$  evolved ( $m/z \sim 17$ ) versus temperature) for the catalysts.[253–256] Typically, the catalyst surfaces were purged with a He at 100 ° C for an hour, cooled to 50 ° C under a He, exposed to 5 vol. %  $NH_3/He$  at 50 ° C for an hour, exposed to a He at 50 ° C for an hour, and finally heated to 700 ° C under a He with a ramping rate ( $\beta$ ) of 10 ° C  $\text{min}^{-1}$ , 15 ° C  $\text{min}^{-1}$ , or 20 ° C  $\text{min}^{-1}$ . [253–256] The resulting  $NH_3$ -TPD profiles were implemented to evaluate binding energies of the surfaces with  $NH_3$  ( $E_{NH3}$ ) via TPD theory (Equation S3), where  $\nu_n$  and  $n$  denote the lumped constants indigenous to the catalyst surfaces.[253–256]  $NH_3$ -TPD profiles were de-convoluted using Gaussian functions to reveal four sub-bands with peak temperatures ( $T_M$ ). Slopes of the plots of  $\ln (\beta / T_M^2)$  versus ( $1/T_M$ ) are identical to  $-E_{NH3}/R$  values for the catalysts with the presumption that  $E_{NH3}$  values do not rely on surface  $NH_3$  coverages at  $T_M$  (*i.e.*,  $\theta_M$ ). [253–256]

$$\ln \left( \frac{\beta}{T_M^2} \right) = - \left( \frac{E_{NH3}}{R} \right) \left( \frac{1}{T_M} \right) - \frac{2.303 \times \log \left( \frac{E_{NH3}}{\nu_n R n \theta_M^{n-1}} \right)}{\text{CONSTANT}} \quad (S3)$$

An FT/IR/4200 (Jasco) equipped with KBr optics and a mercury–cadmium–telluride (MCT) detector served to acquire background-subtracted, in situ diffuse reflectance infrared Fourier transform (DRIFT) spectra of the catalysts under a dry/wet  $NH_3$  or  $NO/O_2$  streams with the resolution of 4  $\text{cm}^{-1}$ . [253–256] The catalysts were loaded in a reaction cell (Harrick Scientific) and purged with a  $N_2$  at 100 ° C for an hour prior to in situ DRIFT spectroscopy

experiments.[253–256] Detailed protocols concerning *in situ* DRIFT spectroscopy experiments are depicted in Figure 5–2 and 5–3 captions. A 10D (XAS KIST) beamline in Pohang Light Source (South Korea) operated in top–up mode did serve to acquire X–ray absorption near edge structure (XANES) spectrum of  $\text{ZrO}_2\text{–N}$  under analytic conditions of the energy of 3 GeV, the storage current of 250 mA, and the resolution of 0.2 eV post  $\text{ZrO}_2\text{–N}$  was purged under vacuum.[250] XANES spectrum was curve–fitted using Gaussian function.[250] A Zetasizer Nano ZS ZEN3602 (Malvern) equipped with a 633 nm He–Ne laser and a MPT–2 auto–titrator served to acquire the plots of zeta potential versus pH for aqueous mixtures including the catalysts and  $\text{Na}_2\text{SO}_4$ , for which pH values of aqueous mixtures were adjusted using aqueous NaOH (Daejung, 97.0%) and/or HCl (J. T. Baker, 36.5–38.0 wt.% in  $\text{H}_2\text{O}$ ) solutions, whereas zeta potentials were determined using Smoluchowski equation.[257] An MX–plus (Bruker) served to acquire electron paramagnetic resonance (EPR) spectra of reaction mixtures/solutions for assessing relative abundance of  $\cdot\text{OH}$ ,  $\cdot\text{OOH}$ ,  $\text{O}_2^{\cdot-}$ , or supported  $\text{ONO}_z^{\cdot}$  ( $Z=1$  or  $2$ ).[250, 258–262] 5,5–dimethyl–1–pyrroline N–oxide ( $\text{C}_6\text{H}_{11}\text{NO}$ , DMPO, Sigma–Aldrich,  $\geq 98.0\%$ ) was used as a spin trapping agent[250, 258–262] under analytic conditions of the center magnetic field of 3435 G, the resonance frequency of 9.64 GHz, the microwave power of 2.95 mW, the modulation amplitude of 1 G, the sweep width of 120 G, and the sweep time of 48 seconds.

### 5.2.3. Computations

Given the calculation literature concerning  $\text{ZrO}_2$  cluster interacting with  $\cdot\text{OH}$ , all the calculations were conducted using Gaussian 16 (Revision C.01) package with B3LYP level of density functional theory (DFT).[263] Initially, tetragonal  $\text{ZrO}_2$  was terminated on the (1 0 1) facet with the inclusion of [4 X 3] Zr atoms along with the saturation of edges with hydrogens to achieve good computational performance on a relatively small  $\text{ZrO}_2$  cluster (Figure 5-5).[9, 42] Moreover, basis sets of 6-311+G (d,p) and LanL2DZ were adopted for C/H/O/N and Zr atoms with the inclusion of effective core potentials and associated pseudo-potentials, whereas an ultra-fine grid was utilized for the atomic integrals with symmetry being turned-off via external command. Furthermore, unrestricted DFT on an open shell system served to precisely evaluate the energy change involved in the adsorption of  $\text{NO}_3^-$  on  $\text{ZrO}_2$  cluster (to form  $\text{NO}_3^-_{\text{SUP}}$  in Figure 5-5) or the radicalization of supported  $\text{NO}_3^-$  (to form  $\text{NO}_3^{\cdot}_{\text{SUP}}$  in Figure 5-5).[39] Harmonic frequency analysis of all the  $\text{ZrO}_2$  clusters considered herein was performed at the same level of theory to ensure their successful structural relaxation with minimum energies.[25] Indeed, all stationary points in the potential energy surfaces were proven to be the local minima. (No imaginary frequency was found across the frequency calculations.) Notably, a solvation model of density served to inspect the viability of  $\text{NO}_3^{\cdot}_{\text{SUP}}$  evolution under an aqueous environment. Reactions were conducted by following the procedures depicted in our previous studies with minor modifications.[196, 248, 249, 251, 252] Typically, N-Methyl-2-pyrrolidone (46.5 g,  $\text{C}_5\text{H}_9\text{NO}$ , Sigma-Aldrich,  $\geq 99.0\%$ ) and poly(vinylidene fluoride) (3.5 g,  $(\text{CH}_2\text{CF}_2)_n$ , average  $M_w \sim 180,000$ , Sigma-Aldrich) were mixed to form a binder solution.[196, 248, 249, 251, 252] The binder solution (0.2 g) was then mixed with the catalyst (0.2 g) to form a catalyst slurry.[196, 248, 249, 251, 252] The catalyst slurry was coated on a graphite plate (3 cm  $\times$  4 cm, grade 2124, Groupe Carbone Lorraine), dried at 100 ° C, and served as a cathode, whereas a bare graphite plate served as

an anode.[196, 248, 249, 251, 252] The anode/cathode were vertically positioned with the gap of 3.0 cm and loaded in aqueous reaction mixtures including Na<sub>2</sub>SO<sub>4</sub> (supporting electrolyte, Sigma–Aldrich, ≥99.0%), H<sub>2</sub>O<sub>2</sub> (·OH/·OOH/O<sub>2</sub>·<sup>-</sup> source, Daejung, 30.0 wt.% in H<sub>2</sub>O), H<sub>2</sub>O<sub>2</sub>, or phenol (model compound of refractory contaminants, Daejung, 99.0%),[196, 248, 249, 251, 252] as detailed in Figure 5–6 and 5–7. Reaction mixtures were stirred at 300 (or 400) rpm and 25 ° C (or 35–55 ° C) in the presence (or absence) of an electric potential of 1 V (~30 mA), 2 V (~24 mA), or 3 V (~15 mA).[196, 248, 249, 251, 252] Details concerning reaction environments can also be found in the figure captions and texts, where necessary. Reaction aliquots (1 mL) were taken at time intervals of 10, 20, 30, 40, 50, and 60 minutes, quenched with methanol (1 μL, Sigma–Aldrich, 99.8%), and filtered using a 0.45 μm–sized PES syringe filter (Whatman®).[196, 248–252] The resulting aliquots were finally analyzed in terms of H<sub>2</sub>O<sub>2</sub> or phenol concentration with the use of UV–Visible spectroscopy (Cary 100, Agilent Technologies) or reverse–phase high–performance liquid chromatography (HPLC, LC–20A, Shimadzu) technique, in which LC–20A was equipped with a Shim–pack GIS C18 column (5 μm, 4.6 X 150 mm, Shimadzu), an automatic injector (SIL–20A, Shimadzu), a pump (LC–20AT, Shimadzu), and an UV/Vis detector (SPD–20A, Shimadzu).[196, 248–252] Details concerning protocols for UV–Visible spectroscopy and reverse–phase HPLC techniques can be found in our previous studies.[196, 248–252] Initial H<sub>2</sub>O<sub>2</sub> dissection rate of the catalyst (–r<sub>H<sub>2</sub>O<sub>2</sub></sub>) was assessed using Equation S4, where k<sub>APP</sub> denotes the apparent reaction rate constant (slope of –ln (C<sub>H<sub>2</sub>O<sub>2</sub></sub>/C<sub>H<sub>2</sub>O<sub>2</sub>, 0</sub>) versus time), whereas C<sub>H<sub>2</sub>O<sub>2</sub>, 0</sub> and C<sub>H<sub>2</sub>O<sub>2</sub></sub> indicate the H<sub>2</sub>O<sub>2</sub> concentration initially fed and that monitored at a specific reaction time, respectively.[196, 248–252] In addition, N<sub>H<sub>2</sub>O<sub>2</sub>, 0</sub> and N<sub>CO, 0.2g</sub> indicate the H<sub>2</sub>O<sub>2</sub> quantity initially fed and the number of CO–accessible sites contained in 0.2 g of the catalyst (quantified using CO isotherm at 20 ° C), respectively.[196, 248–252]

$$-r_{H_2O_2} \text{ (min}^{-1}\text{)} = \frac{k_{APP} \text{ (min}^{-1}\text{)} \times N_{H_2O_2,0} \text{ (mol}_{H_2O_2}\text{)}}{N_{CO,0.2g} \text{ (mol}_{CO}\text{)}} \text{ (S4)}$$

Initial phenol degradation rates of the catalyst ( $-r_{\text{PHENOL}}$  and  $-r'_{\text{PHENOL}}$ ) was assessed using Equation S5 and S6, where  $k_{\text{APP}}$  denotes the apparent reaction rate constant (slope of  $-\ln(C_{\text{PHENOL}}/C_{\text{PHENOL},0})$  versus time), whereas  $C_{\text{PHENOL},0}$  and  $C_{\text{PHENOL}}$  indicate the phenol concentration initially fed and that monitored at a specific reaction time, respectively.[196, 248–252] In addition,  $N_{\text{PHENOL},0}$  and  $N_{\text{CO},0.2\text{g}}$  indicate the phenol quantity initially fed and the number of CO-accessible sites contained in 0.2 g of the catalyst (quantified using CO isotherm at 20 ° C), respectively.[196, 248–252]

$$-r_{\text{PHENOL}} (\text{min}^{-1}) = \frac{k_{\text{APP}} (\text{min}^{-1}) \times N_{\text{PHENOL},0} (\text{mol}_{\text{PHENOL}})}{N_{\text{CO},0.2\text{g}} (\text{mol}_{\text{CO}})} \quad (\text{S5})$$

$$-r'_{\text{PHENOL}} (\text{mol}_{\text{PHENOL}} \text{ g}_{\text{CAT}}^{-1} \text{ min}^{-1}) = \frac{k_{\text{APP}} (\text{min}^{-1}) \times N_{\text{PHENOL},0} (\text{mol}_{\text{PHENOL}})}{0.2 \text{ g} (\text{g}_{\text{CAT}})} \quad (\text{S6})$$

In phenol degradation runs, energy barriers ( $E_{\text{BARRIER}}$  in Equation S7) and pre-factors mediated by CO-accessible sites ( $k_{\text{APP},0}$  in Equation S7) for the catalysts were evaluated using their Arrhenius plots of  $\ln(-r_{\text{PHENOL}})$  versus  $1/T$  (Equation S7), where T indicates the reaction temperature.[196, 250, 252]

$$\ln(-r_{\text{PHENOL}}) = \ln(k_{\text{APP},0} \times C_{\text{PHENOL},0}) + \frac{-E_{\text{BARRIER}}}{R} \times \left(\frac{1}{T}\right) \quad (\text{S7})$$

#### 5.2.4. Reactions: textile wastewater degradation

Textile wastewater (DYETEC, total organic carbon (TOC) of  $52.7 (\pm 0.4)$   $\text{mmol}_C \text{ L}^{-1}$ ; total organic nitrogen (TN) of  $5.6 (\pm 0.1)$   $\text{mmol}_N \text{ L}^{-1}$ ; pH of  $11.0 (\pm 0.5)$ ) was initially vacuum-filtered using a  $1.2 \mu\text{m}$ -sized GF/C filter (Whatman®) to remove suspended solids.[250] The pH of the resulting filtrate was then adjusted to  $7.0 (\pm 0.1)$  using  $\text{H}_2\text{SO}_4$  (Kanto Chemical, 96.0%). 2 g of the catalyst was then put into 200 mL of the filtrate, stirred at 300 rpm and  $25^\circ \text{C}$  for 3 minutes, and mixed with 150 mmol of  $\text{H}_2\text{O}_2$  to start off with textile wastewater degradation.[250] Details concerning reaction environments can also be found in Figure 5–7. Reaction aliquots (10 mL) were taken at time intervals of 5, 10, 15, 20, 25, and 30 minutes and filtered using a  $0.20 \mu\text{m}$ -sized mixed cellulose ester filter (Hyundai Micro.).[250] The resulting aliquots were finally analyzed in terms of C/N contents with the use of TOC (TOC–L, Shimadzu)/TN analyzers.[250] Initial degradation rates of textile wastewater for the catalyst ( $-r'_C$  and  $-r'_N$ ) were assessed using Equation S8 and S9, where  $k_{\text{APP}}$  denotes the apparent reaction rate constant (slope of  $-\ln (C_C/C_{C,0})$  versus time or slope of  $-\ln (C_N/C_{N,0})$  versus time), whereas  $C_{C,0}$  (or  $C_{N,0}$ ) and  $C_C$  (or  $C_N$ ) indicate the carbon (or nitrogen) concentration initially fed and that monitored at a specific reaction time, respectively.[250] In addition,  $N_{C,0}$  (or  $N_{N,0}$ ) indicates the carbon (or nitrogen) quantity initially fed.[250]

$$-r'_C (\text{mol}_C \text{ g}_{\text{CAT}}^{-1} \text{ min}^{-1}) = \frac{k_{\text{APP}} (\text{min}^{-1}) \times N_{C,0} (\text{mol}_C)}{2 \text{ g } (\text{g}_{\text{CAT}})} \quad (\text{S8})$$

$$-r'_N (\text{mol}_N \text{ g}_{\text{CAT}}^{-1} \text{ min}^{-1}) = \frac{k_{\text{APP}} (\text{min}^{-1}) \times N_{N,0} (\text{mol}_N)}{2 \text{ g } (\text{g}_{\text{CAT}})} \quad (\text{S9})$$

## 5.3. Results and Discussion

### 5.3.1. Generic properties of $\text{ZrO}_2/\text{ZrO}_2\text{-N}$

$\text{ZrO}_2$  was synthesized via precipitation technique,[25, 39] during which oxalic acid served to isolate  $\text{ZrO}(\text{C}_2\text{O}_4)$  intermediate prior to its calcination utilized to produce porous  $\text{ZrO}_2$  architecture. The use of oxalic acid was because  $(\text{C}_2\text{H}_4)^{2-}$  anion present in  $\text{ZrO}(\text{C}_2\text{O}_4)$  can act as a pore-generating agent through its oxidative transition to evolve and liberate  $\text{CO}/\text{CO}_2/\text{H}_2\text{O}$  from  $\text{ZrO}_2$  particulates during calcination.[25, 39]  $\text{ZrO}_2\text{-N}$  was then synthesized by exposing  $\text{ZrO}_2$  to  $\text{NO}/\text{O}_2$  stream,[18] for which  $100^\circ\text{C}$  was selected because a larger bulk N constituent ( $\text{NO}_{\text{Y-SUP}}^-$  composition  $\uparrow$ ) was observed in the resulting  $\text{ZrO}_2\text{-N}$  at  $100^\circ\text{C}$  in comparison with those at  $50^\circ\text{C}$  and/or  $\geq 150^\circ\text{C}$  (not shown). Textural properties of the catalysts were assessed using their  $\text{N}_2$  isotherms at  $-196^\circ\text{C}$ . Although  $\text{N}_2$ -accessible BJH pore volumes of the catalysts were comparable ( $\sim 0.1\text{ cm}_{\text{N}_2}^3\text{ g}_{\text{CAT}}^{-1}$ ),  $\text{N}_2$ -accessible BET surface area of  $\text{ZrO}_2$  ( $\sim 95\text{ m}_{\text{N}_2}^2\text{ g}_{\text{CAT}}^{-1}$ ) was  $\sim 10\text{ m}_{\text{N}_2}^2\text{ g}_{\text{CAT}}^{-1}$  higher than that of  $\text{ZrO}_2\text{-N}$ , which could result from  $\text{NO}_{\text{Y-SUP}}^-$  species grafted inside pores of  $\text{ZrO}_2\text{-N}$ . Apparently,  $\text{ZrO}_2\text{-N}$  surface bore  $\text{NO}_{\text{Y-SUP}}^-$  modifiers, as evidenced by its molar ratio of N to Zr (surface N/Zr via XP spectroscopy) of  $\sim 0.10$ , which was around two-fold larger than bulk N/Zr analogue of  $\sim 0.06$  (via EA/XRF).

Macroscopic morphological characteristics of the catalysts were examined using their SEM images, where the catalysts were comprised of shapeless agglomerates with similar sizes of  $36 (\pm 10)\ \mu\text{m}$  for  $\text{ZrO}_2$  and  $32 (\pm 10)\ \mu\text{m}$  for  $\text{ZrO}_2\text{-N}$ . Irregular particle shapes of the catalysts in macroscopic scale were consistent to microscopic scale, as demonstrated by their HRTEM images. HRTEM images of the catalysts also revealed lattice fringes of  $2.95\text{ \AA}$  and  $3.16\text{ \AA}$ , which could be assigned to surface diffractions of  $(1\ 0\ 1)$  for tetragonal  $\text{ZrO}_2$  and  $(-1\ 1\ 1)$  for *monoclinic*  $\text{ZrO}_2$ , respectively. This was in exact agreement with XRD patterns of the catalysts, whose bulk diffractions were indexed to those of *tetragonal*  $\text{ZrO}_2$  and/or *monoclinic*  $\text{ZrO}_2$ .



Polymorphic nature of the catalysts was further confirmed by their XP spectra in the Zr 3d regimes. These were curve-fitted to four sub-bands, among which sub-bands with binding energies centered at 181.8 eV/184.2 eV and with those centered at 182.7 eV/185.1 eV were indexed to surface  $\text{Zr}^{4+}$  species belonging to monoclinic and tetragonal  $\text{ZrO}_2$ , respectively, with peak separations ( $\Delta\text{BE}$ ) of  $\sim 2.4$  eV.[273, 274] SEM, HRTEM, XRD, and XP spectroscopy experiments demonstrated that crystallographic traits of the catalysts were polymorphic yet alike and that  $\text{ZrO}_2$  retained its morphological/structural features even post the modification with  $\text{NO}_Y^- \text{SUP}$  species.

### 5.3.2. Acidic properties of $\text{ZrO}_2/\text{ZrO}_2\text{-N}$

Dissociative  $\text{H}_2\text{O}$  adsorption on the catalyst surfaces can induce the loss of  $\text{LA}_{\text{II}} (\bullet \text{Zr}^{4+} \bullet)$  sites alongside with the evolution of additional BA sites.[256–259] (See the Introduction section.) In this regard,  $\text{H}_2\text{O}$  isotherms of the catalysts were collected at 20–40 ° C and subjected to Toth fittings,[18, 107, 200, 225, 264, 275, 276] as detailed in the Methods section. The objective of  $\text{H}_2\text{O}$  isotherm experiments was to evaluate binding strengths of the catalyst surfaces with  $\text{H}_2\text{O}$  using their isosteric heats of  $\text{H}_2\text{O}$  adsorption at near-zero  $\text{H}_2\text{O}$  coverage at 20–40 ° C.[18, 107, 200, 225, 264, 275, 276] The surfaces displayed  $E_{\text{H}_2\text{O}}$  values of  $< 20 \text{ kJ mol}_{\text{H}_2\text{O}}^{-1}$  (Figure 5–2C), which indicated that the surfaces could bind with  $\text{H}_2\text{O}$  weakly via physisorption.

On the other hand,  $\text{NH}_3$  binds with  $\text{LA}_{\text{II}}$  and BA ( $-\text{OH}$ ) sites through the formation of  $\text{LA}_{\text{II}} \bullet \bullet \bullet \text{NH}_3$  and  $-\text{O}-\text{NH}_4^+$ , respectively, and thereby can provide venue as a probe to inspect the quantitative alteration of  $\text{LA}_{\text{II}}$  and/or BA sites innate to the surface with  $\text{H}_2\text{O}$  fed.[200, 225, 226, 264, 275, 276] In this regard, in situ DRIFT spectra of the catalysts were collected under controlled conditions, where the catalyst surfaces were purged and exposed to a dry  $\text{N}_2$  at 50 ° C, a dry  $\text{N}_2$  at 150 ° C, or a humid  $\text{N}_2$  at 150 ° C for collecting background signals.[200, 225, 226, 264, 275, 276] The surfaces

were then exposed to a dry  $\text{NH}_3$  at 50 ° C or a dry  $\text{NH}_3$  at 150 ° C to monitor their *in situ*  $\text{NH}_3$ -DRIFT spectra upon the elimination of corresponding backgrounds (Figure 5-2A to 5-2B).[200, 225, 226, 264, 275, 276] The surfaces showed a group of bands assigned to symmetric (or asymmetric) stretching (or wagging) vibrations of N-H bonds of  $\text{NH}_3$  coordinated to BA (BA bands) or  $\text{LA}_{\text{II}}$  sites (LA bands) across all the spectra collected.[246, 277] However, the *in situ* DRIFT spectra showed such BA/LA bands that significantly overlapped in addition to revealing skewed baselines, thereby barely allowing for precise quantification of BA/LA sites using the areas under the spectral signals.[200, 225, 226, 264, 275, 276]

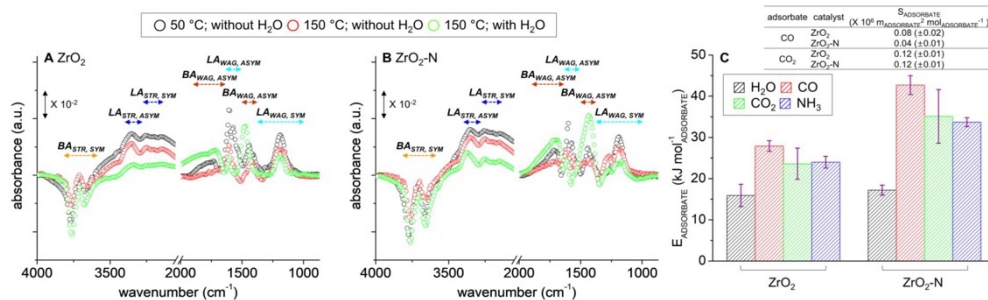


**Figure 5-2.** Background-subtracted, *in situ*  $\text{NH}_3$ -DRIFT spectra of the catalysts at 50/150 ° C ( $\text{ZrO}_2$  for (A);  $\text{ZrO}_2$ -N for (B)). The catalyst surfaces were purged under a dry  $\text{N}_2$  at 100 ° C for an hour, exposed to a dry  $\text{N}_2$  at 50/150 ° C or a wet  $\text{N}_2$  at 150 ° C for collecting background signals. Background-corrected DRIFT spectra of the catalysts were then recorded under dry 1,000 ppm  $\text{NH}_3/\text{N}_2$  at 50/150 ° C with a ramping rate and a total flow rate of 10 ° C  $\text{min}^{-1}$  and 200  $\text{mL min}^{-1}$ , respectively. In (A-B), *BA* and *LA* denote  $\text{NH}_3$ -accessible Brönsted acidic and Lewis acidic sites, respectively, whereas *SYM/ASYM* and *STR/WAG* stand for symmetric/asymmetric and stretching/wagging vibrations of N-H bonds for  $\text{NH}_3$  coordinated to *BA* and/or *LA* sites, respectively. (C) Binding energies ( $E_{\text{ADSORBATE}}$ ) of the catalyst surfaces with  $\text{H}_2\text{O}$  at 20–40 ° C,  $\text{CO}$  at 0–40 ° C,  $\text{CO}_2$  at 0–40 ° C, and  $\text{NH}_3$  at 50 ° C in tandem with surface areas of  $\text{CO}$  (or  $\text{CO}_2$ )-accessible sites innate to the catalysts ( $S_{\text{ADSORBATE}}$  in inset table).

Nonetheless, one could observe the quantitative changes in individual BA and/or LA bands upon the variation of surface temperatures and/or wetness. Of note, the intensities of BA/LA bands were reduced with the elevation of surface temperature from 50 ° C to 150 ° C. This could originate from the escalation of surface energies to prevent the coordinative interactions of –O–

$\text{NH}_4^+/\text{LA}_{\text{II}} \cdots \text{NH}_3$  from being developed.[226, 264, 275, 278] Of additional note, the intensities of BA and LA bands became enlarged and weakened at 150 ° C, respectively, with the inclusion of  $\text{H}_2\text{O}$  into a  $\text{N}_2$  feed stream prior to collecting *in situ*  $\text{NH}_3$ -DRIFT spectra. This could provide concrete evidence concerning the production of additional BA sites and the loss of  $\text{LA}_{\text{II}}$  sites mediated by dissociative  $\text{H}_2\text{O}$  adsorption on the surfaces,[226, 264, 275, 278] albeit with their  $E_{\text{H}_2\text{O}}$  values of  $<20 \text{ kJ mol}_{\text{H}_2\text{O}}^{-1}$  at 20–40 ° C. This also unveiled the nature of wet catalyst surfaces, where BA and  $\text{LA}_{\text{II}}$  sites were abundant and deficient, respectively. Contemplating that the rate-determining step of homolytic  $\text{H}_2\text{O}_2$  dissection or overall  $\cdot\text{OH} \rightarrow \text{NO}_3 \cdot_{\text{SUP}}$  route can be  $\cdot\text{OH}$  desorption stage directed by BA/ $\text{LA}_{\text{II}}$  sites and that the catalyst surface soaked in an aqueous phase could be  $\text{LA}_{\text{II}}$ -limited, the reaction efficiencies should be assessed in a per- $\text{LA}_{\text{II}}$  site basis rather than in a per-BA site basis. (See the sub-sections below.)

Numbers and strengths (acidities) of BA and  $\text{LA}_{\text{II}}$  sites inherent to the catalyst surface are central because these sites dictate binding affinity of O of  $\text{BA} \cdots \text{H}$  of  $\cdot\text{OH}$  (hydrogen bond) or  $\text{LA}_{\text{II}} \cdots \text{O}$  of  $\cdot\text{OH}$  (covalent bond), thus directing the energy needed to desorb  $\cdot\text{OH}$  from the surface ( $E_{\text{BARRIER}}$  of rate-determining step).[252–255, 264] In addition, larger areas of BA and  $\text{LA}_{\text{II}}$  sites are also essential in elevating collisional chances of O of  $\text{BA} \cdots \text{H}$  of  $\text{H}_2\text{O}_2$  (hydrogen bond) and  $\text{LA}_{\text{II}} \cdots \text{O}$  of  $\text{H}_2\text{O}_2$  (coordinative bond) for  $\text{H}_2\text{O}_2$  adsorption and  $\text{H}_2\text{O}_2$  distortion stages, respectively ( $k_{\text{APP}, 0} \uparrow$ ).[256, 257, 262, 264]  $\text{CO}$ ,  $\text{CO}_2$ , and  $\text{NH}_3$  are accessible to  $\text{LA}_{\text{II}}$  and/or BA sites,[18, 107, 264] have similar kinetic diameters (2.6–3.2 Å) to those of  $\text{H}_2\text{O}_2/\cdot\text{OH}$  (2.4–2.7 Å),[25, 134, 214] and therefore served as probes to explore Brönsted/Lewis acidities of the catalysts by quantifying the moles of probes adsorbed in a per-gram basis for the catalysts ( $N_{\text{XX}}$ , where XX:  $\text{CO}$ ,  $\text{CO}_2$ , or  $\text{NH}_3$ ), their binding energies with probes ( $E_{\text{XX}}$ ), *etc.*

It was reported that lone electron pair of C atom for  $\text{CO}$  binds with  $\text{LA}_{\text{II}}$  site only.[252, 255]  $\text{CO}$  was thus utilized as a probe to investigate Lewis acidities

of the catalysts via CO isotherm experiments at 0–40 ° C.[18, 107, 200, 225, 264, 275, 276] The analytic techniques used to fit CO isotherms of the catalysts and extract their isosteric heats of CO adsorption at near-zero CO coverage ( $E_{CO}$ ) at 0–40 ° C were analogous to those used for H<sub>2</sub>O isotherm experiments.[18, 107, 200, 225, 264, 275, 276] Interestingly,  $N_{CO}$  ( $\sim N_{LA}$ ) values of the catalysts at  $\sim 1$  bar were comparable. This provided sound proofs concerning our hypotheses that the production of coordinative bonds between O of  $NO_3^-_{SUP}$  and  $LA_{II}$  can be of little likelihood for ZrO<sub>2</sub>–N and that  $NO_3^-_{SUP}$  functionalities can be featured by mono-dentate binding configuration, as stated in the Introduction section. Moreover,  $E_{CO}$  ( $\sim E_{LA}$ ) of ZrO<sub>2</sub>–N was about 1.5-fold higher than that of ZrO<sub>2</sub> (Figure 5–2C), which could demonstrate the merits associated with the immobilization of  $NO_2^-$  (electron acceptor)[265] and  $NO_3^-$  (electron donator; unique electronic trait reported elsewhere)[266, 267] functionalities on ZrO<sub>2</sub>–N surface, as also detailed earlier. Meanwhile, the area in a per-CO-accessible site basis ( $S_{CO}$ ) for the catalyst can be assessed by dividing its CO-accessible BET surface area ( $S_{BET, CO}$ ) by  $N_{CO}$ . [264, 275]  $S_{CO}$  ( $\sim S_{LA}$ ) of ZrO<sub>2</sub> ( $0.08 \times 10^6 \text{ m}_{CO}^2 \text{ mol}_{CO}^{-1}$ ) was two-fold larger than that of ZrO<sub>2</sub>–N (Figure 5–2C), in spite of desired  $E_{CO}$  ( $\sim E_{LA}$ ) for ZrO<sub>2</sub>–N. This might result from steric effect incurred by  $NO_Y^-_{SUP}$  functionalities adjacent to  $LA_{II}$  sites and indicated that collision frequency of  $LA_{II} \cdots O$  of H<sub>2</sub>O<sub>2</sub> on ZrO<sub>2</sub>–N surface could be smaller than that on ZrO<sub>2</sub> during H<sub>2</sub>O<sub>2</sub> distortion stage.

On the other hand, CO<sub>2</sub> can bind with  $LA_{II}$  and BA sites through the formation of coordinative bond ( $LA_{II} \cdots O$  of CO<sub>2</sub>) and hydrogen bond (H of BA  $\cdots O$  of CO<sub>2</sub>), respectively.[252, 255, 260] Hence, CO<sub>2</sub> isotherms of the catalysts were collected at 0–40 ° C for assessing their  $N_{CO_2}/E_{CO_2}/S_{CO_2}$  values, while using such analytic methodologies that were analogous to those utilized to evaluate  $N_{CO}/E_{CO}/S_{CO}$  values for the catalysts.[18, 107, 200, 225, 264, 275, 276] Similar to  $N_{CO}$  ( $\sim N_{LA}$ ) values of the catalysts, their  $N_{CO_2}$  values ( $\sim N_{LA}$  coupled with  $N_{BA}$ ) at  $\sim 1$  bar were verified alike. This indicated that the

number of LA<sub>II</sub> or BA sites innate to ZrO<sub>2</sub> was invariant even post NO<sub>3</sub><sup>-</sup><sub>SUP</sub> functionalization. This was in close line with XP spectra of the catalysts in the O 1s domains, which were curve-fitted to two sub-bands positioned with binding energies centered at 530.4 eV and 531.9 eV. These were assigned to surface O species belonging to Zr–O and Zr–OH (BA site), respectively,[279, 280] whose relative concentrations were almost identical across the catalysts. Interestingly, S<sub>CO2</sub> values of the catalysts were similar in magnitude (Figure 5–2C) yet distinct from their S<sub>CO</sub> analogues with regard to hierarchy (S<sub>CO</sub> (~S<sub>LA</sub>) of ZrO<sub>2</sub>>ZrO<sub>2</sub>–N). This could indicate that the area in a per-BA site basis (S<sub>BA</sub>) of ZrO<sub>2</sub>–N was higher than that of ZrO<sub>2</sub>, which suggested that ZrO<sub>2</sub>–N could attain a higher collision frequency of O of BA • • • H of H<sub>2</sub>O<sub>2</sub> during H<sub>2</sub>O<sub>2</sub> adsorption stage compared to ZrO<sub>2</sub>. Again, the catalyst surfaces could be BA-rich and LA-limited even under a dry environment (*e.g.*, formation of additional BA sites via interactions of O<sup>•-</sup> bound to Zr<sup>4+</sup> • • • H<sup>•</sup> wandering on the surface[256–259]). BA-rich trait of the catalyst surfaces made it convincing that CO<sub>2</sub> could preferentially bind with BA sites rather than with LA<sub>II</sub> counterparts at near-zero CO<sub>2</sub> coverage. This highly suggested that E<sub>CO2</sub> could be identical to E<sub>BA</sub>. Importantly, E<sub>CO2</sub> (~E<sub>BA</sub>) of ZrO<sub>2</sub>–N (~35 kJ mol<sub>CO2</sub><sup>-1</sup>) was ~11 kJ mol<sub>CO2</sub><sup>-1</sup> greater than that of ZrO<sub>2</sub> (Figure 5–2C). This could be ascribed to the merit provided by NO<sub>3</sub><sup>-</sup><sub>SUP</sub> functioning as electron donors (E<sub>BA</sub> ↑) and was in good agreement with our previous study concerning ZrO<sub>2</sub> on N/S-doped carbons,[264] as mentioned in the Introduction section.

NH<sub>3</sub> also binds with LA<sub>II</sub> and BA sites and thereby served as additional adsorbate utilized to perform NH<sub>3</sub>–TPD experiments.[18, 107, 200, 225, 226, 264, 275, 276] The catalyst surfaces were purged and subjected to NH<sub>3</sub> chemisorption at 50 ° C, and heated up to 700 ° C with various ramping rates (β) of 10–20 ° C min<sup>-1</sup> for collecting NH<sub>3</sub>–TPD profiles.[18, 107, 200, 225, 226, 264, 275, 276] The areas under NH<sub>3</sub>–TPD profiles of the catalysts then served to quantify their N<sub>NH3</sub> values at 50 ° C.[18, 107, 200, 225, 226,

264, 275, 276]  $N_{\text{NH}_3}$  values of the catalysts were of comparable magnitude, which again suggested that BA/LA<sub>II</sub> sites included in ZrO<sub>2</sub> were intact during NO<sub>Y</sub><sup>-SUP</sup> functionalization. Moreover, NH<sub>3</sub>-TPD profiles were de-convoluted to show four sub-bands with dissimilar peak temperatures. Plots of  $(\beta/T_M^2)$  versus  $1/T_M$  for individual sub-bands of the catalysts provided a bunch of slopes that are identical to  $(-E_{\text{NH}_3}/R)$  values, where  $E_{\text{NH}_3}$  and  $R$  stand for NH<sub>3</sub> binding energy of the surface and ideal gas constant, respectively, according to TPD theory.[18, 107, 200, 225, 226, 264, 275, 276] The hierarchy of  $E_{\text{NH}_3}$  values for the catalysts were identical to that of  $E_{\text{CO}_2}$  analogues (Figure 5-2C). Again, NH<sub>3</sub> and CO<sub>2</sub> can be bound to BA/LA<sub>II</sub> sites,[18, 107, 264] whose relative concentration on the catalyst surfaces was greater in BA sites than in LA<sub>II</sub> counterparts, as discussed earlier. Hence, it was logically impeccable that NH<sub>3</sub> could prefer interacting with BA to binding with LA<sub>II</sub> ( $E_{\text{NH}_3} \sim E_{\text{BA}}$ ), as could also be the case with CO<sub>2</sub> isotherm experiments depicted above. All of these were gathered to add weight on the claims that  $E_{\text{BA}}$  values of the catalysts were quantifiable by utilizing their  $E_{\text{CO}_2}/E_{\text{NH}_3}$  values and that ZrO<sub>2</sub>-N possessed a greater Brönsted acidity than ZrO<sub>2</sub>. In sum, compared to ZrO<sub>2</sub>, ZrO<sub>2</sub>-N was anticipated to be more proper to accelerate homolytic H<sub>2</sub>O<sub>2</sub> dissection cycle (Figure 5-1B) because of a higher  $E_{\text{LA}}$  ( $\sim E_{\text{CO}}$ ;  $E_{\text{BARRIER}} \downarrow$ ), a higher  $E_{\text{BA}}$  ( $\sim E_{\text{CO}_2}/E_{\text{NH}_3}$ ;  $E_{\text{BARRIER}} \downarrow$ ), and a larger  $S_{\text{BA}}$  ( $k_{\text{APP}, 0} \uparrow$ ) imparted by ZrO<sub>2</sub>-N, albeit ZrO<sub>2</sub>-N provided a smaller  $S_{\text{LA}}$  ( $\sim S_{\text{CO}}$ ; steric hindrance of NO<sub>Y</sub><sup>-SUP</sup>).

### 5.3.3. Properties of $\text{NO}_Y^-_{\text{SUP}}$ functionalities

Compositions of  $\text{NO}_Y^-_{\text{SUP}}$  species on  $\text{ZrO}_2\text{-N}$  surface were then explored using XP and XANES spectroscopy. XP spectrum of  $\text{ZrO}_2\text{-N}$  in the N 1s region was de-convoluted to two sub-bands with binding energies centered at 403.6 eV and 407.4 eV (Figure 5-3A). These could be indexed to N species inherent to  $\text{NO}_2^-$  and  $\text{NO}_3^-$  functionalities, respectively,[281, 282] whereas relative abundance of  $\text{NO}_3^-$  (65.6%) was about two-fold greater than that of  $\text{NO}_2^-$  (34.4%). Moreover, XANES spectrum of  $\text{ZrO}_2\text{-N}$  at the N K-edge was further collected to ensure relative  $\text{NO}_2^-/\text{NO}_3^-$  concentrations explored via XP spectroscopy. XANES domain with photon energies of  $\leq 410$  eV can be indexed to  $\pi^*$  resonance regime and was curve-fitted to unveil two sub-bands with photon energies centered at 402.5 eV (a in Figure 5-3B) and 406.2 eV (b in Figure 5-3B), respectively.[18, 240, 241] Sub-bands marked with a and b originate from electronic transitions of  $1s \rightarrow 2b_1$  for  $\text{NO}_2^-$  and  $1s \rightarrow 2a_2''$  for  $\text{NO}_3^-$ , respectively,[18, 240, 241] with relative abundances of the former and the latter being 15.4% and 47.7%. In addition, XANES domain with photon energies of  $>410$  eV can be indexed to  $\sigma^*$  resonance regime.[18, 240, 241]  $\sigma^*$  resonance region was curve-fitted to show three sub-bands marked with a', b', and b'', whose peaks were located at photon energies of 413.0 eV, 416.0 eV, and 418.0 eV, respectively (Figure 5-3B).[18, 240, 241] a' and b'/b'' result from electronic excitations of  $1s \rightarrow 7a_1/5b_2$  for  $\text{NO}_2^-$  and  $1s \rightarrow 5a_1'/5e_1'$  for  $\text{NO}_3^-$ , respectively,[18, 240, 241] with relative abundances of the former and the latter being 20.4% and 16.5%. Importantly, it was identified via XANES spectroscopy that relative abundances of  $\text{NO}_2^-$  and  $\text{NO}_3^-$  were 35.8% and 64.2%, respectively, both of which were alike to those obtained via XP spectroscopy. Indeed,  $\text{ZrO}_2\text{-N}$  surface bore a greater number of  $\text{NO}_3^-_{\text{SUP}}$  functionalities in comparison with  $\text{NO}_2^-_{\text{SUP}}$  counterparts.

Furthermore,  $\text{ZrO}_2$  was subjected to *in situ* DRIFT spectroscopy experiment with the simulation of synthetic conditions used to form  $\text{ZrO}_2\text{-N}$  (Figure 5-3C).[18]





The objective of this experiment was to monitor the type and binding configurations of  $\text{NO}_Y^-_{\text{SUP}}$  functionalities present in  $\text{ZrO}_2\text{-N}$  surface.[18] For this purpose,  $\text{ZrO}_2$  surface was purged, exposed to a dry  $\text{N}_2$  at  $100^\circ\text{C}$  for collecting background signal, and fed with  $\text{NO/O}_2$  stream at  $100^\circ\text{C}$  post the removal of background.[282] The resulting in situ  $\text{NO/O}_2\text{-DRIFT}$  spectrum of  $\text{ZrO}_2$  showed three broad bands highlighted with orange/cyan arrows. These were ascribed to symmetric or asymmetric stretching vibrations of N–O bonds for gaseous  $\text{N}_2\text{O}_4$  and  $\text{N}_2\text{O}_3$  physisorbed on the surface.[267, 283] Apparently,  $\text{NO}_2^-$  species were anchored on the surface. This was demonstrated by blue arrows, resulting from the vibrations of N–O bonds for  $\text{NO}_2^-_{\text{SUP}}$  species.[267, 283] Moreover, it was identified that  $\text{NO}_3^-$  species were also grafted on the surface with mono–dentate and bi–dentate arrays, as highlighted with gold arrows.[267, 277, 283] It should be stressed that the bands located at wavenumber domains of  $1,210\text{--}1,260\text{ cm}^{-1}$  and  $1,600\text{--}1,650\text{ cm}^{-1}$  could be indexed to N–O vibrations of bi–dentate  $\text{NO}_3^-_{\text{SUP}}$  species, yet, substantially overlapped with those of gaseous  $\text{N}_2\text{O}_3$ ,  $\text{NO}_2^-_{\text{SUP}}$ , or mono–dentate  $\text{NO}_3^-_{\text{SUP}}$ , [267, 277, 283] thus making it persuasive that the majority of  $\text{NO}_3^-$  species on  $\text{ZrO}_2\text{-N}$  surface could be characterized by mono–dentate binding configuration. All the results suggested that  $\text{ZrO}_2\text{-N}$  could outperform  $\text{ZrO}_2$  in degrading pollutants with the use of mono–dentate  $\text{NO}_3^\bullet_{\text{SUP}}$  decomposers, whose evolution enabled by  $\cdot\text{OH}\rightarrow\text{NO}_3^\bullet_{\text{SUP}}$  cycle could be accelerated by enhanced  $\cdot\text{OH}$  productivity of  $\text{ZrO}_2\text{-N}$  over that of  $\text{ZrO}_2$ .

#### 5.3.4. Proofs of $\cdot\text{OH} \rightarrow \text{NO}_3^{\cdot\text{SUP}}$

Aside from producing  $\cdot\text{OH}$ , homolytic  $\text{H}_2\text{O}_2$  dissection also evolves  $\cdot\text{OOH}$  and  $\text{O}_2^{\cdot-}$  on  $\text{LA}_{\text{II}}$  sites via  $\text{LA}_{\text{II}}-\cdot\text{OH}+\text{H}_2\text{O}_2 \rightarrow \text{LA}_{\text{II}}-\cdot\text{OOH}+\text{H}_2\text{O}$  and  $\text{LA}_{\text{II}}-\cdot\text{OOH} \rightarrow \text{LA}_{\text{II}}-\text{O}_2^{\cdot-}+\text{H}^+$ , respectively, in which the latter can occur at pH values of  $>4.8$ , whereas the resulting  $\text{LA}_{\text{II}}-\text{O}_2^{\cdot-}$  could tend to liberate  $\text{O}_2^{\cdot-}$  to an aqueous environment, if the surface were negatively-charged.[261–263, 284] To inspect surface charges (zeta-potentials) of the catalysts exposed to reaction-limited domains considered below, aqueous mixtures of the catalysts and  $\text{Na}_2\text{SO}_4$  (supporting electrolyte) were subjected to pH alteration of 3–7 for collecting profiles of zeta potential versus pH for the catalysts.[264] Notably, reaction mixtures rapidly dropped their pH values from 7.0 to 4.9 ( $\pm 0.1$ ) within 10 minutes and retained their pH values of  $\sim 4.9$  up to the termination of reaction runs. Surface charges of  $\text{ZrO}_2$  and  $\text{ZrO}_2\text{-N}$  were proved to be negative and positive at pH domains of 4.9 ( $\pm 0.1$ ), respectively, which indicated that  $\text{O}_2^{\cdot-}$  species could be anchored on  $\text{ZrO}_2\text{-N}$  surface only during the reaction runs.

Meanwhile, EPR spectroscopy experiments were conducted for reaction mixtures (catalysts mixed with reaction solutions) and reaction solutions ( $\text{H}_2\text{O}_2$  and water) used to simulate homolytic  $\text{H}_2\text{O}_2$  dissection cycle for  $\text{ZrO}_2$  and overall  $\cdot\text{OH} \rightarrow \text{NO}_3^{\cdot\text{SUP}}$  cycle (homolytic  $\text{H}_2\text{O}_2$  dissection cycle coupled with  $\cdot\text{OH} \rightarrow \text{NO}_3^{\cdot\text{SUP}}$  cycle) for  $\text{ZrO}_2\text{-N}$ . [18, 101, 140, 141, 229, 230] DMPO were added to reaction mixtures and served as a spin trapping agent of  $\cdot\text{OH}$ ,  $\cdot\text{OOH}$ ,  $\text{O}_2^{\cdot-}$ , or  $\text{NO}_Y^{\cdot\text{SUP}}$ , whose evolution was enabled by  $\text{H}_2\text{O}_2$  fed to the catalyst surfaces, whereas reaction solutions were isolated via syringe filtration of reaction mixtures.[18, 101, 140, 141, 229, 230]

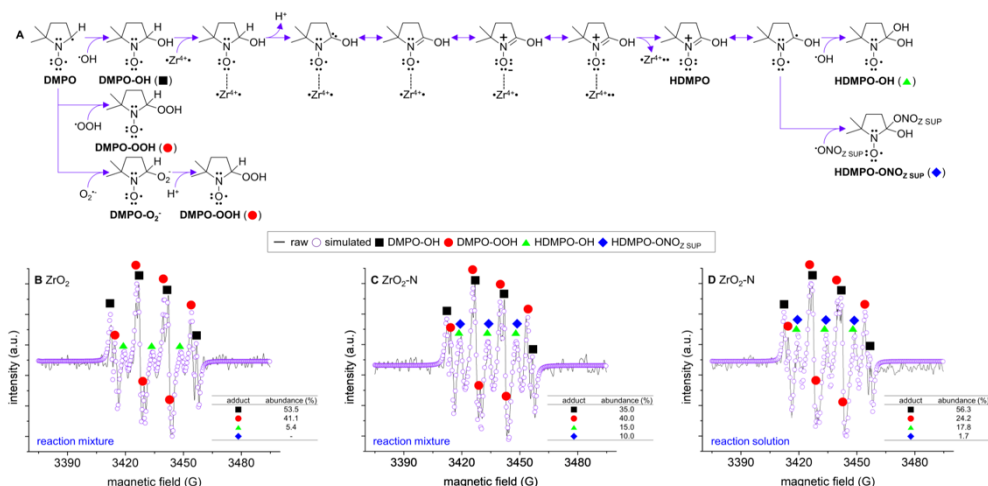


**Figure 5-4.** (A) Proposed transformation routes of DMPO to DMPO-OH, DMPO-OOH, HDMPO-OH, and HDMPO-ONO<sub>Z SUP</sub> (Z= 1 or 2). EPR spectra of reaction mixtures (ZrO<sub>2</sub> for (B); ZrO<sub>2</sub>-N for (C)) and reaction solution (ZrO<sub>2</sub>-N for (D)) collected through the filtration of reaction mixture with the use of a 0.45  $\mu\text{m}$ -sized PES syringe. Reaction mixture was comprised of the catalyst (2 mg; sizes of  $<60\ \mu\text{m}$ ), de-ionized H<sub>2</sub>O (1.0 mL), H<sub>2</sub>O<sub>2</sub> (0.3 mmol), and 5,5-dimethyl-1-pyrroline N-oxide (DMPO; spin trapper; 3 mmol) and stirred using vortex for 2 minutes at 25 ° C prior to the analysis (B-C) or the filtration (D). Gray solid lines and violet empty circles indicate raw EPR spectra and those simulated. Black solid squares and red solid circles denote DMPO adducted to  $\cdot\text{OH}$  (DMPO-OH) and  $\cdot\text{OOH}/\text{O}_2^{\cdot-}$  (DMPO-OOH), respectively, whereas green solid upper triangles and blue solid diamonds indicate HDMPO adducted to  $\cdot\text{OH}$  (HDMPO-OH) and supported ONO<sub>Z</sub> $\cdot$  (HDMPO-ONO<sub>Z SUP</sub>), respectively. Relative abundances of adducts stated above were also assessed and exhibited in inset tables.

Moreover, the resulting EPR spectra were computed to identify or quantify the radicals present in reaction mixtures and solutions. Of note, unpaired electron adjacent to  $\beta$ -H of DMPO can bind with  $\cdot\text{OH}$  and  $\cdot\text{OOH}/\text{O}_2^{\cdot-}$  via electron sharing to yield DMPO-OH (black solid square in Figure 5-4) and DMPO-OOH (red solid circle in Figure 5-4), respectively, where the latter's production is realized by two routes such as DMPO directly adducted to  $\cdot\text{OOH}$  and DMPO initially adducted to  $\text{O}_2^{\cdot-}$  to generate DMPO-O<sub>2</sub> $\cdot^-$  followed by its protonation with the use of roaming, aqueous H<sup>+</sup>. [18, 229–231, 264] Of additional note, a portion of DMPO-OH adducts were hypothesized to undergo coordination to LA<sub>II</sub> ( $\cdot\text{Zr}^{4+}\cdot$ ) site, H<sup>+</sup> release, free electron confinement adjacent to LA<sub>II</sub> site ( $\cdot\text{Zr}^{4+}\cdot\cdot$ ), and  $\cdot\text{Zr}^{4+}\cdot\cdot$  liberation to finally evolve HDMPO. [18] The resulting HDMPO in turn can

potentially shares electron with aqueous  $\cdot\text{OH}$  to produce HDMPO-OH (green solid upper triangle in Figure 5-4) or is adducted by  $\text{NO}_Y\cdot_{\text{SUP}}$  to generate HDMPO- $\text{ONO}_{Z\text{SUP}}$  ( $Z=1$  or  $2$ ) on  $\text{ZrO}_2\text{-N}$  (blue solid diamond in Figure 5-4).[18]

The EPR spectra of reaction mixtures were characterized by quartet signals with intensity ratios of 1:2:2:1, sextet signals with intensity ratios of 1:1:1:1:1:1, and trio signals with intensity ratios of 1:1:1 for DMPO-OH, DMPO-OOH, and HDMPO-OH (Figure 5-4B to 5-4C), respectively.[18, 229-231, 264] This apparently validated the evolution of  $\cdot\text{OH}$ ,  $\cdot\text{OOH}$ , and  $\text{O}_2^{\cdot-}$  via homolytic  $\text{H}_2\text{O}_2$  evolution. Interestingly,  $\text{ZrO}_2\text{-N}$  also showed trio signals with intensity ratio of 1:1:1 and hyperfine splitting constants of 14.7 G for  $a(^{14}\text{N})$  and 1.1 G for  $a(^1\text{H})$ .[18] This could indicate the evolution  $\text{NO}_Y\cdot_{\text{SUP}}$  adducted to HDMPO (HDMPO- $\text{ONO}_{Z\text{SUP}}$ ), whose hyperfine splitting constants and signal traits were postulated based on those of a group of reported five-/six-membered spin adducts with multi, bulky substituents, as specified in our previous study.[18]

Relative abundances of spin adducts stated above were then computed in the EPR spectra of reaction mixtures for comparison. It should be emphasized that homolytic  $\text{H}_2\text{O}_2$  dissection efficiency was potentially higher in  $\text{ZrO}_2\text{-N}$  compared to  $\text{ZrO}_2$ , as postulated in the sub-section concerning acidic properties of the catalysts. Hence, the numbers of  $\cdot\text{OH}/\cdot\text{OOH}/\text{O}_2^{\cdot-}$  released from the surface could be larger in  $\text{ZrO}_2\text{-N}$  than in  $\text{ZrO}_2$  (DMPO-OH/DMPO-OOH of  $\text{ZrO}_2\text{-N} > \text{ZrO}_2$ ; 1<sup>st</sup> scenario). However, DMPO-OH near  $\text{ZrO}_2\text{-N}$  surface could possess a higher tendency to coordinate to  $\text{LA}_{\text{II}}$  site because of its greater  $E_{\text{LA}}$  compared to that of  $\text{ZrO}_2$ . This could lead to the formation of a larger amount of HDMPO (Figure 5-4A) near  $\text{ZrO}_2\text{-N}$  surface in comparison with  $\text{ZrO}_2$  counterpart, as corroborated by a larger abundance of HDMPO for  $\text{ZrO}_2\text{-N}$  (15.0%) than that for  $\text{ZrO}_2$  (5.4%), in addition to producing a moderate quantity of HDMPO- $\text{ONO}_{Z\text{SUP}}$  for  $\text{ZrO}_2\text{-N}$  (10.0%). Again,  $\text{ZrO}_2\text{-N}$  could consume a greater number of DMPO-OH

for the generation of HDMPO, thus possibly showing a smaller abundance of DMPO-OH (35.0%) compared to ZrO<sub>2</sub> (53.5%). Meanwhile, in comparison with ZrO<sub>2</sub>-N surface, ZrO<sub>2</sub> counterpart was negatively-charged during homolytic H<sub>2</sub>O<sub>2</sub> dissection, could liberate a greater number of O<sub>2</sub><sup>•-</sup> species to an aqueous medium, and thus potentially formed a larger quantity of DMPO-OOH by way of DMPO-O<sub>2</sub><sup>-</sup> production (DMPO-OOH of ZrO<sub>2</sub>-N < ZrO<sub>2</sub>; 2<sup>nd</sup> scenario). Two scenarios contradicting each other might bring about the evolution of DMPO-OOH with similar quantities across reaction mixtures (40–41.1%).

The EPR spectra of reaction solutions were also featured by DMPO-OH, DMPO-OOH, HDMPO-OH, or HDMPO-ONO<sub>Z SUP</sub> (Figure 5-4D). In the case of ZrO<sub>2</sub>, the EPR spectrum simulated for reaction solution was comparable to that for reaction mixture in terms of relative abundances of spin adducts. This suggested that most of <sup>•</sup>OH/<sup>•</sup>OOH/O<sub>2</sub><sup>•-</sup> species evolved via homolytic H<sub>2</sub>O<sub>2</sub> dissection did migrate from ZrO<sub>2</sub> surface to an aqueous medium. In the case of ZrO<sub>2</sub>-N, a small amount of HDMPO-ONO<sub>Z SUP</sub> (1.7%) were detected in the EPR spectrum simulated for reaction solution. This could be responsible for few ZrO<sub>2</sub>-N particulates with sizes of <0.45 μm, which passed through a 0.45 μm-sized syringe filter utilized to isolate reaction solution.[18] On the other hand, ZrO<sub>2</sub>-N surface was positively-charged, attracted O<sub>2</sub><sup>•-</sup> species, potentially released only a few O<sub>2</sub><sup>•-</sup> species to an aqueous medium, and thus generated a small number of DMPO-OOH species originating from DMPO-O<sub>2</sub><sup>-</sup> intermediates. Indeed, the amount of DMPO-OOH was smaller in reaction solution (24.2 %) than in reaction mixture (40.0%). All the results on the EPR spectroscopy experiments could corroborate the feasibility of homolytic H<sub>2</sub>O<sub>2</sub> dissection and <sup>•</sup>OH→NO<sub>3</sub><sup>•</sup><sub>SUP</sub> cycles on the catalyst surfaces.

DFT calculation techniques were utilized to further substantiate <sup>•</sup>OH→NO<sub>3</sub><sup>•</sup><sub>SUP</sub> cycle on ZrO<sub>2</sub>-N (Figure 5-5), for which tetragonal ZrO<sub>2</sub> was terminated on the surface (1 0 1) facet for the creation of ZrO<sub>2</sub> cluster

including  $[4 \times 3]$  Zr atoms with hydrogens being bound to oxygens positioned at cluster edges. Surface (1 0 1) facet possesses the lowest surface energy among all the diffractions defined for *tetragonal*  $\text{ZrO}_2$  architecture (JCPDF No. of 01-080-0965) and thus was expected to help precisely simulating the change in thermodynamic energies ( $\Delta E$ ) involved in  $\cdot\text{OH} \rightarrow \text{NO}_3^{\cdot\text{SUP}}$  cycle at 300 K. In addition, hydrogens present in  $\text{ZrO}_2$  cluster edges were anticipated to improve calculational performance and accuracy for  $\cdot\text{OH} \rightarrow \text{NO}_3^{\cdot\text{SUP}}$  cycle, as reported elsewhere.[285, 286] Moreover,  $\text{NO}_2^{\cdot}$  is inferior to  $\text{NO}_3^{\cdot}$  with regard to  $E_0$  and  $t_{1/2}$  values.[111, 185, 201, 269]  $\text{NO}_3^-$  and  $\text{NO}_3^{\cdot}$  thus served to simulate adsorption step and  $\cdot\text{OH}$ -mediated radicalization step under aqueous phase, respectively, with the confirmation that the surfaces computed were in local-energy-minima.

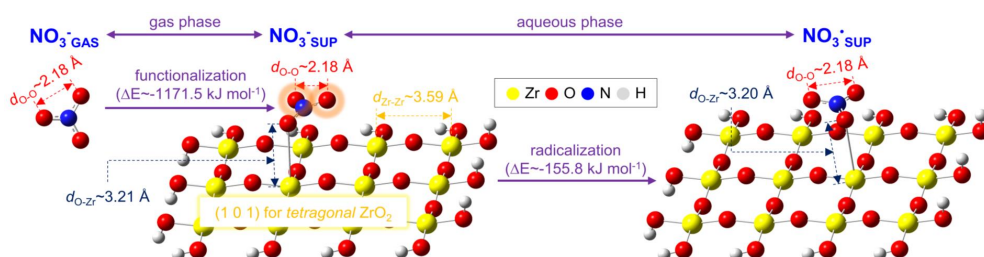


Figure 5-5. Computations concerning the energies released/up-taken for the adsorption of gaseous  $\text{NO}_3^-$  on the surface terminated at the (1 0 1) facet for tetragonal  $\text{ZrO}_2$  to form supported  $\text{NO}_3^-$  ( $\text{NO}_3^{\text{SUP}}$ ) with mono-dentate binding array and its radicalization to produce supported  $\text{NO}_3^{\cdot}$  ( $\text{NO}_3^{\cdot\text{SUP}}$ ) under aqueous phase at 300 K. Bond lengths of O-O innate to  $\text{NO}_3^-/\text{NO}_3^{\text{SUP}}/\text{NO}_3^{\cdot\text{SUP}}$ , Zr-Zr inherent to  $\text{ZrO}_2$ , and O-Zr indigenous  $\text{NO}_3^{\text{SUP}}/\text{NO}_3^{\cdot\text{SUP}}$  on  $\text{ZrO}_2$  were also computed for comparison.

Gaseous  $\text{NO}_3^-$  was verified to preferentially bind with  $\text{ZrO}_2$  cluster via mono-dentate configuration rather than bi-dentate counterpart. This was proved by exothermicity of  $\text{ZrO}_2$  cluster functionalized with mono-dentate  $\text{NO}_3^-$  ( $\text{NO}_3^{\text{SUP}}$ ), as quantified by  $\Delta E$  of  $-1171.5 \text{ kJ mol}^{-1}$  ( $\Delta E \sim \Delta E_{\text{NO}_3^{\text{SUP}} \text{ ON } \text{ZrO}_2} - (\Delta E_{\text{NO}_3^-} + \Delta E_{\text{ZrO}_2})$ ). This was in close agreement with *in situ*  $\text{NO}/\text{O}_2$ -DRIFT spectrum of  $\text{ZrO}_2$  surface (Figure 5-3C), where  $\text{NO}_3^{\text{SUP}}$  species were grafted on the surface primarily via mono-dentate binding array. Meanwhile, the distance of oxygens ( $d_{\text{O-O}}$ ) for gaseous  $\text{NO}_3^-$  was  $2.18 \text{ \AA}$  and maintained post its

transformation into  $\text{NO}_3^-_{\text{SUP}}$  (orange circle in Figure 5-5). Interestingly, oxygen of  $\text{NO}_3^-_{\text{SUP}}$  was 3.21 Å distant from lattice zirconium of  $\text{ZrO}_2$  cluster ( $d_{\text{O-Zr}}$ ), whereas the distance of two lattice zirconium atoms ( $d_{\text{Zr-Zr}}$ ) for  $\text{ZrO}_2$  cluster was 3.59 Å. Considering  $d_{\text{Zr-Zr}}$  was slightly longer than  $d_{\text{O-Zr}}$ , the formation of bi-dentate  $\text{NO}_3^-$  functionalities could be of high likelihood on  $\text{ZrO}_2$  cluster, yet, was demonstrated energetically unfeasible. This could provide additional evidence concerning mono-dentate  $\text{NO}_3^-_{\text{SUP}}$  species as prime functionalities for  $\text{ZrO}_2$  surface. In addition,  $\cdot\text{OH}$ -assisted radicalization of  $\text{NO}_3^-_{\text{SUP}}$  to produce  $\text{NO}_3\cdot$  analogue ( $\text{NO}_3\cdot_{\text{SUP}}$ ) and  $\text{OH}^-$  was also verified exothermic, as demonstrated by  $\Delta E$  involved of  $-155.8 \text{ kJ mol}^{-1}$  ( $\Delta E \sim (\Delta E_{\text{NO}_3\cdot_{\text{SUP}} \text{ ON ZrO}_2} + \Delta E_{\text{OH}^-}) - (\Delta E_{\text{NO}_3^-_{\text{SUP}} \text{ ON ZrO}_2} + \Delta E_{\text{OH}\cdot})$ ) in addition to the maintenance of  $d_{\text{O-O}}/d_{\text{O-Zr}}$  values and mono-dentate binding configuration even post the production of  $\text{NO}_3\cdot_{\text{SUP}}$  species via radicalization. This was con-current to the energetics on  $\cdot\text{OH} \rightarrow \text{NO}_3\cdot_{\text{SUP}}$  cycle for  $\text{MnO}_2$  polymorphs modified with  $\text{NO}_Y^-_{\text{SUP}}$  species in conjunction with  $\cdot\text{OH}$ -mediated, rapid transformation of  $\text{NO}_3^-$  (unsupported) to  $\text{NO}_3\cdot$  ( $\cdot\text{OH} \rightarrow \text{NO}_3\cdot$ ;  $k$  of  $10^5$ – $10^8 \text{ M}^{-1} \text{ sec}^{-1}$ ), as reported elsewhere.[18, 180, 181, 183] DFT calculations validated that  $\cdot\text{OH} \rightarrow \text{NO}_3\cdot_{\text{SUP}}$  cycle on  $\text{ZrO}_2\text{-N}$  was exothermic and made it persuasive that endothermic  $\cdot\text{OH}$  desorption was the rate-determining step to dictate the efficiency of overall  $\cdot\text{OH} \rightarrow \text{NO}_3\cdot_{\text{SUP}}$  cycle on  $\text{ZrO}_2\text{-N}$ .

### 5.3.5. Kinetics of homolytic H<sub>2</sub>O<sub>2</sub> dissection and $\cdot\text{OH} \rightarrow \text{NO}_3 \cdot_{\text{SUP}}$ cycles

Control reaction runs were performed under reaction-limited domains to further explore the tangibility of homolytic H<sub>2</sub>O<sub>2</sub> dissection cycle on ZrO<sub>2</sub> and overall  $\cdot\text{OH} \rightarrow \text{NO}_3 \cdot_{\text{SUP}}$  cycle on ZrO<sub>2</sub>-N. Their efficiencies, recyclabilities, and practicabilities in degrading aqueous contaminants were assessed using kinetic parameters such as initial reaction rates ( $-r$ ), energy barriers ( $E_{\text{BARRIER}}$ ), or pre-factors ( $k_{\text{APP},0}$ ). [25, 39, 107, 264] Phenol is feature by sp<sup>2</sup>-hybridized aromatics with -OH substituent and thereby was reported to possess high resistance against decomposition enabled by radicals. [25, 39, 107, 264] In addition, phenol can undergo initial degradation via radical ( $\cdot\text{OH}/\text{NO}_3 \cdot_{\text{SUP}}$ ) addition, H $\cdot$  abstraction, or electron transfer, where  $\cdot\text{OH}$  addition and H $\cdot$  abstraction can facilitate the accumulation of oligomeric compounds (poisons) on/near the catalyst surface through the formation of phenoxyl radical and reduce the recyclability of the surface in degrading phenol, as opposed to electron transfer. [114, 264, 270–272] Phenol was thus utilized as a model of refractory contaminants with the assumption that  $\cdot\text{OH}$  (from ZrO<sub>2</sub>) and  $\text{NO}_3 \cdot_{\text{SUP}}$  (from ZrO<sub>2</sub>-N) could initiate phenol degradation via distinct routes.

Meanwhile, electro-Fenton configuration was used to degrade phenol owing to continuous H<sub>2</sub>O<sub>2</sub> generation in the presence of electric potential, thus rendering the amount of H<sub>2</sub>O<sub>2</sub> fed to the catalyst surface to barely affect its efficiency to recur homolytic H<sub>2</sub>O<sub>2</sub> dissection or overall  $\cdot\text{OH} \rightarrow \text{NO}_3 \cdot_{\text{SUP}}$  cycle per unit time. [25, 39, 107, 264] For this purpose, a graphite coated with the catalyst and a graphite uncoated were used as the cathode and the anode, respectively, and were situated vertically under an aqueous phase including phenol prior to the initiation of its degradation by applying electric potential across the electrodes. [25, 39, 107, 264] Of note, H<sub>2</sub>O is oxidized on the anode via  $\text{H}_2\text{O} \rightarrow 2\text{H}^+ + 1/2\text{O}_2 + 2\text{e}^-$  and  $\text{H}_2\text{O} \rightarrow \text{H}^+ + \cdot\text{OH} + \text{e}^-$ , where the former produces H<sup>+</sup>, O<sub>2</sub>, and e<sup>-</sup>, all of which migrate to the cathode for the continuous H<sub>2</sub>O<sub>2</sub> evolution on/near the catalyst surface via  $2\text{H}^+ + \text{O}_2 + 2\text{e}^-$



→H<sub>2</sub>O<sub>2</sub>. [25, 39, 107, 264] In addition, anodic H<sub>2</sub>O oxidation also generates  $\cdot\text{OH}$  on/near the anodic surface, whereas the anodic surface in turn can interact with  $\cdot\text{OH}$  to produce surface O species prone to degrade phenol via anodic oxidation. [25, 39, 107, 264] Phenol degradation mediated by anodic oxidation should be deemed as a background and thus served to correct the reaction data for assessing  $\cdot\text{OH}$  or NO<sub>3</sub> $\cdot_{\text{SUP}}$ -mediated phenol degradation efficiency in accurate fashion. [25, 39, 107, 264] Of additional note, electric potentials were varied from 1 V to 3 V for phenol degradation runs. This can alter the energies exerted on the catalyst surfaces and helps verify the significance of  $\cdot\text{OH}$  desorption stage as the rate-determining step for homolytic H<sub>2</sub>O<sub>2</sub> dissection (on ZrO<sub>2</sub>) or overall  $\cdot\text{OH} \rightarrow \text{NO}_3\cdot_{\text{SUP}}$  cycle (on ZrO<sub>2</sub>-N). [25, 39, 107, 264] The selection of 1–3 V was owing to the similarity of kinetic data for the catalysts to that for background (anodic oxidation) at <1 V and substantial detachment of the catalyst particles from the cathode at >3 V, as also observed elsewhere. [25, 39, 107, 264]

Again, homolytic H<sub>2</sub>O<sub>2</sub> dissection cycle was deployed for ZrO<sub>2</sub> and ZrO<sub>2</sub>-N to evolve  $\cdot\text{OH}$  and NO<sub>3</sub> $\cdot_{\text{SUP}}$ , respectively, both of which potentially acted as the main degraders of phenol. The amounts of H<sub>2</sub>O<sub>2</sub> evolved on/near the catalysts in the presence of electric potential (N<sub>H<sub>2</sub>O<sub>2</sub></sub>) were assessed under the identical conditions to those used to conduct phenol degradation runs at 1–3 V and 25 ° C except for the exclusion of phenol. [25, 39, 47, 107, 264] N<sub>H<sub>2</sub>O<sub>2</sub></sub> values of the catalysts were comparable at an identical electric potential, increased rapidly to 0.07–0.12 mmol within 10 minutes, yet, were unaltered up to 8 hours of reaction runs. N<sub>H<sub>2</sub>O<sub>2</sub></sub> values of the catalysts hardly increased upon the elevation of electric potential applied (surface energy ↑) and/or the alteration of the catalysts utilized, which suggested their main role as H<sub>2</sub>O<sub>2</sub> scissors.

To simulate electric potential-assisted H<sub>2</sub>O<sub>2</sub> dissection cycle on the catalysts, these were exposed to the identical environments to those utilized to perform phenol degradation runs at 1–3 V and 25 ° C except for the exclusion of

phenol and electric potential along with the addition of  $\text{H}_2\text{O}_2$  to reaction mixtures.[25, 39, 47, 107, 264] Noteworthy,  $\text{H}_2\text{O}_2$  can be self-decomposed in the absence of the catalysts to produce  $\cdot\text{OH}$ ,  $\cdot\text{OOH}$ , or  $\text{O}_2\cdot^-$ , all of which can serve to degrade phenol.[18, 25, 39, 47, 107, 264]  $\text{H}_2\text{O}_2$  self-decomposition was thus regarded as a background[18, 25, 39, 47, 107, 264] and used to correct the reaction data considered up to an hour of reaction runs, whose  $\text{H}_2\text{O}_2$  conversions were  $<25\%$  and unlikely to be affected by internal/external diffusions. Background-subtracted pseudo-1<sup>st</sup>-order kinetic models of  $-\ln(C_{\text{H}_2\text{O}_2}/C_{\text{H}_2\text{O}_2,0})$  versus time for the catalysts served to extract their apparent reaction rate constants utilized to calculate initial  $\text{H}_2\text{O}_2$  dissection rates ( $-\text{r}_{\text{H}_2\text{O}_2}$ )[18, 25, 39, 47, 107, 264], as detailed in the Methods section.  $-\text{r}_{\text{H}_2\text{O}_2}$  is defined as the moles of  $\text{H}_2\text{O}_2$  consumed in a per- $\text{LA}_{\text{II}}$  site basis per unit time (Equation S4).[18, 25, 39, 47, 107, 264]  $-\text{r}_{\text{H}_2\text{O}_2}$  values of  $\text{ZrO}_2\text{-N}$  ( $\sim 0.10 \text{ min}^{-1}$ ) were  $\sim 0.04 \text{ min}^{-1}$  higher than those of  $\text{ZrO}_2$  across all the  $\text{N}_{\text{H}_2\text{O}_2}$  considered (Figure 5–6A), which could result from a higher  $E_{\text{LA}}$  ( $E_{\text{BARRIER}} \downarrow$ ), a higher  $E_{\text{BA}}$  ( $E_{\text{BARRIER}} \downarrow$ ), or a larger  $S_{\text{BA}}$  ( $k_{\text{APP},0} \uparrow$ ) for  $\text{ZrO}_2\text{-N}$  in comparison with the corresponding value for  $\text{ZrO}_2$ , as demonstrated above. In addition,  $-\text{r}_{\text{H}_2\text{O}_2}$  values of the catalysts were invariant under such conditions that could simulate electric potential-assisted  $\text{H}_2\text{O}_2$  dissection cycle on the catalysts. This suggested that the catalysts retained their  $\text{H}_2\text{O}_2$  scission abilities at all the electric potentials varied and that  $\text{H}_2\text{O}_2$  scission stage could not direct  $\text{H}_2\text{O}_2$  dissection cycle on  $\text{ZrO}_2$  and overall  $\cdot\text{OH} \rightarrow \text{NO}_3\cdot_{\text{SUP}}$  cycle on  $\text{ZrO}_2\text{-N}$  as the rate-determining step.

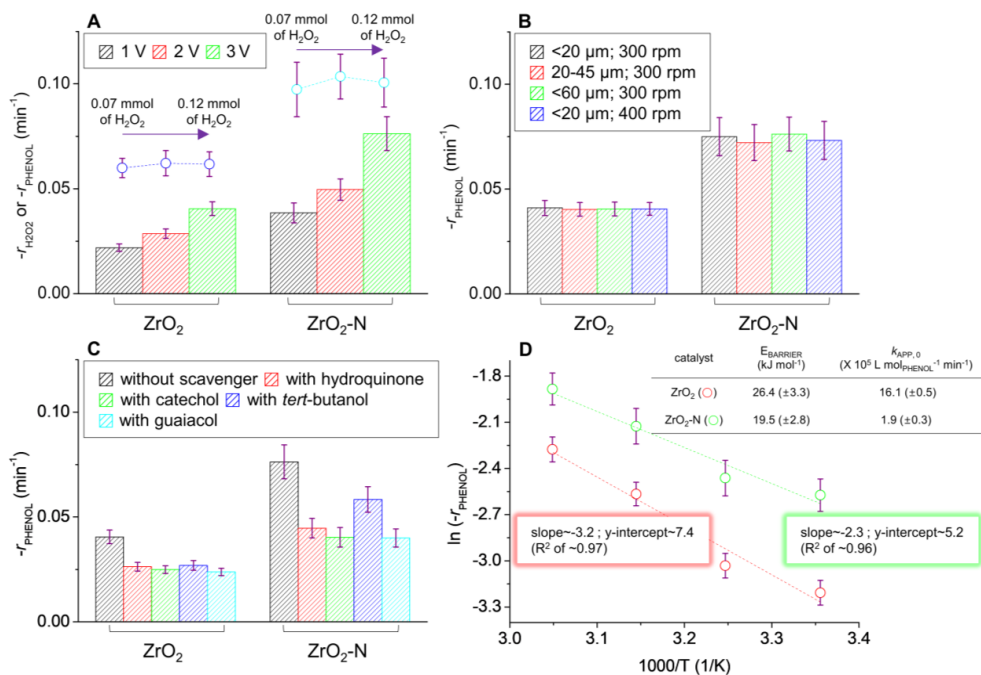


**Figure 5-6.** (A) Backgrounds-subtracted initial  $H_2O_2$  dissection rates per CO-accessible site basis ( $-r_{H_2O_2}$ ) for the catalysts with the variation of the amount of  $H_2O_2$  fed (0.07–0.12 mmol) at 0 V and 25 ° C. (B) Backgrounds-subtracted initial phenol degradation rates per CO-accessible site basis ( $-r_{PHENOL}$ ) for the catalysts with the variation of an electric potential (1–3 V) at 25 ° C. (C)  $-r_{PHENOL}$  values of the catalysts with the variation of a catalyst particle size and/or a stirring speed at 3 V and 25 ° C. (D)  $-r_{PHENOL}$  values of the catalysts in the absence or the presence of a scavenger (hydroquinone, catechol, *tert*-butanol, or guaiacol) at 3 V and 25 ° C. (E) Arrhenius plots (logarithmic apparent reaction rate constant ( $k_{APP}$ ) versus reciprocal of reaction temperature with regression factors ( $R^2$ ) of  $\geq 0.96$ ) for the catalysts to assess their energy barriers ( $E_{BARRIER}$  in inset table) and pre-factors directed by CO-accessible sites ( $k_{APP,0}$  in inset table) at 3 V and 25–55 ° C. In (D), slopes and y-intercepts correspond to  $-E_{BARRIER}/R \times 10^{-3}$  and  $\ln(C_{PHENOL,0} \times k_{APP,0})$ , respectively, where  $C_{PHENOL,0}$  denotes the initial phenol concentration ( $1.0 \times 10^{-3}$  mol L<sup>-1</sup>).

Phenol degradation efficiencies of the catalysts were then assessed in the presence of electric potential with the use of background-subtracted, initial phenol degradation rates ( $-r_{PHENOL}$ ), whose definition is analogous to that of  $-r_{H_2O_2}$  values, as depicted in Equation S5.[18, 25, 39, 47, 107, 264] Moreover, the methodologies used to assess  $-r_{PHENOL}$  values were also comparable to those utilized to evaluate  $-r_{H_2O_2}$  counterparts[18, 25, 39, 47, 107, 264], as specified in the Methods section. Phenol degradation runs were initially performed at 3 V with the alteration of the catalyst particulate sizes (<20  $\mu$ m, 20–45  $\mu$ m, or <60  $\mu$ m) and/or stirring speeds (300 rpm or 400 rpm) for ensuring that internal/external diffusional artifacts were absent across all

phenol degradation runs.[18, 25, 39, 47, 107, 264] The resulting  $-r_{\text{PHENOL}}$  values of the catalysts were indeed consistent regardless of the changes in the catalyst particle sizes and/or stirring speeds (Figure 5–6B), which validated the reactions were performed under reaction–limited domains.  $-r_{\text{PHENOL}}$  values of the catalysts were further assessed upon the change in electric potentials of 1–3 V, at which the catalysts showed greater  $-r_{\text{PHENOL}}$  values at a higher electric potential (Figure 5–6A). Again,  $\text{H}_2\text{O}_2$  adsorption on the surfaces could be hindered to greater extent at a higher electric potential because the energies acting on the catalyst surfaces were larger. This could decline  $-r_{\text{PHENOL}}$  values of the catalysts at a higher electric potential, if  $\text{H}_2\text{O}_2$  adsorption stage were the rate–determining step. This was counter–current to the trends found in  $-r_{\text{PHENOL}}$  values of the catalysts at dissimilar electric potentials. In conjunction with the retention of  $-r_{\text{H}_2\text{O}_2}$  values for the catalysts under the conditions utilized to simulate phenol degradation runs at 1–3 V (Figure 5–6A),  $-r_{\text{PHENOL}}$  values of the catalysts at 1–3 V suggested that  $\cdot\text{OH}$  desorption stage could direct homolytic  $\text{H}_2\text{O}_2$  dissection cycle on  $\text{ZrO}_2$  and overall  $\cdot\text{OH} \rightarrow \text{NO}_3^{\cdot\text{SUP}}$  cycle on  $\text{ZrO}_2\text{--N}$  as the rate–determining step.

It should be emphasized that  $-r_{\text{H}_2\text{O}_2}$  values of the catalysts were always higher than their  $-r_{\text{PHENOL}}$  counterparts (Figure 5–6A). This could originate from short lifetime of  $\cdot\text{OH}$  species ( $t_{1/2}$  of  $10^{-3}$   $\mu\text{second}$ ) to limit the chances utilized to degrade phenol for  $\text{ZrO}_2$  and to function as  $\text{NO}_3^{\cdot\text{SUP}}$  radicalizers for the formation of  $\text{NO}_3^{\cdot\text{SUP}}$  species on  $\text{ZrO}_2\text{--N}$ . In addition,  $\cdot\text{OOH}$  and  $\text{O}_2^{\cdot-}$  could also be evolved on the catalysts via homolytic  $\text{H}_2\text{O}_2$  dissection cycle, as evidenced by their EPR spectroscopy experiments. Despite having smaller  $E_0$  values of  $\leq 1.8$  V than that of  $\cdot\text{OH}$ , [18, 227]  $\cdot\text{OOH}$  and  $\text{O}_2^{\cdot-}$  might primarily contribute to degrade phenol. Furthermore, while  $\text{ZrO}_2\text{--N}$  displayed higher  $-r_{\text{PHENOL}}$  values than  $\text{ZrO}_2$  at 1–3 V (Figure 5–6A), it was inconclusive concerning whether  $\cdot\text{OH}$  and  $\text{NO}_3^{\cdot\text{SUP}}$  could function as major species utilized to decompose phenol for  $\text{ZrO}_2$  and  $\text{ZrO}_2\text{--N}$ , respectively. In this regard, phenol degradation runs were performed at 3 V and 25 ° C with

the inclusion of a scavenger exhibiting distinct secondary rate constants to terminate  $\cdot\text{OH}$ ,  $\cdot\text{OOH}$ ,  $\text{O}_2^{\cdot-}$ ,  $\text{NO}_2^{\cdot}$ , or  $\text{NO}_3^{\cdot}$ . Given  $k_{\cdot\text{OOH}/\text{O}_2^{\cdot-}}$  values of scavengers,  $-r_{\text{PHENOL}}$  values of the catalysts should be reduced in the order to without scavenger > with tert-butanol (or with guaiacol) > with catechol > with hydroquinone, if phenol degradation were dictated primarily by  $\cdot\text{OOH}$  or  $\text{O}_2^{\cdot-}$ . The resulting  $-r_{\text{PHENOL}}$  values of the catalysts, however, were of similar magnitude in the presence of all the scavengers depicted above for  $\text{ZrO}_2$  and in the presence of hydroquinone, catechol, and guaiacol for  $\text{ZrO}_2\text{-N}$  (Figure 5-6C). This indicated that phenol degradation efficiencies of the catalysts were not directed by  $\cdot\text{OOH}$  or  $\text{O}_2^{\cdot-}$ . Meanwhile, if  $\text{NO}_2^{\cdot\text{SUP}}$  functioned as the main degrader of phenol,  $-r_{\text{PHENOL}}$  of  $\text{ZrO}_2\text{-N}$  should not decrease in the presence of hydroquinone because of its  $k_{\text{NO}_2^{\cdot}}$  of  $\sim 0 \text{ M}^{-1} \text{ sec}^{-1}$ . However,  $-r_{\text{PHENOL}}$  of  $\text{ZrO}_2\text{-N}$  was severely reduced in the presence of hydroquinone (Figure 5-6C), which indicated that  $\text{NO}_2^{\cdot\text{SUP}}$  played a minor role in degrading phenol on  $\text{ZrO}_2\text{-N}$ . Importantly,  $\cdot\text{OH}$  can be quenched similarly in the presence of scavengers stated above ( $k_{\cdot\text{OH}}$  values of  $10^8\text{--}10^{10} \text{ M}^{-1} \text{ sec}^{-1}$ ), by which  $-r_{\text{PHENOL}}$  values of the catalyst should not be distinct in the presence of scavengers, if  $\cdot\text{OH}$  acted as the main decomposer of phenol.  $\text{ZrO}_2$  exhibited similar  $-r_{\text{PHENOL}}$  values, irrespectively of the type of scavengers utilized (Figure 5-6C). This indicated that homolytic  $\text{H}_2\text{O}_2$  dissection cycle on  $\text{ZrO}_2$  could provide  $\cdot\text{OH}$  as the main decomposer of phenol. On the other hand,  $\text{NO}_3^{\cdot\text{SUP}}$  can be quenched moderately in the presence of tert-butanol ( $k_{\text{NO}_3^{\cdot}}$  of  $10^4\text{--}10^5 \text{ M}^{-1} \text{ sec}^{-1}$ ) and should be scavenged severely yet similarly in the presence of hydroquinone, catechol, or guaiacol ( $k_{\text{NO}_3^{\cdot}}$  values of  $10^8\text{--}10^9 \text{ M}^{-1} \text{ sec}^{-1}$ ). This was in exact alignment with the trend found in  $-r_{\text{PHENOL}}$  values of  $\text{ZrO}_2\text{-N}$  in the presence of scavengers (Figure 5-6C). This indicated overall  $\cdot\text{OH} \rightarrow \text{NO}_3^{\cdot\text{SUP}}$  cycle on  $\text{ZrO}_2\text{-N}$  could provide  $\text{NO}_3^{\cdot\text{SUP}}$  as the main degrader of phenol.

Despite it was identified that  $\cdot\text{OH}$  and  $\text{NO}_3^{\cdot\text{SUP}}$  were the prime species to decompose phenol for  $\text{ZrO}_2$  and  $\text{ZrO}_2\text{-N}$ , respectively,  $\cdot\text{OH}$  and  $\text{NO}_3^{\cdot}$

(unsupported) might be generated by BA/LA<sub>II</sub> or NO<sub>3</sub><sup>-</sup> species leached from the catalyst surfaces. Their filtration runs were thus carried out under the identical environments to those used to perform phenol degradation runs at 3 V except for removing the catalysts after an hour for collecting reaction solutions via vacuum filtration.[18, 25, 39, 47, 107, 264] The resulting reaction solutions were then monitored with regard to the amount of phenol consumed ( $C^*_{\text{PHENOL}}$ ) versus time up to 8 hours.[18, 25, 39, 47, 107, 264] The profile of  $C^*_{\text{PHENOL}}$  versus time in the absence of the catalyst (blank run) could be dictated by H<sub>2</sub>O<sub>2</sub> self-decomposition and was also monitored for comparison.[18, 25, 39, 47, 107, 264] Blank run revealed  $C^*_{\text{PHENOL}}$  of 200 ( $\pm 30$ )  $\mu\text{M}$  at 1–8 hours, which was comparable to those of filtration runs at 1–8 hours (180 ( $\pm 10$ )  $\mu\text{M}$  for ZrO<sub>2</sub>; 180 ( $\pm 15$ )  $\mu\text{M}$  for ZrO<sub>2</sub>-N), mainly resulting from phenol decomposition mediated by the products of H<sub>2</sub>O<sub>2</sub> self-decomposition ( $\cdot\text{OH}$ ,  $\cdot\text{OOH}$ , or O<sub>2</sub> $\cdot^-$ ). This apparently validated that BA/LA<sub>II</sub> sites of the catalysts could cleave H<sub>2</sub>O<sub>2</sub> to form  $\cdot\text{OH}$  via heterogeneously catalysis and that ZrO<sub>2</sub>-N deployed supported NO<sub>3</sub> $\cdot$  (NO<sub>3</sub> $\cdot$ <sub>SUP</sub>) to decompose phenol.

It was demonstrated that homolytic H<sub>2</sub>O<sub>2</sub> dissection and overall  $\cdot\text{OH} \rightarrow \text{NO}_3\cdot_{\text{SUP}}$  cycles could escalate their efficiencies ( $-r_{\text{PHENOL}}$ ) by lowering  $E_{\text{BARRIER}}$  needed to desorb  $\cdot\text{OH}$  ( $E_{\text{BA}} \uparrow$  or  $E_{\text{LA}} \uparrow$ ) in tandem with the elevation of collision frequency ( $k_{\text{APP},0}$ ) for BA $\leftrightarrow$ H<sub>2</sub>O<sub>2</sub> ( $S_{\text{BA}} \uparrow$  for H<sub>2</sub>O<sub>2</sub> adsorption) or LA<sub>II</sub> $\leftrightarrow$ H<sub>2</sub>O<sub>2</sub> ( $S_{\text{LA}} \uparrow$  for H<sub>2</sub>O<sub>2</sub> distortion). In spite of having smaller  $S_{\text{LA}}$ , ZrO<sub>2</sub>-N possessed larger  $E_{\text{BA}}$ ,  $E_{\text{LA}}$ , and  $S_{\text{BA}}$  values compared to ZrO<sub>2</sub> and thereby was hypothesized to increase  $-r_{\text{PHENOL}}$  values with  $E_{\text{BARRIER}}$  and  $k_{\text{APP},0}$  being tentatively reduced and escalated. To demonstrate the postulation mentioned above, phenol degradation runs on the catalysts were performed identically to those at 3 V and 25 ° C with the exception of altering reaction temperature to 35–55 ° C, across which  $-r_{\text{PHENOL}}$  values of ZrO<sub>2</sub>-N were consistently higher than those of ZrO<sub>2</sub>. The energy acting on the catalyst surface can be elevated at a higher temperature, at which  $\cdot\text{OH}$  desorption from the surface

is more pronounced ( $E_{\text{BARRIER}} \downarrow$ ). [18, 25, 39, 47, 107, 264] This indicates that  $-r_{\text{PHENOL}}$  values of the catalyst should conform to Arrhenius behavior. [18, 47, 107] Arrhenius plots of logarithmic  $-r_{\text{PHENOL}}$  ( $\ln(-r_{\text{PHENOL}})$ ) versus reciprocal of reaction temperature ( $1/T$ ) were constructed for the catalysts (Figure 5–6D), showed good fits (regression factors ( $R^2$ ) of  $\geq 0.96$ ), and provided  $E_{\text{BARRIER}}$  (slopes) and  $k_{\text{APP},0}$  values (y–intercepts) of the catalysts (Equation S7). Interestingly, in spite of providing a higher  $S_{\text{BA}}$ ,  $\text{ZrO}_2\text{–N}$  exhibited a smaller  $k_{\text{APP},0}$  than that of  $\text{ZrO}_2$ . This might be attributed to steric hinderance caused by  $\text{NO}_3^-_{\text{SUP}}$  functionalities vicinal to  $\text{LA}_{\text{II}}$  sites, which could severely hamper the collisions of  $\text{LA}_{\text{II}} \leftrightarrow \text{H}_2\text{O}_2$  needed for geometric distortion of  $\text{H}_2\text{O}_2$ . In contrast, as anticipated,  $\text{ZrO}_2\text{–N}$  unveiled a smaller  $E_{\text{BARRIER}}$  than that of  $\text{ZrO}_2$ . This demonstrated the merits of mono–dentate  $\text{NO}_2^-_{\text{SUP}}$  ( $E_{\text{LA}} \uparrow$ ) and  $\text{NO}_3^-_{\text{SUP}}$  ( $E_{\text{BA}}/E_{\text{LA}} \uparrow$ ) functionalities, both of which made  $\text{LA}_{\text{II}}/\text{BA}$  sites intact, aided in accelerating  $\cdot\text{OH}$  productivity, and ultimately led to enhancing  $-r_{\text{PHENOL}}$  values of  $\text{ZrO}_2\text{–N}$  over those of  $\text{ZrO}_2$  via  $\cdot\text{OH} \rightarrow \text{NO}_3^-_{\text{SUP}}$  route.

### 5.3.6. Recyclability and practicability of $\text{ZrO}_2/\text{ZrO}_2\text{-N}$

Recyclabilities of the catalysts were then examined by exposing them to phenol degradation environments at 3 V multiple times, across which the catalyst-coated cathode subjected to the reaction run was rinsed with  $\text{H}_2\text{O}$ /ethanol and dried overnight at  $80^\circ\text{C}$  under vacuum prior to conducting the next reaction run.[18, 25, 39, 47, 107, 264] Phenol degradation efficiency of the (used) catalyst was assessed using  $-r'_{\text{PHENOL}}$ , which is defined as the moles of phenol consumed in a per-gram basis per unit time subjected to background subtraction for diagnosis in terms of commercial availability.[18, 25, 39, 47, 107, 264] The catalysts leached minute quantities of Zr and/or N contents throughout the recycle runs. This could indicate the retention of BA/LA<sub>II</sub> and/or  $\text{NO}_3^-_{\text{SUP}}$  species included in the catalysts, which were essential to activate homolytic  $\text{H}_2\text{O}_2$  scission and/or  $\cdot\text{OH} \rightarrow \text{NO}_3 \cdot_{\text{SUP}}$  cycles, respectively. Nonetheless,  $\text{ZrO}_2$  continuously declined its  $-r'_{\text{PHENOL}}$  values during each of the recycle runs (Figure 5-7A). This potentially resulted from the accumulation of oligomeric compounds (poisons) on LA<sub>II</sub>/BA sites, which could be incurred by phenoxy radicals (precursors of oligomeric compounds) generated via  $\cdot\text{OH}$  addition to and/or  $\text{H} \cdot$  abstraction from phenol, as discussed earlier.[114, 264, 270-272, 276] Conversely,  $\text{ZrO}_2\text{-N}$  outperformed  $\text{ZrO}_2$  in recycling phenol degradation. This was corroborated by  $-r_{\text{PHENOL}}$  values of  $\text{ZrO}_2\text{-N}$ , which were consistently higher than those of  $\text{ZrO}_2$  during each of the recycle runs (Figure 5-7A). In addition,  $\text{ZrO}_2\text{-N}$  maintained its  $-r'_{\text{PHENOL}}$  values throughout the recycle runs. This tentatively originated from the circumvention of phenoxy radical formation with the deployment of electron transfer as a primary pathway to initiate phenol degradation on  $\text{NO}_3 \cdot_{\text{SUP}}$  species.[270] Meanwhile, the intermediates evolved via  $\text{NO}_3 \cdot_{\text{SUP}}$  addition to and  $\text{H} \cdot$  abstraction from phenol could severely limit the recurrence of phenol degradation on  $\text{NO}_3 \cdot_{\text{SUP}}$  species per unit time ( $-r'_{\text{PHENOL}}$  of  $\sim 0 \mu\text{mol}_{\text{PHENOL}} \text{g}_{\text{CAT}}^{-1} \text{min}^{-1}$ ), as was not the case with phenol degradation recycle runs on  $\text{ZrO}_2\text{-N}$ .



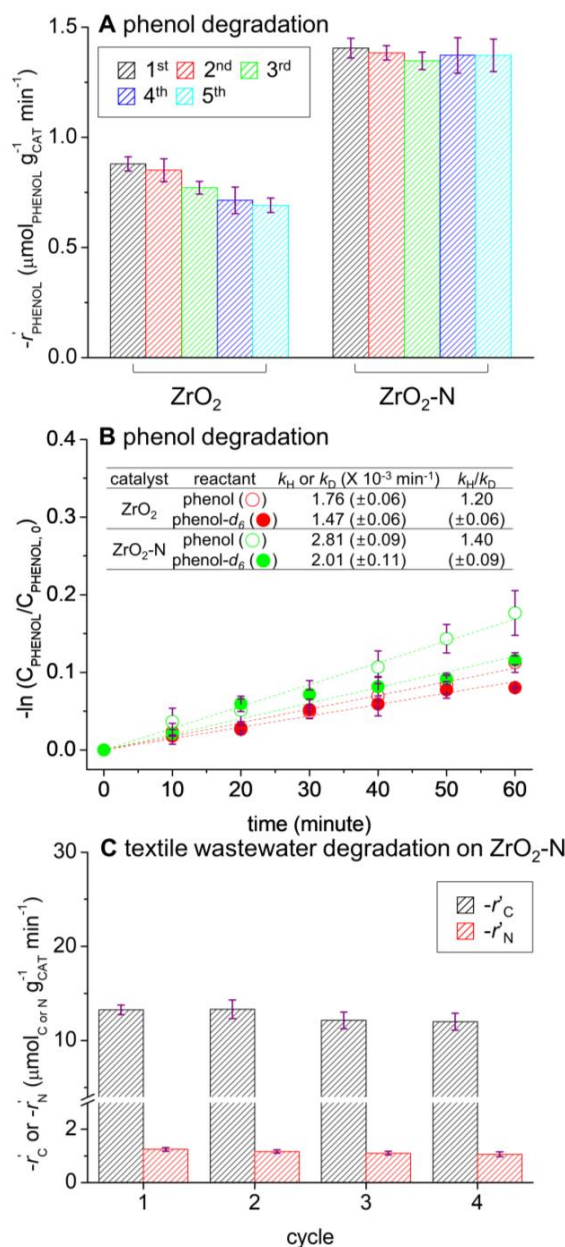


**Figure 5–7.** (A)  $-r'_{\text{PHENOL}}$  values of the catalysts exposed to recycle environments at 3 V and 25 ° C. (B) Fittings of background-subtracted phenol degradation data to pseudo-1st-order kinetic model ( $-\ln(C_{\text{PHENOL}}/C_{\text{PHENOL},0})$ ) versus time with regression factors ( $R^2$ ) of  $\geq 0.99$  for assessing apparent phenol degradation rate constants ( $k_H$  for phenol;  $k_D$  for phenol-*d*<sub>6</sub> in inset table) of the catalysts and their  $k_H/k_D$  values at 3 V and 25 ° C.  $k_H/k_D$  values served to identify the significance of hydrogen ( $\text{H}^\bullet$ ) abstraction to initially degrade phenol mediated by  $\cdot\text{OH}$  (for  $\text{ZrO}_2$ ) or  $\text{NO}_3^\bullet\text{SUP}$  (for  $\text{ZrO}_2\text{-N}$ ). In (B), background originates from the transition of  $\text{H}_2\text{O}_2$  into  $\cdot\text{OH}/\cdot\text{OOH}/\text{O}_2^\bullet$  in the absence of the catalyst, whereas  $C_{\text{PHENOL},0}$  and  $C_{\text{PHENOL}}$  denote phenol concentration initially fed and that monitored at a specific reaction time, respectively. Reaction conditions for (B): 0.2 g of catalyst with sizes of  $<60 \mu\text{m}$ ; 0.1 mmol of phenol or phenol-*d*<sub>6</sub>; 100 mL of de-ionized  $\text{H}_2\text{O}$ ; 0.05 mmol of  $\text{Na}_2\text{SO}_4$ ; 0 mmol of  $\text{H}_2\text{O}_2$ ; 3 V; 25 ° C; 300 rpm. (C) Backgrounds-subtracted initial textile wastewater mineralization rates per mass basis ( $-r'_C/-r'_N$ ) for  $\text{ZrO}_2\text{-N}$  exposed to recycle environments in the presence of  $\text{H}_2\text{O}_2$  at 0 V and 25 ° C.

This again suggested that electron transfer primarily initiated phenol degradation on  $\text{NO}_3^{\cdot\text{SUP}}$  species and could evade the accumulation of surface poisons, as claimed elsewhere.[270] Nevertheless,  $\text{NO}_3^{\cdot}$  (unsupported) was reported to start off with phenol degradation via  $\text{H}^{\cdot}$  abstraction with  $k$  of  $\sim 10^9 \text{ M}^{-1} \text{ sec}^{-1}$ . [271] Moreover, although the production of phenoxyl radicals via  $^{\cdot}\text{OH}$  addition or  $\text{H}^{\cdot}$  abstraction route was highly likely for  $\text{ZrO}_2$ , this opened the question concerning which route should outweigh the other to account for  $^{\cdot}\text{OH}$ -mediated generation of phenoxyl radicals on/near  $\text{ZrO}_2$ . Phenol- $\text{d}_6$  has O-deuterium (D) bond with a lower vibrational frequency compared to that of O-H bond innate to phenol. [287, 288] Phenol- $\text{d}_6$  thus needs a higher energy for O-D cleavage via  $\text{D}^{\cdot}$  abstraction to generate deuterated phenoxyl radical (apparent reaction rate constant  $\downarrow$ ) in comparison with an energy required for O-H cleavage of phenol via  $\text{H}^{\cdot}$  abstraction. [288, 289] In this regard, phenol and phenol- $\text{d}_6$  were degraded on the catalysts at 3 V for evaluating their apparent reaction rate constants referred to as  $k_{\text{H}}$  and  $k_{\text{D}}$ , respectively, post the correction of reaction data using backgrounds (Figure 5-7B). The resulting ratios of  $k_{\text{H}}$  to  $k_{\text{D}}$  ( $k_{\text{H}}/k_{\text{D}}$ ) were merely 1.2-1.4 for the catalysts. Given previous literatures arguing that  $\text{H}^{\cdot}$  (or  $\text{D}^{\cdot}$ ) abstraction becomes significant at  $k_{\text{H}}/k_{\text{D}}$  values of  $>2$ , [290, 291]  $k_{\text{H}}/k_{\text{D}}$  values assessed herein could indicate that  $\text{H}^{\cdot}$  (or  $\text{D}^{\cdot}$ ) abstraction route was insignificant to initially dictate phenol (or phenol- $\text{d}_6$ ) degradation, where  $^{\cdot}\text{OH}$  (for  $\text{ZrO}_2$ ) or  $\text{NO}_3^{\cdot\text{SUP}}$  (for  $\text{ZrO}_2\text{-N}$ ) served as the major degrader of phenol. This also clarified that phenol degradation could be initiated by  $^{\cdot}\text{OH}$  addition and electron transfer on/near  $\text{ZrO}_2$  and  $\text{ZrO}_2\text{-N}$ , respectively.

To present additional proofs concerning primary pathways to initiate phenol degradation on the catalysts, EDX mapping images of the catalysts subjected to the 1<sup>st</sup>, 3<sup>rd</sup>, and 5<sup>th</sup> recycle runs for 8 hours (Figure 5-7A) were collected to explore their surface elemental ratios of N/Zr or C to Zr (C/Zr).  $\text{ZrO}_2\text{-N}$  highly dispersed surface N species and displayed N/Zr of 0.09 prior to the 1<sup>st</sup> cycle, which was in close line with N/Zr (0.10) of  $\text{ZrO}_2\text{-N}$  analyzed via XP

spectroscopy. Moreover, N/Zr of ZrO<sub>2</sub>-N was maintained up the 5<sup>th</sup> cycle, which was also in agreement with negligible N leaching of ZrO<sub>2</sub>-N up to the 5<sup>th</sup> cycle, as discussed earlier. Noteworthy, ZrO<sub>2</sub>-N exhibited C/Zr values of 0.09 post the 1<sup>st</sup> cycle, 0.10 post the 3<sup>rd</sup>/5<sup>th</sup> cycles, all of which were a third–a sixth of C/Zr values for ZrO<sub>2</sub> (0.30/0.37/0.63 post the 1<sup>st</sup>/3<sup>rd</sup>/5<sup>th</sup> cycles). This apparently unveiled  $\cdot\text{OH}$  addition–mediated accumulation of poisons on ZrO<sub>2</sub> surface via  $\cdot\text{OH}$  addition. This was opposed to NO<sub>3</sub> $\cdot_{\text{SUP}}$ –enabled circumvention of poison deposition on ZrO<sub>2</sub>-N surface via electron transfer, although few  $\cdot\text{OH}$  in excess relative to NO<sub>3</sub> $\cdot_{\text{SUP}}$  served to trigger phenol degradation via  $\cdot\text{OH}$  addition rather than to radicalize NO<sub>3</sub> $\cdot_{\text{SUP}}$  for the production of NO<sub>3</sub> $\cdot_{\text{SUP}}$  (C/Zr of  $\leq 0.10$  up to the 5<sup>th</sup> cycle).

$\alpha$ -MnO<sub>2</sub> modified with NO<sub>Y</sub><sup>-</sup> functionalities ( $\alpha$ -MnO<sub>2</sub>-N) could afford NO<sub>3</sub> $\cdot_{\text{SUP}}$  species evolved via overall  $\cdot\text{OH} \rightarrow \text{NO}_3\cdot_{\text{SUP}}$  route, whose rate–determining step was to desorb  $\cdot\text{OH}$  from reducible Mn<sup>2+/3+</sup> species, whereas  $\cdot\text{OH}$  desorption could be accelerated to greater extent at a smaller E<sub>LA</sub>.<sup>26</sup> E<sub>LA</sub> of Mn<sup>2+/3+</sup> species innate to  $\alpha$ -MnO<sub>2</sub>-N was far smaller than that of LA<sub>II</sub> counterparts inherent to ZrO<sub>2</sub>-N. This was evidenced by minute N<sub>CO</sub> values of  $\alpha$ -MnO<sub>2</sub>-N, which were obtained from its CO isotherm experiments at  $\geq -20^\circ \text{C}$ . [18] This highly suggested that E<sub>BARRIER</sub> of overall  $\cdot\text{OH} \rightarrow \text{NO}_3\cdot_{\text{SUP}}$  route could be lower in  $\alpha$ -MnO<sub>2</sub>-N than in ZrO<sub>2</sub>-N. In addition, although  $\alpha$ -MnO<sub>2</sub>-N and ZrO<sub>2</sub>-N contained similar bulk (or surface) N contents relative to metals,  $\alpha$ -MnO<sub>2</sub>-N provided a larger number of NO<sub>3</sub> $\cdot_{\text{SUP}}$  precursors (NO<sub>3</sub><sup>-</sup><sub>SUP</sub>) than ZrO<sub>2</sub>-N, as corroborated by their XP/XANES spectroscopy experiments. [18] This also suggested that  $\alpha$ -MnO<sub>2</sub>-N could enhance collision frequencies of  $\cdot\text{OH} \leftrightarrow \text{NO}_3\cdot_{\text{SUP}}$  or NO<sub>3</sub> $\cdot_{\text{SUP}} \leftrightarrow$  pollutant over ZrO<sub>2</sub>-N. All of these were coupled to allow us to postulate that  $\alpha$ -MnO<sub>2</sub>-N can outperform ZrO<sub>2</sub>-N in mineralizing pollutants by lowering E<sub>BARRIER</sub> yet elevating k<sub>APP,0</sub> better than ZrO<sub>2</sub>-N.

To verify the hypothesis stated above, ZrO<sub>2</sub>-N were subjected to textile wastewater mineralization runs multiple times, during which the reaction

conditions were regulated identically to those on  $\alpha$ -MnO<sub>2</sub>-N we reported previously, while using an excess amount of H<sub>2</sub>O<sub>2</sub> species as  $\cdot$ OH precursors in the absence of electric potential.[18] Moreover, suspended solids and  $\cdot$ OH scavengers (CO<sub>3</sub><sup>2-</sup>/HCO<sub>3</sub><sup>-</sup>) were removed from textile wastewater identically via vacuum filtration and pH regulation, respectively.[18] Notably, the resulting textile wastewater and that utilized previously were verified to have TOC/TN values almost identical each other, as detailed in the Methods section. In addition, mineralization efficiencies of textile wastewater on  $\alpha$ -MnO<sub>2</sub>-N and ZrO<sub>2</sub>-N were assessed using  $-r'_C/-r'_N$  values, whose definitions are the moles of carbon/nitrogen mineralized in a per-gram basis per unit time (Equation S8 and S9) post the correction of reaction data using backgrounds such as H<sub>2</sub>O<sub>2</sub> self-decomposition and wastewater adsorption on the surface.[18] Apparently,  $-r'_C/-r'_N$  values of  $\alpha$ -MnO<sub>2</sub>-N were about 2-fold/1.3-fold greater than the corresponding values of ZrO<sub>2</sub>-N during the 1<sup>st</sup> cycle (Figure 5-7C), as predicted earlier. However, throughout the recycle runs,  $\alpha$ -MnO<sub>2</sub>-N continuously leached moderate quantities of Mn species, whose nature was proved Lewis acidic, as we reported elsewhere.[18] This resulted in considerable reduction of  $-r'_C$  and  $-r'_N$  values for  $\alpha$ -MnO<sub>2</sub>-N subjected to the 4<sup>th</sup> cycle, which were only a sixth and a half of the corresponding values for  $\alpha$ -MnO<sub>2</sub>-N at the 1<sup>st</sup> cycle.[18] In contrast, ZrO<sub>2</sub>-N leached negligible quantities of Zr species and retained  $-r'_C/-r'_N$  values throughout the recycle runs. Importantly,  $-r'_C/-r'_N$  values of ZrO<sub>2</sub>-N were larger than those of  $\alpha$ -MnO<sub>2</sub>-N from the 2<sup>nd</sup> cycle. This apparently demonstrated that in comparison with  $\alpha$ -MnO<sub>2</sub>-N, ZrO<sub>2</sub>-N could exploit overall  $\cdot$ OH $\rightarrow$ NO<sub>3</sub> $\cdot$ <sub>SUP</sub> route in more sustainable fashion and that non-reducible metal oxide (ZrO<sub>2</sub>) could be particularly conducive to deploy NO<sub>3</sub> $\cdot$ <sub>SUP</sub> as the prime degrader/mineralizer of aqueous refractory pollutants.

## 5.4. Conclusions

This study has deployed radical transfer from  $\cdot\text{OH}$  to surface  $\text{NO}_3^-$  functionality ( $\text{NO}_3^-_{\text{SUP}}$ ) to generate  $\text{NO}_3\cdot$  analogue ( $\cdot\text{OH}\rightarrow\text{NO}_3\cdot_{\text{SUP}}$ ), for which a catalytic scaffold utilized to activate  $\text{H}_2\text{O}_2$  dissection and  $\cdot\text{OH}\rightarrow\text{NO}_3\cdot_{\text{SUP}}$  (denoted as overall  $\cdot\text{OH}\rightarrow\text{NO}_3\cdot_{\text{SUP}}$ ) was altered from reducible metal oxide to non-reducible counterpart. The primary motivation of this study was the centrality of catalytic  $\text{H}_2\text{O}_2$  dissection, whose  $\cdot\text{OH}$  productivity could direct the efficiency of  $\text{NO}_3\cdot_{\text{SUP}}$  formation via  $\cdot\text{OH}\rightarrow\text{NO}_3\cdot_{\text{SUP}}$ . Additional impetus of this study was the benefits of homolytic  $\text{H}_2\text{O}_2$  dissection ( $\text{H}_2\text{O}_2\rightarrow 2\cdot\text{OH}$ ) relative to heterolytic counterpart ( $\text{H}_2\text{O}_2+\text{electron}\rightarrow\cdot\text{OH}+\text{OH}^-$ ) such as a higher  $\cdot\text{OH}$  productivity, minute leaching of  $\text{H}_2\text{O}_2$  scissors (Lewis acidic metal (LA) or Brönsted acidic -OH (BA)) alongside with intermolecular electron exchange between LA and  $\text{H}_2\text{O}_2$  being uninvolved. Thus, overall  $\cdot\text{OH}\rightarrow\text{NO}_3\cdot_{\text{SUP}}$  on non-reducible metal oxides was expected to advance degradation or mineralization efficiency of aqueous refractory contaminants (phenol or textile wastewater) via sustainable manner with the use of  $\text{NO}_3\cdot_{\text{SUP}}$  species.

In this regard,  $\text{ZrO}_2$  served as a representative of non-reducible metal oxides activating homolytic  $\text{H}_2\text{O}_2$  dissection to evolve  $\cdot\text{OH}$ , whereas  $\text{ZrO}_2$  functionalized with  $\text{NO}_3^-$  species ( $\text{ZrO}_2\text{-N}$ ) served to activate overall  $\cdot\text{OH}\rightarrow\text{NO}_3\cdot_{\text{SUP}}$  to evolve  $\text{NO}_3\cdot_{\text{SUP}}$ . In conjunction with DFT calculations, in situ NO/ $\text{O}_2$ -DRIFT, XP, and XANES spectroscopy experiments provided evidence that  $\text{NO}_3^-$  functionalities were grafted on  $\text{ZrO}_2\text{-N}$  surface with mono-dentate binding array only. Moreover, DFT calculations and EPR spectroscopy experiments demonstrated that  $\text{ZrO}_2$  and  $\text{ZrO}_2\text{-N}$  could evolve  $\cdot\text{OH}$  and  $\cdot\text{OH}/\text{NO}_3\cdot_{\text{SUP}}$ , respectively, with  $\cdot\text{OH}\rightarrow\text{NO}_3\cdot_{\text{SUP}}$  on  $\text{ZrO}_2\text{-N}$  being exothermic and spontaneous. This left endothermic  $\cdot\text{OH}$  desorption as the rate-determining step of homolytic  $\text{H}_2\text{O}_2$  dissection and overall  $\cdot\text{OH}\rightarrow\text{NO}_3\cdot_{\text{SUP}}$ , as also substantiated by a series of kinetic runs to dissect  $\text{H}_2\text{O}_2$  or degrade phenol with the variation of energies exerted on  $\text{ZrO}_2$

surfaces.

Of note, strong acidic strengths of BA/LA sites ( $E_{BA}/E_{LA}$ ) are desired to decline energy barriers ( $E_{BARRIER}$ ) needed to desorb  $\cdot OH$  for homolytic  $H_2O_2$  dissection and overall  $\cdot OH \rightarrow NO_3 \cdot_{SUP}$ . Meanwhile, large areas of BA/LA sites ( $S_{BA}/S_{LA}$ ) are beneficial to elevate collision frequencies of  $BA \leftrightarrow H_2O_2$  (for  $H_2O_2$  adsorption) and  $LA \leftrightarrow H_2O_2$  (for  $H_2O_2$  distortion), resulting in the increase in pre-factors ( $k_{APP,0}$ ) for homolytic  $H_2O_2$  dissection and overall  $\cdot OH \rightarrow NO_3 \cdot_{SUP}$ . CO/CO<sub>2</sub> isotherms and NH<sub>3</sub>-TPD experiments validated that compared to ZrO<sub>2</sub>, ZrO<sub>2</sub>-N with mono-dentate  $NO_3^-$  species provided larger  $E_{BA}/E_{LA}$  values and a higher  $S_{BA}$ , where the formers were identified to reduce  $E_{BARRIER}$  of ZrO<sub>2</sub>-N, albeit the latter hardly elevated  $k_{APP,0}$  of ZrO<sub>2</sub>-N due possible to steric hindrance incurred by  $NO_3^-$  functionalities vicinal to BA sites, as evidenced by Arrhenius plots of the catalysts.

Of additional note, filtration/scavenging runs demonstrated that  $\cdot OH$  and  $NO_3 \cdot_{SUP}$  functioned as primary decomposers of contaminants for ZrO<sub>2</sub> and ZrO<sub>2</sub>-N, respectively.  $NO_3 \cdot_{SUP}$  was verified to enhance efficiencies ( $-r_{PHENOL}$ ) in recycling phenol degradation over  $\cdot OH$ . In particular,  $\cdot OH$  initiated phenol degradation via  $\cdot OH$  addition, continuously accumulated poisons on LA/BA sites of ZrO<sub>2</sub> across the recycle runs, thereby gradually declining its  $-r_{PHENOL}$  values throughout the recycle runs. Conversely,  $NO_3 \cdot_{SUP}$  initiated phenol degradation via electron transfer and evaded the generation/accumulation of poisons on ZrO<sub>2</sub>-N surface, as evidenced by the retention of its  $-r_{PHENOL}$  values throughout the recycle runs. Furthermore, ZrO<sub>2</sub>-N functioned as a scaffold to immobilize  $NO_3 \cdot_{SUP}$  species better than a representative of reducible metal oxides ( $\alpha$ -MnO<sub>2</sub>-N) we reported previously, as proved by their efficiencies ( $-r'_C/-r'_N$ ) in recycling textile wastewater mineralization.  $-r'_C/-r'_N$  values of ZrO<sub>2</sub>-N were maintained throughout the recycle runs and higher than those of  $\alpha$ -MnO<sub>2</sub>-N from the 2<sup>nd</sup> cycle with the numbers of Zr leached from ZrO<sub>2</sub>-N being marginal in comparison with those of Mn leached from  $\alpha$ -MnO<sub>2</sub>-N.

# Chapter 6

## Summary and Future Work

### 6.1. Summary

This dissertation reports a study on pursuing several primary objectives with the functionalized metal oxide catalysts, as shown below.

(1) The types of advanced oxidation processes and the Fenton reaction are discussed in Chapter 1. Particularly, radical chemistry has been the core of environmental catalysis because radicals with high oxidation potentials ( $\cdot\text{OH}$  and  $\text{SO}_4^{\cdot-}$ ) can degrade aqueous contaminants (such as phenol) via oxidation. Furthermore, the rationales for using metal oxides in water treatment are suggested.

(2) Chapter 2 proposed and pioneered a novel methodology to accommodate  $\text{SO}_4^{\cdot-}$  on the surface of the NiO platform, wherein  $\text{Ni}^{\delta+}$  species ( $\delta \leq 2$ ) and  $\text{SO}_4^{2-}$  functionalities are dispersed and act as a  $\text{H}_2\text{O}_2$  decomposer ( $\cdot\text{OH}$  producers) and  $\text{SO}_4^{\cdot-}$  precursors, respectively. The key part of the Chapter 2 describes the radical transfer from  $\cdot\text{OH}$  to  $\text{SO}_4^{\cdot-}$  ( $\cdot\text{OH} \rightarrow \text{SO}_4^{\cdot-}$ ), which occurred as long as the  $\text{SO}_4^{2-}$  functionalities were immobilized on the NiO surface. Additionally, the supported  $\text{SO}_4^{\cdot-}$  species generated via the  $\cdot\text{OH} \rightarrow \text{SO}_4^{\cdot-}$  route outperformed traditional  $\cdot\text{OH}$  species in efficiently and sustainably decomposing aqueous pollutants.

The surface reaction dynamics/energetics of  $\cdot\text{OH} \rightarrow \text{SO}_4^{\cdot-}$  were clarified via a kinetic assessment and DFT calculations, both of which have never been implemented in previous studies on the radical-mediated oxidation of recalcitrant contaminants. Importantly, NiO served as a platform to afford  $\text{Ni}^{\delta+}$  and  $\text{SO}_4^{2-}$ . This was motivated by our previous study on metal sulfides, in which the use of  $\text{Ni}^{\delta+}$  helped determine the Lewis acidity most desired to fragment  $\text{H}_2\text{O}_2$  among Period-4 elements, such as  $\text{Mn}^{\delta+}$ ,  $\text{Fe}^{\delta+}$ ,  $\text{Co}^{\delta+}$ ,  $\text{Ni}^{\delta+}$ , and  $\text{Cu}^{\delta+}$ .

(3) In Chapter 3, the aforementioned  $\cdot\text{OH} \rightarrow \text{SO}_4^{\cdot-}$  pathway was discussed as a unique, and significant route, thereby motivating a study on altering the platform used to accelerate this pathway better than NiO. The radical ( $\cdot\text{OH}$  or  $\text{SO}_4^{\cdot-}$ )–assisted degradation of aqueous refractory pollutants faces two conundrums: such as 1) periodic demand of the radical precursor ( $\text{H}_2\text{O}_2$  or  $\text{HSO}_5^-/\text{S}_2\text{O}_8^{2-}$ ) upon the exhaustion of the radical to compensate for its short lifespan, and 2) limited number/strength of the Lewis acidic metal innate to the catalyst for cleaving the radical precursor. These issues can be resolved mostly by positioning a bare anode and a cathode coated with a  $\text{SO}_4^{2-}$ –functionalized metal oxide catalyst in an aqueous electric environment, as pioneered in this study and demonstrated in Chapter 2. This can permit continuous evolution of  $\text{H}_2\text{O}_2$  on/near the cathode, sustainable catalytic  $\text{H}_2\text{O}_2$  cleavage on the Lewis acidic metal for evolving  $\cdot\text{OH}$ , consistent recovery of the Lewis acidic metal by  $\text{e}^-$  reduction, and recurrent radicalization of the  $\text{SO}_4^{2-}$  functionality by  $\cdot\text{OH}$  to generate supported  $\text{SO}_4^{\cdot-}$  ( $\cdot\text{OH} \rightarrow \text{SO}_4^{\cdot-}$ ), all of which are coupled to enhance the contaminant–degrading activity and reusability of supported  $\text{SO}_4^{\cdot-}$  over those of conventional  $\cdot\text{OH}$ .

However, NiO should only include a coordinatively–saturated  $\text{Ni}^{2+}$  species that is inaccessible to the  $\cdot\text{OH}$  precursor ( $\text{H}_2\text{O}_2$ ), as indicated by their crystal structures. Hence, NiO can significantly accelerate  $\cdot\text{OH} \rightarrow \text{SO}_4^{\cdot-}$  if it is synthesized under conditions that favor the formation of numerous Lewis acidic  $\text{Ni}^{2+}$  defects. The Lewis acidic strength of surface metals is critical in promoting the  $\cdot\text{OH} \rightarrow \text{SO}_4^{\cdot-}$  pathway because it is primarily directed by  $\cdot\text{OH}$  desorption from the Lewis acidic metals as the rate–determining stage. Additionally, oxo–spinel is a fascinating class of metal oxides that intrinsically bears  $\text{H}_2\text{O}_2$ –accessible/open metal sites, whose quantity, Lewis acidic strength, accessibility, or stability in an aqueous electric environment can be tuned according to changes in the properties of the metals used such as their type and compositions.



(4) In Chapter 4, we pioneered the use of  $\alpha$ -/ $\beta$ -/ $\gamma$ -MnO<sub>2</sub> polymorphs as they contain Lewis acidic Mn<sup>2+/3+</sup> species, which can be exploited for heterolytic scission of excess H<sub>2</sub>O<sub>2</sub> to produce large quantities of  $\cdot$ OH/ $\cdot$ OOH/O<sub>2</sub><sup>•-</sup>, among which the abundant  $\cdot$ OOH and O<sub>2</sub><sup>•-</sup> can regenerate Mn<sup>2+/3+</sup> species for the recurrence of  $\cdot$ OH evolution. Additionally,  $\alpha$ -/ $\beta$ -/ $\gamma$ -MnO<sub>2</sub> exhibit high intimacy with NO<sub>3</sub><sup>-</sup> species and thus immobilize NO<sub>3</sub><sup>-</sup> functionalities (the NO<sub>3</sub><sup>•</sup> precursor) on their surfaces. Oxidative degradation of aqueous pollutants is conventionally enabled by surface-unbound  $\cdot$ OH and SO<sub>4</sub><sup>•-</sup>, both of which can readily deprive of contaminants of electrons (e<sup>-</sup>) for their rapid mineralization. However,  $\cdot$ OH and SO<sub>4</sub><sup>•-</sup>, have short lifetimes and/or a high inclination to being quenched by the background scavengers present in water matrices. Interestingly, NO<sub>3</sub><sup>•</sup> has a lengthy lifetime and a strong resistance to being scavenged by water matrices despite having a moderate oxidizing power. However, the generation of NO<sub>3</sub><sup>•</sup> is arduous owing to requirements such as the presence of a labile O<sub>3</sub> coupled NO<sub>2</sub><sup>•</sup> in the absence of sunlight, an element exhibiting activity in high-energy e<sup>-</sup>-beam-assisted radiolysis, and a high-power laser for radicalizing NO<sub>3</sub><sup>-</sup> ions in an acidic environment.

Consequently, we envisioned that the radical transfer from surface-unbound  $\cdot$ OH species to the NO<sub>3</sub><sup>-</sup> functionalities supported on  $\alpha$ -/ $\beta$ -/ $\gamma$ -MnO<sub>2</sub> surfaces was energetically favorable (exothermic) and highly tangible under a circumneutral pH environment (denoted as  $\cdot$ OH  $\rightarrow$  NO<sub>3</sub><sup>•</sup><sub>SUP</sub>). Of additional significance, we hypothesized that the  $\cdot$ OH  $\rightarrow$  NO<sub>3</sub><sup>•</sup><sub>SUP</sub> efficiency on  $\alpha$ -/ $\beta$ -/ $\gamma$ -MnO<sub>2</sub> is influenced by their geometrical traits. Through a series of kinetic runs performed using a model compound (phenol) and/or real (textile) wastewater, NO<sub>3</sub><sup>•</sup><sub>SUP</sub> was confirmed to be superior to conventional  $\cdot$ OH and SO<sub>4</sub><sup>•-</sup><sub>SUP</sub> (produced via  $\cdot$ OH  $\rightarrow$  SO<sub>4</sub><sup>•-</sup><sub>SUP</sub>) in degrading pollutants.

(5) In Chapter 5, as detailed below, an altered methodology was presented to catalyze the  $\cdot\text{OH}$  produced via heterolytic  $\text{H}_2\text{O}_2$  dissection on a reducible metal oxide ( $\text{MnO}_2$ ) to its homolytic counterpart on a nonreducible metal oxide ( $\text{ZrO}_2$ ).  $\cdot\text{OH}$  acts as a powerful trigger (standard reduction potential ( $E_0$ ) of 2.7 V) to radicalize aqueous refractory pollutants (such as phenol) via  $\cdot\text{OH}$  addition/ $\cdot\text{H}$  abstraction and forms intermediates (such as the phenoxyl radical) that are susceptible to evolving oligomeric compounds via couplings. However, these compounds function as surface poisons and are deposited onto/near surface  $\text{H}_2\text{O}_2$  activators, which produce  $\cdot\text{OH}$  via  $\text{H}_2\text{O}_2$  cleavage, thereby reducing the efficiency of catalysts used in cyclic pollutant degradation or mineralization. Although,  $\text{NO}_3\cdot$  is considered a moderate initiator of pollutant radicalization ( $E_0$  of 2.4 V), it can substitute  $\cdot\text{OH}$  owing to its longer half-life (6  $\mu$ seconds) than that of  $\cdot\text{OH}$  ( $10^{-3}$   $\mu$ second) and a greater tolerance against aqueous backgrounds. Nevertheless,  $\text{NO}_3\cdot$  has rarely been used as a contaminant degrader primarily owing to the requirement of a radioactive element, unstable  $\text{NO}_2\cdot$ ,  $\text{HNO}_3$ , or highly excited electrons for  $\text{NO}_3\cdot$  generation via photolysis/radiolysis.

The overall  $\cdot\text{OH} \rightarrow \text{NO}_3\cdot_{\text{SUP}}$  reaction and the  $\text{MnO}_2$  polymorphs serving as scaffolds that include  $\text{H}_2\text{O}_2$  activators ( $\text{Mn}^{2+/3+}$ ) and anchoring spots for  $\text{NO}_3^-$  species were discussed in Chapter 4. However, the resulting  $\text{NO}_3^-$ -functionalized  $\text{MnO}_2$  ( $\text{MnO}_2\text{-N}$ ) suffered from the severe leaching-induced loss of the surface  $\text{Mn}^{2+/3+}$  species, decreasing the  $\cdot\text{OH}$  productivity. Additionally,  $\text{MnO}_2\text{-N}$  primarily bore *bi*-dentate  $\text{NO}_3^-$  functionalities rather than *mono*-dentate counterparts. However, the *bi*-dentate  $\text{NO}_3^-$  species led to the loss of  $\text{Mn}^{2+/3+}$  species (decreased  $\cdot\text{OH}$  productivity) and provided only one O atom in a per- $\text{NO}_3^-$  functionality available for activating  $\cdot\text{OH} \rightarrow \text{NO}_3\cdot_{\text{SUP}}$ . Therefore, conclusions were drawn that  $\text{ZrO}_2$  modified with  $\text{NO}_3^-$  functionalities ( $\text{ZrO}_2\text{-N}$ ) was more efficient and stable than  $\text{MnO}_2\text{-N}$  in the cyclic textile-wastewater mineralization, as evidenced by the recycle runs and quantities of leached Zr/Mn.

## 6.2. Future work and perspectives

To achieve higher activities than those of the aforementioned functionalized metal oxide catalysts, one can suggest the further modification of the functionalities (*e.g.*, phosphate functional group). The  $\text{H}_{3-X}\text{PO}_4 \cdot^{(X-1)-}$  species and their precursors ( $\text{H}_{3-X}\text{PO}_4^{X-}$ ) can be grafted onto the surface exclusively via *mono*-dentate binding arrays, for instance, by utilizing  $(\text{NH}_4)_2\text{HPO}_4$  as  $\text{H}_{3-X}\text{PO}_4^{X-}_{\text{SUP}}$  precursors and exploiting the thermal transition of  $\text{H}_3\text{PO}_4$  (to  $\text{H}_2\text{PO}_4^-$ ,  $\text{HPO}_4^{2-}$ , and eventually  $\text{PO}_4^{3-}$  at 250–450 ° C). Importantly, all  $\text{H}_{3-X}\text{PO}_4 \cdot^{(X-1)-}$  species have standard reduction potentials ( $E_0$  of 2.3–2.5 V) and lifespans ( $t_{1/2}$  values of  $< \sim 10^2$   $\mu$  seconds) that are similar to and longer than those of their  $\text{SO}_4^{\cdot-}/\text{NO}_3^{\cdot}$  counterparts, respectively ( $E_0$  of 2.4–2.6 V;  $t_{1/2}$  values of  $\sim 10^1$   $\mu$  seconds).

Additionally, an identical platform should preferentially be established to conduct a fair comparison. This dissertation proposed various monometallic- and bimetallic-oxide-immobilized  $\text{SO}_4^{2-}/\text{NO}_3^-$  functionalities. To ensure a fair comparison between the activities and performances of the catalysts and functionalities, further studies should employ an identical platform for modification with different functional groups and modulated the Lewis acidic sites and strengths.

# Bibliography

1. Saleem, H., et al., *Advances of nanomaterials for air pollution remediation and their impacts on the environment*. Chemosphere, 2022. **287**: p. 132083.
2. Zhao, B., et al., *Characterization of nitrosamines and nitrosamine precursors as non-point source pollutants during heavy rainfall events in an urban water environment*. Journal of Hazardous Materials, 2022. **424**: p. 127552.
3. Nasrollahi, N., V. Vatanpour, and A. Khataee, *Removal of antibiotics from wastewaters by membrane technology: Limitations, successes, and future improvements*. Science of The Total Environment, 2022. **838**: p. 156010.
4. Liu, S., et al., *Critical influences of metal compounds on the formation and stabilization of environmentally persistent free radicals*. Chemical Engineering Journal, 2022. **427**: p. 131666.
5. Xu, L., E.E. Stangland, and M. Mavrikakis, *Ethylene versus ethane: A DFT-based selectivity descriptor for efficient catalyst screening*. Journal of Catalysis, 2018. **362**: p. 18–24.
6. Fu, W., et al., *When bimetallic oxides and their complexes meet Fenton-like process*. Journal of Hazardous Materials, 2022. **424**: p. 127419.
7. Li, W., et al., *A Rapid Effervescent Route to Rational Activation of Cu/g-C<sub>3</sub>N<sub>4</sub> and bulk MoS<sub>2</sub> Cocatalyst for Highly Efficient and Robust Photo-Fenton Process*. Advanced Materials Interfaces, 2022: p. 2201552.
8. Ding, C., et al., *Mesoporous structure and amorphous Fe-N sites regulation in Fe-g-C<sub>3</sub>N<sub>4</sub> for boosted visible-light-driven photo-Fenton reaction*. Journal of Colloid and Interface Science, 2022. **608**: p. 2515–2528.
9. Brillas, E., I. Sirés, and M.A. Oturan, *Electro-Fenton Process and Related Electrochemical Technologies Based on Fenton's Reaction Chemistry*. Chemical Reviews, 2009. **109**(12): p. 6570–6631.
10. Thomas, N., D.D. Dionysiou, and S.C. Pillai, *Heterogeneous Fenton catalysts: A review of recent advances*. Journal of Hazardous Materials, 2021. **404**: p. 124082.
11. Sun, Y., et al., *Oxidative degradation of nitrobenzene by a Fenton-like reaction with Fe-Cu bimetallic catalysts*. Applied Catalysis B: Environmental, 2019. **244**: p. 1–10.
12. Georgi, A., et al., *Humic acid modified Fenton reagent for enhancement of the working pH range*. Applied Catalysis B: Environmental, 2007. **72**(1): p. 26–36.
13. Pariente, M.I., et al., *Heterogeneous photo-Fenton oxidation of benzoic acid in water: Effect of operating conditions, reaction by-products and coupling with biological treatment*. Applied Catalysis B: Environmental, 2008. **85**(1): p. 24–32.

14. Yang, Z., et al., *Mn(II) Acceleration of the Picolinic Acid-Assisted Fenton Reaction: New Insight into the Role of Manganese in Homogeneous Fenton AOPs*. Environmental Science & Technology, 2022. **56**(10): p. 6621–6630.
15. Aghdasinia, H., et al., *Central composite design optimization of pilot plant fluidized-bed heterogeneous Fenton process for degradation of an azo dye*. Environmental Technology, 2016. **37**(21): p. 2703–2712.
16. Zhang, H., et al., *Hydroxylamine enables rapid heterogeneous-homogeneous coupled Fenton sulfamethazine degradation on ferric phosphate*. Applied Catalysis B: Environmental, 2022. **312**: p. 121410.
17. Yang, X.-j., et al., *Catalytic decomposition of H<sub>2</sub>O<sub>2</sub> over a Au/carbon catalyst: A dual intermediate model for the generation of hydroxyl radicals*. Journal of Catalysis, 2016. **336**: p. 126–132.
18. Kim, J., et al., *Deciphering Evolution Pathway of Supported NO<sub>3</sub>• Enabled via Radical Transfer from •OH to Surface NO<sub>3</sub>– Functionality for Oxidative Degradation of Aqueous Contaminants*. JACS Au, 2021. **1**(8): p. 1158–1177.
19. Faust, B.C. and J. Hoigné, *Photolysis of Fe (III)-hydroxy complexes as sources of OH radicals in clouds, fog and rain*. Atmospheric Environment. Part A. General Topics, 1990. **24**(1): p. 79–89.
20. Dai, H., et al., *Oxalate regulate the redox cycle of iron in heterogeneous UV-Fenton system with Fe<sub>3</sub>O<sub>4</sub> nanoparticles as catalyst: Critical role of homogeneous reaction*. Chemosphere, 2022. **298**: p. 134240.
21. Brillas, E., *Fenton, photo-Fenton, electro-Fenton, and their combined treatments for the removal of insecticides from waters and soils. A review*. Separation and Purification Technology, 2022. **284**: p. 120290.
22. Ioan, I., et al., *Comparison of Fenton and sono-Fenton bisphenol A degradation*. Journal of Hazardous Materials, 2007. **142**(1): p. 559–563.
23. Yao, Y., et al., *Bifunctional catalysts for heterogeneous electro-Fenton processes: a review*. Environmental Chemistry Letters, 2022.
24. Kim, J., et al., *Grasping periodic trend and rate-determining step for S-modified metals of metal sulfides deployable to produce OH via H<sub>2</sub>O<sub>2</sub> cleavage*. Applied Catalysis B: Environmental, 2019. **253**: p. 60–68.
25. Choe, Y.J., et al., *Open Ni site coupled with SO<sub>4</sub><sup>2-</sup> functionality to prompt the radical interconversion of OH ↔ SO<sub>4</sub>– exploited to decompose refractory pollutants*. Chemical Engineering Journal, 2020. **400**: p. 125971.
26. Ganiyu, S.O., S. Sable, and M. Gamal El-Din, *Advanced oxidation processes for the degradation of dissolved organics in produced water: A review of process performance, degradation kinetics and pathway*. Chemical Engineering Journal, 2022. **429**: p. 132492.
27. Fang, G.-D., et al., *Sulfate radical-based degradation of polychlorinated biphenyls: effects of chloride ion and reaction kinetics*. Journal of Hazardous Materials, 2012. **227**: p. 394–401.

28. Du, J., et al., *Efficient activation of peroxymonosulfate by magnetic Mn-MGO for degradation of bisphenol A*. Journal of hazardous materials, 2016. **320**: p. 150–159.
29. Song, C., et al., *Overtuned Loading of Inert CeO<sub>2</sub> to Active Co<sub>3</sub>O<sub>4</sub> for Unusually Improved Catalytic Activity in Fenton-Like Reactions*. Angewandte Chemie, 2022. **134**(16): p. e202200406.
30. Duan, X., et al., *Limitations and prospects of sulfate–radical based advanced oxidation processes*. Journal of Environmental Chemical Engineering, 2020. **8**(4): p. 103849.
31. Choe, Y.J., et al., *Open Ni site coupled with SO<sub>4</sub><sup>2-</sup> functionality to prompt the radical interconversion of OH ↔ SO<sub>4</sub><sup>-</sup> exploited to decompose refractory pollutants*. Chem. Eng. J., 2020. **400**: p. 125971.
32. McCue, A.J. and J.A. Anderson, *Sulfur as a catalyst promoter or selectivity modifier in heterogeneous catalysis*. Catal. Sci. Technol., 2014. **4**(2): p. 272–294.
33. Wang, A., et al., *Remarkably enhanced sulfate radical-based photo-Fenton-like degradation of levofloxacin using the reduced mesoporous MnO@MnOx microspheres*. Chem. Eng. J., 2020. **379**: p. 122340.
34. Wang, A., et al., *Controllable synthesis of mesoporous manganese oxide microsphere efficient for photo-Fenton-like removal of fluoroquinolone antibiotics*. Appl. Catal. B, 2019. **248**: p. 298–308.
35. Pu, M., et al., *Fe/S doped granular activated carbon as a highly active heterogeneous persulfate catalyst toward the degradation of Orange G and diethyl phthalate*. J. Colloid Interface Sci., 2014. **418**: p. 330–337.
36. Du, J., et al., *Facile preparation of S/Fe composites as an effective peroxydisulfate activator for RhB degradation*. Sep. Purif. Technol., 2016. **163**: p. 145–152.
37. Leng, Y., et al., *Degradation of Rhodamine B by persulfate activated with Fe<sub>3</sub>O<sub>4</sub>: Effect of polyhydroquinone serving as an electron shuttle*. Chem. Eng. J., 2014. **240**: p. 338–343.
38. Liang, C., C.-F. Huang, and Y.-J. Chen, *Potential for activated persulfate degradation of BTEX contamination*. Water Res., 2008. **42**(15): p. 4091–4100.
39. Kim, J., et al., *Enhancing the decomposition of refractory contaminants on SO<sub>4</sub><sup>2-</sup>-functionalized iron oxide to accommodate surface SO<sub>4</sub><sup>-</sup> generated via radical transfer from OH*. Applied Catalysis B: Environmental, 2019. **252**: p. 62–76.
40. Pennington, D.E. and A. Haim, *Stoichiometry and mechanism of the chromium(II)–peroxydisulfate reaction*. J. Am. Chem. Soc., 1968. **90**(14): p. 3700–3704.
41. Liang, C. and H.-W. Su, *Identification of Sulfate and Hydroxyl Radicals in Thermally Activated Persulfate*. Ind. Eng. Chem. Res., 2009. **48**(11): p. 5558–5562.
42. Ganiyu, S.O., M. Zhou, and C.A. Martínez-Huitle, *Heterogeneous electro-Fenton and photoelectro-Fenton processes: A critical review*

- of fundamental principles and application for water/wastewater treatment.* Appl. Catal. B, 2018. **235**: p. 103–129.
43. Bokare, A.D. and W. Choi, *Review of iron-free Fenton-like systems for activating H<sub>2</sub>O<sub>2</sub> in advanced oxidation processes.* J. Hazard. Mater., 2014. **275**: p. 121–135.
  44. Fernández-Sáez, N., et al., *Heteroatom-doped graphene aerogels and carbon-magnetite catalysts for the heterogeneous electro-Fenton degradation of acetaminophen in aqueous solution.* J. Catal., 2019. **378**: p. 68–79.
  45. Firak, D.S., E.S. Orth, and P. Peralta-Zamora, *Unraveling the sigmoidal profiles in Fenton catalysis: Toward mechanistic elucidation.* J. Catal., 2018. **361**: p. 214–221.
  46. Gao, C., et al., *Enhanced Fenton-like catalysis by iron-based metal organic frameworks for degradation of organic pollutants.* J. Catal., 2017. **356**: p. 125–132.
  47. Kim, M., et al., *Unravelling lewis acidic and reductive characters of normal and inverse nickel-cobalt thiospinels in directing catalytic H<sub>2</sub>O<sub>2</sub> cleavage.* J. Hazard. Mater., 2020. **392**: p. 122347.
  48. Choe, Y.J., et al., *Fe<sub>3</sub>S<sub>4</sub>/Fe<sub>7</sub>S<sub>8</sub>-promoted degradation of phenol via heterogeneous, catalytic H<sub>2</sub>O<sub>2</sub> scission mediated by S-modified surface Fe<sup>2+</sup> species.* Appl. Catal. B, 2018. **233**: p. 272–280.
  49. Panizza, M. and G. Cerisola, *Direct And Mediated Anodic Oxidation of Organic Pollutants.* Chem. Rev., 2009. **109**(12): p. 6541–6569.
  50. Zhou, Y., et al., *Structure-based synergistic mechanism for the degradation of typical antibiotics in electro-Fenton process using Pd-Fe<sub>3</sub>O<sub>4</sub> model catalyst: Theoretical and experimental study.* J. Catal., 2018. **365**: p. 184–194.
  51. Ghosh, S., et al., *Selective Oxidation of Propylene to Propylene Oxide over Silver-Supported Tungsten Oxide Nanostructure with Molecular Oxygen.* ACS Catal., 2014. **4**(7): p. 2169–2174.
  52. Dixon, S.J. and B.R. Stockwell, *The role of iron and reactive oxygen species in cell death.* Nat. Chem. Biol., 2014. **10**(1): p. 9–17.
  53. Zhang, G., et al., *Transition metal oxides with one-dimensional/one-dimensional-analogue nanostructures for advanced supercapacitors.* J. Mater. Chem. A, 2017. **5**(18): p. 8155–8186.
  54. Amini, A., et al., *Effect of the Ratio of Magnetite Particle Size to Microwave Penetration Depth on Reduction Reaction Behaviour by H<sub>2</sub>.* Sci. Rep., 2018. **8**(1): p. 15023.
  55. Wang, X., et al., *High performance porous nickel cobalt oxide nanowires for asymmetric supercapacitor.* Nano Energy, 2014. **3**: p. 119–126.
  56. Linnera, J., et al., *Thermoelectric Properties of p-Type Cu<sub>2</sub>O, CuO, and NiO from Hybrid Density Functional Theory.* J. Phys. Chem. C, 2018. **122**(27): p. 15180–15189.
  57. Zhao, W., et al., *Water Dissociative Adsorption on NiO(111): Energetics and Structure of the Hydroxylated Surface.* ACS Catal., 2016. **6**(11): p. 7377–7384.

58. Rohr, F., et al., *Hydroxyl driven reconstruction of the polar NiO(111) surface*. Surf. Sci., 1994. **315**(1): p. L977-L982.
59. Kim, J., et al., *Rational selection of Fe<sub>2</sub>V<sub>4</sub>O<sub>13</sub> over FeVO<sub>4</sub> as a preferred active site on Sb-promoted TiO<sub>2</sub> for catalytic NO<sub>x</sub> reduction with NH<sub>3</sub>*. Catal. Sci. Technol., 2018. **8**(18): p. 4774-4787.
60. Kim, J., et al., *Exploration of surface properties of Sb-promoted copper vanadate catalysts for selective catalytic reduction of NO<sub>x</sub> by NH<sub>3</sub>*. Appl. Catal. B, 2018. **236**: p. 314-325.
61. Vailionis, A., et al., *Evidence of superdense aluminium synthesized by ultrafast microexplosion*. Nature Commun., 2011. **2**(1): p. 445.
62. Kosaka, K., et al., *Comparison among the Methods for Hydrogen Peroxide Measurements To Evaluate Advanced Oxidation Processes: Application of a Spectrophotometric Method Using Copper(II) Ion and 2,9-Dimethyl-1,10-phenanthroline*. Environ. Sci. Technol., 1998. **32**(23): p. 3821-3824.
63. Kresse, G. and J. Hafner, *Ab initio molecular dynamics for liquid metals*. Phys. Rev. B, 1993. **47**(1): p. 558-561.
64. Kresse, G. and J. Furthmüller, *Efficient iterative schemes for ab initio total-energy calculations using a plane-wave basis set*. Phys. Rev. B, 1996. **54**(16): p. 11169-11186.
65. Blöchl, P.E., *Projector augmented-wave method*. Phys. Rev. B, 1994. **50**(24): p. 17953-17979.
66. Kresse, G. and D. Joubert, *From ultrasoft pseudopotentials to the projector augmented-wave method*. Phys. Rev. B, 1999. **59**(3): p. 1758-1775.
67. Ivanov, B.A. and E.V. Tartakovskaya, *Stabilization of Long-Range Magnetic Order in 2D Easy-Plane Antiferromagnets*. Phys. Rev. Lett., 1996. **77**(2): p. 386-389.
68. Dudarev, S.L., et al., *Electron-energy-loss spectra and the structural stability of nickel oxide: An LSDA+U study*. Phys. Rev. B, 1998. **57**(3): p. 1505-1509.
69. Sanville, E., et al., *Improved grid-based algorithm for Bader charge allocation*. J. Comput. Chem., 2007. **28**(5): p. 899-908.
70. Henkelman, G., A. Arnaldsson, and H. Jónsson, *A fast and robust algorithm for Bader decomposition of charge density*. Comput. Mater. Sci., 2006. **36**(3): p. 354-360.
71. Monkhorst, H.J. and J.D. Pack, *Special points for Brillouin-zone integrations*. Phys. Rev. B, 1976. **13**(12): p. 5188-5192.
72. Cococcioni, M. and S. de Gironcoli, *Linear response approach to the calculation of the effective interaction parameters in the  $\text{LDA}+U$  method*. Phys. Rev. B, 2005. **71**(3): p. 035105.
73. Fievet, F., et al., *Lattice parameter, microstrains and non-stoichiometry in NiO. Comparison between mosaic microcrystals and quasi-perfect single microcrystals*. J. Appl. Cryst., 1979. **12**(4): p. 387-394.
74. Fender, B.E.F., A.J. Jacobson, and F.A. Wedgwood, *Covalency*



- Parameters in MnO,  $\alpha$ -MnS, and NiO.* J. Chem. Phys., 1968. **48**(3): p. 990–994.
75. Cheetham, A.K. and D.A.O. Hope, *Magnetic ordering and exchange effects in the antiferromagnetic solid solutions  $\text{Mn}_{1-x}\text{Ni}_x\text{O}$* . Phys. Rev. B, 1983. **27**(11): p. 6964–6967.
  76. Neubeck, W., et al., *Observation of orbital moment in NiO using magnetic x-ray scattering.* J. Appl. Phys., 1999. **85**(8): p. 4847–4849.
  77. Sasi, B., et al., *Preparation of transparent and semiconducting NiO films.* Vacuum, 2002. **68**(2): p. 149–154.
  78. Hüfner, S., et al., *Photoemission and inverse photoemission spectroscopy of NiO.* Solid State Commun., 1984. **52**(9): p. 793–796.
  79. Sawatzky, G.A. and J.W. Allen, *Magnitude and Origin of the Band Gap in NiO.* Phys. Rev. Lett., 1984. **53**(24): p. 2339–2342.
  80. Henkelman, G., B.P. Uberuaga, and H. Jónsson, *A climbing image nudged elastic band method for finding saddle points and minimum energy paths.* J. Chem. Phys., 2000. **113**(22): p. 9901–9904.
  81. Du, J., et al., *Mesoporous sulfur-modified iron oxide as an effective Fenton-like catalyst for degradation of bisphenol A.* Applied Catalysis B: Environmental, 2016. **184**: p. 132–141.
  82. Liu, J., et al., *Facile synthesis of tube-shaped Mn–Ni–Ti solid solution and preferable Langmuir–Hinshelwood mechanism for selective catalytic reduction of NO<sub>x</sub> by NH<sub>3</sub>.* Appl. Catal. A, 2018. **549**: p. 289–301.
  83. Liu, Z., et al., *Selective Catalytic Reduction of NO<sub>x</sub> with NH<sub>3</sub> over Novel Fe–Ni–Ti Catalyst.* Ind. Eng. Chem. Res., 2018. **57**(22): p. 7458–7465.
  84. Chen, L., J. Li, and M. Ge, *DRIFT Study on Cerium–Tungsten/Titanium Catalyst for Selective Catalytic Reduction of NO<sub>x</sub> with NH<sub>3</sub>.* Environ. Sci. Technol., 2010. **44**(24): p. 9590–9596.
  85. Vargas, M.A.L., et al., *An IR study of thermally stable V<sub>2</sub>O<sub>5</sub>–WO<sub>3</sub>–TiO<sub>2</sub> SCR catalysts modified with silica and rare-earths (Ce, Tb, Er).* Appl. Catal. B, 2007. **75**(3): p. 303–311.
  86. Rensel, D.J., et al., *Composition-directed FeXMo<sub>2</sub>–XP bimetallic catalysts for hydrodeoxygenation reactions.* Catal. Sci. Technol., 2017. **7**(9): p. 1857–1867.
  87. Jalilvand, F., *Sulfur: not a “silent” element any more.* Chem. Soc. Rev., 2006. **35**(12): p. 1256–1268.
  88. Kasrai, M., et al., *Sulphur characterization in coal from X-ray absorption near edge spectroscopy.* Int. J. Coal Geol., 1996. **32**(1): p. 107–135.
  89. Kim, J., et al., *SO<sub>2</sub>–/SO<sub>4</sub>– functionalization-tailorable catalytic surface features of Sb-promoted Cu<sub>3</sub>V<sub>2</sub>O<sub>8</sub> on TiO<sub>2</sub> for selective catalytic reduction of NO<sub>x</sub> with NH<sub>3</sub>.* Appl. Catal. A, 2019. **570**: p. 355–366.
  90. Kim, J., D. Ho Kim, and H.P. Ha, *Investigating multi-functional traits of metal-substituted vanadate catalysts in expediting NO<sub>x</sub> reduction*

- and poison degradation at low temperatures.* J. Hazard. Mater., 2020. **397**: p. 122671.
91. Rose, K., et al., *Investigation of Iron–Sulfur Covalency in Rubredoxins and a Model System Using Sulfur K-Edge X-ray Absorption Spectroscopy.* J. Am. Chem. Soc., 1998. **120**(41): p. 10743–10747.
  92. Wu, Y., et al., *Electron density modulation of NiCo<sub>2</sub>S<sub>4</sub> nanowires by nitrogen incorporation for highly efficient hydrogen evolution catalysis.* Nat. Commun., 2018. **9**(1): p. 1425.
  93. Sarret, G., et al., *Chemical forms of sulfur in geological and archeological asphaltenes from Middle East, France, and Spain determined by sulfur K- and L-edge X-ray absorption near-edge structure spectroscopy.* Geochim. Cosmochim. Acta, 1999. **63**(22): p. 3767–3779.
  94. Yu, Y., et al., *Facile synthesis of CuSO<sub>4</sub>/TiO<sub>2</sub> catalysts with superior activity and SO<sub>2</sub> tolerance for NH<sub>3</sub>–SCR: physicochemical properties and reaction mechanism.* Catal. Sci. Technol., 2017. **7**(7): p. 1590–1601.
  95. Sugimoto, T. and Y. Wang, *Mechanism of the Shape and Structure Control of Monodispersed  $\alpha$ -Fe<sub>2</sub>O<sub>3</sub> Particles by Sulfate Ions.* J. Colloid Interface Sci., 1998. **207**(1): p. 137–149.
  96. Jiang, B.Q., et al., *DRIFT Study of the SO<sub>2</sub> Effect on Low-Temperature SCR Reaction over Fe–Mn/TiO<sub>2</sub>.* J. Phys. Chem. C, 2010. **114**(11): p. 4961–4965.
  97. Xu, Y., et al., *SO<sub>2</sub> promoted V<sub>2</sub>O<sub>5</sub>–MoO<sub>3</sub>/TiO<sub>2</sub> catalyst for NH<sub>3</sub>–SCR of NO<sub>x</sub> at low temperatures.* Appl. Catal. A, 2019. **570**: p. 42–50.
  98. Yang, W., et al., *Heterogeneous Reaction of SO<sub>2</sub> on Manganese Oxides: the Effect of Crystal Structure and Relative Humidity.* Sci. Rep., 2017. **7**(1): p. 4550.
  99. Nidheesh, P.V. and R. Gandhimathi, *Trends in electro-Fenton process for water and wastewater treatment: An overview.* Desalination, 2012. **299**: p. 1–15.
  100. Zhang, Y., et al., *Degradation of benzotriazole by a novel Fenton-like reaction with mesoporous Cu/MnO<sub>2</sub>: Combination of adsorption and catalysis oxidation.* Appl. Catal. B, 2016. **199**: p. 447–457.
  101. Feng, Y., et al., *Activation of Persulfates Using Siderite as a Source of Ferrous Ions: Sulfate Radical Production, Stoichiometric Efficiency, and Implications.* ACS Sustainable Chem. Eng., 2018. **6**(3): p. 3624–3631.
  102. Fontmorin, J.M., et al., *Stability of 5,5-dimethyl-1-pyrroline-N-oxide as a spin-trap for quantification of hydroxyl radicals in processes based on Fenton reaction.* Water Res., 2016. **99**: p. 24–32.
  103. Fang, G., et al., *Key Role of Persistent Free Radicals in Hydrogen Peroxide Activation by Biochar: Implications to Organic Contaminant Degradation.* Environ. Sci. Technol., 2014. **48**(3): p. 1902–1910.
  104. Buxton, G.V., et al., *Critical Review of rate constants for reactions of hydrated electrons, hydrogen atoms and hydroxyl radicals ( $\cdot$ OH/ $\cdot$ O $\cdot$  in Aqueous Solution.* J. Phys. Chem. Ref. Data, 1988. **17**(2): p. 513–

- 886.
105. Clifton, C.L. and R.E. Huie, *Rate constants for hydrogen abstraction reactions of the sulfate radical, SO<sub>4</sub><sup>-</sup>. Alcohols*. Int. J. Chem. Kinet., 1989. **21**(8): p. 677-687.
106. Huie, R.E., C.L. Clifton, and S.A. Kafafi, *Rate constants for hydrogen abstraction reactions of the sulfate radical, SO<sub>4</sub><sup>-</sup>: experimental and theoretical results for cyclic ethers*. J. Phys. Chem., 1991. **95**(23): p. 9336-9340.
107. Kim, J., Y.J. Choe, and S.H. Kim, *Tailoring Lewis acidic metals and SO<sub>4</sub><sup>2-</sup> functionalities on bimetallic Mn-Fe oxo-spinels to exploit supported SO<sub>4</sub><sup>-</sup> in aqueous pollutant fragmentation*. Chemical Engineering Journal, 2021. **413**: p. 127550.
108. Rastogi, A., S.R. Al-Abed, and D.D. Dionysiou, *Sulfate radical-based ferrous-peroxymonosulfate oxidative system for PCBs degradation in aqueous and sediment systems*. Appl. Catal. B, 2009. **85**(3): p. 171-179.
109. Yuan, S., P. Liao, and A.N. Alshawabkeh, *Electrolytic Manipulation of Persulfate Reactivity by Iron Electrodes for Trichloroethylene Degradation in Groundwater*. Environ. Sci. Technol., 2014. **48**(1): p. 656-663.
110. Liu, Y., et al., *Degradation of aniline by heterogeneous Fenton's reaction using a Ni-Fe oxalate complex catalyst*. J. Environ. Manage., 2016. **182**: p. 367-373.
111. Połczyński, P., R. Jurczakowski, and W. Grochala, *Stabilization and strong oxidizing properties of Ag(ii) in a fluorine-free solvent*. Chem. Commun., 2013. **49**(68): p. 7480-7482.
112. Du, J., et al., *Facile preparation of porous Mn/Fe<sub>3</sub>O<sub>4</sub> cubes as peroxymonosulfate activating catalyst for effective bisphenol A degradation*. Chem. Eng. J., 2019. **376**: p. 119193.
113. Mahdi Ahmed, M., et al., *Sulfate radical anion oxidation of diclofenac and sulfamethoxazole for water decontamination*. Chem. Eng. J., 2012. **197**: p. 440-447.
114. Luo, S., et al., *Mechanistic insight into reactivity of sulfate radical with aromatic contaminants through single-electron transfer pathway*. Chem. Eng. J., 2017. **327**: p. 1056-1065.
115. Antoniou, M.G., A.A. de la Cruz, and D.D. Dionysiou, *Intermediates and Reaction Pathways from the Degradation of Microcystin-LR with Sulfate Radicals*. Environ. Sci. Technol. , 2010. **44**(19): p. 7238-7244.
116. Moreira, F.C., et al., *Electrochemical advanced oxidation processes: A review on their application to synthetic and real wastewaters*. Appl. Catal. B, 2017. **202**: p. 217-261.
117. Pegis, M.L., et al., *Oxygen Reduction by Homogeneous Molecular Catalysts and Electrocatalysts*. Chem. Rev., 2018. **118**(5): p. 2340-2391.
118. deKrafft, K.E., et al., *Electrochemical Water Oxidation with Carbon-Grafted Iridium Complexes*. ACS Appl. Mater. Interfaces, 2012. **4**(2): p. 608-613.

119. El-Desoky, H.S., et al., *Oxidation of Levafix CA reactive azo-dyes in industrial wastewater of textile dyeing by electro-generated Fenton's reagent*. J. Hazard. Mater., 2010. **175**(1): p. 858–865.
120. Weng, Z., et al., *Surfactant-free porous nano-Mn<sub>3</sub>O<sub>4</sub> as a recyclable Fenton-like reagent that can rapidly scavenge phenolics without H<sub>2</sub>O<sub>2</sub>*. J. Mater. Chem. A, 2017. **5**(30): p. 15650–15660.
121. Kraushofer, F., et al., *Atomic-Scale Structure of the Hematite  $\alpha$ -Fe<sub>2</sub>O<sub>3</sub>(1102) "R-Cut" Surface*. J. Phys. Chem. C, 2018. **122**(3): p. 1657–1669.
122. Sahu, S.K., et al., *Thermodynamics of Fe<sub>3</sub>O<sub>4</sub>-Co<sub>3</sub>O<sub>4</sub> and Fe<sub>3</sub>O<sub>4</sub>-Mn<sub>3</sub>O<sub>4</sub> spinel solid solutions at the bulk and nanoscale*. Phys. Chem. Chem. Phys., 2015. **17**(34): p. 22286–22295.
123. Zhao, Q., et al., *Spinel: Controlled Preparation, Oxygen Reduction/Evolution Reaction Application, and Beyond*. Chem. Rev., 2017. **117**(15): p. 10121–10211.
124. Yan, L., J. Bing, and H. Wu, *The behavior of ozone on different iron oxides surface sites in water*. Sci. Rep., 2019. **9**(1): p. 14752.
125. Hou, L., et al., *Shape-controlled nanostructured magnetite-type materials as highly efficient Fenton catalysts*. Appl. Catal. B, 2014. **144**: p. 739–749.
126. Kaczmarczyk, J., et al., *Thermodynamic Stability, Redox Properties, and Reactivity of Mn<sub>3</sub>O<sub>4</sub>, Fe<sub>3</sub>O<sub>4</sub>, and Co<sub>3</sub>O<sub>4</sub> Model Catalysts for N<sub>2</sub>O Decomposition: Resolving the Origins of Steady Turnover*. ACS Catal., 2016. **6**(2): p. 1235–1246.
127. Ma, Z., et al., *Sodium Dodecyl Sulfate Modified FeCo<sub>2</sub>O<sub>4</sub> with Enhanced Fenton-Like Activity at Neutral pH*. J. Phys. Chem. C, 2015. **119**(40): p. 23068–23074.
128. Costa, R.C.C., et al., *Novel active heterogeneous Fenton system based on Fe<sub>3</sub>-xM<sub>x</sub>O<sub>4</sub> (Fe, Co, Mn, Ni): The role of M<sup>2+</sup> species on the reactivity towards H<sub>2</sub>O<sub>2</sub> reactions*. Journal of Hazardous Materials, 2006. **129**(1): p. 171–178.
129. Jing, P., et al., *Efficient photocatalytic degradation of acid fuchsin in aqueous solution using separate porous tetragonal-CuFe<sub>2</sub>O<sub>4</sub> nanotubes*. J. Hazard. Mater., 2015. **284**: p. 163–170.
130. Popescu, I., et al., *Study of the electrical and catalytic properties of spinels with CuFe<sub>2</sub>-xMnxO<sub>4</sub> composition (x=0, 0.4, 0.8, 1.6 and 2)*. Appl. Catal. A, 2015. **504**: p. 29–36.
131. Ferreira, T.A.S., et al., *Structural and morphological characterization of FeCo<sub>2</sub>O<sub>4</sub> and CoFe<sub>2</sub>O<sub>4</sub> spinels prepared by a coprecipitation method*. Solid State Sci., 2003. **5**(2): p. 383–392.
132. Ruby, C., B. Humbert, and J. Fusy, *Surface and interface properties of epitaxial iron oxide thin films deposited on MgO(001) studied by XPS and Raman spectroscopy*. Surf. Interface Anal., 2000. **29**(6): p. 377–380.
133. Guillemet-Fritsch, S., et al., *Thermochemistry of iron manganese oxide spinels*. J. Solid State Chem., 2005. **178**(1): p. 106–113.
134. Duan, J., et al., *High CO<sub>2</sub>/N<sub>2</sub>/O<sub>2</sub>/CO separation in a chemically robust*

- porous coordination polymer with low binding energy*. Chem. Sci., 2014. **5**(2): p. 660–666.
135. Deng, H., et al., *Monodisperse Magnetic Single-Crystal Ferrite Microspheres*. Angew. Chem. Int. Ed., 2005. **44**(18): p. 2782–2785.
  136. Hao, G.-P., et al., *Structurally Designed Synthesis of Mechanically Stable Poly(benzoxazine-co-resol)-Based Porous Carbon Monoliths and Their Application as High-Performance CO<sub>2</sub> Capture Sorbents*. J. Am. Chem. Soc., 2011. **133**(29): p. 11378–11388.
  137. Kim, J., A.G. Oliver, and J.C. Hicks, *Enhanced CO<sub>2</sub> capture capacities and efficiencies with N-doped nanoporous carbons synthesized from solvent-modulated, pyridinedicarboxylate-containing Zn-MOFs*. CrystEngComm, 2015. **17**(42): p. 8015–8020.
  138. Park, Y., et al., *Adsorption isotherms of CO<sub>2</sub>, CO, N<sub>2</sub>, CH<sub>4</sub>, Ar and H<sub>2</sub> on activated carbon and zeolite LiX up to 1.0 MPa*. Adsorption, 2014. **20**(4): p. 631–647.
  139. Park, H.J. and M.P. Suh, *Enhanced isosteric heat, selectivity, and uptake capacity of CO<sub>2</sub> adsorption in a metal-organic framework by impregnated metal ions*. Chem. Sci., 2013. **4**(2): p. 685–690.
  140. Cui, J., et al., *Chemical oxidation of benzene and trichloroethylene by a combination of peroxymonosulfate and permanganate linked by in-situ generated colloidal/amorphous MnO<sub>2</sub>*. Chem. Eng. J., 2017. **313**: p. 815–825.
  141. Pi, L., et al., *Heterogeneous activation of peroxymonocarbonate by Co-Mn oxides for the efficient degradation of chlorophenols in the presence of a naturally occurring level of bicarbonate*. Chem. Eng. J., 2018. **334**: p. 1297–1308.
  142. Magon, C.J., et al., *Electron Paramagnetic Resonance (EPR) studies on the photo-thermo ionization process of photo-thermo-refractive glasses*. J. Non-Cryst. Solids, 2016. **452**: p. 320–324.
  143. Clayton, J.A., et al., *Quantitative analysis of zero-field splitting parameter distributions in Gd(III) complexes*. Phys. Chem. Chem. Phys., 2018. **20**(15): p. 10470–10492.
  144. Kim, J., et al., *Er composition (X)-mediated catalytic properties of Ce<sub>1-x</sub>Er<sub>x</sub>V<sub>2</sub>O<sub>7</sub> surfaces for selective catalytic NO<sub>x</sub> reduction with NH<sub>3</sub> at elevated temperatures*. Catalysis Today, 2021. **359**: p. 65–75.
  145. Kim, J., et al., *Unveiling the traits of rare earth metal (RM)-substituted bimetallic Ce<sub>0.5</sub>RM<sub>0.5</sub>V<sub>2</sub>O<sub>7</sub> phases to activate selective NH<sub>3</sub> oxidation and NO<sub>x</sub> reduction*. Appl. Surf. Sci., 2020. **518**: p. 146238.
  146. Will, G., *The crystal structure of MnSO<sub>4</sub>*. Acta Cryst., 1965. **19**(5): p. 854–857.
  147. Yang, S., et al., *Low temperature selective catalytic reduction of NO with NH<sub>3</sub> over Mn-Fe spinel: Performance, mechanism and kinetic study*. Appl. Catal. B, 2011. **110**: p. 71–80.
  148. Zhang, L., et al., *Rational Design of High-Performance DeNO<sub>x</sub> Catalysts Based on Mn<sub>x</sub>Co<sub>3-x</sub>O<sub>4</sub> Nanocages Derived from Metal-Organic Frameworks*. ACS Catal., 2014. **4**(6): p. 1753–1763.
  149. Lei, W., et al., *Synthesis and magnetic properties of octahedral Fe<sub>3</sub>O<sub>4</sub>*

- via a one-pot hydrothermal route*. Phys. Lett. A, 2017. **381**(4): p. 314–318.
150. Liu, Y., et al., *One-Dimensional Fe<sub>2</sub>P Acts as a Fenton Agent in Response to NIR II Light and Ultrasound for Deep Tumor Synergetic Theranostics*. Angew. Chem. Inter. Ed., 2019. **58**(8): p. 2407–2412.
  151. Lee, G.-H., Y. Seon Kim, and D.-W. Kim, *Redox effect of Fe<sup>2+</sup>/Fe<sup>3+</sup> in iron phosphates for enhanced electrocatalytic activity in Li-O<sub>2</sub> batteries*. Chem. Eng. J., 2020. **388**: p. 124294.
  152. Kim, J., et al., *Zn-MOFs Containing Pyridine and Bi-pyridine Carboxylate Organic Linkers and Open Zn<sup>2+</sup> Sites*. Eur. J. Inorg. Chem., 2015. **2015**(18): p. 3011–3018.
  153. Möncke, D., et al., *Partitioning and structural role of Mn and Fe ions in ionic sulfophosphate glasses*. 2014. **141**(22): p. 224509.
  154. Frost, R.L. and E.C. Keeffe, *Raman spectroscopic study of the sulfite-bearing minerals scotlandite, hannebachite and orschallite: implications for the desulfation of soils*. J. Raman Spectrosc., 2009. **40**(3): p. 244–248.
  155. Konwar, L.J., et al., *Towards carbon efficient biorefining: Multifunctional mesoporous solid acids obtained from biodiesel production wastes for biomass conversion*. Appl. Catal. B, 2015. **176–177**: p. 20–35.
  156. Li, W., et al., *Efficient removal of aniline by micro-scale zinc-copper (mZn/Cu) bimetallic particles in acidic solution: An oxidation degradation mechanism via radicals*. J. Hazard. Mater., 2019. **366**: p. 482–491.
  157. Li, X., et al., *Ultrasonic-enhanced Fenton-like degradation of bisphenol A using a bio-synthesized schwertmannite catalyst*. J. Hazard. Mater., 2018. **344**: p. 689–697.
  158. Li, X., et al., *High calcium resistance of CeO<sub>2</sub>-WO<sub>3</sub> SCR catalysts: Structure investigation and deactivation analysis*. Chem. Eng. J., 2017. **317**: p. 70–79.
  159. Shim, J.-O., et al., *Effect of preparation method on the oxygen vacancy concentration of CeO<sub>2</sub>-promoted Cu/γ-Al<sub>2</sub>O<sub>3</sub> catalysts for HTS reactions*. Chem. Eng. J., 2016. **306**: p. 908–915.
  160. Zhang, W., et al., *Electrocatalytic removal of humic acid using cobalt-modified particle electrodes*. Appl. Catal. A, 2018. **559**: p. 75–84.
  161. Lakshmipathiraj, P., et al., *Studies on electrochemical detoxification of trichloroethene (TCE) on Ti/IrO<sub>2</sub>-Ta<sub>2</sub>O<sub>5</sub> electrode from aqueous solution*. Chem. Eng. J., 2012. **198–199**: p. 211–218.
  162. Hayyan, M., M.A. Hashim, and I.M. AlNashef, *Superoxide Ion: Generation and Chemical Implications*. Chem. Rev., 2016. **116**(5): p. 3029–3085.
  163. Plauck, A., et al., *Active sites and mechanisms for H<sub>2</sub>O<sub>2</sub> decomposition over Pd catalysts*. Proc. Natl. Acad. Sci. , 2016. **113**(14): p. E1973–E1982.
  164. Chen, Q., et al., *Intelligent Albumin-MnO<sub>2</sub> Nanoparticles as pH-/H<sub>2</sub>O<sub>2</sub>-Responsive Dissociable Nanocarriers to Modulate Tumor*

- Hypoxia for Effective Combination Therapy*. Adv. Mater., 2016. **28**(33): p. 7129–7136.
165. Lunsford, J.H., *The direct formation of H<sub>2</sub>O<sub>2</sub> from H<sub>2</sub> and O<sub>2</sub> over palladium catalysts*. J. Catal., 2003. **216**(1): p. 455–460.
  166. Wang, G., et al., *Removal of norfloxacin by surface Fenton system (MnFe<sub>2</sub>O<sub>4</sub>/H<sub>2</sub>O<sub>2</sub>): kinetics, mechanism and degradation pathway*. Chemical Engineering Journal, 2018. **351**: p. 747–755.
  167. Brillas, E., et al., *Aniline mineralization by AOP's: anodic oxidation, photocatalysis, electro-Fenton and photoelectro-Fenton processes*. Appl. Catal. B, 1998. **16**(1): p. 31–42.
  168. Zazo, J.A., et al., *Chemical Pathway and Kinetics of Phenol Oxidation by Fenton's Reagent*. Environ. Sci. Technol., 2005. **39**(23): p. 9295–9302.
  169. Pinkernell, U. and U. Von Gunten, *Bromate minimization during ozonation: mechanistic considerations*. Environmental Science & Technology, 2001. **35**(12): p. 2525–2531.
  170. Debnath, B., et al., *Efficient dye degradation catalyzed by manganese oxide nanoparticles and the role of cation valence*. ChemistrySelect, 2016. **1**(14): p. 4265–4273.
  171. Sun, Y., L. Zhao, and Y. Teng, *Insight into influence mechanisms of pyrite and vernadite on the degradation performance of 2, 2', 5-trichlorodiphenyl in a pyrophosphate-chelated Fenton-like reaction*. Chemical Engineering Journal, 2021. **410**: p. 128345.
  172. Yang, J., et al., *Immobilization of chitosan-templated MnO<sub>2</sub> nanoparticles onto filter paper by redox method as a retrievable Fenton-like dip catalyst*. Chemosphere, 2021. **268**: p. 128835.
  173. Xiao, R., et al., *Quantitative structure–activity relationship (QSAR) for the oxidation of trace organic contaminants by sulfate radical*. Environmental science & technology, 2015. **49**(22): p. 13394–13402.
  174. Huie, R.E. and J.T. Herron, *The rate constant for the reaction O<sub>3</sub>+ NO<sub>2</sub>→ O<sub>2</sub>+ NO<sub>3</sub> over the temperature range 259–362 K*. Chemical Physics Letters, 1974. **27**(3): p. 411–414.
  175. Musat, R., et al., *Pulse radiolysis study on the reactivity of NO<sub>3</sub><sup>•</sup> radical toward uranous (iv), hydrazinium nitrate and hydroxyl ammonium nitrate at room temperature and at 45° C*. Physical Chemistry Chemical Physics, 2020. **22**(9): p. 5188–5197.
  176. Musat, R., et al., *Decoding the three-pronged mechanism of NO<sub>3</sub><sup>•</sup> radical formation in HNO<sub>3</sub> solutions at 22 and 80° C using picosecond pulse radiolysis*. The Journal of Physical Chemistry B, 2018. **122**(7): p. 2121–2129.
  177. Goldstein, S. and J. Rabani, *Mechanism of nitrite formation by nitrate photolysis in aqueous solutions: the role of peroxyxynitrite, nitrogen dioxide, and hydroxyl radical*. Journal of the American Chemical Society, 2007. **129**(34): p. 10597–10601.
  178. Barzaghi, P. and H. Herrmann, *Kinetics and mechanisms of reactions of the nitrate radical (NO<sub>3</sub><sup>•</sup>) with substituted phenols in aqueous solution*. Physical Chemistry Chemical Physics, 2004. **6**(23): p. 5379–

- 5388.
179. Villegas-Guzman, P., et al., *Role of sulfate, chloride, and nitrate anions on the degradation of fluoroquinolone antibiotics by photoelectro-Fenton*. Environmental Science and Pollution Research, 2017. **24**: p. 28175-28189.
  180. Nakatani, N., et al., *Determination of photoformation rates and scavenging rate constants of hydroxyl radicals in natural waters using an automatic light irradiation and injection system*. Analytica chimica acta, 2007. **581**(2): p. 260-267.
  181. Liu, Z., et al., *Alpha radiolysis of nitric acid aqueous solution irradiated by 238 Pu source*. Nuclear Science and Techniques, 2017. **28**: p. 1-10.
  182. Chen, L., J. Li, and M. Ge, *Promotional effect of Ce-doped V2O5-WO3/TiO2 with low vanadium loadings for selective catalytic reduction of NO<sub>x</sub> by NH3*. The Journal of Physical Chemistry C, 2009. **113**(50): p. 21177-21184.
  183. Vinge, S.L., et al., *Nitrate with benefits: Optimizing radical production during UV water treatment*. Environmental Science: Water Research & Technology, 2020. **6**(4): p. 1163-1175.
  184. Madsen, D., et al., *The primary photodynamics of aqueous nitrate: Formation of peroxyxynitrite*. Journal of the American Chemical Society, 2003. **125**(50): p. 15571-15576.
  185. Julian, R.R., J. Beauchamp, and W.A. Goddard, *Cooperative salt bridge stabilization of gas-phase zwitterions in neutral arginine clusters*. The Journal of Physical Chemistry A, 2002. **106**(1): p. 32-34.
  186. Chen, C., et al., *Comparative study for interactions of sulfate radical and hydroxyl radical with phenol in the presence of nitrite*. Environmental Science & Technology, 2020. **54**(13): p. 8455-8463.
  187. Bartberger, M.D., et al., *The reduction potential of nitric oxide (NO) and its importance to NO biochemistry*. Proceedings of the National Academy of Sciences, 2002. **99**(17): p. 10958-10963.
  188. Samuel, E.L., et al., *Highly efficient conversion of superoxide to oxygen using hydrophilic carbon clusters*. Proceedings of the National Academy of Sciences, 2015. **112**(8): p. 2343-2348.
  189. Keen, O.S., N.G. Love, and K.G. Linden, *The role of effluent nitrate in trace organic chemical oxidation during UV disinfection*. Water research, 2012. **46**(16): p. 5224-5234.
  190. Zhao, J., J. Yang, and J. Ma, *Mn (II)-enhanced oxidation of benzoic acid by Fe (III)/H2O2 system*. Chemical Engineering Journal, 2014. **239**: p. 171-177.
  191. Hansard, S.P., H.D. Easter, and B.M. Voelker, *Rapid reaction of nanomolar Mn (II) with superoxide radical in seawater and simulated freshwater*. Environmental science & technology, 2011. **45**(7): p. 2811-2817.
  192. Schneider, W., *Qualitative differences in the adsorption chemistry of acidic (CO<sub>2</sub>, SO<sub>x</sub>) and amphiphilic (NO<sub>x</sub>) species on the alkaline earth oxides*. The Journal of Physical Chemistry B, 2004. **108**(1): p. 273-



- 282.
193. Gonzalez, C.M., et al., *Sorption kinetic study of selenite and selenate onto a high and low pressure aged iron oxide nanomaterial*. Journal of hazardous materials, 2012. **211**: p. 138–145.
  194. Wang, F., et al., *Manganese oxides with rod-, wire-, tube-, and flower-like morphologies: highly effective catalysts for the removal of toluene*. Environmental science & technology, 2012. **46**(7): p. 4034–4041.
  195. Li, L., et al., *Investigation of two-phase intergrowth and coexistence in Mn-Ce-Ti-O catalysts for the selective catalytic reduction of NO with NH<sub>3</sub>: structure-activity relationship and reaction mechanism*. Industrial & Engineering Chemistry Research, 2018. **58**(2): p. 849–862.
  196. Helali, Z., et al., *Scaling reducibility of metal oxides*. Theoretical Chemistry Accounts, 2017. **136**: p. 1–16.
  197. Zhu, B., et al., *Adsorption properties of NO, NH<sub>3</sub>, and O<sub>2</sub> over  $\beta$ -MnO<sub>2</sub> (110) surface*. Journal of Materials Science, 2018. **53**(16): p. 11500–11511.
  198. Liu, L., et al., *NO adsorption and oxidation on Mn doped CeO<sub>2</sub> (111) surfaces: A DFT+ U study*. Aerosol and Air Quality Research, 2018. **18**(4): p. 1080–1088.
  199. Yuan, H., et al., *Insight into the NH<sub>3</sub>-assisted selective catalytic reduction of NO on  $\beta$ -MnO<sub>2</sub> (110): reaction mechanism, activity descriptor, and evolution from a pristine state to a steady state*. ACS Catalysis, 2018. **8**(10): p. 9269–9279.
  200. Kim, J., S. Lee, and H.P. Ha, *Supercritical Carbon Dioxide Extraction-Mediated Amendment of a Manganese Oxide Surface Desired to Selectively Transform Nitrogen Oxides and/or Ammonia*. ACS Catalysis, 2021. **11**(2): p. 767–786.
  201. Borgmann, S., *Electrochemical quantification of reactive oxygen and nitrogen: challenges and opportunities*. Analytical and bioanalytical chemistry, 2009. **394**: p. 95–105.
  202. Nawaz, F., et al., *The influence of the substituent on the phenol oxidation rate and reactive species in cubic MnO<sub>2</sub> catalytic ozonation*. Catalysis Science & Technology, 2016. **6**(21): p. 7875–7884.
  203. Xu, H., et al., *Gaseous heterogeneous catalytic reactions over Mn-based oxides for environmental applications: a critical review*. Environmental science & technology, 2017. **51**(16): p. 8879–8892.
  204. Li, Y.-F., S.-C. Zhu, and Z.-P. Liu, *Reaction network of layer-to-tunnel transition of MnO<sub>2</sub>*. Journal of the American Chemical Society, 2016. **138**(16): p. 5371–5379.
  205. Hayashi, E., et al., *Effect of MnO<sub>2</sub> crystal structure on aerobic oxidation of 5-hydroxymethylfurfural to 2, 5-furandicarboxylic acid*. Journal of the American Chemical Society, 2019. **141**(2): p. 890–900.
  206. Bi, R., et al., *3D Hollow  $\alpha$ -MnO<sub>2</sub> framework as an efficient electrocatalyst for lithium-oxygen batteries*. Small, 2019. **15**(10): p. 1804958.

207. Ren, Y., et al., *Influence of size on the rate of mesoporous electrodes for lithium batteries*. Journal of the American Chemical Society, 2010. **132**(3): p. 996–1004.
208. Dong, Y., et al., *Simple hydrothermal preparation of  $\alpha$ -,  $\beta$ -, and  $\gamma$ - $\text{MnO}_2$  and phase sensitivity in catalytic ozonation*. RSC advances, 2014. **4**(74): p. 39167–39173.
209. Saputra, E., et al., *Different Crystallographic One-dimensional  $\text{MnO}_2$  Nanomaterials and Their Superior Performance in Catalytic Phenol Degradation*. Environmental Science & Technology, 2013. **47**(11): p. 5882–5887.
210. Dong, Y., et al.,  *$\beta$ - $\text{MnO}_2$  nanowires: a novel ozonation catalyst for water treatment*. Applied Catalysis B: Environmental, 2009. **85**(3–4): p. 155–161.
211. Liu, W., et al.,  *$\beta$ - $\text{MnO}_2$  with proton conversion mechanism in rechargeable zinc ion battery*. Journal of Energy Chemistry, 2021. **56**: p. 365–373.
212. Meng, H., et al., *Insight into the effect of lignocellulosic biomass source on the performance of biochar as persulfate activator for aqueous organic pollutants remediation: Epicarp and mesocarp of citrus peels as examples*. Journal of Hazardous Materials, 2020. **399**: p. 123043.
213. Mo, S., et al., *Highly efficient mesoporous  $\text{MnO}_2$  catalysts for the total toluene oxidation: Oxygen-Vacancy defect engineering and involved intermediates using in situ DRIFTS*. Applied Catalysis B: Environmental, 2020. **264**: p. 118464.
214. Borgschulte, A., et al., *Manipulating the reaction path of the  $\text{CO}_2$  hydrogenation reaction in molecular sieves*. Catalysis Science & Technology, 2015. **5**(9): p. 4613–4621.
215. Chen, L., et al., *Simple strategy for the construction of oxygen vacancies on  $\alpha$ - $\text{MnO}_2$  catalyst to improve toluene catalytic oxidation*. Journal of Hazardous Materials, 2021. **409**: p. 125020.
216. Liu, Y. and P. Zhang, *Removing surface hydroxyl groups of Ce-modified  $\text{MnO}_2$  to significantly improve its stability for gaseous ozone decomposition*. The Journal of Physical Chemistry C, 2017. **121**(42): p. 23488–23497.
217. Huang, Y., et al., *Degradation of gaseous unsymmetrical dimethylhydrazine by vacuum ultraviolet coupled with  $\text{MnO}_2$* . New Journal of Chemistry, 2021. **45**(3): p. 1194–1202.
218. Kakazey, M., et al., *Electron paramagnetic resonance in  $\text{MnO}_2$  powders and comparative estimation of electric characteristics of power sources based on them in the  $\text{MnO}_2$ -Zn system*. Journal of Power Sources, 2003. **114**(1): p. 170–175.
219. Yang, W., et al., *Controllable redox-induced in-situ growth of  $\text{MnO}_2$  over  $\text{Mn}_2\text{O}_3$  for toluene oxidation: Active heterostructure interfaces*. Applied Catalysis B: Environmental, 2020. **278**: p. 119279.
220. Tovar, T.M., et al., *Diffusion of  $\text{CO}_2$  in large crystals of Cu-BTC MOF*. Journal of the American Chemical Society, 2016. **138**(36): p. 11449–

- 11452.
221. Alkhabbaz, M.A., et al., *Important roles of enthalpic and entropic contributions to CO<sub>2</sub> capture from simulated flue gas and ambient air using mesoporous silica grafted amines*. Journal of the American Chemical Society, 2014. **136**(38): p. 13170–13173.
  222. Sillar, K., A. Kundu, and J. Sauer, *Ab initio adsorption isotherms for molecules with lateral interactions: CO<sub>2</sub> in metal–organic frameworks*. The Journal of Physical Chemistry C, 2017. **121**(23): p. 12789–12799.
  223. Pulido, A., et al., *Combined DFT/CC and IR spectroscopic studies on carbon dioxide adsorption on the zeolite H-FER*. Energy & Environmental Science, 2009. **2**(11): p. 1187–1195.
  224. Lee, S., et al., *Porous Zr<sub>6</sub>L<sub>3</sub> metallocage with synergetic binding centers for CO<sub>2</sub>*. ACS applied materials & interfaces, 2018. **10**(10): p. 8685–8691.
  225. Kim, J., K.B. Nam, and H.P. Ha, *Comparative study of HSOA-/SOA2- versus H3- BPO4B-functionalities anchored on TiO<sub>2</sub>-supported antimony oxide–vanadium oxide–cerium oxide composites for low-temperature NO<sub>x</sub> activation*. Journal of Hazardous Materials, 2021. **416**: p. 125780.
  226. An, H.J., et al., *NO<sub>x</sub> reduction consequences of lanthanide-substituted vanadates functionalized with S or P poisons under oxidative environments*. Journal of Materials Chemistry A, 2021. **9**(13): p. 8350–8371.
  227. He, W., et al., *Photogenerated charge carriers and reactive oxygen species in ZnO/Au hybrid nanostructures with enhanced photocatalytic and antibacterial activity*. Journal of the American Chemical Society, 2014. **136**(2): p. 750–757.
  228. Huang, S., et al., *Constructing magnetic catalysts with in-situ solid-liquid interfacial photo-Fenton-like reaction over Ag<sub>3</sub>PO<sub>4</sub>@ NiFe<sub>2</sub>O<sub>4</sub> composites*. Applied Catalysis B: Environmental, 2018. **225**: p. 40–50.
  229. He, X., et al., *Highly efficient simultaneous catalytic degradation and defluorination of perfluorooctanoic acid by the H<sub>2</sub>O<sub>2</sub>-carbon/MnO<sub>2</sub> system generating O<sub>2</sub>-and OH synchronously*. Applied Catalysis B: Environmental, 2020. **277**: p. 119219.
  230. Xiao, J., et al., *Fast electron transfer and •OH formation: key features for high activity in visible-light-driven ozonation with C<sub>3</sub>N<sub>4</sub> catalysts*. ACS Catalysis, 2017. **7**(9): p. 6198–6206.
  231. Villamena, F.A., et al., *Superoxide radical anion adduct of 5, 5-dimethyl-1-pyrroline N-oxide (DMPO). 1. The thermodynamics of formation and its acidity*. The Journal of Physical Chemistry A, 2005. **109**(27): p. 6083–6088.
  232. Lawrence, C.C., et al., *High-field EPR detection of a disulfide radical anion in the reduction of cytidine 5'-diphosphate by the E441Q R1 mutant of Escherichia coli ribonucleotide reductase*. Proceedings of the National Academy of Sciences, 1999. **96**(16): p. 8979–8984.
  233. Prisner, T., M. Rohrer, and F. MacMillan, *Pulsed EPR spectroscopy: biological applications*. Annual review of physical chemistry, 2001.

- 52(1): p. 279–313.
234. Ren, J., et al., *Free radical EPR spectroscopy analysis using blind source separation*. Journal of Magnetic Resonance, 2004. **166**(1): p. 82–91.
  235. Bautista, F., et al., *Continuous flow toluene methylation over AlPO<sub>4</sub> and AlPO<sub>4</sub>-Al<sub>2</sub>O<sub>3</sub> catalysts*. Catalysis letters, 1994. **26**: p. 159–167.
  236. Kim, J., D.B. Go, and J.C. Hicks, *Synergistic effects of plasma-catalyst interactions for CH<sub>4</sub> activation*. Physical Chemistry Chemical Physics, 2017. **19**(20): p. 13010–13021.
  237. Kozmér, Z., et al., *Determination of the rate constant of hydroperoxyl radical reaction with phenol*. Radiation Physics and Chemistry, 2014. **102**: p. 135–138.
  238. Wang, B., et al., *Improved activity and SO<sub>2</sub> resistance by Sm-modulated redox of MnCeSmTiO<sub>x</sub> mesoporous amorphous oxides for low-temperature NH<sub>3</sub>-SCR of NO*. ACS Catalysis, 2020. **10**(16): p. 9034–9045.
  239. Wen, T., et al., *Effect of anions species on copper removal from wastewater by using mechanically activated calcium carbonate*. Chemosphere, 2019. **230**: p. 127–135.
  240. Rodriguez, J.A., et al., *Chemistry of NO<sub>2</sub> on oxide surfaces: formation of NO<sub>3</sub> on TiO<sub>2</sub> (110) and NO<sub>2</sub> ↔ O vacancy interactions*. Journal of the American Chemical Society, 2001. **123**(39): p. 9597–9605.
  241. Szanyi, J., et al., *Characterization of NO<sub>x</sub> species in dehydrated and hydrated Na- and Ba-Y, FAU zeolites formed in NO<sub>2</sub> adsorption*. Journal of electron spectroscopy and related phenomena, 2006. **150**(2–3): p. 164–170.
  242. Makino, K., et al., *Mechanistic studies on the formation of aminoxyl radicals from 5, 5-dimethyl-1-pyrroline-N-oxide in Fenton systems. Characterization of key precursors giving rise to background ESR signals*. Canadian Journal of Chemistry, 1992. **70**(11): p. 2818–2827.
  243. Chávez, A., et al., *Treatment of highly polluted industrial wastewater by means of sequential aerobic biological oxidation-ozone based AOPs*. Chemical Engineering Journal, 2019. **361**: p. 89–98.
  244. Martinez, N.S.S., et al., *Pre-oxidation of an extremely polluted industrial wastewater by the Fenton's reagent*. Journal of hazardous materials, 2003. **101**(3): p. 315–322.
  245. Zhang, G., et al., *The effect of basic pH and carbonate ion on the mechanism of photocatalytic destruction of cylindrospermopsin*. water research, 2015. **73**: p. 353–361.
  246. Liu, Y., et al., *Photochemical degradation of oxytetracycline: Influence of pH and role of carbonate radical*. Chemical Engineering Journal, 2015. **276**: p. 113–121.
  247. Choe, Y.J., et al., *Deploying radical inter-transition from OH to supported NO<sub>3</sub> on Mono-dentate NO<sub>3</sub>--modified ZrO<sub>2</sub> to sustain fragmentation of aqueous contaminants*. Separation and Purification Technology, 2023. **310**: p. 123146.

248. Prabhu, S.M., et al., *A mechanistic investigation of highly stable nano ZrO<sub>2</sub> decorated nitrogen-rich azacytosine tethered graphene oxide-based dendrimer for the removal of arsenite from water*. Chemical Engineering Journal, 2019. **370**: p. 1474–1484.
249. Wang, Z., et al., *One-step synthesis of magnetite core/zirconia shell nanocomposite for high efficiency removal of phosphate from water*. Applied Surface Science, 2016. **366**: p. 67–77.
250. Liu, C., et al., *Effect of zirconia morphology on sulfur-resistant methanation performance of MoO<sub>3</sub>/ZrO<sub>2</sub> catalyst*. Applied Surface Science, 2018. **441**: p. 482–490.
251. Jacob, K.-H., E. Knözinger, and S. Benier, *Adsorption sites on polymorphic zirconia*. Journal of Materials Chemistry, 1993. **3**(6): p. 651–657.
252. Pokrovski, K., K.T. Jung, and A.T. Bell, *Investigation of CO and CO<sub>2</sub> adsorption on tetragonal and monoclinic zirconia*. Langmuir, 2001. **17**(14): p. 4297–4303.
253. Martínez-Arias, A., et al., *Characterization of high surface area Zr–Ce (1: 1) mixed oxide prepared by a microemulsion method*. Langmuir, 1999. **15**(14): p. 4796–4802.
254. Preda, G., et al., *Formation of superoxide anions on ceria nanoparticles by interaction of molecular oxygen with Ce<sup>3+</sup> sites*. The Journal of Physical Chemistry C, 2011. **115**(13): p. 5817–5822.
255. Bolis, V., et al., *Temkin-type model for the description of induced heterogeneity: CO adsorption on group 4 transition metal dioxides*. Langmuir, 1993. **9**(6): p. 1521–1528.
256. Lousada, C.M., et al., *Mechanism of H<sub>2</sub>O<sub>2</sub> decomposition on transition metal oxide surfaces*. The Journal of Physical Chemistry C, 2012. **116**(17): p. 9533–9543.
257. Lousada, C.M., et al., *Reactivity of metal oxide clusters with hydrogen peroxide and water—a DFT study evaluating the performance of different exchange–correlation functionals*. Physical Chemistry Chemical Physics, 2013. **15**(15): p. 5539–5552.
258. Sato, R., et al., *Proton migration on hydrated surface of cubic ZrO<sub>2</sub>: ab initio molecular dynamics simulation*. The Journal of Physical Chemistry C, 2015. **119**(52): p. 28925–28933.
259. Kauppinen, M.M., et al., *Unraveling the role of the Rh–ZrO<sub>2</sub> interface in the water–gas–shift reaction via a first-principles microkinetic study*. ACS Catalysis, 2018. **8**(12): p. 11633–11647.
260. Ma, X., et al., *Heteroatom-doped nanoporous carbon derived from MOF-5 for CO<sub>2</sub> capture*. Applied Surface Science, 2018. **435**: p. 494–502.
261. Sobańska, K., P. Pietrzyk, and Z. Sojka, *Generation of reactive oxygen species via electroprotic interaction of H<sub>2</sub>O<sub>2</sub> with ZrO<sub>2</sub> gel: ionic sponge effect and pH-switchable peroxidase-and catalase-like activity*. ACS Catalysis, 2017. **7**(4): p. 2935–2947.
262. Lousada, C.M. and M. Jonsson, *Kinetics, mechanism, and activation energy of H<sub>2</sub>O<sub>2</sub> decomposition on the surface of ZrO<sub>2</sub>*. The Journal of

- Physical Chemistry C, 2010. **114**(25): p. 11202–11208.
263. Yang, M. and M. Jonsson, *Evaluation of the O<sub>2</sub> and pH effects on probes for surface bound hydroxyl radicals*. The Journal of Physical Chemistry C, 2014. **118**(15): p. 7971–7979.
  264. Kim, M., et al., *Metal-organic framework-derived ZrO<sub>2</sub> on N/S-doped porous carbons for mechanistic and kinetic inspection of catalytic H<sub>2</sub>O<sub>2</sub> homolysis*. Carbon, 2023. **203**: p. 630–649.
  265. Guo, Y., et al., *Transition metal (Pd, Pt, Ag, Au) decorated InN monolayer and their adsorption properties towards NO<sub>2</sub>: Density functional theory study*. Applied Surface Science, 2018. **455**: p. 106–114.
  266. Bauzá, A., A. Frontera, and T.J. Mooibroek, *NO<sub>3</sub><sup>–</sup> anions can act as Lewis acid in the solid state*. Nature Communications, 2017. **8**(1): p. 14522.
  267. Hadjiivanov, K., et al., *Surface species formed after NO adsorption and NO<sup>+</sup> O<sub>2</sub> coadsorption on ZrO<sub>2</sub> and sulfated ZrO<sub>2</sub>: an FTIR spectroscopic study*. Langmuir, 2002. **18**(5): p. 1619–1625.
  268. Wan, D., et al., *Adsorption of nitrate and nitrite from aqueous solution onto calcined (Mg–Al) hydrotalcite of different Mg/Al ratio*. Chemical Engineering Journal, 2012. **195**: p. 241–247.
  269. Del Giacco, T., E. Baciocchi, and S. Steenken, *One-electron oxidation of alkylbenzenes in acetonitrile by photochemically produced nitrate radical: evidence for an inner-sphere mechanism*. The Journal of Physical Chemistry, 1993. **97**(21): p. 5451–5456.
  270. Mvula, E., M.N. Schuchmann, and C. von Sonntag, *Reactions of phenol-OH-adduct radicals. Phenoxyl radical formation by water elimination vs. oxidation by dioxygen*. Journal of the Chemical Society, Perkin Transactions 2, 2001(3): p. 264–268.
  271. Barzaghi, P. and H. Herrmann, *A mechanistic study of the oxidation of phenol by OH/NO<sub>2</sub>/NO<sub>3</sub> in aqueous solution*. Physical Chemistry Chemical Physics, 2002. **4**(15): p. 3669–3675.
  272. Liu, T.-Y., et al., *Oxidative polymerization of bisphenol A (BPA) via H-abstraction by Bi<sub>2</sub>WO<sub>6</sub> and persulfate: Importance of the surface complexes*. Chemical Engineering Journal, 2022. **435**: p. 134816.
  273. Wadhwa, R., et al., *Mechanistic Insights for Photoelectrochemical Ethanol Oxidation on Black Gold Decorated Monoclinic Zirconia*. ACS Applied Materials & Interfaces, 2021. **13**(8): p. 9942–9954.
  274. Chen, D., et al., *UiO-66 derived zirconia/porous carbon nanocomposites for efficient removal of carbamazepine and adsorption mechanism*. Applied Surface Science, 2020. **507**: p. 145054.
  275. Lee, S., et al., *Contrasting Catalytic Functions of Metal Vanadates and Their Oxide Composite Analogues for NH<sub>3</sub>-Assisted, Selective NO<sub>x</sub> Transformation*. Chemistry of Materials, 2022. **34**(3): p. 1078–1097.
  276. Kim, J., et al., *Decrypting Catalytic NO<sub>x</sub> Activation and Poison Fragmentation Routes Boosted by Mono-and Bi-Dentate Surface SO<sub>3</sub><sup>2–</sup>/SO<sub>4</sub><sup>2–</sup>-Modifiers under a SO<sub>2</sub>-Containing Flue Gas Stream*.

- ACS Catalysis, 2022. **12**(3): p. 2086–2107.
277. Zhang, Q., et al., *In situ DRIFTS investigation of NH<sub>3</sub>-SCR reaction over CeO<sub>2</sub>/zirconium phosphate catalyst*. Applied Surface Science, 2018. **435**: p. 1037–1045.
  278. Li, X., et al., *Selective catalytic reduction of NO with NH<sub>3</sub> over novel iron-tungsten mixed oxide catalyst in a broad temperature range*. Catalysis Science & Technology, 2015. **5**(9): p. 4556–4564.
  279. Liu, J., et al., *Low on-resistance diamond field effect transistor with high- $k$  ZrO<sub>2</sub> as dielectric*. Scientific Reports, 2014. **4**(1): p. 6395.
  280. Park, J.H., et al., *Low-temperature, solution-processed ZrO<sub>2</sub>: B thin film: a bifunctional inorganic/organic interfacial glue for flexible thin-film transistors*. ACS applied materials & interfaces, 2015. **7**(8): p. 4494–4503.
  281. Baltrusaitis, J., P.M. Jayaweera, and V.H. Grassian, *XPS study of nitrogen dioxide adsorption on metal oxide particle surfaces under different environmental conditions*. Physical Chemistry Chemical Physics, 2009. **11**(37): p. 8295–8305.
  282. Rosseler, O., et al., *Chemistry of NO<sub>x</sub> on TiO<sub>2</sub> surfaces studied by ambient pressure XPS: products, effect of UV irradiation, water, and coadsorbed K<sup>+</sup>*. The journal of physical chemistry letters, 2013. **4**(3): p. 536–541.
  283. Debeila, M., et al., *The effect of calcination temperature on the adsorption of nitric oxide on Au-TiO<sub>2</sub>: Drifts studies*. Applied Catalysis A: General, 2005. **291**(1–2): p. 98–115.
  284. Parrino, F., et al., *Role of hydroxyl, superoxide, and nitrate radicals on the fate of bromide ions in photocatalytic TiO<sub>2</sub> suspensions*. ACS Catalysis, 2020. **10**(14): p. 7922–7931.
  285. Rittner, F., et al., *Adsorption of nitrogen on rutile (110). 2. Construction of a full five-dimensional potential energy surface*. Langmuir, 1999. **15**(4): p. 1449–1455.
  286. Rittner, F., et al., *Adsorption of nitrogen on rutile (110): Ab initio cluster calculations*. Physical Review B, 1998. **57**(7): p. 4160.
  287. Cerretani, C., et al., *The effect of deuterium on the photophysical properties of DNA-stabilized silver nanoclusters*. Chemical science, 2021. **12**(48): p. 16100–16105.
  288. Scheiner, S. and M. Čuma, *Relative stability of hydrogen and deuterium bonds*. Journal of the American Chemical Society, 1996. **118**(6): p. 1511–1521.
  289. De Visser, S.P., *Substitution of hydrogen by deuterium changes the regioselectivity of ethylbenzene hydroxylation by an oxo-iron-porphyrin catalyst*. Chemistry—A European Journal, 2006. **12**(31): p. 8168–8177.
  290. Wang, J., et al., *Interlayer structure manipulation of iron oxychloride by potassium cation intercalation to steer H<sub>2</sub>O<sub>2</sub> activation pathway*. Journal of the American Chemical Society, 2022. **144**(10): p. 4294–4299.
  291. Jawad, A., et al., *Tuning of persulfate activation from a free radical to*

*a nonradical pathway through the incorporation of non-redox magnesium oxide.* Environmental science & technology, 2020. **54**(4): p. 2476–2488.



## Abstract

본 학위논문에서는 근래 강화되는 수질 규제 및 국민의 눈높이에 부응하기 위한 수계의 오염도 조절의 핵심인 하·폐수의 효율적 안정적 처리를 위한 고도산화공정에 관련된 방법을 제시한다. 고도산화공정이란  $\cdot\text{OH}$ 와 같은 강력한 산화제를 이용하여 유기물을 산화·광물화시키는 방법을 일컫는다.  $\cdot\text{OH}$ 의 경우, addition이나 H abstraction 방법으로 유기물을 광물화하되, 광물화에 가장 큰 활성(환원전위가 가장 큼)을 가지는 화합물로 알려져 있으나, 그 수명이 매우 짧다는 한계점을 갖는다. 반면  $\text{SO}_4^{\cdot-}$ ,  $\text{NO}_3^{\cdot}$ 의 경우, 환원전위가  $\cdot\text{OH}$  대비 다소 작음에도 불구하고, 수명이 획기적으로 길다는 장점을 갖는다. 중요하게도,  $\text{SO}_4^{\cdot-}$ ,  $\text{NO}_3^{\cdot}$ 는 electron transfer가 가능하므로, 이들이 유기물로부터 전자를 제공받아  $\text{SO}_4^{2-}$ ,  $\text{NO}_3^-$ 로 변환된 후, 다시 라디칼화제에 의하여  $\text{SO}_4^{\cdot-}$ ,  $\text{NO}_3^{\cdot}$ 로 재변환 될 수 있다면, 그리고 상술한 라디칼들의 산화환원 현상이 안정적으로 지속될 수 있다면,  $\cdot\text{OH}$ 와 달리 유기물 분해를 위한 라디칼의 사용횟수가 기하급수적으로 늘어날 수 있다.

다시 말해 제한된 또는 극한의 조건에서만 생성되는 라디칼들(예를 들어,  $\text{SO}_4^{\cdot-}$ ,  $\text{NO}_3^{\cdot}$ )을 용이하게 생성시킬 수 있는 방법론에 관한 것이다. 구체적으로  $\cdot\text{OH}$  대비 상대적으로 작은 산화-환원전위(redox potential)를 가짐에도 불구하고, 획기적으로 향상된 수명(lifespan)을 지니는  $\text{SO}_4^{\cdot-}$ ,  $\text{NO}_3^{\cdot}$ 을 금속산화물 표면에 고정시키기 위하여 이들의 전구체인  $\text{SO}_4^{2-}$ ,  $\text{NO}_3^-$  기능기들을 금속산화물 표면에 안정적으로 anchoring시키고, 이들이 라디칼 전이 기작(radical transfer mechanism)에 의하여 전자(electron)를 하나 잃고, 라디칼화(radicalization)되는 방법론에 관한 것이다.

따라서 본 학위논문은 생성된 표면고정화 라디칼인  $\text{SO}_4^{\cdot-}$ ,  $\text{NO}_3^{\cdot}$ 를 고정화하기 위한 지지체로써 다양한 종류의 금속산화물을 사용하여 표면을 기능화 한 뒤, 이를 이용하여 하·폐수의 오염물을 광물화(mineralization)하는 효율을 향상시키는 방법론을 제시함과 동시에 실제 상용화 될 수 있음을 시사한다.